OBSERVATION OF ANTINEUTRINO OSCILLATIONS FROM SPECTRAL DISTORTIONS AT THE DAYA BAY REACTOR NEUTRINO EXPERIMENT

by

Michael C. McFarlane

A dissertation submitted in partial fulfillment of
the requirements for the degree of

Doctor of Philosophy
(Physics Department)

at the
UNIVERSITY OF WISCONSIN–MADISON
2014

Date of final oral examination: May 29, 2014

The dissertation is approved by the following members of the Final Oral Committee:

Karsten Heeger, Professor, Physics
Segev BenZvi, Assistant Scientist, WIPAC
Matthew Herndon, Professor, Physics
Daniel McCammon, Professor, Physics
Stefan Westerhoff, Associate Professor, Physics

© Copyright by Michael C. McFarlane 2014
All Rights Reserved

To the following antineutrinos:

ACKNOWLEDGMENTS

Over the course of my graduate school career, I have lived and labored in the company of many individuals to whom I owe my acknowledgment. More appreciation than I can give is due to my wife Zilin for standing beside me and sharing my life and travails as a graduate student. I also thank my siblings-in-arms, fellow students Adam Dally, Paul Hinrichs, Bryce Littlejohn, Christine Lewis, Larissa Milicic and Dante Passmore as we pursued research together, assisted one another, and commiserated. I am grateful to post-docs Wei Wang and David Webber for their expertise, direction and mentoring whenever I needed it. I thank my advisor Karsten Heeger for providing me the opportunity to be a part of our collaboration, and Baha Balantekin for his insights. It was a privilege to work alongside great scientists and engineers such as Tom Wise, Jeff Cherwinka, Qiang Xiao and Patrick Huber at Wisconsin, and many Daya Bay collaborators, who made our experiment a success. It is my further honor to have worked with and befriended many young Daya Bay collaborators from the US and other nations. During my life at the University of Wisconsin, I bonded with many classmates who provided me with stimulating discussions and joyful company; among them are Michael Glatzmaier, Elliot Kaplan, Tom Garvey, Andrew Long, Paul McGuirk, Hiren Patel, Michael Baker, Daniel Sikes, Mark Stockett, Don Huynh, Steve Sendelbach, Carl Pfendner and Jeff Klukas. I would like to thank members of my defense committee, Segev BenZvi, Matthew Herndon, Daniel McCammon and Stefan Westerhoff, for taking the time to learn about my research. Finally, I acknowledge my parents, brother and extended family for providing me support and the occasional needed respite.

DISCARD THIS PAGE

TABLE OF CONTENTS

Page

LIST OF TABLES . . . viii

LIST OF FIGURES . . . xiii

NOMENCLATURE . . . xxxv

ABSTRACT . . . xxxvii

1 Neutrino and Particle Physics . . . 1

1.1 The Standard Model of Particle Physics . . . 1
1.1.1 Particles of the Standard Model . . . 2
1.1.2 Forces . . . 5
1.2 Theory of Massive Neutrinos . . . 10
1.2.1 Neutrino Mass . . . 11
1.2.1.1 Experimental Limits . . . 12
1.2.1.2 Theoretical Descriptions . . . 12
1.2.2 Neutrino Mixing . . . 16
1.2.3 Neutrino Oscillation . . . 18
1.2.4 Neutrino Oscillation Parameters . . . 20
1.3 History of Neutrino Experiments . . . 23
1.3.1 Detection of Neutrinos . . . 23
1.3.1.1 Savannah River and Hanford, 1953–1956 . . . 23
1.3.1.2 Davis Experiment, 1954 . . . 25
1.3.1.3 Parity Violation, 1957 . . . 25
1.3.1.4 Neutrino Helicity, 1958 . . . 26
1.3.1.5 Brookhaven Neutrino Experiment, 1962 . . . 26
1.3.1.6 Charge-Parity Violation, 1964 . . . 27
1.3.1.7 Homestake 1970–1994 . . . 29
1.3.1.8 Supernova SN1987A: IMB, Kamiokande-II and Baksan . . . 30
1.3.1.9 DONUT, 2000 . . . 31
1.3.2 Neutrino Oscillations . . . 33

Page

1.3.2.1 Super Kamiokande . . . 33
1.3.2.2 Sudbury Neutrino Observatory . . . 35
1.3.2.3 KamLAND . . . 39
1.3.2.4 K2K . . . 41
1.3.2.5 Main Injector Neutrino Oscillation Search . . . 44
1.3.2.6 Liquid Scintillator Neutrino Detector . . . 45
1.3.2.7 Mini Booster Neutrino Experiment (MiniBooNE) . . . 47
1.3.2.8 T2K . . . 48
1.3.2.9 Bugey . . . 50
1.3.2.10 Palo Verde and Chooz . . . 51
1.3.2.11 RENO and Double Chooz . . . 53
1.3.3 Significance of the Measurement of θ_{13} . . . 54

2 Daya Bay Strategy and Overview . . . 59

2.1 Antineutrinos at Daya Bay . . . 60
2.2 Relative Measurement . . . 64
2.3 Detection Principle . . . 66
2.4 History . . . 66
2.5 Summary . . . 67

3 Reactor Antineutrino Flux Prediction . . . 69

3.1 Operation of Pressure Water Reactors . . . 69
3.2 Information Provided by the Power Plant . . . 71
3.3 Flux Modeling . . . 73
3.4 IBD Prediction . . . 77
3.5 Antineutrino Prediction Uncertainties . . . 78
3.6 Summary . . . 82

4 Daya Bay Detector Construction . . . 83

4.1 Detector Construction . . . 84
4.1.1 Liquid Composition . . . 85
4.1.2 Acrylic and Steel Vessels . . . 86
4.1.3 Light Collection . . . 88
4.1.4 Detector Monitoring . . . 89
4.1.5 Detector Filling . . . 90
4.2 Calibration . . . 92
4.2.1 Automated Calibration . . . 93

Page

4.2.2 Manual Calibration . . . 95
4.3 Underground Sites . . . 96
4.3.1 Water Pool Muon Veto . . . 97
4.3.2 Resistive Plate Muon Veto . . . 98
4.4 Summary . . . 99

5 Detector Monitoring Cameras . . . 102

5.1 Goals and Design Requirements of the System . . . 102
5.1.1 Design Specifications . . . 104
5.2 Design of the Monitoring Camera System . . . 107
5.2.1 Camera and Optics . . . 107
5.2.2 Lighting . . . 110
5.2.3 Integration into Detector . . . 113
5.2.4 System Readout and Control . . . 116
5.3 Background Levels . . . 121
5.4 Performance . . . 121
5.5 Summary . . . 122

6 Daya Bay Detector Analysis . . . 127

6.1 Data Sets . . . 128
6.2 Reconstructed Energy and Position . . . 129
6.2.1 Position Reconstruction . . . 129
6.2.2 Energy Reconstruction . . . 130
6.3 Selection Cuts for Antineutrino-Induced IBD Events . . . 132
6.3.1 Good Run Selection . . . 133
6.3.2 Prompt Energy Cut . . . 134
6.3.3 Delayed Energy Cut . . . 135
6.3.4 Prompt-Delayed Time Cut . . . 136
6.3.5 PMT Flasher Cut . . . 137
6.3.6 Muon Rejection . . . 139
6.3.7 Multiplicity Cut . . . 140
6.4 Corrections for Detector Effects . . . 141
6.5 Backgrounds . . . 142
6.5.1 Accidental Background . . . 142
6.5.2 Muon-Induced ^{9}Li and ^{8}He Background . . . 142
6.5.3 Fast Neutrons Background . . . 143
6.5.4 Americium Carbon and Carbon Alpha Backgrounds . . . 144
6.6 Summary . . . 146

Page

7 Prediction and Modeling of Daya Bay Sensitivity to θ_{13} . . . 148

7.1 Daya Bay Experiment Modeling . . . 149
7.1.1 IBD Event Rates and Detector Efficiencies . . . 151
7.1.2 Backgrounds . . . 152
7.2 Daya Bay Experiment Model . . . 153
7.2.1 Daya Bay Model χ^2 . . . 153
7.2.2 Systematic Uncertainties . . . 156
7.3 Daya Bay Sensitivity to $\sin^2 2\theta_{13}$ . . . 158
7.3.1 Sensitivity and Discovery Reach . . . 159
7.3.2 Systematic Uncertainty Studies . . . 161
7.3.3 Limited Detector Sensitivity . . . 167
7.3.3.1 Early Measurement of $\sin^2 2\theta_{13}$ . . . 167
7.3.3.2 Lost Detectors . . . 172
7.4 Summary . . . 173

8 Oscillation Analysis Modeling and Validation . . . 174

8.1 Daya Bay Experiment Model . . . 174
8.1.1 Physical Processes and Systematics . . . 176
8.1.1.1 Predicted Reactor Spectra . . . 180
8.1.1.2 Fission Fraction . . . 181
8.1.1.3 Spent Nuclear Fuel . . . 181
8.1.1.4 Nonequilibrium Flux . . . 182
8.1.1.5 $\beta \to \bar{\nu}$ Conversion . . . 182
8.1.1.6 Oscillation and Reactor Flux Summation . . . 183
8.1.1.7 IAV Correction . . . 185
8.1.1.8 Detector Nonlinearity and Energy Scale . . . 187
8.1.1.9 Energy Resolution . . . 188
8.1.1.10 Rebinning . . . 190
8.1.1.11 Backgrounds . . . 190
8.1.1.12 Detector and Energy Bin Normalizations . . . 195
8.1.2 χ^2 Model . . . 195
8.1.3 Numerical χ^2 Minimization . . . 198
8.2 Validation with Internal Monte Carlo . . . 199
8.2.1 Monte Carlo Generation . . . 199
8.2.2 Validation on Monte Carlo Without Statistical Fluctuations . . . 200
8.2.2.1 Best Fits . . . 200
8.2.2.2 Best Fit Diagnostics . . . 201
8.2.2.3 Accuracy over Wider $\sin^2 2\theta_{13}$ and Δm^2_{32} Ranges . . . 209

Page

8.2.2.4 Error Budget . . . 212
8.2.2.5 Best Fits Versus N_{bins} . . . 214
8.2.3 Validation on Monte Carlo with Statistical Fluctuations . . . 215
8.2.4 Many Monte Carlo with Statistical Fluctuations . . . 225
8.2.4.1 Oscillation Parameter Spread . . . 225
8.2.4.2 Fitting with Only Oscillation Parameters . . . 230
8.2.5 Commutation of Model Components . . . 230
8.3 Validation with External Monte Carlo . . . 232
8.4 Summary . . . 234

9 Measurements of Oscillation Parameters $\sin^2 2\theta_{13}$ and Δm^2_{32} . . . 236

9.1 Primary Measurement of $\sin^2 2\theta_{13}$ and Δm^2_{32} . . . 236
9.1.1 Best Fit Results . . . 237
9.1.2 Best Fit Diagnostics . . . 239
9.1.3 Energy Scale Treatment . . . 246
9.1.4 Best Fit Spectra . . . 252
9.1.5 Error Budget . . . 252
9.1.6 Best Fit Versus Number of Bins . . . 257
9.1.7 Alternate Flux Models . . . 259
9.1.8 Search for Alternate Minima . . . 260
9.1.9 Treatment of ^{238}U Systematic . . . 262
9.2 Measurement with Constrained Δm^2_{32}, and Neutrino Mass Hierarchy . . . 265
9.2.1 Best Fits . . . 268
9.2.2 Best Fit Diagnostics . . . 270
9.3 Measurement with Detector Rates Only . . . 276
9.3.1 Best Fit Results . . . 276
9.3.2 Best Fit Diagnostics . . . 279
9.4 Measurement with Spectral Distortions Only . . . 286
9.4.1 Best Fits . . . 286
9.4.2 Best Fit Diagnostics . . . 287
9.4.3 Energy Scale Treatment . . . 295
9.5 Summary of Oscillation Measurements . . . 296

10 Conclusion . . . 299

LIST OF REFERENCES . . . 301

DISCARD THIS PAGE

LIST OF TABLES

Table Page

1.1 Experimental neutrino properties [1, 2]. 12

1.2 The state of knowledge of the neutrino mixing parameters from global data at the time of the analysis presented in this dissertation [1, 2, 3]. The value of $|\Delta m^2_{31}| \approx |\Delta m^2_{32}|$ has been more recently measured to be $2.41^{+0.09}_{-0.10} \cdot 10^{-3}\,\mathrm{eV}^2$ [4]. In that case, $m_1 + m_2 + m_3 > 5.85^{+0.0895}_{-0.101} \cdot 10^{-2}$ eV. 57

1.3 Comparison of RENO, Double Chooz and Daya Bay experiments. Note that Double Chooz has not constructed its near detector yet, and that Daya Bay's published measurements are based on six-detector data [5]. 57

1.4 Systematic uncertainties in % (correlated and uncorrelated) for RENO, Double Chooz and Daya Bay. Since Double Chooz has only the far detector at the moment, Double Chooz uncertainties do not break down into correlated and uncorrelated [5]. 58

2.1 Detector to reactor baselines in meters for the six-detector configuration of the Daya Bay experiment [6]. At each nuclear power plant (NPP), the higher-numbered reactor core is west of the lower-numbered core. At the Daya Bay near site, detector 2 is east of detector 1, while at the Ling Ao near site, the detector is south of the open slot. At the far site, detectors 1 and 2 are closest to the reactors, while detectors 1 and 3 are east of detector 2 and the open slot. 63

3.1 The fractions of the top four isotopes in the reactors at the beginning and end of the fuel cycle [7], and on average [8]. 73

3.2 Energy released as the given isotope fissions, and the fission products decay until stable nuclei remain [9]. 73

4.1 The rock overburden in meters and meters of water equivalent (m.w.e.), and muon rates and energies incident on the detectors, at each underground site. . 97

Table Page

5.1 Total radioactivity level of one camera assembly. The activity of an assembly is dominated by ^{232}Th-chain decays, and the total activity is lower than a typical PMT [10]. 121

6.1 Daya Bay's data sets from the installation of the first two detectors to present. The first data set was used to assess the identicalness of the detectors; the rest were dedicated to oscillation analyses with published results indicated. The quantity Δm^2_{ee} is a linear combination of Δm^2_{31} and Δm^2_{32}, which are indistinguishable at Daya Bay because their difference is much smaller than the precision at which they can be measured. 128

6.2 Summary of detector runs during the three month Data Set 0. Proportion of rejected runs and reasons are indicated [11]. 134

6.3 Rates of antineutrino candidate IBD events and various backgrounds and uncertainties for Data Set 3 [3]. 147

6.4 Summary of detector-independent absolute efficiencies, and correlated and uncorrelated systematic uncertainties for Data Set 3 [3]. *The total efficiency listed does not include the detector-dependent components from the muon and multiplicity cuts that are shown in Table 6.5. 147

6.5 Detector-dependent efficiencies for the muon and multiplicity cuts reported for Data Sets 2 and 3. 147

7.1 IBD event rates per day per 20 ton detector given the baselines in Figure 7.1. Also provided are the event rates including detection efficiencies from Table 7.2, and with a live-time of 300 days per year. The simulated event rates are within 10% of the latest detected rates (Table 6.3). 152

7.2 Summary of all detection efficiencies in the simulation model based on the Technical Design Report and detector simulations [12]. 153

7.3 Systematic uncertainty values in the sensitivity model. 0.38% is the nominal value of the detector systematic uncertainty given in the Daya Bay proposal, but 0.18% was seen as attainable. 157

Table Page

7.4 Sensitivity (90% confidence limit) and 3σ and 5σ discovery reach for various detector uncertainty values and running times. Scenarios with σ_{det}=0.12% were considered during the design of the experiment, to be pursued by swapping detectors among sites. But this plan was eliminated due to operational constraints of the experiment and lack of need. 165

7.5 Sensitivity to $\sin^2 2\theta_{13}$ at various combinations of reactor flux normalization and reactor fuel composition uncertainties, assuming either σ_{det} equal to either 0.18% or 0.38%. 166

7.6 Comparison of candidate six detector deployment schemes. Values are the 3σ discovery limit assuming a detector systematic uncertainty of 0.38% [13]. . . . 169

8.1 The sequence of corrections and uncertainties applied in the antineutrino prediction model, starting from the initial antineutrino flux predicted at the reactors to the final antineutrino expectation at the detector based on oscillations, and reactor and detector effects. The number of fitting parameters, and their correlations are shown: "U" indicates uncorrelated, "C" indicates correlated, "—" indicates no relevance. 177

8.2 The values of systematic uncertainties in the model; see Table 8.1 for descriptions. Where uncertainties are listed at 100%, the uncertainty is relative to the size of the correction not the detector data. Of these, all corrections but detector response take the form of fixed spectra added with a normalization nuisance parameter. The detector normalization uncertainty is reduced from 0.20% to 0.16% when the effect of the energy scale on the 6 MeV cut is accounted for explicitly by the $0.24\eta_{scale}$ term, which is the default choice. The IAV and $\beta \to \bar{\nu}$ conversion uncertainties each have two components, energy-correlated/detector-uncorrelated and energy-uncorrelated/detector-correlated. The energy-uncorrelated/detector-correlated components are absorbed into the bin normalization. Background uncertainties and are quoted as a percentage of the background rate. 178

8.3 Oscillation parameter values assumed in the model. By choice, Δm^2_{32} is the fit parameter and Δm^2_{31} is constrained to $\Delta m^2_{31} = \pm\Delta m^2_{32} + \Delta m^2_{21}$, where +1(–1) is for normal(inverted) hierarchy. 186

Table Page

8.4 Fits to a five-point grid of $\sin^2 2\theta_{13}$ and Δm^2_{32}: (0.01, $2.35{\cdot}10^{-3}\,\mathrm{eV}^2$), (0.07, $2.05{\cdot}10^{-3}\,\mathrm{eV}^2$), (0.13, $2.05{\cdot}10^{-3}\,\mathrm{eV}^2$), (0.07, $2.65{\cdot}10^{-3}\,\mathrm{eV}^2$), (0.13, $2.65{\cdot}10^{-3}\,\mathrm{eV}^2$), with rate+shape and rate-only χ^2s. The fitter replicates the expected results to at least 30 parts per million. 210

8.5 The error budget for a Monte Carlo without statistical fluctuations. The size of each contribution is a determined by a trade off between the physical importance of the uncertainty and its magnitude. Important systematics like the detector uncorrelated normalization are understated because the uncertainty value is small. 213

9.1 The contribution of each systematic to the χ^2_{min} value of the rate and shape analysis. Except for the statistical part, the quantities above are the size of each set of pull terms $(\eta_\iota/\sigma_\iota)^2$, in total and where applicable averaged per detector, reactor or bin. The statistical part is the lead term in the χ^2: $\chi^2 - \sum(\eta_\iota/\sigma_\iota)^2$. The percentages are based on the total pull terms per systematic. 248

9.2 Rate and shape analysis results with either the energy scale fit parameters disabled (primary analysis) or enabled. 252

9.3 Error budget computed for $\sin^2 2\theta_{13}$ and Δm^2_{32} via one- or zero-systematic fits. Asterisks denote sign reversal in Equation 9.5. 258

9.4 Rate and shape analysis with three antineutrino flux models. Huber-French is the primary flux model of this analysis. The oscillation parameter measurements vary little, but the overall normalization $\mathcal{H}$ varies to match the predicted rates. 260

9.5 Rate and shape analysis with the spectral uncertainty of the ^{238}U either energy-correlated or energy-uncorrelated. The nominal case is energy-uncorrelated. . . 265

9.6 Rate and shape analysis with different cases of Δm^2_{32} constraint or hierarchy. Units of Δm^2_{32} and Δm^2_{31} are $10^{-3}\mathrm{eV}^2$ and NH(IH) stands for normal(inverted) hierarchy. Δm^2_{31} is not fit, but equated to either $\Delta m^2_{31} = \Delta m^2_{21} + \Delta m^2_{32}$ (NH) or $\Delta m^2_{31} = \Delta m^2_{21} - \Delta m^2_{32}$ (IH). 268

9.7 The contribution of each systematic to the value of χ^2_{min} for a rate and shape analysis with Δm^2_{32}=2.32±0.12 and normal hierarchy. Except for the statistical part, the quantities listed are the size of each set of pull terms $(\eta_\iota/\sigma_\iota)^2$, in total and where applicable averaged per detector, reactor or bin. The percentages are based on the total pull terms per systematic. The statistical part is the lead term in the χ^2: $\chi^2 - \sum(\eta_\iota/\sigma_\iota)^2$. 271

Table Page

9.8 The reduction of uncertainties in the rate-only analysis. Uncertainties listed on the indented lines are combined into a single uncertainty above. Correlations are also listed: "U" indicates uncorrelated, "C" indicates correlated, "—" indicates no relevance. 277

9.9 The contribution of each systematic to χ^2_{min} for the rate-only analysis. Except for the statistical part, the quantities above are the size of each set of pull terms $(\eta_\iota/\sigma_\iota)^2$, in total and where applicable averaged per detector, reactor or bin. The statistical part is the lead term in the χ^2: $\chi^2 - \sum(\eta_\iota/\sigma_\iota)^2$. The percentages are based on the total pull terms per systematic. 284

9.10 The contribution of each systematic to χ^2_{min} from a shape-only analysis. Except for the statistical part, the quantities above are the size of each set of pull terms $(\eta_\iota/\sigma_\iota)^2$, in total and where applicable averaged per detector, reactor or bin. The statistical part is the lead term in the χ^2: $\chi^2 - \sum(\eta_\iota/\sigma_\iota)^2$. Since the detector normalizations are unconstrained but the overall normalization is disabled, the number of degrees of freedom is lower than the rate and shape analysis by five. 293

9.11 Shape-only analysis results with either the energy scale fit parameters disabled (baseline choice) or enabled. 295

DISCARD THIS PAGE

LIST OF FIGURES

Figure Page

1.1 A diagram of the elementary particles in the Standard Model. Quarks, leptons, force carriers and the Higgs Boson are grouped according to generation, electric charge, interaction, mass, and spin [14]. 3

1.2 The strength of the four fundamental forces as a function of distance. For particle interactions, the strong force is much stronger than electromagnetism, which is much stronger than the weak force, while gravitation is negligible. Gravitation and electromagnetism follow straight $1/r^2$ dependences, whereas the strengths of the weak and strong forces drop precipitously beyond atomic radii [15]. 7

1.3 The Feynman diagram of the basic strong interaction vertex, the constituent of strong interaction processes. Two quarks q of colors c and c' interact at a vertex with a gluon carrying colors c and $\bar{c}'$, the opposite of c'. If time is read in the upward direction, a quark is emitting a gluon and changing color. Other interaction vertices exist that couple three or four gluons together, but the impact of these is highly suppressed in interactions. 8

1.4 The Feynman diagram of the basic electromagnetic vertex, the constituent of electromagnetic processes. Two charged particles, either a lepton l or a quark q, join at a vertex with a photon γ. If time is read as flowing vertically, the diagram represents emission of a photon; horizontally, it represents pair production or annihilation. 9

1.5 The three most common basic Feynman diagrams for the weak interaction, corresponding to the three force carriers W^+, W^- and Z. For these diagrams, time flows top to bottom. When a charged lepton emits a W, the W carries the charge while an (anti)neutrino is created to conserve lepton number. When a quark emits a W, the resulting quark must carry the charge that balances the reaction, for instance a quark of charge $+2/3$ in the initial state and a W^+ and a quark of charge $-1/3$ in the final state. This does not conserve quark flavor. 10

Figure Page

1.6 Graphical representation of the mixing angles θ_{ij} as rotations between mass and flavor eigenstates [16]. 17

1.7 Electron neutrino survival probability assuming the parameter values of Table 1.2, over a wide range of neutrino energies and baselines. 20

1.8 Relative neutrino mass-squared values plotted against mass eigenstate flavor content for normal and inverted hierarchies. For this graph, mixing angles are set to: $\sin\theta_{12} = 0.30$, $\sin\theta_{13} = 0.03$ and $\sin\theta_{23} = 0.50$ [17, 18]. 22

1.9 Illustration of Savannah River detector [19, 20]. 24

1.10 Diagram of the beam and shielding of the Brookhaven neutrino experiment [21]. 28

1.11 Schematic of the Homestake experiment [22]. 29

1.12 Readout of the Kamiokande-II events in a 45 s interval about the neutrino burst. The height of each line indicates the relative energy of the event. Solid lines represent electron events in units of the number of hit PMTs. Dashed fines represent muon events in units of the number of photoelectrons. [23] 31

1.13 The timing and energy of the Baksan, IMB and Kamiokande-II experiments' detection of SN1987a neutrinos [24]. 32

1.14 Diagram of the DONUT experiment [25]. 33

1.15 Drawing of Super Kamiokande detector [26]. 34

1.16 Zenith angle distributions of Super Kamiokande events associated with muon and electron neutrinos, grouped by energy: above or below 1.33 GeV. Events with $\cos\theta < 0$ are traveling upward, traversing a chord through the Earth in addition to traveling through the atmosphere. Such events show a greater deficit than neutrinos traveling through the atmosphere alone. This is the first evidence of neutrino oscillations [27]. 36

1.17 Super Kamiokande fits for $\sin^2\theta_{23}$ and Δm^2_{23} assuming normal hierarchy (left) and inverted hierarchy (right) [28]. 37

1.18 Diagram of the SNO detector [29]. 38

Figure Page

1.19 Left: SNO-only oscillation fits with Phase 1–3 data, including neutral current, charged current and elastic scattering events. Center and right: after the inclusion of KamLAND data [30]. 39

1.20 Diagram of the KamLAND detector [31]. 40

1.21 The ratio of detected electron antineutrino flux divided by expectation for KamLAND and previous experiments. The diameter of the KamLAND marker is indicative of the reactor distance uncertainty. The dashed line and shaded region indicate contemporary best fits on oscillation parameters and error margins; the dashed line represents no flavor mixing. [31] 41

1.22 Left: KamLAND reactor electron antineutrino energy spectrum compared to both a no-oscillation hypothesis and the best fit oscillation. The no-oscillation hypothesis is ruled out at over 5σ. Right: Best fit contours for neutrino oscillation parameters θ_{12} and Δm^2_{21} [32]. 42

1.23 K2K near detector. From left to right: the water Cherenkov detector, the scintillator fiber and water-target tracker, the second scintillating apparatus, and the muon range detector. A lead-glass calorimeter was once in place of the second scintillator [33]. 43

1.24 Best fit oscillation parameters from K2K [34]. 44

1.25 Diagram of the NuMI beam [35]. 45

1.26 MINOS shows evidence of neutrino oscillations in muon neutrino and antineutrino data [4]. 46

1.27 Left: LSND electron antineutrino excess versus energy. The shaded region shows the expected distribution from neutrino oscillations and backgrounds. Right: LSND-favored oscillation parameters compared to exclusion contours of previous experiments [36]. 47

1.28 A diagram of the MiniBooNE beam and detector [37]. 48

Figure Page

1.29 Allowed neutrino oscillation parameters at the indicated confidence limits for MiniBooNE compared to the LSND, KARMEN and ICARUS experiments. The stars indicate the MiniBooNE best fits, but although the best fit contours for neutrinos are shown, the absolute agreement of the neutrino data and oscillations are low. There is possible agreement between MiniBooNE and LSND for antineutrinos, but much less agreement for neutrino data. 49

1.30 The reactor electron antineutrino oscillation parameters excluded by Bugey are shown, indicated by the label "THIS EXPERIMENT", along with exclusions from previous experiments at Goesgen and Krasnoyarsk [38, 39, 40]. The Kamiokande contour refers to a then-allowed region of oscillation parameters. The true mass-splitting for reactor antineutrinos is now known to fall below the range of the y-axis. 51

1.31 Values of $\sin^2 2\theta_{13}$ greater than the Palo Verde and Chooz contours were excluded at 90% confidence (the plot is from Palo Verde [41]). The Palo Verde result is shown for two analysis methods described in the reference. Also shown is the allowed space for muon neutrino to electron neutrino oscillations to explain the atmospheric neutrino anomaly reported by Kamiokande. 52

1.32 Detector diagrams for RENO, left, and Double Chooz, right [42, 43]. 54

1.33 World measurements of $\sin^2 2\theta_{13}$ since 2011 [44]. 56

2.1 Left: Daya Bay is indicated by the blue marker on China's southern coast. Right: Daya Bay nuclear power station with detectors and reactors indicated [45, 46]. . 60

2.2 The available parameter space for $\sin^2 2\theta_{13}$ and Δm^2 at 90% confidence, prior to the construction of Daya Bay [47]. Δm^2 is the two-neutrino oscillation approximation to Δm^2_{31} and Δm^2_{32}. The goal of Daya Bay is to exclude the vast majority of this space; a line drawn demarcating Daya Bay's sensitivity would fall just inside the left minor tick marks. 61

2.3 The antineutrino spectra for the top four reactor isotopes that comprise 99.9% of the reactor antineutrino flux [48]. 62

Figure Page

2.4 Left: The topography of the Daya Bay experiment. Eight detectors are deployed at three underground sites to observe the antineutrino flux from six reactors. The baselines between the detectors and reactors are indicated. The mountain overburden above the detectors is shown in the inset. Right: The oscillation probability for reactor antineutrinos. The near sites observe the antineutrino flux at little probability of oscillation, while the far site observes the flux at maximal sensitivity to $\sin^2 2\theta_{13}$ and minimal sensitivity to other mixing parameters. The vertical dashed lines indicate the flux-weighted average baselines of the three sites. 63

2.5 The electron antineutrino survival probability versus energy at the Daya Bay near site, Ling Ao near site, and far site, for the sample case of $\sin^2 2\theta_{13}$=0.10. . 65

2.6 Diagram of inverse beta decay, $\overline{\nu}_e + p \rightarrow n + e^+$. An antineutrino enters the target volume, then interacts with a proton to generate a neutron and positron. The positron annihilates promptly while the neutron captures on a gadolinium shortly after. The energy released and timing provides Daya Bay with a unique signal of an antineutrino. 67

3.1 Diagram of a Pressurized Water Reactor [49]. 70

3.2 Left: diagram of a fuel assembly consisting of pure fuel rods, guide rods and an instrument tube. Right: the combination of fuel assemblies into a core, with regular and instrumented fuel rods [48]. 71

3.3 The composition of the reactor fuel as a function of burn up [50]. ^{235}U is converted to ^{239}Pu and ^{241}Pu as the burn up progresses. 74

3.4 The antineutrino spectra for the top four reactor isotopes that comprise 99.9% of the reactor antineutrino flux [48]. 75

3.5 Comparison of the three flux models, ILL, Mueller and Huber [7]. From left to right, the plots show the flux predictions for ^{235}U, ^{239}Pu, and ^{241}Pu, relative to the ILL flux. The error bars of the top plot are uncorrelated in energy, while the error bars of the bottom plot are energy-correlated. 76

3.6 The black line shows a toy model of the detected antineutrino spectrum, in arbitrary units, which is a product of the antineutrino flux and IBD cross-section. The red increasing line shows the IBD reaction cross-section as a function of antineutrino energy, while the blue decreasing line shows a typical antineutrino flux [8]. 79

Figure Page

3.7 The five reactor uncertainty spectra, which can be added to, or subtracted from the flux prediction, normalized by the associated uncertainty [51, 52]. The small contributions at low energies are uncertainties from spent nuclear fuel and the nonequilibrium corrections. The medium-sized uncertainty is from the fission fraction, which has a linear trend from 2–8 MeV. The largest two uncertainties are the energy-correlated, and energy-uncorrelated components of the $\beta \rightarrow \bar{\nu}$ conversion uncertainty. The ^{238}U is modeled as part of the energy correlated uncertainty in this case. 81

4.1 A diagram of a detector with several components labeled [53]. 85

4.2 Illustration of the stainless steel vessel, with lid at right [8]. 87

4.3 Illustration of the inner and outer acrylic vessels with key features labeled [54]. 88

4.4 Explanation of detector overflow tanks (top) and lid sensors contained therein (bottom) [55]. The overflow tanks can be seen in context on the detector in Figure 4.1. 91

4.5 Automated calibration unit open to the inside [56]. Calibration sources and motion and monitoring devices are labeled. 94

4.6 Conversion from LED voltage to photoelectrons using the calibration LED and diffusing ball apparatus in a dry detector [56]. 95

4.7 Schematic of the manual calibration system: (a) before source rod insertion into the detector, and (b) after insertion and deployment of the source arm [57]. . . 96

4.8 The energy spectra for muons passing through the overburden at each site. The two near site spectra are indistinguishable on this plot. The overburden is higher at the far site, which disproportionately attenuates lower energy muons. 98

4.9 Diagram of two detectors in a near site muon veto consisting of a water pool and RPCs [58]. 99

4.10 Diagram of detectors in a near site pool (left) and four detectors in a far site water pool (right) [59]. 100

4.11 A cross-section of a single RPC plate [59]. Narrow strips in this plate read out the position of a passing charged particle in one dimension. An assembly of four of the plates provide the location and trajectory of a through-going muon. . . . 101

Figure Page

4.12 The far site with all four detectors during the filling of the muon veto water pool [60]. 101

5.1 The monitoring cameras, indicated by the white arrows, in the context of the detector [53]. 104

5.2 Left: front of camera on bench during preparation for installation. The camera opening and light source are prominent. Center: back of camera during assembly with power and readout cables, leak-tight feed-throughs and leak check port are visible. Right: camera on PMT support ladder showing the adjustable mount that attaches it in place. The components and system design are explicated in the sections to follow. 105

5.3 Left: Views from the cameras in an empty detector with some features labeled for reference. Right: Cutaway view of the detector with opaque inner acrylic vessel. Shaded triangles show design vertical field of view, which is 43° in an empty detector and 30° when filled with liquid scintillator. Cameras are installed with a 6° tilt away from the center of the detector to provide a better view of critical features. 105

5.4 Top-down view of detector lid schematic, with camera locations and detector features indicated. Shaded regions show design lateral field of view: 56° in an empty detector and 37° after filling. Both cameras are panned 7° counterclockwise with respect to this view axis in order to photograph more critical features. 106

5.5 Left: Back view of camera installed on a PMT ladder. Right: Front view of camera installed on a PMT ladder. Major features of the camera assembly and PMT ladder are labeled. 108

5.6 Left: The IDS *UI5480SE-MGL*, the camera chosen for this system. Right: The relative quantum efficiency of: the camera (blue solid line) [61, 62], the emission spectrum of the infrared LEDs (red dotted line) [63], and the Hamamatsu *R5912* PMTs used in the detectors (green dashed line) [64]. The LED spectrum overlaps with the camera sensor spectrum, while overlapping minimally with the PMTs. 110

Figure Page

5.7 Top: The LED illumination element at the front of the camera assembly. The assembly includes five rings of LEDs, of which the outer and inner rings are white LEDs and the middle three are infrared. The camera peers through a light baffle at the center of the portal. Bottom: Diagram of the light baffle consisting of two opposing rings and a perpendicular annulus. The baffle prevents the backward reflection of LED light into the camera. 112

5.8 Hit rates of an empty detector with camera and infrared LEDs off (black triangles), camera on and infrared LEDs off (red circles), and camera off and infrared LEDs at 10% luminosity (blue squares). The infrared LEDs cause an increase in hit rates in a dry detector. Dashed lines represent averages [65]. 113

5.9 Right: Assembly of camera components. Top Left: A camera during assembly. The front portal and LEDs have been attached; the cables have been connected, passed through the back flange and secured; the adjustor plate has been connected and positioned and the camera awaits connection with internal electrical components, followed by vessels closure. Bottom Left: Rendered model showing the camera enclosure assembled and adjusted, as though installed in a detector [53]. 114

5.10 Left: Back view of top camera newly installed on a PMT ladder, awaiting installation of PMTs. Center: Back view of top camera installed at the top of a PMT ladder loaded with PMTs, awaiting installation into a detector. Right: Front view of top camera installed in a detector. Key detector features are labeled. . 116

5.11 Schematic of the readout system. The center and top left of the diagram describes the readout system in the electronics rack outside the detector. To the left, separated by a double dotted line (coaxial cable) are the loads: the camera and LEDs inside the detector. To the bottom right is an Ethernet to coaxial cable conversion circuit using balun transformers. This simplified schematic depicts one camera control; each readout box controls four cameras in parallel. An Ethernet-controlled relay selects one camera and light source to power at a time. 118

5.12 One panel of the control software. The user can operate the LED light source in the upper left, readout power supply and relay bank statuses in the lower left, adjust camera settings in the lower right, and check a preview of the image in the upper right. Functions not shown include: device connection, network monitors, image saving, image autosaving, image commenting, interlocks and some alarms. 120

Figure Page

5.13 Left: Gamma spectrum of one assembled camera [10]. Black, thin peaks denote the measurement chamber alone; thick red denotes the measurement of the camera system and chamber. Right: Difference between camera and background radiation. The camera activity is typically consistent with background. The sharp, upward and downward fluctuations in adjacent energy bins near radioactivity peaks result from a small energy calibration difference between the source and background measurements. 122

5.14 Photograph of the deployment of a calibration LED photographed by the bottom camera. The detector has not been filled yet. The light source is the white LEDs of the top camera. 123

5.15 Photograph from the bottom camera during filling. Gadolinium-doped liquid scintillator is visible in the center of the detector, while undoped scintillator is visible at the bottom of the image. The boundary between them is formed by the inner acrylic vessel. The light source is the white LEDs of the top camera. 124

5.16 View from the top camera in a dry detector. Calibration ports and acrylic vessel lids are prominent above the midline of the image, while below, several rows of PMTs can be seen. The light source is the white LEDs of the bottom camera. 124

5.17 Photograph from the top camera after filling completion. The light source is the white LEDs from the same camera. The reflections of the LEDs are visible at the bottom left, where the missing LED reflections are due to the curvature of the acrylic vessels. The photograph appears magnified relative to Figure 5.16 because the scintillator and mineral oil have a higher index of refraction than air. 125

5.18 Left: A photograph taken with the bottom camera under infrared light from the top camera. The acrylic vessels and PMTs are visible in this detector waiting to be filled. The quality is lesser compared to white light, but still effective. . . . 125

5.19 A photograph taken of the manual calibration test in a partially constructed detector, under white light from the top camera. The manual calibration arm is seen extended from the center of the detector toward the camera to the left. In the background, only the outer acrylic vessel and stainless steel vessel are present; the PMT ladders were not installed at the time of this test. 126

6.1 The conversion of photoelectrons per 1 MeV versus time determined by AdSimple from spallation neutrons [66]. “AD” refers to antineutrino detector. 131

Figure Page

6.2 Visible energy of nGd captures in detectors 1 and 2 at the Daya Bay near site versus position in polar coordinates r, z and ϕ [66]. From the reference, "AD" means antineutrino detector. 132

6.3 Prompt and delayed energies deposited in the two Daya Bay near detectors during Data Set 0 [67]. The boxed region indicates events passing the IBD selection cuts for nGd capture. The peak at $E_d = 2.2\,\text{MeV}$ corresponds to IBDs with nH capture. The peak of $E_d < 4\,\text{MeV}$ and $E_p < 4\,\text{MeV}$ is from accidental background. 136

6.4 The delayed energy E_d (left) and neutron capture time ΔT (right) in detector 1 over Data Set 2 [68]. The peak at $8\,\mu\text{s}$ corresponds to the neutron thermalization time. 137

6.5 Deposition of energy from a flashing PMT. The high fraction of energy deposited in one PMT, and the disproportionate deposition of energy in the columns of PMTs adjacent to and facing the flasher, are distinct characteristics of PMT flashers [69]. 138

6.6 Flasher discriminant variable FID from Data Set 1. Values of $FID > 0$ indicate a flasher [69]. 139

6.7 Energy deposits for a given time after muon for a subset of Data Set 2. The peak below 1 s corresponds to decays of muon-induced ^{9}Li and ^{8}He, which decay with a half-life of about 0.1 s [68]. 144

6.8 The spectra of ^{9}Li and ^{8}He background predicted from theory [70]. The expected ratio of lithium to helium among the background events is 4:1. 145

6.9 Events passing all IBD selection cuts except $E_p < 12\,\text{MeV}$ [68]. The $E_p > 12\,\text{MeV}$ events are ascribed to the fast neutrons. The fast neutron background rate in the IBD energy window is deduced from extrapolating the rate of fast neutrons above 12 MeV. The inset shows the subset of fast neutron-like events following a muon tagged by the veto as a cross-check. 146

7.1 Layout of Daya Bay with eight identical detectors and six identical reactors assumed for the sensitivity model. Antineutrino propagation lengths (baselines) are indicated in meters by the arrows. 150

Figure Page

7.2 Background energy spectra with arbitrary normalization for fast neutrons (red dashed line), accidentals (blue dotted line) and ^{8}He/^{9}Li (black solid line), as assumed in the sensitivity model. The energy spectra follow the description in [71]. 154

7.3 Solid line: Sensitivity of Daya Bay as a function of running time for the systematic uncertainties of Table 8.2 and $\Delta m^2_{31} = 2.40 \cdot 10^{-3}$ eV^2 [72]. Dashed lines: 3σ and 5σ confidence limits with improved detector systematic uncertainties. 159

7.4 Left: The sensitivity and the 3σ discovery limit of Daya Bay based on the model of Section 7.1. Right: Comparison between the sensitivity predicted by the model and the Daya Bay proposal [8]. Agreement in the then-allowed region of Δm^2_{31} (Δm^2_{31}=$2.40^{+0.20}_{-0.15}\cdot 10^{-3}$ eV^2 [72]) is nearly exact; the difference outside this region is due to the differences in the modeling of the number of detectors and reactors, and the χ^2 parameterization. 160

7.5 The 3σ (left) and 5σ (right) discovery reach for sample cases of running time and uncorrelated detector normalization uncertainty value. 161

7.6 Left: Sensitivity after three years running as a function of each systematic uncertainty value. The thin lines correspond to a detector systematic uncertainty value of 0.38%, while the thick lines below correspond to a detector systematic uncertainty value of 0.18% (and occur lower in sensitivity value in the plot). Right: Change in the sensitivity with respect to the detector systematic uncertainty, the dominant systematic uncertainty in the error budget. The three points indicate the baseline, goal, and swapping values defined in the Technical Design Report [8]. 162

7.7 Left: Sensitivity to $\sin^2 2\theta_{13}$ as a function of the uncorrelated reactor flux normalization uncertainty, σ_{core}, assuming either 0.18% or 0.38% for the detector systematic uncertainty, and σ_{fuel}=2%. Right: Sensitivity to $\sin^2 2\theta_{13}$ as a function of the reactor fuel composition uncertainty, σ_{fuel}, assuming either 0.18% or 0.38% for the detector systematic uncertainty, and σ_{core}=2%. 163

7.8 Sensitivity for configurations 2–0–2, 2–2–2 and 2–0–4 for short running times [73]. The X–Y–Z notation refers to the number of detectors at the Daya Bay Near, Ling Ao Near, and Far sites respectively 168

Figure Page

7.9 The discovery limit of the 2–1–3 configuration at 3σ and 5σ versus running time. Three uncorrelated detector systematic uncertainties are considered because at the time the six detector analysis was being considered, the actual uncertainty was yet unknown. For comparison, the dots indicate the moment that the rate of change of the curve is –0.001/month. 170

7.10 The sensitivity (90% confidence) of the 2–1–3 configuration versus running time compared to RENO's goal at full running time [74]. Daya Bay's short term six detector analysis is competitive. 170

7.11 The 3σ and 5σ discovery reach for Daya Bay for the transition from the six detector analysis to eight detectors. The solid blue line shows the limit for six detectors, assuming detector uncertainties of $\sigma_{det} = 0.38\%$, 0.6% or 0.8%. After six months of data taking, the experiment is taken offline for a projected four months to install the last two detectors, during which the limit stays flat. After the installation of all detectors, the red line indicates the discovery limit for the anticipated range of σ_{det}, between 0.18% and 0.38%. 171

7.12 Sensitivity to $\sin^2 2\theta_{13}$ versus running time for incomplete configurations of Daya Bay. Left: The loss of one detector. Right: The loss of one detector or a near-far pair. 173

8.1 Predicted reactor spectra at each detector, without oscillations, over 240 energy bins [51]. Statistics correspond to the latest data set. 181

8.2 Reactor flux uncertainties: spent nuclear fuel and nonequilibrium fluxes at low energy, as well as fission fraction and the $\beta \to \bar{\nu}$ conversion spectra. The $\beta \to \bar{\nu}$ conversion is correlated among reactors, but one component is energy-correlated while the other is energy-uncorrelated [51]. 182

8.3 The fission fraction uncertainty spectrum, in this example from Daya Bay Nuclear Power Plant 1 (DBNPP1) to Detector 1 at the Daya Bay near site, at the statistics and efficiencies of the latest data set. The uncertainty spectra are normalized with nuisance parameters then added or subtracted to each reactor-detector flux prediction. 183

Figure Page

8.4 Left: The spent nuclear fuel uncertainty spectrum. Right: nonequilibrium uncertainty spectrum. Plotted are contributions from Daya Bay Nuclear Power Plant 1 (DBNPP1) to Detector 1 at the Daya Bay near site, at the statistics and efficiencies of the latest data set. The uncertainty spectra are normalized with nuisance parameters then added or subtracted to each reactor-detector flux prediction. 184

8.5 The $\beta \to \bar{\nu}$ conversion uncertainty spectra, in this example from Daya Bay Nuclear Power Plant 1 to Detector 1 at the statistics and efficiencies of the latest data set. Left: energy-correlated/reactor-correlated spectrum; right: energy-uncorrelated/reactor-correlated spectrum. The spectra are normalized with nuisance parameters then added or subtracted to each reactor-detector flux prediction. 185

8.6 Left: IAV correction matrix [75]. It is highly diagonal, with some off-diagonal elements representing events that lose energy in the acrylic. Right: application of the IAV correction matrix to a typical IBD spectrum. 186

8.7 IAV correction uncertainty spectra. Left: detector-uncorrelated/energy-correlated. Right: detector-correlated/energy-uncorrelated. The spectra are normalized with nuisance parameters then added or subtracted to each reactor-detector flux prediction. 186

8.8 The $E_{\text{meas.}}/E_{\text{dep.}}$ ratio (f_{nl} of Equation) from the nonlinearity function of Equation 8.8. The solid black line is the baseline correction, and the colored lines represent the variation of the four fit parameters by 1σ. 189

8.9 A 1% energy scale applied to a typical detector flux prediction. 190

8.10 Application of energy resolution based on Equation 8.16 to a typical detector flux prediction. 191

8.11 The accidentals spectrum for Detector 1. 192

8.12 The ^{9}Li/^{8}He spectrum for Detector 1, from [76]. 193

8.13 The AmC spectrum for Detector 1, from [77]. 193

8.14 The C(α, n)O spectrum for Detector 1, from [78]. 194

Figure Page

8.15 The magnitude of the energy-uncorrelated/detector-reactor-correlated bin normalization uncertainty. Due to the $\beta \to \bar{\nu}$ and IAV uncertainties, each bin can fluctuate in the fit according to the uncertainty above. 196

8.16 $\Delta\chi^2(\sin^2 2\theta_{13})$ for a fit to Monte Carlo with no statistical fluctuations, generated with $\sin^2 2\theta_{13} = 0.10$ and $\Delta m^2_{32} = 2.32{\cdot}10^{-3}\,\mathrm{eV}^2$. 201

8.17 $\Delta\chi^2(\sin^2 2\theta_{13},\ \Delta m^2_{32})$ for a fit to Monte Carlo with no statistical fluctuations, generated with $\sin^2 2\theta_{13} = 0.10$ and $\Delta m^2_{32} = 2.32{\cdot}10^{-3}\,\mathrm{eV}^2$. 203

8.18 $\Delta\chi^2(\Delta m^2_{32})$ for a fit to Monte Carlo with no statistical fluctuations, generated with $\sin^2 2\theta_{13} = 0.10$ and $\Delta m^2_{32} = 2.32{\cdot}10^{-3}\,\mathrm{eV}^2$. 204

8.19 $\Delta\chi^2(\mathcal{H})$ for a fit to Monte Carlo with no statistical fluctuations, generated with $\sin^2 2\theta_{13} = 0.10$ and $\Delta m^2_{32} = 2.32{\cdot}10^{-3}\,\mathrm{eV}^2$. 204

8.20 $\Delta\chi^2(\sin^2 2\theta_{13},\ \mathcal{H})$ for a fit to Monte Carlo with no statistical fluctuations, generated with $\sin^2 2\theta_{13} = 0.10$ and $\Delta m^2_{32} = 2.32{\cdot}10^{-3}\,\mathrm{eV}^2$. 205

8.21 For a validation Monte Carlo sample without statistical fluctuations, the covariance matrix is shown. Variable names are listed on the axes. 206

8.22 For a validation Monte Carlo sample with no statistical fluctuations, a matrix of fit parameter correlations is shown. Variable names are listed on the axes. . . . 207

8.23 For a validation Monte Carlo sample with no statistical fluctuations, the correlations of oscillation parameters with systematic nuisance parameters are shown. Variable names are listed on the axes. 208

8.24 The accuracy of the fitter is verified using Monte Carlo samples generated with oscillation parameters sampled over the ranges $0 \geq \sin^2 2\theta_{13} \geq 0.2$ and $0 \geq \Delta m^2_{32} \geq 4.64 \cdot 10^{-3}\,\mathrm{eV}^2$. Clockwise from the top left the plots show: $(\sin^2 2\theta_{13}\big|_{fitted} - \sin^2 2\theta_{13}\big|_{true})$, $(\Delta m^2_{32}\big|_{fitted} - \Delta m^2_{32}\big|_{true})$, χ^2_{min} and fit success or failure. The axes indicate the oscillation parameter values used to generate the Monte Carlo sample at that point. The thin horizontal and vertical lines indicate the previous measurement error bars on $\sin^2 2\theta_{13}$ and Δm^2_{32} respectively [68, 1]. Note that failures of the fit appear as zero in all the plots. 211

Figure Page

8.25 Measurements of $\sin^2 2\theta_{13}$ and Δm^2_{32} on a toy Monte Carlo samples without fluctuations, as a function of N_{bins}. Left: $\sin^2 2\theta_{13}$, right: Δm^2_{32}. As the number of bins increases, the spectral distortion information becomes better resolved, which results in a stronger Δm^2_{32} measurement. The measurement of $\sin^2 2\theta_{13}$ is less dependent on shape information. 214

8.26 $\Delta\chi^2(\sin^2 2\theta_{13})$ for a Monte Carlo programmed with $\sin^2 2\theta_{13} = 0.10$ and $\Delta m^2_{32} = 2.32{\cdot}10^{-3}\,\mathrm{eV}^2$, with statistical fluctuations, and fit over 24 energy bins. 217

8.27 $\Delta\chi^2(\Delta m^2_{32})$ for a Monte Carlo programmed with $\sin^2 2\theta_{13} = 0.10$ and $\Delta m^2_{32} = 2.32{\cdot}10^{-3}\,\mathrm{eV}^2$, with statistical fluctuations, and fit over 24 energy bins. 218

8.28 $\Delta\chi^2(\mathcal{H})$ for a Monte Carlo programmed with $\sin^2 2\theta_{13} = 0.10$ and $\Delta m^2_{32} = 2.32{\cdot}10^{-3}\,\mathrm{eV}^2$, with statistical fluctuations, and fit over 24 energy bins. 218

8.29 $\Delta\chi^2(\sin^2 2\theta_{13},\ \Delta m^2_{32})$ for a validation Monte Carlo run. The Monte Carlo is programmed with $\sin^2 2\theta_{13} = 0.10$ and $\Delta m^2_{32} = 2.32{\cdot}10^{-3}\,\mathrm{eV}^2$, with statistical fluctuations, and fit over 24 energy bins. Compared with Figure 8.17, the tail at high $\sin^2 2\theta_{13}$ and low Δm^2_{32} has abated. 219

8.30 $\Delta\chi^2(\sin^2 2\theta_{13},\ \mathcal{H})$ for a validation Monte Carlo run. The Monte Carlo is programmed with $\sin^2 2\theta_{13} = 0.10$ and $\Delta m^2_{32} = 2.32{\cdot}10^{-3}\,\mathrm{eV}^2$, with statistical fluctuations, and fit over 24 energy bins. 220

8.31 Covariance matrix for a Monte Carlo programmed with $\sin^2 2\theta_{13} = 0.10$ and $\Delta m^2_{32} = 2.32{\cdot}10^{-3}\,\mathrm{eV}^2$, with statistical fluctuations, and fit over 24 energy bins. Variable names are listed on the axes. 221

8.32 Correlation matrix for a Monte Carlo programmed with $\sin^2 2\theta_{13} = 0.10$ and $\Delta m^2_{32} = 2.32{\cdot}10^{-3}\,\mathrm{eV}^2$, with statistical fluctuations, and fit over 24 energy bins. Variable names are listed on the axes. 222

8.33 Correlations of $\sin^2 2\theta_{13}$ and Δm^2_{32} with systematic fit parameters for a Monte Carlo programmed with $\sin^2 2\theta_{13} = 0.10$ and $\Delta m^2_{32} = 2.32{\cdot}10^{-3}\,\mathrm{eV}^2$, with statistical fluctuations, and fit over 24 energy bins. Variable names are listed on the axes. 223

8.34 Values of nuisance parameter divided by uncertainty (η_i/σ_i) for a Monte Carlo programmed with $\sin^2 2\theta_{13} = 0.10$ and $\Delta m^2_{32} = 2.32{\cdot}10^{-3}\,\mathrm{eV}^2$, with statistical fluctuations, and fit over 24 energy bins. 223

Figure Page

8.35 Distribution of nuisance parameter divided by uncertainty (η_i/σ_i) for a validation Monte Carlo run. Variable names are listed on the axes. The Monte Carlo is programmed with $\sin^2 2\theta_{13} = 0.10$ and $\Delta m^2_{32} = 2.32{\cdot}10^{-3}\,\mathrm{eV}^2$, with statistical fluctuations, and fit over 24 energy bins. 224

8.36 Distribution of measured $\sin^2 2\theta_{13}$ values over 1000 Monte Carlo samples generated with either statistical fluctuations (left) or fluctuations of systematics (right). The programmed oscillation parameter values are $\sin^2 2\theta_{13} = 0.10$ and $\Delta m^2_{32} = 2.32{\cdot}10^{-3}\,\mathrm{eV}^2$. 227

8.37 Distribution of measured Δm^2_{32} values over 1000 Monte Carlo samples generated with either statistical fluctuations (left) or fluctuations of systematics (right). The programmed oscillation parameter values are $\sin^2 2\theta_{13} = 0.10$ and $\Delta m^2_{32} = 2.32{\cdot}10^{-3}\,\mathrm{eV}^2$. 227

8.38 Distribution of measured χ^2_{min} values over 1000 Monte Carlo samples generated with either statistical fluctuations (left) or fluctuations of systematics (right). The programmed oscillation parameter values are $\sin^2 2\theta_{13} = 0.10$ and $\Delta m^2_{32} = 2.32{\cdot}10^{-3}\,\mathrm{eV}^2$. 228

8.39 Measured $\sin^2 2\theta_{13}$ and Δm^2_{32} values over 1000 Monte Carlo samples generated with either statistical fluctuations (left) or fluctuations of systematics (right). The programmed oscillation parameter values are $\sin^2 2\theta_{13} = 0.10$ and $\Delta m^2_{32} = 2.32{\cdot}10^{-3}\,\mathrm{eV}^2$. 228

8.40 Measured $\sin^2 2\theta_{13}$ and χ^2_{min} values over 1000 Monte Carlo samples generated with either statistical fluctuations (left) or fluctuations of systematics (right). The programmed oscillation parameter values are $\sin^2 2\theta_{13} = 0.10$ and $\Delta m^2_{32} = 2.32{\cdot}10^{-3}\,\mathrm{eV}^2$. 229

8.41 Measured Δm^2_{32} and χ^2_{min} values over 1000 Monte Carlo samples generated with either statistical fluctuations (left) or fluctuations of systematics (right). The programmed oscillation parameter values are $\sin^2 2\theta_{13} = 0.10$ and $\Delta m^2_{32} = 2.32{\cdot}10^{-3}\,\mathrm{eV}^2$. 229

8.42 Measured $\sin^2 2\theta_{13}$ (left) and Δm^2_{32} (right) values over 1000 Monte Carlo samples with statistical fluctuations. Only $\sin^2 2\theta_{13}$, Δm^2_{32} and $\mathcal{H}$ were enabled during the fit. The programmed oscillation parameter values are $\sin^2 2\theta_{13} = 0.10$ and $\Delta m^2_{32} = 2.32{\cdot}10^{-3}\,\mathrm{eV}^2$. 230

Figure Page

8.43 Measured χ^2_{min} values (left) and both $\sin^2 2\theta_{13}$ and Δm^2_{32} (right) over 1000 Monte Carlo samples with statistical fluctuations. Only $\sin^2 2\theta_{13}$, Δm^2_{32} and $\mathcal{H}$ were enabled during the fit. The programmed oscillation parameter values are $\sin^2 2\theta_{13}$ = 0.10 and $\Delta m^2_{32} = 2.32{\cdot}10^{-3}\,\mathrm{eV}^2$. 231

8.44 Measured $\sin^2 2\theta_{13}$ and χ^2_{min} values (left) and Δm^2_{32} and χ^2_{min} (right) over 1000 Monte Carlo samples with statistical fluctuations. Only $\sin^2 2\theta_{13}$, Δm^2_{32} and $\mathcal{H}$ were enabled during the fit. The programmed oscillation parameter values are $\sin^2 2\theta_{13} = 0.10$ and $\Delta m^2_{32} = 2.32{\cdot}10^{-3}\,\mathrm{eV}^2$. 232

8.45 Measurements of $\sin^2 2\theta_{13}$ with five models performed on five Monte Carlo samples [79]. The samples are generated at five ($\sin^2 2\theta_{13}$, Δm^2_{32}) points: (0.07, 2.05), (0.07, 2.65), (0.10, 2.35), (0.13, 2.05), and (0.13, 2.65), where the units on Δm^2_{32} are $10^{-3}\mathrm{eV}^2$. 234

8.46 Measurements of Δm^2_{32} with five models performed on five Monte Carlo samples [79]. The samples are generated at five ($\sin^2 2\theta_{13}$, Δm^2_{32}) points: (0.07, 2.05), (0.07, 2.65), (0.10, 2.35), (0.13, 2.05), and (0.13, 2.65), where the units on Δm^2_{32} are $10^{-3}\mathrm{eV}^2$. 235

9.1 Best fit $\sin^2 2\theta_{13}$-Δm^2_{32} contours for rate and shape data, where the overall normalization $\mathcal{H}$, $\sin^2 2\theta_{13}$ and Δm^2_{32} are free parameters, and normal hierarchy is assumed. The central dot denotes the best fit, and the five contours correspond to two-dimensional 1–5σ confidence limits. 240

9.2 Best fit $\sin^2 2\theta_{13}$-$\mathcal{H}$ 1σ contour for rate and shape data, where $\mathcal{H}$, $\sin^2 2\theta_{13}$ and Δm^2_{32} are free parameters and normal hierarchy is assumed. The central dot denotes the best fit. 240

9.3 The best fit $\Delta\chi^2(\sin^2 2\theta_{13})$ from the rate and shape analysis with $\sin^2 2\theta_{13}$, Δm^2_{32} and $\mathcal{H}$ as free parameters and normal hierarchy assumed. 241

9.4 The best fit $\Delta\chi^2(\Delta m^2_{32})$ from the rate and shape analysis, with $\sin^2 2\theta_{13}$, Δm^2_{32} and $\mathcal{H}$ as free parameters and normal hierarchy assumed. 241

9.5 The best fit $\Delta\chi^2(\mathcal{H})$ to rate and shape data, with $\sin^2 2\theta_{13}$, Δm^2_{32} and $\mathcal{H}$ as free parameters and normal hierarchy assumed. 242

9.6 Correlation matrix from the rate and shape and shape analysis. Variable names are listed on the axes. 243

Figure Page

9.7 Correlations between $\sin^2 2\theta_{13}$ and Δm^2_{32} and the systematic fit parameters from the rate and shape analysis. Fit parameters are listed on the axes. 244

9.8 Covariance matrix from the rate and shape analysis. Variable names are listed on the axes. 247

9.9 Histogram of systematic nuisance parameters divided by uncertainty values (η_ι/σ_ι) at best fit to rate and shape data. 248

9.10 Systematic nuisance parameters divided by uncertainties (η_ι/σ_ι) at best fit from a rate and shape analysis, where Δm^2_{32} is unconstrained and normal hierarchy is assumed. Variable names are listed on the axes. 249

9.11 The detector response model is indicated by the solid black line. 1σ uncertainties on the four individual nonlinearity parameters are indicated by the colored lines. The dashed line shows the best fit detector response after fit parameters are applied. 249

9.12 Ratio of data in 240 bins divided by the predicted flux, which includes the best fit systematics and oscillation from the 24 bin rate and shape analysis. 250

9.13 Best fit contours $\Delta\chi^2(\sin^2 2\theta_{13}, \Delta m^2_{13})$ for rate and shape data with the exclusion of the energy scale parameter (left) and its inclusion (right). The energy scale parameters and Δm^2_{32} form a possible degeneracy, which is difficult to resolve in a limited data set. 253

9.14 Detector 1 spectra after each stage of the rate and shape data fit: absolute (left) and ratio (right) in which the spectrum at each stage is divided by the initial unoscillated predicted spectrum (right). The model progression starts from the solid blue line, which is the initial reactor flux prediction, to the black dashed line, which includes best fit systematics and oscillations. In red are IBD candidates including backgrounds (solid line) and backgrounds (dashed). 253

9.15 Detector 2 spectra after each stage of the rate and shape data fit: absolute (left) and ratio (right) in which the spectrum at each stage is divided by the initial unoscillated predicted spectrum (right). The model progression starts from the solid blue line, which is the initial reactor flux prediction, to the black dashed line, which includes best fit systematics and oscillations. In red are IBD candidates (solid line) and backgrounds (dashed). 254

Figure Page

9.16 Detector 3 spectra after each stage of the rate and shape data fit: absolute (left) and ratio (right) in which the spectrum at each stage is divided by the initial unoscillated predicted spectrum (right). The model progression starts from the solid blue line, which is the initial reactor flux prediction, to the black dashed line, which includes best fit systematics and oscillations. In red are IBD candidates (solid line) and backgrounds (dashed). 254

9.17 Detector 4 spectra after each stage of the rate and shape data fit: absolute (left) and ratio (right) in which the spectrum at each stage is divided by the initial unoscillated predicted spectrum (right). The model progression starts from the solid blue line, which is the initial reactor flux prediction, to the black dashed line, which includes best fit systematics and oscillations. In red are IBD candidates (solid line) and backgrounds (dashed). 255

9.18 Detector 5 spectra after each stage of the rate and shape data fit: absolute (left) and ratio (right) in which the spectrum at each stage is divided by the initial unoscillated predicted spectrum (right). The model progression starts from the solid blue line, which is the initial reactor flux prediction, to the black dashed line, which includes best fit systematics and oscillations. In red are IBD candidates (solid line) and backgrounds (dashed). 255

9.19 Detector 6 spectra after each stage of the rate and shape data fit: absolute (left) and ratio (right) in which the spectrum at each stage is divided by the initial unoscillated predicted spectrum (right). The model progression starts from the solid blue line, which is the initial reactor flux prediction, to the black dashed line, which includes best fit systematics and oscillations. In red are IBD candidates (solid line) and backgrounds (dashed). 256

9.20 Best fit $\sin^2 2\theta_{13}$ (left) and Δm^2_{32} (right) versus number of energy bins. The y-axis is the deviation (%) from the primary measurement at 24 bins. 259

9.21 Histogram of χ^2_{min} values for 1000 fits to data with random starting values for nuisance parameters. The histograms successively zoom into the low χ^2_{min} region. Top left: all results. Top right: $\chi^2_{min} < 270$. Bottom left: $\chi^2_{min} < 125$. Bottom right: $\chi^2_{min} < 114.48$. The true $\chi^2_{min} = 114.26$. 263

9.22 Best fit $\sin^2 2\theta_{13}$ and Δm^2_{32} for fits with randomized starting values of nuisance parameters. Left: $\chi^2_{min} < 125$. Right: $\chi^2_{min} = 114.426$, the true minimum. . . . 263

Figure Page

9.23 Best fit values of $\sin^2 2\theta_{13}$ for randomized nuisance parameter starting values. Left: χ^2_{min}<115.426. Right: χ^2_{min}=114.426. The small RMS of the spread of fit values indicates the χ^2 minimization process does not add significantly to the uncertainty of the fit result. 264

9.24 Best fit values of Δm^2_{32} for randomized nuisance parameter starting values. Left: χ^2_{min}<115.426. Right: χ^2_{min}=114.426. The small RMS of the spread of fit values indicates the χ^2 minimization process does not add significantly to the uncertainty of the fit result. 264

9.25 Covariance matrix for analyses with the ^{238}U flux uncertainties energy-correlated (left) or uncorrelated (right). The latter is the primary analysis. 266

9.26 Correlation matrix for analyses with the ^{238}U flux uncertainties energy-correlated (left) or uncorrelated (right). The latter is the primary analysis. 266

9.27 1σ $\sin^2 2\theta_{13}$-Δm^2_{32} contours for rate and shape analyses with unconstrained Δm^2_{32}, and both normal and inverted hierarchy. 269

9.28 1σ $\sin^2 2\theta_{13}$-Δm^2_{32} contours for rate and shape analyses with two cases of constrained Δm^2_{32}, and both normal and inverted hierarchy. 269

9.29 Correlation matrix from a rate and shape analysis where Δm^2_{32} is constrained to Δm^2_{32}=2.32±0.12, assuming normal hierarchy. Variable names are listed on the axes. 272

9.30 Correlations among oscillation parameters and systematics from a rate and shape analysis where Δm^2_{32} is constrained to Δm^2_{32}=2.32±0.12, assuming normal hierarchy. Variable names are listed on the axes. 273

9.31 Covariance matrix from a rate and shape analysis where Δm^2_{32} is constrained to Δm^2_{32}=2.32±0.12, assuming normal hierarchy. Variable names are listed on the axes. 274

9.32 Histogram of systematic nuisance parameters divided by uncertainties (η_ι/σ_ι) at best fit from a rate and shape analysis where Δm^2_{32} is constrained to Δm^2_{32} = 2.32±0.12, assuming normal hierarchy. 275

9.33 Systematic nuisance parameters divided by uncertainties (η_ι/σ_ι) at best fit from a rate and shape analysis where Δm^2_{32} is constrained to Δm^2_{32} = 2.32±0.12, assuming normal hierarchy. Variable names are listed on the axes. 275

Figure Page

9.34 The best fit $\Delta\chi^2(\sin^2 2\theta_{13})$ for the rate-only analysis. 278

9.35 The best fit $\Delta\chi^2(\Delta m^2_{32})$ for the rate-only analysis. Δm^2_{32} is constrained to Δm^2_{32} $= 2.32\pm0.12\cdot10^{-3}\,\mathrm{eV}^2$ for the fit. 279

9.36 The best fit $\Delta\chi^2(\mathcal{H})$ for the rate-only analysis. 280

9.37 The best fit $\sin^2 2\theta_{13}$-Δm^2_{32} point from a rate-only analysis surrounded by the 1σ contour. 280

9.38 The best fit $\sin^2 2\theta_{13}$-$\mathcal{H}$ point from a rate-only analysis surrounded by the 1σ contour. 281

9.39 Correlation matrix from a rate-only analysis. The right matrix is the zoomed-in portion of the left plot showing systematics, but omitting the oscillation parameters which are in the upper right of the left plot. Variable names are listed on the axes. 282

9.40 Oscillation parameter correlations with systematics from a rate-only analysis. Variable names are listed on the axes. 283

9.41 Covariance matrix from a rate-only analysis. The right matrix is the zoomed-in portion of the left plot showing systematics, but omitting the oscillation parameters which are in the upper right of the left plot. Variable names are listed on the axes. 283

9.42 Histogram of systematic nuisance parameters divided by uncertainties $(\eta_\iota/\sigma_\iota)$ at best fit from a rate-only analysis. 284

9.43 Nuisance parameters divided by uncertainties $(\eta_\iota/\sigma_\iota)$ at best fit from a rate-only analysis. Variable names are listed on the axes. 285

9.44 The best fit $\sin^2 2\theta_{13}$-Δm^2_{32} point surrounded by 1–3σ contours from a shape-only analysis. 288

9.45 The best fit $\Delta\chi^2(\sin^2 2\theta_{13})$ from a shape-only analysis. 288

9.46 The best fit $\chi^2(\Delta m^2_{32})$ from a shape-only analysis. 289

9.47 Correlation matrix from a shape-only analysis. Variable names are listed on the axes. 290

Figure Page

9.48 Correlations among oscillation parameters and systematics from a shape-only analysis. Variable names are listed on the axes. 291

9.49 Covariance matrix from a shape-only analysis. Variable names are listed on the axes. 292

9.50 Histogram of systematic nuisance parameters divided by uncertainties (η_ι/σ_ι) at best fit, from a shape-only analysis. 293

9.51 Systematic nuisance parameters divided by uncertainties (η_ι/σ_ι) at best fit from a shape-only analysis. Variable names are listed on the axes. 294

9.52 The detector response model is indicated by the solid black line, with 1σ uncertainties on each of the four nonlinearity parameters indicated by the colored lines. The dashed line shows the shape-only best fit detector response after fit parameters are applied. 294

9.53 Best fit contours $\Delta\chi^2(\sin^2 2\theta_{13}, \Delta m^2_{32})$ for the shape-only fit with the exclusion of the energy scale parameter (left) and its inclusion (right). 296

9.54 Summary of all the measurements of $\sin^2 2\theta_{13}$ presented in Chapter 9 under various conditions. Best fits and 1σ error bands are shown. The primary reported result is at the top; rate-only and shape-only represent analyses with limited information; the rest reflect analyses with alternate choices. 297

9.55 Summary of all the measurements of Δm^2_{32} presented in Chapter 9 under various conditions. Best fits and 1σ error bands are shown. The primary reported result is at the top; rate-only and shape-only represent analyses with limited information; the rest reflect analyses with alternate choices. 298

DISCARD THIS PAGE

NOMENCLATURE

AV	Acrylic Vessel
CP	Charge-Parity (symmetry)
DAQ	Data Acquisition
EH	Electronics Hall
FEE	Front-end Electronics
GdLS	Gadolinium-doped Liquid Scintillator
GLoBES	General Long Baseline Experiment Simulator
IAV	Inner Acrylic Vessel
IBD	Inverse Beta Decay
IH	Inverted Hierarchy
ILL	Institut Laue-Langevin
LAB	Linear Alkylbenzene
LS	Liquid Scintillator
MO	Mineral Oil
m.w.e.	meters of water equivalent
NEQ	Nonequilibrium (flux)

NH	Normal Hierarchy
NPP	Nuclear Power Plant
OAV	Outer Acrylic Vessel
OWS	Outer Water Shield
PE	Photoelectron
PMT	Photomultiplier Tube
RPC	Resistive Plate Chambers
SI	International System of Units
SNF	Spent Nuclear Fuel
SSV	Stainless Steel Vessel
TDR	Technical Design Report

OBSERVATION OF ANTINEUTRINO OSCILLATIONS FROM SPECTRAL DISTORTIONS AT THE DAYA BAY REACTOR NEUTRINO EXPERIMENT

Michael C. McFarlane

Under the supervision of Professor Karsten M. Heeger

At the University of Wisconsin-Madison

Neutrino oscillation is the quantum mechanical phenomenon whereby neutrinos or antineutrinos can spontaneously transform from one of three flavors— electron, muon, or tau— to another. The Daya Bay Reactor Neutrino Experiment has measured neutrino mixing angle θ_{13}, for the first time, to world-leading precision. The analysis in this dissertation reports $\sin^2 2\theta_{13} = 0.088 \pm 0.0088$, $\Delta m^2_{32} = 2.54^{+0.17}_{-0.18}\cdot 10^{-3}\,\mathrm{eV}^2$ and $\Delta m^2_{31} = 2.62\cdot 10^{-3}\,\mathrm{eV}^2$, assuming Δm^2_{21}=$7.50\cdot 10^{-5}\,\mathrm{eV}^2$ and normal hierarchy. These measurements were accomplished by the early deployment of six functionally identical detectors to observe antineutrino flux from six nuclear reactors, between 2 to 12 MeV. Half the detectors are sited near the position of maximal oscillation, about 1600 m from the reactors, while the rest are located 500 m and 550 m away at two sites, where the oscillation probability is low. The relative comparison of antineutrino rates and energies at identical near and far detectors provides a direct measurement of θ_{13} and Δm^2, while greatly reducing systematic uncertainties. The chapters that follow explain neutrino oscillations, and experiment strategy and construction. My contributions to the experiment are highlighted in more detail in the introductions to chapters 3 through 9. These include a detector camera monitoring system, a sensitivity calculation that helped motivate the early six-detector analysis, and the measurements of oscillation parameters from antineutrino rates and spectra.

Karsten M. Heeger

ABSTRACT

Neutrino oscillation is the quantum mechanical phenomenon whereby neutrinos or antineutrinos can spontaneously transform from one of three flavors— electron, muon, or tau— to another. The Daya Bay Reactor Neutrino Experiment has measured neutrino mixing angle θ_{13}, for the first time, to world-leading precision. The analysis in this dissertation reports $\sin^2 2\theta_{13} = 0.088 \pm 0.0088$, $\Delta m^2_{32} = 2.54^{+0.17}_{-0.18}{\cdot}10^{-3}\,\mathrm{eV}^2$ and $\Delta m^2_{31} = 2.62{\cdot}10^{-3}\,\mathrm{eV}^2$, assuming Δm^2_{21}=$7.50{\cdot}10^{-5}\,\mathrm{eV}^2$ and normal hierarchy. These measurements were accomplished by the early deployment of six functionally identical detectors to observe antineutrino flux from six nuclear reactors, between 2 to 12 MeV. Half the detectors are sited near the position of maximal oscillation, about 1600 m from the reactors, while the rest are located 500 m and 550 m away at two sites, where the oscillation probability is low. The relative comparison of antineutrino rates and energies at identical near and far detectors provides a direct measurement of θ_{13} and Δm^2, while greatly reducing systematic uncertainties. The chapters that follow explain neutrino oscillations, and experiment strategy and construction. My contributions to the experiment are highlighted in more detail in the introductions to chapters 3 through 9. These include a detector camera monitoring system, a sensitivity calculation that helped motivate the early six-detector analysis, and the measurements of oscillation parameters from antineutrino rates and spectra.

Chapter 1

Neutrino and Particle Physics

The Daya Bay Reactor Neutrino Experiment must be understood in the full context of the discipline of particle physics. Neutrinos are fundamental particles— they cannot be broken down so far as known, but are necessary components of basic interactions. The most comprehensive theory of particle physics is the Standard Model, which is described in the following sections. The Standard Model describes the particles, their properties, and the ways in which they interact.

Neutrino oscillations represent one of the few, if only, shortcomings discovered in the Standard Model. Neutrino oscillations proved that neutrinos have mass, whereas the Standard Model assumes massless neutrinos. Neutrino oscillations are a well-understood phenomenon, but other aspects of neutrino physics, such as the nature of their mass, are still mysterious.

The discussion in this chapter describes the Standard Model, focusing on neutrinos and their rich experimental history, and concludes with the motivation of the Daya Bay experiment.

1.1 The Standard Model of Particle Physics

The Standard Model of particle physics is the comprehensive theory of fundamental subatomic particles, their properties, and the forces by which they interact [80]. The Standard Model is a triumph of modern physics that has consistently predicted or been sustained by subsequent discoveries. Thus far, the only phenomenon of physics discovered beyond the Standard Model is neutrino mass and oscillation.

1.1.1 Particles of the Standard Model

Figure 1.1 presents a concise diagram of the irreducible set of fundamental particles, their relationships, and some of their properties like spin and charge. These particles can be classified into three categories: quarks, leptons and finally gauge or symmetry-breaking bosons.

Six quark species exist in nature— the up, down, charm, strange, top and bottom quarks— plus their antimatter counterparts— up antiquark, etc. The quarks range in mass from the up quark at 2.4 MeV to the top quark at 171 GeV. Each possesses a fractional charge of either $+2/3$ for up, charm and top, or $-1/3$ for down, strange and bottom. For the antimatter counterparts, these charges are multiplied by -1. While the masses and charges differ, three other properties unify the quarks: They are all spin-$\frac{1}{2}$ fermions, they carry a color charge, and they are never solitary.

By definition, fermions such as quarks are particles with half-integer spin, and thus share quantum characteristics special to fermions. Notably, fermions in a system are barred from sharing quantum numbers, referred to as the Pauli Exclusion Principle. For example, another fermion, the electron, cannot share the atomic quantum numbers n, l, m_l or m_s (respectively the energy level, angular momentum, projection of the angular momentum and spin) with another electron in the same atom.

Another important property of quarks is that they form composite particles, and cannot exist independently. Quarks join to create hadrons, either in pairs (mesons, which are bosons) or triads (baryons, which are fermions). Hadrons are all color-neutral, where "color" is the charge associated with the strong nuclear force. There are three strong force colors blue, green and red, as well as anti-color equivalents. Mesons' quarks are of opposite color, e.g. blue and antiblue, while baryons contain three quarks, one color each. Meson and baryons are also limited in constitution by electric charge; since quarks only have charges of $+2/3$

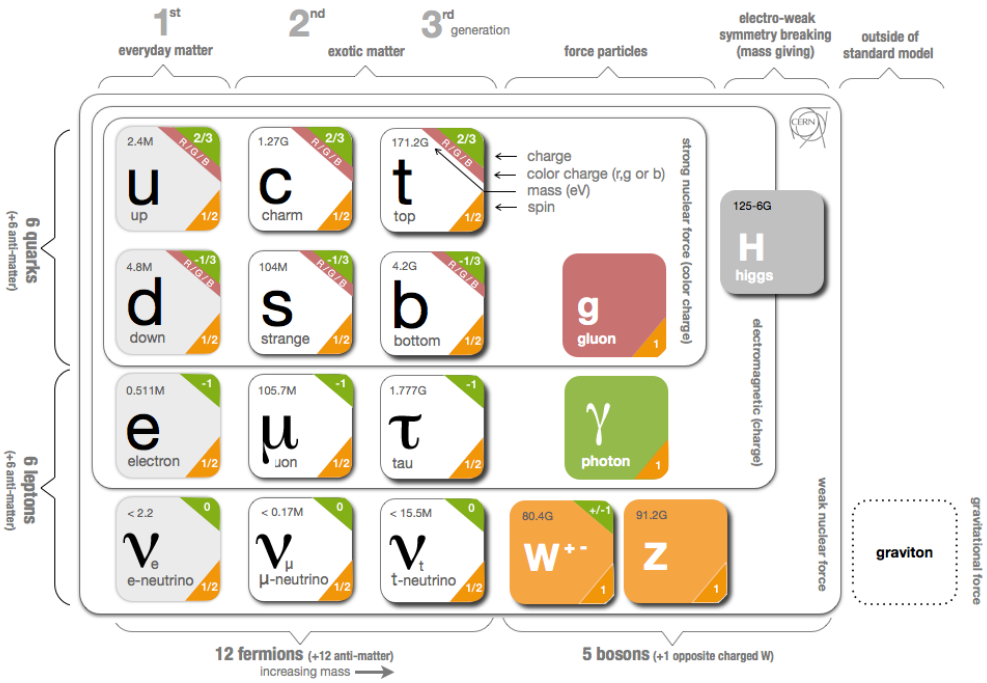


Figure 1.1 A diagram of the elementary particles in the Standard Model. Quarks, leptons, force carriers and the Higgs Boson are grouped according to generation, electric charge, interaction, mass, and spin [14].

or $-1/3$, mesons must be composed of a quark and an antiquark to ensure the necessary integer charge. Baryon composition is similarly restricted.

In addition to the six quarks, there are six leptons: the electron, muon, tau, electron neutrino, muon neutrino and tau neutrino, as well as their antimatter counterparts. Like quarks, leptons are also fermions. The electron, muon and tau possess an electric charge of -1 and are much more massive than the electrically neutral neutrinos. The neutrinos in fact have the lowest mass of any known massive particle. A charged lepton and its associated neutrino are related by the conserved quantity, lepton number. Electrons and electron neutrinos have electron number $+1$ while their antimatter equivalents, the positron and electron antineutrino, have electron number -1. The same holds for muon and tau numbers. As a result, a charged lepton is more likely to be involved in interactions involving its neutrino.

Unlike the quarks, the leptons can exist alone. Charged leptons can form composite particles bound by the electromagnetic force; all leptons interact via the weak force, but not the strong force. Two of the leptons, the muon and the tau, are unstable and spontaneously decay via the weak force.

Quarks and leptons are grouped into three generations on the basis of flavor and stability. The first generation consists of particles found readily in nature: the up and down quarks (which form neutrons and protons) and the electron and electron neutrino, and the antimatter counterparts of each. Each of these particles is stable, or forms stable baryons. The second generation consists of the charm, strange, muon and muon neutrino. Muons are not stable, but are found at the Earth via cosmic ray interactions with the atmosphere. Charm and strange quarks form short-lived hadrons. Rarer yet, the particles of the third generation— the top, bottom, tau and tau neutrino— are difficult to observe in nature and even physics laboratories (although tau neutrinos can be created during neutrino oscillation, which is discussed at length below). The particles of each generation are more massive and less stable than the previous generation, except for the neutrinos, which are all stable and of unknown mass. Further generations are ruled out by properties of the Higgs boson [81].

Finally, there are six Standard Model bosons. Five of them mediate forces— the photon, gluon, and the $W^{\pm}$ and Z bosons. The Higgs boson is responsible for electroweak symmetry breaking, and hence the masses of particles. Bosons differ from fermions in that they have integer spin, and are not subject to the Pauli Exclusion Principle— multiple bosons within a system can share the same quantum numbers and even the same location. Except for the W, the fundamental bosons do not have distinct antimatter counterparts (the $W^{\pm}$ are antiparticles of each other).

Also excepting the $W^{\pm}$, fundamental bosons are electrically neutral, and all but the spin-0 Higgs have spin 1. They range considerably in mass from the massless photon and gluon, to the Higgs, heavy at 125 GeV [82, 83]. The photon mediates electromagnetic interactions, the gluon, strong interactions, and the $W^{\pm}$ and Z, weak. Additionally, the gluons have two color charges— one color and one anticolor— reflecting the fact that they transfer color charge between quarks to maintain a hadron.

1.1.2 Forces

Four forces govern every interaction and decay in the known universe: electromagnetism, gravity, and the strong nuclear force and weak nuclear force. All but gravitation, which scarcely affects fundamental particles, are woven into the Standard Model. The strong nuclear force holds quarks together into nucleons, and nucleons together into nuclei. Electromagnetism holds electrons to atoms and determines the chemistry of substances. The weak force underlies many radioactive decays. The final force, gravitation, does not affect subatomic particles, due its slight strength.

Three of the forces are mediated by the exchange of the gauge bosons of the Standard Model, listed in Figure 1.1. The mediator of gravity, the massless spin-2 graviton, has not been confirmed by discovery, nor incorporated into the Standard Model [15].

The forces vary widely in both strength and range. At a reference distance of 10^{-16} cm or smaller, for instance, the strong nuclear force is strongest at two orders of magnitude more powerful than the electromagnetic force. Meanwhile, the electromagnetic force is over ten

orders stronger than the weak force, which is stronger than gravitation by about 38 orders of magnitude yet. Note, however, that the strengths depend on distance, although for particle interactions the order of strength typically holds. Figure 1.2 shows a graph of the forces as a function of distance.

The range of the force is determined by the properties of the force carrier. Photons and gravitons are massless and stable, so the electromagnetic and gravitational forces exert influence at any distance, although the strengths of these forces drop as $1/r^2$ for distance r. Since the weak force is mediated by the very massive and short-lived (about 90 GeV and 10^{-25} s) W and Z bosons, the weak force is more limited, dropping as e^{-mr}/r over distance, where m is the mass of the W or Z. The massless and color-charged gluon mediates the strong force, but color-charged particles cannot exist alone, so the strong force is the most limited in range.

For decays, the lifetime of the decay correlates to the strength of the force. Strong decays typically take 10^{-23} s, electromagnetic decays take 10^{-16} s, while weak decays range in lifetime from 10^{-13} s for the tau to 15 minutes for the neutron [84].

Leptons, quarks and force carriers are affected differently by the strong, weak and electromagnetic forces. All leptons interact via the weak force and all charged leptons interact with the electromagnetic force, and no leptons interact via the strong force. Thus, neutrinos only interact via the weak force. Quarks couple to all forces. The photon and W and Z bosons interact with one another, while the gluon interacts with none of them.

All known interactions conserve electric charge, color charge and each lepton number. The strong and electromagnetic forces conserve flavor, but the weak force does not conserve flavor for quarks. Weak interactions change quark flavor for every charge-current quark interaction (those that involve a W) while preserving it for neutral-current interactions (Z-mediated). If the quark emits a W, it must change flavor, for instance, down to up, in order for a full unit of charge to be passed. The weak force does not change lepton flavor; flavor-changing neutrino oscillations occur for free neutrinos.

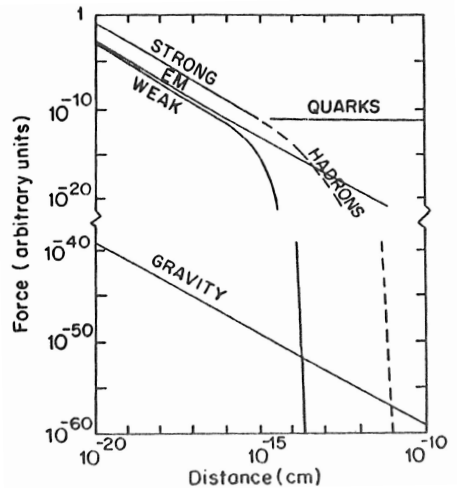


Figure 1.2 The strength of the four fundamental forces as a function of distance. For particle interactions, the strong force is much stronger than electromagnetism, which is much stronger than the weak force, while gravitation is negligible. Gravitation and electromagnetism follow straight $1/r^2$ dependences, whereas the strengths of the weak and strong forces drop precipitously beyond atomic radii [15].

The weak force alone violates the symmetries of parity, charge conjugation and charge-parity. Parity refers to the spatial coordinates of an interaction: if a process violates parity, that process exhibits different behavior when spatial axes are mirrored. Charge conjugation symmetry holds if an interaction is identical under the replacement of all particles with antiparticles. The joint symmetry of parity and charge conjugation is the straightforward union of the two. These are discussed in more detail in Section 1.3.

The most basic interactions of particles and forces can be described by the Feynman diagrams [85] of Figures 1.3 through 1.5. All processes in particle physics can be described by the combination of many such diagrams. Feynman diagrams efficiently illustrate the details of particle interactions and provide prescriptions to calculate properties such as interaction probabilities and decay times. However, beyond providing the basic components of strong, electromagnetic and weak interactions for descriptive purposes, calculations involving these diagrams are outside the scope of this dissertation.

Strong interactions are described by the theory of quantum chromodynamics, based upon the mathematics of the SU(3) group [86]. Figure 1.3 shows the basic Feynman diagram of

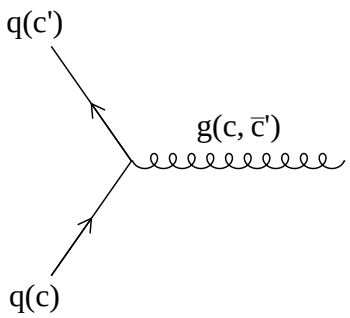


Figure 1.3 The Feynman diagram of the basic strong interaction vertex, the constituent of strong interaction processes. Two quarks q of colors c and c' interact at a vertex with a gluon carrying colors c and $\bar{c}'$, the opposite of c'. If time is read in the upward direction, a quark is emitting a gluon and changing color. Other interaction vertices exist that couple three or four gluons together, but the impact of these is highly suppressed in interactions.

a strong interaction vertex. If time flows from bottom up, this diagram represents a quark radiating a gluon, and changing color in the process. In this case, a quark of color c is converted to color c', while the gluon carries the opposites of both colors. The emitted gluon can then change the color of another quark. More complex strong processes, for example $\Delta^+ \rightarrow p^+ + \pi^0$, can be built up from the basic single-vertex interactions like Figure 1.3, and optionally those involving three or four gluons at a vertex (not shown). However, these additional gluon vertices only contribute to higher order versions of interactions that can be described in simpler terms; gluons cannot be particles left over in the final state of an interaction.

Electromagnetism is described by the theory of quantum electrodynamics, represented by the group U(1). Figure 1.4 illustrates the basic Feynman diagram of an electromagnetic interaction vertex. If time flows upward, a lepton or quark is radiating a photon. If time is progressing along the horizontal axis, then the diagram represents annihilation or pair production. More complex processes can be built up from these interaction vertices.

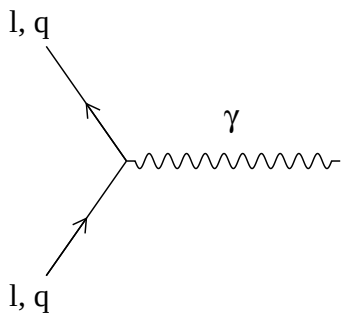


Figure 1.4 The Feynman diagram of the basic electromagnetic vertex, the constituent of electromagnetic processes. Two charged particles, either a lepton l or a quark q, join at a vertex with a photon γ. If time is read as flowing vertically, the diagram represents emission of a photon; horizontally, it represents pair production or annihilation.

Weak interactions are described by the Glashow-Weinberg-Salam model, which also incorporates electromagnetism. Weak interactions are represented mathematically by the SU(2) group. There are three basic Feynman diagrams for the weak interaction, one each for processes mediated by the W^+, W^- and Z bosons. Figure 1.5 provides the diagrams, in which leptons or quarks emit a W or Z boson as time flows upward. Complete reactions like $\mu \rightarrow e + \nu_\mu + \overline{\nu}_e$ can be described with such diagrams. Interactions also exist that couple Ws, Zs and γs together in vertices with three or four particles, but such interactions are suppressed.

The weak force is peculiar in that it only acts on particles of left-handed chirality and right-handed antiparticles. Chirality is a Lorentz-invariant quantum field characteristic related to helicity, the alignment of particle spin and momentum. If the spin and momentum are parallel, the helicity is right-handed; if antiparallel, the particle is left-handed. Chirality is inherent to the particle field. Helicity depends on reference frame for particles traveling slower than light because a frame traveling faster than the particle will see it travel backward, but retain its spin. But in the case of neutrinos, as the lightest massive particle, another particle reaching a faster frame is nearly impossible, so all observed neutrino interactions feature left-handed neutrinos and right-handed antineutrinos. In the limit as the particle velocity approaches the speed of light, chirality and helicity share the same value.

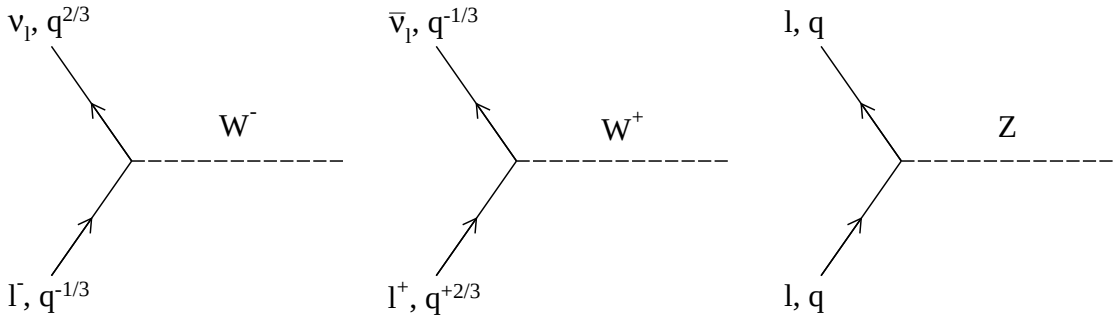


Figure 1.5 The three most common basic Feynman diagrams for the weak interaction, corresponding to the three force carriers W^+, W^- and Z. For these diagrams, time flows top to bottom. When a charged lepton emits a W, the W carries the charge while an (anti)neutrino is created to conserve lepton number. When a quark emits a W, the resulting quark must carry the charge that balances the reaction, for instance a quark of charge $+2/3$ in the initial state and a W^+ and a quark of charge $-1/3$ in the final state. This does not conserve quark flavor.

1.2 Theory of Massive Neutrinos

Neutrinos are the most ubiquitous elementary particle, but their difficulty to observe leaves them a mystery in many ways. However, this ensures they present some of the richest opportunities to explore physics.

As described in Section 1.1 and Table 1.1, neutrinos are spin-$\frac{1}{2}$ leptons with no electric charge and very small, nonzero, unknown mass. There are three flavors of neutrinos: electron (ν_e), muon (ν_μ) and (ν_τ), and their corresponding antineutrinos $\overline{\nu}_e$, $\overline{\nu}_\mu$, and $\overline{\nu}_\tau$. Within experimental limits, neutrinos are point-like particles with a magnetic moment less than $3.2 \cdot 10^{-11}\mu_B$ at 90% confidence [1]. Since neutrinos only interact with other particles via the weak force, all neutrinos are observed to have left-handed chirality and helicity, while all antineutrinos are observed to be right-handed. Right-handed neutrinos and left-handed antineutrinos (so-called "sterile" neutrinos) have not been ruled out, but these could never interact via the weak force, and would be especially inert.

Neutrinos were first theorized in 1930 by Wolfgang Pauli [87] to understand the spectrum of beta decay. Prior to that point, nuclei were thought to be composed of electrons and protons, and beta decay was understood to be a process where a nucleus ${}^{A}_{Z}\mathrm{X}$ transformed into ${}^{A}_{Z+1}\mathrm{X}$ plus an electron, and no other daughters. In this theory of beta decay, the electron must absorb nearly all energy of the reaction. However, experimental data showed that the electron spectrum continuously spanned the energy range from zero to the expected peak value [88]. Clearly, either an additional particle existed, or energy was not conserved in the decay. Pauli reasoned this particle must be light, spin-$\frac{1}{2}$ and neutral, but discovery would wait several decades.

The neutrino was confirmed experimentally in 1956 by the Savannah River experiment [20]. The experiment detected antineutrinos by way of a scintillation counter near the Savannah River nuclear reactor. Savannah River relied on the same signal as the Daya Bay experiment— the characteristic energy and timing of positrons and neutrinos generated by inverse beta decay ($\overline{\nu}_e + p \rightarrow n + e^+$). Starting in the 1970s, the Homestake experiment [89] measured the flux of electron neutrinos from the sun, but observed only one third of the expectation. This mystery was later solved by the Super Kamiokande experiment in 1998 [27], which discovered neutrino oscillations, and the Sudbury Neutrino Observatory in 2001, which measured all types of solar neutrinos [90] at once. Solar neutrino flux models were correct, but due to neutrino oscillations, Homestake could not observe electron neutrinos that became muon and tau neutrinos. All of these experiments and many others are discussed further in Section 1.3.

1.2.1 Neutrino Mass

Neutrinos are known to have mass due to the existence of neutrino oscillation, which will be shown in Section 1.2.3. Aside from this fact, however, little more is known about the values and nature of neutrino mass.

Property	Value(s)		
	ν_e	ν_μ	ν_τ
Electric Charge	0		
Spin	1/2		
Magnetic moment	$< 3.2{\cdot}10^{-11}\mu_B$, 90% C.L.		
$\sum m_\nu$	$0.0576\text{eV} < \sum m_\nu < 0.39\,\text{eV}$ at 95% C.L.		
Chirality	left (neutrino), right (antineutrino)		
Mass	<2 eV, 95% CL	<190 keV, 90% CL	<18.2 MeV 95% CL
Discovery	1956	1962	2000

Table 1.1 Experimental neutrino properties [1, 2].

1.2.1.1 Experimental Limits

The neutrino mass limits for the flavor states are indicated in Table 1.1. The most easily studied neutrino, the electron neutrino, is known to have mass less than 2 eV at 95% confidence [1]. The bounds on the other neutrino mass states are thus far on the order of MeV. The three mass eigenvalues, on the other hand, are unknown apart from the differences between their squares the "mass-square splittings"

$$\Delta m_{ij} \equiv m_j^2 - m_i^2 \tag{1.1}$$

and the sum of all three. The mass splittings are on the order of 10^{-3}–10^{-5} eV, and are listed in Table 1.2 in Section 1.2.4. Additionally, the sum of the mass states are bounded by cosmic microwave background surveys to be $\sum m_i < 0.39\,\text{eV}$ at 95% confidence [2]. The minimum value of the neutrino mass sum can be calculated from the mass splittings by setting the lowest neutrino mass to zero. Normal mass hierarchy then gives the lowest possible mass sum, 0.0576 eV.

1.2.1.2 Theoretical Descriptions

In particle physics, a Lagrangian characterizes the interactions of particles and the fundamental forces in an isolated system. For comprehensive theories, the Lagrangian contains

mass terms that dictate the nature of the particle mass. In the case of a free neutrino, the mass term provides the nature of neutrino mass and mixing [91].

Two types of mass models can explain neutrino mass: Dirac, Majorana, or a combination of both. In either case, the derivation begins with the neutrino weak interaction currents:

$$\begin{aligned} j_\alpha^{CC}(x) &= 2\sum_{l=e,\mu,\tau} \bar{\nu}_{lL}(x)\gamma_\alpha l_L(x) \qquad \text{Charged Current} \\ j_\alpha^{NC}(x) &= 2\sum_{l=e,\mu,\tau} \bar{\nu}_{lL}(x)\gamma_\alpha \nu_{lL}(x) \qquad \text{Neutral Current.} \end{aligned} \tag{1.2}$$

The first line in Equation 1.2 is the neutrino-lepton charged current interaction and the second line is the neutrino-neutrino neutral current interaction. The left-handed (L) neutrino fields (alone) interacting with the current are the flavor states, thus the mass term must be adapted from the flavor states. The mass states are invoked from the flavor states by way of neutrino mixing.

The Dirac mass term can be derived by permitting the right handed neutrinos into the mass term:

$$\mathcal{L}^D = -\sum_{l',l} \bar{\nu}_{l'L} M^D_{l'l} \nu_{lR}(x) + \text{h.c.}, \tag{1.3}$$

where "h.c." stands for hermitian conjugate [91]. The matrix M^D is a complex non-diagonal Dirac mass matrix. It can be diagonalized with a pair of unitary matrices U and V, which also serve to relate the neutrino mass and flavor states:

$$M^D = U^\dagger_{li} m_{ik} V_{lk}\,, \tag{1.4}$$

where the matrix m is diagonal and

$$\nu_{lL}(x) = U_{li}\nu_{iL}(x) \tag{1.5}$$

$$\nu_{lR}(x) = V_{li}\nu_{iR}(x)\,. \tag{1.6}$$

Here, ν_i are the neutrino mass states. Then, the Dirac mass term is:

$$\mathcal{L}^D = -\sum_i m_i \bar{\nu}_i(x)\nu_i(x)\,. \tag{1.7}$$

The Majorana mass term can be derived in a similar fashion, but with the added step of expressing the sterile right-handed neutrino and left-handed antineutrino fields in terms of the active fields. Sterile fields are replaced by applying charge conjugation to the active fields so that $(\nu_{lL})^c$ is the right-handed neutrino field. Then, the mass term has the form:

$$\mathcal{L}^M = -\frac{1}{2}\sum_{l',l} \bar{\nu}_{l'L} M^M_{l'l} (\nu_{lL})^c + \text{h.c.} \tag{1.8}$$

$$= -\frac{1}{2}\sum_{l'l} \bar{\nu}_{l'L} M^M_{l'l} C\nu^T_{lL} + \text{h.c.}, \tag{1.9}$$

where M^M is the complex, symmetric, non-diagonal Majorana mass matrix, and $M^M \neq M^D$. M^M can be diagonalized as before with unitary matrices U:

$$M^M = UmU^T\,, \tag{1.10}$$

where m is a diagonal mass matrix. Then,

$$\mathcal{L}^M = -\frac{1}{2}\bar{\nu}_L UmU^T C\bar{\nu}^T_L + \text{h.c.} \tag{1.11}$$

$$= -\frac{1}{2}\bar{\nu}^M m\nu^M. \tag{1.12}$$

By expressing ν^M of both terms of Equation 1.11 (written plus hermitian conjugate), note that

$$\nu^M = U^\dagger \nu_L + (U^\dagger \nu_L)^c\,. \tag{1.13}$$

From Equation 1.13, the fact that $(\nu^M(x))^c = \nu^M(x)$ follows. Thus, the Majorana mass term causes neutrinos and antineutrinos to be identical because the application of the charge conjugation to a field creates the antiparticle, and as a result, lepton number conservation cannot hold. Another consequence of Equation 1.13, and the creation of right-handed neutrino fields from charge conjugation applied to left-handed neutrinos, is that ν^M contains both right and left-handed components:

$$\nu^M = U^\dagger \nu_L + (U^\dagger \nu_L)^c = \nu^M_L(x) + \nu^M_R(x)\,. \tag{1.14}$$

It then follows that

$$\nu_R^M(x) = \left(\nu_L^M(x)\right)^c \tag{1.15}$$

$$\nu_{iR}(x) = (\nu_{iL}(x))^c \ . \tag{1.16}$$

This mixing of right and left fields distinguishes Majorana mass from Dirac mass.

One popular explanation of why neutrinos have nonzero mass, but much smaller mass than any other fermion, is the Seesaw Mechanism, which combines Dirac and Majorana mass terms [92]. The combined term is:

$$\mathcal{L}^{DM} = -\frac{1}{2}\bar{\nu}M_L^M(\nu_L)^c - \bar{\nu}_L M^D \nu_R - \frac{1}{2}(\bar{\nu}_R)^c M_R^M \nu_R + \text{h.c.}. \tag{1.17}$$

Equation 1.17 can be expressed as:

$$\mathcal{L}^{DM} = -\frac{1}{2}\bar{n}_L M^{DM}(n_L)^c + \text{h.c.} \tag{1.18}$$

by defining a six component field n_L:

$$n_L = \begin{pmatrix} \nu_L \\ (\nu_R)^c \end{pmatrix} \tag{1.19}$$

and the symmetric 6×6 matrix M^{DM}:

$$M^{DM} = \begin{pmatrix} M_L^M & M^D \\ (M^D)^T & M_R^M \end{pmatrix}, \tag{1.20}$$

where the components M_b^a are the 3×3 matrices previously discussed.

The Seesaw Mechanism invokes the Dirac and Majorana mass term with three assumptions. The first is that there is no left-handed Majorana mass term. The second is that the Dirac mass is generated by a Higgs mechanism, on the order of a lepton or quark mass. Finally, the right-handed Majorana mass term breaks lepton number conservation at energy scales much larger scale than the Dirac mass.

The show the generation of neutrino masses, take the simplified case of a 2×2 Dirac and Majorana mass matrix (Equation 1.20 with four mass values M rather than four matrices). The eigenvalues of this matrix are

$$\lambda_\pm = \frac{1}{2}\left(M_L^M + M_R^M\right) \pm \frac{1}{2}\sqrt{(M_L^M + M_R^M)^2 - 4(M_l^M M_R^M - M_D^2)}\,. \tag{1.21}$$

If λ_- is assumed to be zero, then

$$M_L^M M_R^M = M_D^2 \tag{1.22}$$

$$\lambda_+ = M_L^M + M_R^M \,. \tag{1.23}$$

Due to the assumption $M_R^M \gg M^D$, Equation 1.22 enforces an opposing relationship between M_L^M and M_R^M, where if one is large the other must be small (hence the name "Seesaw Mechanism"). The eigenvalues correspond to mass eigenstates $\psi_\pm$:

$$\psi_- = (\nu_L + \nu_L^c) + \frac{M^D}{M_R^M}(\nu_R + \nu_R^c) \simeq (\nu_L + \nu_L^c) \tag{1.24}$$

$$\psi_+ = (\nu_R + \nu_R^c) - \frac{M^D}{M_R^M}(\nu_L + \nu_L^c) \simeq (\nu_R + \nu_R^c)\,, \tag{1.25}$$

where the simplifications on the right hand side occur because $M^D \ll M_R^M$. Thus, the left-handed neutrinos are dominated by the massless state ψ_- while the right-handed (sterile) neutrinos are mostly the massive state ψ_+.

1.2.2 Neutrino Mixing

The concept behind neutrino mixing is that neutrino flavor eigenstates and mass eigenstates do not share the same basis. Rather, the eigenstates are interrelated by a unitary mixing matrix U such that

$$\begin{aligned} |\nu_\alpha\rangle &= U_{\alpha j}\,|\nu_j\rangle \qquad \text{neutrinos} \\ |\nu_\alpha\rangle &= U^*_{\alpha j}\,|\nu_j\rangle \qquad \text{antineutrinos} \end{aligned} \tag{1.26}$$

where α and j index the flavor and mass states respectively, and U is the PMNS matrix indicated in Equation 1.27:

$$U_{\text{PMNS}} = \begin{pmatrix} 1 & 0 & 0 \\ 0 & \cos\theta_{23} & \sin\theta_{23} \\ 0 & -\sin\theta_{23} & \cos\theta_{23} \end{pmatrix} \begin{pmatrix} \cos\theta_{13} & 0 & \sin\theta_{13}e^{-i\delta} \\ 0 & 1 & 0 \\ -\sin\theta_{13}e^{i\delta} & 0 & \cos\theta_{13} \end{pmatrix} \begin{pmatrix} \cos\theta_{12} & \sin\theta_{12} & 0 \\ -\sin\theta_{12} & \cos\theta_{12} & 0 \\ 0 & 0 & 1 \end{pmatrix} \tag{1.27}$$

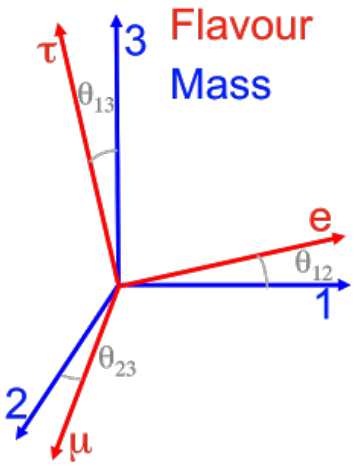


Figure 1.6 Graphical representation of the mixing angles θ_{ij} as rotations between mass and flavor eigenstates [16].

Thus, a neutrino of a definite mass state receives contributions from each of the flavor states according to $||U_{\alpha j}||^2$.

While there are several possible representations, U_{PMNS} in Equation 1.27 is expressed as a product of rotation matrices in which the mixing angles θ_{ij} describe the rotation between the flavor bases and the mass bases, as illustrated in Figure 1.6. The complex phase $e^{\pm i\delta}$ accounts for possible CP violation, but has not been confirmed by experiment, and may be zero. Additionally, for Majorana neutrinos an extra matrix is appended into Equation 1.27:

$$U_{PMNS} \rightarrow U_{PMNS} \begin{pmatrix} 1 & 0 & 0 \\ 0 & e^{i\phi_1} & 0 \\ 0 & 0 & e^{i\phi_2} \end{pmatrix} \tag{1.28}$$

where ϕ_1 and ϕ_2 are Majorana phases. These phases are imperceptible to oscillation experiments since the oscillation probability depends on the magnitudes of matrix values $||U_{\alpha j}||^2$.

1.2.3 Neutrino Oscillation

Neutrino oscillation is the phenomenon whereby a neutrino or antineutrino generated in one flavor state— electron, muon or tau— will propagate as a time-dependent superposition of all states, and may later interact as a different flavor. When a reaction generates a neutrino it has a specific mass and flavor. The neutrino propagates according to its mass, which is conserved, while the flavor is left undefined until another interaction. In the subsequent interaction, the neutrino flavor is established probabilistically within the superposition of flavor states, according to the mixing matrix and propagation.

To derive the oscillation probability P, start with the squared modulus of the inner product between two states:

$$P(\nu_\alpha \to \nu_\beta) = \left\| \langle \nu_\beta | \nu_\alpha(t) \rangle \right\|^2 \tag{1.29}$$

where α and β refer to initial and final flavor states respectively. In a vacuum, neutrinos propagate as plane waves:

$$|\nu_i(t)\rangle = e^{-\mathrm{i}(E_i t - p_i L)} \, |\nu_i(0)\rangle \tag{1.30}$$

where L is the distanced that the neutrino has propagated. The vacuum assumption holds for most circumstances since neutrinos seldom interact, and suits Daya Bay in particular. For relativistic neutrinos, $t \approx L$ in natural units. Given the assumption that the neutrino has an energy E regardless of its mass eigenstate m, and that $E \gg m$, then $p_i = \sqrt{E^2 - m_i^2} \approx E - m_i^2/2E$. This expression holds even when assuming that the momentum P is independent of m_i rather than the energy because neutrinos are relativistic, hence $E \sim p$ [93]. The time evolution of $|\nu_i(t)\rangle$ becomes:

$$|\nu_i(t)\rangle = e^{-\mathrm{i}(m_i^2/2E)L} \, |\nu_i(0)\rangle \ . \tag{1.31}$$

To apply the propagator of Equation 1.31 to neutrino oscillation probability, the flavor states must be converted to the mass states using U_{PMNS} by Equation 1.26, while summing

over the mass states. For antineutrinos, the result is:

$$P(\nu_\alpha \to \nu_\beta) = \left\| \langle \nu_\beta | \nu_\alpha(t) \rangle \right\|^2 \tag{1.32}$$

$$= \left\| \left\langle \nu_\beta \left| U_{\beta i}\, e^{-\mathrm{i}(m_i^2/2E)L}\, U^*_{\alpha i} \right| \nu_\alpha(t) \right\rangle \right\|^2 \tag{1.33}$$

$$= \left\| \sum_i U^*_{\alpha i} e^{-\mathrm{i}(m_i^2/2E)L} U_{\beta i} \right\|^2 \tag{1.34}$$

$$= \left(\sum_i U^*_{\alpha i} e^{-\mathrm{i}(m_i^2/2E)L} U_{\beta i} \right) \left(\sum_j U^*_{\alpha j} e^{-\mathrm{j}(m_j^2/2E)L} U_{\beta j} \right)^* \tag{1.35}$$

From [93], this expression works out to:

$$\begin{aligned} P(\nu_\alpha \to \nu_\beta) \;=\; \delta_{\alpha\beta} \;&-\; 4 \sum_{i>j} \mathrm{Re}\left(U^*_{\alpha i} U_{\beta i} U_{\alpha j} U^*_{\beta j} \right) \sin^2\left(\Delta m^2_{ij} \frac{L}{4E} \right) \\ &+\; 2 \sum_{i>j} \mathrm{Im}\left(U^*_{\alpha i} U_{\beta i} U_{\alpha j} U^*_{\beta j} \right) \sin\left(\Delta m^2_{ij} \frac{L}{2E} \right) . \end{aligned} \tag{1.36}$$

From Equation 1.36, the requirement that neutrinos must have mass for oscillation to occur is clear from the dependence on m^2_{ij}, although, the oscillation has no dependence on the actual neutrino masses m_i. The oscillatory behavior is also evident. The kinematic argument of the first sine of Equation 1.36 (in natural units above) is equivalent to:

$$\Delta m^2_{ij} \frac{L}{4E} = \frac{1.27 \text{ MeV}}{\text{meters eV}^2} \Delta m^2_{ij} \frac{L}{E} \tag{1.37}$$

in SI units.

Equation 1.36 simplifies for neutrino disappearance experiments ($\nu_\alpha \to \nu_\alpha$) such as Daya Bay. In this case, the flavor indices α and β are equal, the product of the matrix elements becomes the product of squares, and the imaginary term becomes zero:

$$P(\nu_\alpha \to \nu_\alpha) = 1 - 4 \sum_{i>j} \|U_{\alpha i}\|^2 \|U_{\alpha j}\|^2 \sin^2\left(\Delta m^2_{ij} \frac{L}{4E} \right) \tag{1.38}$$

The expression is much more complicated for appearance experiments ($\nu_\alpha \to \nu_{\beta \neq \alpha}$).

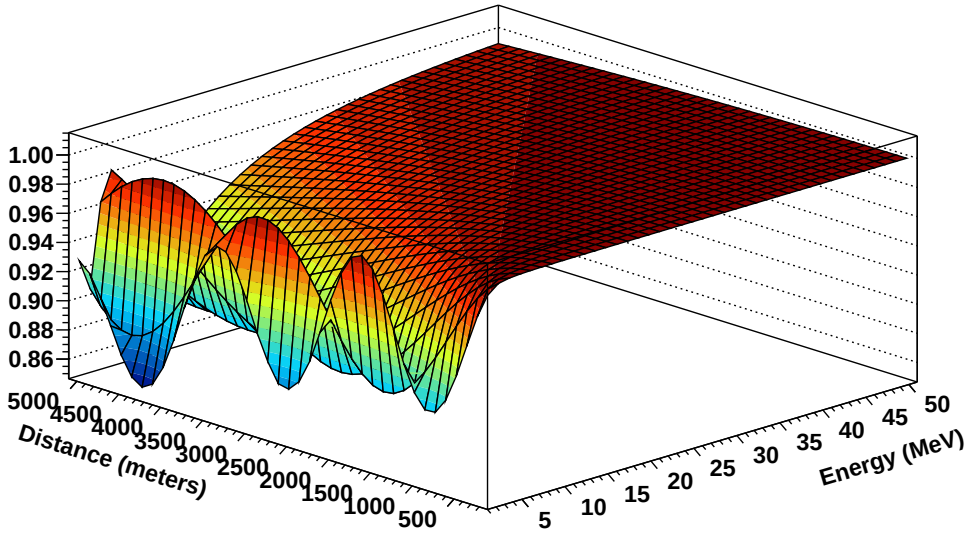


Figure 1.7 Electron neutrino survival probability assuming the parameter values of Table 1.2, over a wide range of neutrino energies and baselines.

1.2.4 Neutrino Oscillation Parameters

The values of physical parameters in Equations 1.27 and 1.36 have been measured by experiments to varying degrees of precision, and the current values as of this work are listed in Table 1.2. Before Daya Bay, other experiments measured mixing angles θ_{12} and θ_{23} and mass-square splittings Δm^2_{21} and $\Delta m^2_{32} \sim \Delta m^2_{31}$. Note that Δm^2_{32} and Δm^2_{31} are thus far indistinguishable in experiment, so experiments have only measured a linear combination of both, and that none have observed the sign of either Δm^2_{31} or Δm^2_{32}. Mixing angle θ_{13} had only been constrained to an upper limit before Daya Bay, and nothing is known about the CP violation phase δ_{CP} or possible Majorana phases ϕ_1 and ϕ_2. For the oscillation parameter values of Table 1.2 the survival probability for electron (anti)neutrinos is shown in Figure 1.7.

At $\sin^2 2\theta_{12} = 0.857 \pm 0.024$, or $\theta_{12} = 34 \pm 1°$, angle θ_{12} turns out to be large, representing a high degree of mixing (from Equation 1.27, 45° would represent maximal mixing) [1]. Solar and atmospheric neutrino experiments are most responsible for this measurement. Solar neutrinos have energies on the order of 10 MeV that travel about $1.5 \cdot 10^6$ km [90]. Atmospheric neutrino experiments rely on neutrinos created by collisions of cosmic rays and atmospheric particles. Thus, the neutrino energies range from 100 MeV and higher and the baselines scale with the diameter of the atmosphere [32]. For solar neutrino experiments, information comes from detecting the disappearance of electron neutrinos, while for both solar and atmospheric experiments, information comes from the appearance of ν_e and ν_μ.

Where θ_{12} is large, θ_{23} is consistent with maximal mixing. Atmospheric and accelerator experiments have measured this angle to be $\sin^2 2\theta_{23} > 0.95$ at 90% confidence, or $39° < \theta_{23} < 51°$ [1]. Accelerators vary, but experiments typically employ a baseline of 100–1000 km, produce neutrinos at energies around 1 GeV, and search for ν_μ disappearance. Whether $\theta_{23} \geq 45°$ or $\theta_{23} \leq 45°$ is unknown.

Until the ongoing reactor experiments Daya Bay [8], RENO [74] and Double Chooz [43], only an upper limit of $\sin^2 2\theta_{13} < 0.17$ at 90% confidence had been established on θ_{13}, which had been consistent with zero [41, 94]. Angle θ_{13} is now the most precisely measured mixing angle at $\sin^2 2\theta_{13} = 0.090^{+0.008}_{-0.009}$ or $8.7^{+0.4}_{-0.5}$ degrees [3].

The mass-square splittings Δm^2_{ij} have been measured with comparable success. The mass splittings exhibit two tiers of value: $|\Delta m^2_{31}| \approx |\Delta m^2_{32}| \gg |\Delta m^2_{21}|$. Solar experiments and KamLAND have provided the most precise data on Δm^2_{21}, measuring $\Delta m^2_{21} = 7.50^{+0.19}_{-0.20} \cdot 10^{-5}\,\text{eV}^2$. Mass splittings Δm^2_{31} and Δm^2_{32} have been measured by accelerator experiments, but are not uniquely separable because the difference between them, which is equal to Δm^2_{21} in value, is smaller than the uncertainties of the measurements. The measurement of record comes from MINOS at $|\Delta m^2_{31}| \approx |\Delta m^2_{32}| = 2.41^{+0.09}_{-0.10} \cdot 10^{-3}\,\text{eV}^2$ [4] (although at the time of the analysis presented in this dissertation, the most recent measurement from MINOS was $|\Delta m^2_{31}| \approx |\Delta m^2_{32}| = 2.32^{+0.12}_{-0.08} \cdot 10^{-3}\,\text{eV}^2$ [95]). Daya Bay has measured $|\Delta m^2_{31}| \approx |\Delta m^2_{32}| = 2.59^{+0.19}_{-0.20} \cdot 10^{-3}\,\text{eV}^2$ [3].

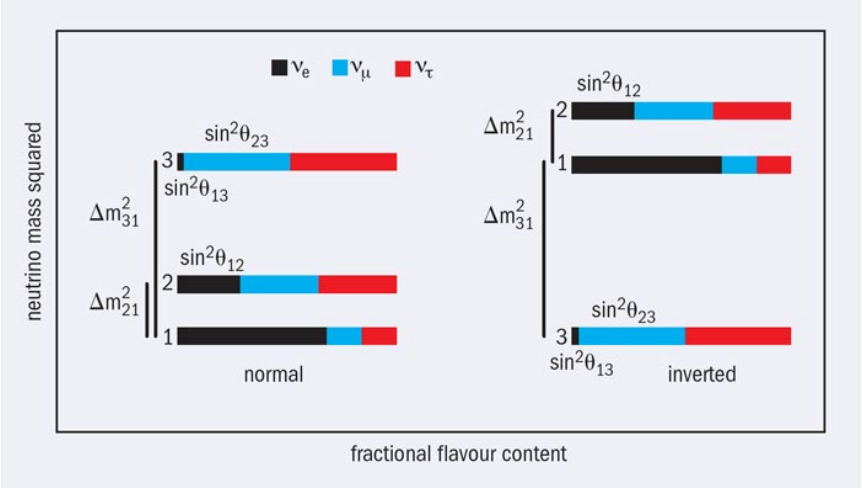


Figure 1.8 Relative neutrino mass-squared values plotted against mass eigenstate flavor content for normal and inverted hierarchies. For this graph, mixing angles are set to: $\sin\theta_{12} = 0.30$, $\sin\theta_{13} = 0.03$ and $\sin\theta_{23} = 0.50$ [17, 18].

The lack of knowledge of the sign of Δm^2_{31} or Δm^2_{32} is referred to as the neutrino mass hierarchy question, which is diagrammed in Figure 1.8. It is unknown whether the mass states rank as $m_3 > m_2 > m_1$ (normal hierarchy) or $m_2 > m_1 > m_3$ (inverted hierarchy), or where all three values lie in absolute mass. Vacuum neutrino oscillation experiments are largely insensitive the signs of the Δm^2_{ij}. Neutrino disappearance ($\nu_\alpha \to \nu_\alpha$) experiments are completely insensitive because in this case the oscillation probability only depends on the squares of sines and cosines of Δm^2_{ij}. For appearance experiments ($\nu_\alpha \to \nu_{\beta\neq\alpha}$), the sign of Δm^2_{ij} has a lower order effect. Solar neutrino oscillations in matter have revealed the sign of Δm^2_{21} because neutrino interactions with matter allow ν_e charge current interactions.

Data from the Planck Cosmic Microwave Background measurements and Baryon Oscillation Spectroscopic Survey provide a limit on the sum of the neutrino masses of $\sum_j m_j < 0.39\,\text{eV}$ [2]. Additionally, the neutrino mass sum is bounded from below at $\sum_j m_j > 0.0576\,\text{eV}$ by the non-zero mass splittings.

1.3 History of Neutrino Experiments

The Daya Bay experiment would not be possible without the knowledge provided by many influential neutrino experiments. A small subset of experiments that discovered neutrinos and explored their properties are discussed in this section.

1.3.1 Detection of Neutrinos

From their theoretical postulation until the late 1950s, neutrinos were thought to be undetectable particles due to their low cross-section. Starting with the Hanford and Savannah River experiments, several vital endeavors proved that neutrinos were not only detectable, but that their properties could be explored as well [96].

1.3.1.1 Savannah River and Hanford, 1953–1956

The existence of the free (anti)neutrino was confirmed by a pair of experiments performed by F. Reines, C. Cowan and others. The first experiment took place at the Hanford reactor, but the antineutrino signal was obscured by excessive cosmic ray backgrounds [97, 98]. The successor experiment at Savannah River was conclusive [19, 20].

At Savannah River and Hanford the team deployed scintillation counters proximal to the nuclear reactors to detect antineutrinos via inverse beta decay:

$$\overline{\nu}_e + p \;\rightarrow\; e^+ + n\,. \tag{1.39}$$

At the time, the distinction between neutrinos and antineutrino was not realized.

The apparatus in these experiments was a "club sandwich" of alternating scintillation counters and target tanks. The scintillator solution consisted of solvent triethylbenzene with terphenyl and scintillator POPOP in a two foot thick chamber read out by photomultiplier tubes (PMTs). The target was an aqueous solution of cadmium chloride. These layers were enveloped by paraffin and lead shielding, and in the case of Savannah River, installed 11 m from the reactor core 12 m underground.

Given the high rate of cosmic ray backgrounds, the team verified the inverse beta decay signal with several techniques. The signal was discriminated from backgrounds by a distinctive double-pulsed energy and timing signature, similar to that at Daya Bay. The positron annihilated promptly, followed by additional deposited energy from the neutron capture on cadmium. The signal rate was proven to be linearly dependent on the number of target protons by the substitution of heavy water for some of the ordinary water. Altering the cadmium concentration or the interlayer shielding thickness also changed the signal in manners consistent with reactor antineutrinos. However, no attenuation in the antineutrino signal was seen after augmenting the shielding. Accidental coincidences of singles radiation were determined by the energy spectrum, and the rate of backgrounds from neutrons entering the target from outside were calculated with a calibration source.

The techniques in this experiment were highly influential. Many subsequent neutrino experiments, even today, rely on similar inverse beta decay signals, scintillation and PMT apparatus, and background suppression as the Reines and Cowan experiments.

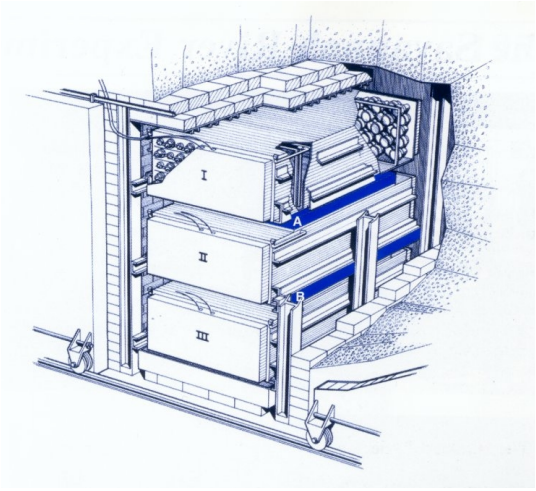


Figure 1.9 Illustration of Savannah River detector [19, 20].

1.3.1.2 Davis Experiment, 1954

Acting on the suggestion by B. Pontecorvo [99] and L. W. Alvarez [100], R. Davis' 1954 experiment proved neutrinos and antineutrino were distinct particles. The experiment sought to detect antineutrinos by the reaction

$$^{37}\mathrm{Cl} + \bar{\nu} \xrightarrow{?} {}^{37}\mathrm{Ar} + e^- \tag{1.40}$$

in carbon tetrachloride exposed to nuclear reactor antineutrino flux [101]. Neutrinos will participate in the reaction whereas antineutrinos will not if they are distinct particles. After exposure, the carbon tetrachloride tanks were sampled for ^{37}Ar by sweeping through with helium gas, then running the helium-argon mixture through a cooled charcoal trap. The ^{37}Ar is radioactive, so its proportion was determined by radiation counting.

Davis saw no ^{37}Ar produced due to reactor antineutrinos. The proportion of ^{37}Ar present was consistent with cosmic ray backgrounds, which was quantified by operating the experiment at sea level and 14,100 ft. Due to the lack of ^{37}Ar, the experiment determined that neutrinos and antineutrinos are distinct particles. At the nucleon level of Equation 1.40, the reaction is

$$n + \overline{\nu}_e \xrightarrow{?} p + e^-, \tag{1.41}$$

which does not conserve lepton number. Neutrinos do trigger the comparable reaction:

$$n + \nu_e \rightarrow p + e^-, \tag{1.42}$$

and thus neutrinos and antineutrinos are not identical.

1.3.1.3 Parity Violation, 1957

While parity conservation had held in all known interactions before C. S. Wu's experiment [102], as T. D. Lee and C. N. Yang observed, it had not been demonstrated in weak interactions [103].

Wu's experiment utilized a cryostat containing radioactive ^{60}Co, which beta decays to produce an electron and an electron antineutrino. In the experiment, the ^{60}Co was cooled

near absolute zero and polarized in a magnetic field. The degree of polarization was measured from emitted gamma rays by the relaxation of the daughter nucleus ^{60}Ni. Electrons were detected by way of a anthracene crystal-based scintillation counter, while NaI crystals measured the ^{60}Co polarization to be 60%. The experiment observed clearly that the electrons were emitted preferentially in the opposite direction to the nuclear spin.

1.3.1.4 Neutrino Helicity, 1958

In this experiment, the neutrino was shown to have left-handed helicity by observing nuclear decays of ^{152m}Eu [104]. The isotope ^{152m}Eu with 0-spin decays by electron capture to a neutrino and an excited ^{152}Sm* nucleus with spin 1, which then relaxes to a spin-0 ground state by emitting a photon. Photons and neutrinos emitted back-to-back will share the same value of helicity by conversation of angular momentum.

The experimental apparatus consisted of the ^{152m}Eu source in an analyzing magnet above lead shielding. Photons that passed by the lead shield resonant-scattered off a Sm surface into a NaI crystal read out by a PMT. With this set up, photons were expected to be 75% circularly polarized, which was consistent with the observation of 68±14%. The circular polarization was all in the positive direction, which indicated negative helitic y.

1.3.1.5 Brookhaven Neutrino Experiment, 1962

The Brookhaven neutrino experiment of 1962 was the first to study neutrinos produced by an accelerator, and the first to demonstrate that there exist more than one flavor of neutrino [21].

The experiment situated at the Alternating Gradient Synchrotron (AGS) relied on a muon neutrino beam created by kaon and pion decay:

$$\begin{aligned} \pi^{\pm} &\rightarrow \mu^{\pm} + (\nu/\bar{\nu}) \\ K^{\pm} &\rightarrow \mu^{\pm} + (\nu/\bar{\nu})\,. \end{aligned} \tag{1.43}$$

Note the decay product is ν rather than ν_μ: before this experiment, it was unknown whether there was more than one type of neutrino. The AGS accelerated a beam of 15 GeV protons into a beryllium target, which produced pions and kaons, a technique that inspires neutrino beam experiments to this day. The pions and kaons decay into multiple possible particles, but all except neutrinos are obstructed by shields of steel, lead and paraffin.

Neutrino interactions were observed in a 10 t aluminum spark chamber. Beam timing, fiducial cuts, and coincidence triggers were used to reduce background events. If there were one type of neutrino, then the neutrinos in the beam would be equally likely to create electrons and muons in the detector by the reactions:

$$\nu + n \xrightarrow{?} p + e^- \qquad \nu + p \xrightarrow{?} n + e^+ \tag{1.44}$$

$$\nu + n \xrightarrow{?} p + \mu^- \qquad \nu + p \xrightarrow{?} n + \mu^+ \tag{1.45}$$

But, the electron reaction products of Equation 1.44 were never observed, hence there had to exist at least two types of neutrinos.

1.3.1.6 Charge-Parity Violation, 1964

Before 1964, physicists suspected all four fundamental forces exhibited charge-parity (CP) symmetry. However, an experiment discovered CP violation in the weak kaon decay to pions [105]. The experiment involved a beam of two species of kaons from the Brookhaven AGS: the K_1, which is the sum of the neutral kaon (K^0) and antikaon states ($\bar{K}^0$), and K_2, their difference. The K_1 decays into two pions with a half-life of of $9 \cdot 10^{-11}$ s while the K_2 decays into three pions (or one pion and two leptons) with a longer half-life of $5 \cdot 10^{-8}$ s. K_1 should not decay into three pions, nor K_2 two pions, because K_1 and the two pion state have CP=+1 while K_2 and the three pion state have CP=−1.

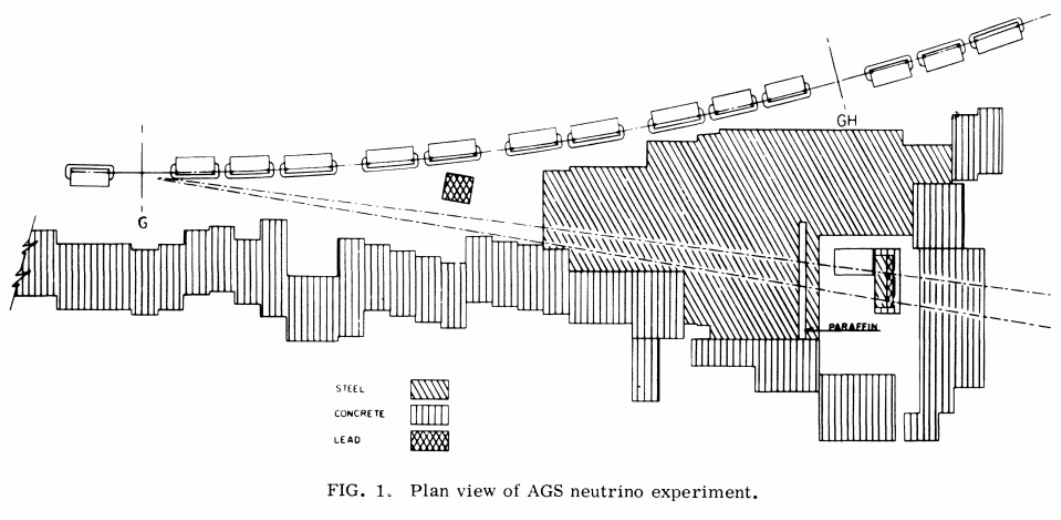


Figure 1.10 Diagram of the beam and shielding of the Brookhaven neutrino experiment [21].

In a similar technique to Brookhaven Neutrino Experiment, the experiment produced a beam of K_1 and K_2, which became a pure K_2 after distance was given for all K_1 to decay. The K_2 beam still showed two pion decays, however, at a proportion of one in 1000. The odd two pion decay was evidence for K_2 becoming K_1 in the beam by way of by flavor-changing charged current weak interactions. This demonstrated CP violation because the K_1 and two pions have a CP value of $+1$ whereas the K_2 and three pions have a CP value of -1.

CP violation is also seen in kaon semi-leptonic decays. A neutral kaon can decays into a positive pion, electron and electron antineutrino, or a negative pion, positron and electron neutrino:

$$K_L^0 \rightarrow \pi^+ + e^- + \overline{\nu}_e \tag{1.46}$$

$$K_L^0 \rightarrow \pi^- + e^+ + \nu_e \,. \tag{1.47}$$

The final states are CP transforms of each other, but their branching ratios differ— the former is 0.33% more likely to occur [84].

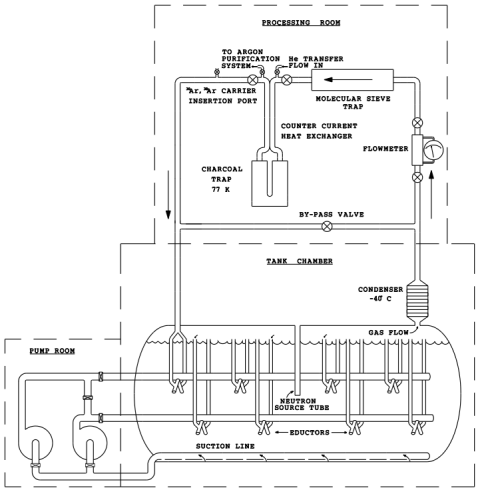


Figure 1.11 Schematic of the Homestake experiment [22].

1.3.1.7 Homestake 1970–1994

By 1970, Davis et al. deployed a larger version of the 1954 chlorine detector to an underground mine at Homestake, South Dakota to detect neutrinos of solar origin [89, 22]. The 390,000 L tank of tetrachloroethylene utilized the same reaction of Equation 1.40:

$$^{37}\mathrm{Cl} + \nu_e \;\rightarrow\; ^{37}\mathrm{Ar} + e^- \,. \tag{1.48}$$

A schematic of the Homestake experiment is shown in Figure 1.11. The detector was installed 4850 ft underground, thus reducing the comic ray neutrino contamination of ^{37}Ar0 to 0.1 per day.

Homestake ran for decades and ultimately showed a factor of three deficit of solar neutrinos compared to theoretical predictions. The count rate was measured over the whole data set to be 2.56±0.16(stat.)±0.16(sys.) counts/Cl atom/s. The expected rates from theory ranged from 6.36 to 9.3 counts/Cl atom/s. This discrepancy, the so-called "solar neutrino problem", was not resolved until the discovery of neutrino oscillations by Super Kamiokande and the simultaneous detection of all neutrino flavors by the Sudbury Neutrino Observatory (Sections 1.3.2.1 and 1.3.2.2).

1.3.1.8 Supernova SN1987A: IMB, Kamiokande-II and Baksan

Three experiments, IMB, Kamiokande-II and Baksan, gained fame from their detection of supernova neutrinos, although they were not dedicated neutrino experiments.

IMB (Irvine-Michigan-Brookhaven) was a water Cherenkov detector to search for proton decay [106]. The experiment deployed a target of 3300 t water underground at a depth of 1570 m.w.e., read out by PMTs. Beside the depth, the cosmic ray background was further reduced by vertex reconstruction: cosmic rays events have vertices reconstructed to a point on the periphery of the detector with daughters traveling downward; neutrino or proton decay events have vertices originating in the fiducial volume.

Typically, IMB received about two neutrino events per day. The SN1987A supernova yielded eight over six seconds, with energies between 20–40 MeV. The calculated flux of neutrinos at the detector extrapolated to the supernova location in the Large Magellanic Cloud gives a neutrino emission of $3{\cdot}10^{56}$ total.

Kamiokande-II was a water Cherenkov detector of 2140 fiducial tons of water located underground [23]. The primary aim of Kamiokande-II was detection of nucleon decay and solar ^{8}B neutrinos. Neutrinos of all flavors were detected through the scattering reaction

$$\nu_x + e \;\rightarrow\; \nu_x + e\,. \tag{1.49}$$

The subsequent scattering of the electron plus the kinematics of the reaction provide incoming neutrino directionality within $\pm 28°$.

Eleven neutrinos of energies 7.5–36 MeV were detected over a 13 s span, with directions pointing back to the Large Magellanic Cloud. The timing and energies of neutrino events are shown in Figure 1.12. The neutrino flux agreed well with supernova models, arriving about 18 hours before the visual detection of SN1987a.

Unlike IMB and Kamiokande, the INR Baksan Underground Scintillation Telescope was not a water Cherenkov detector. PMTs observed 3150 cells of oil-based scintillator totaling

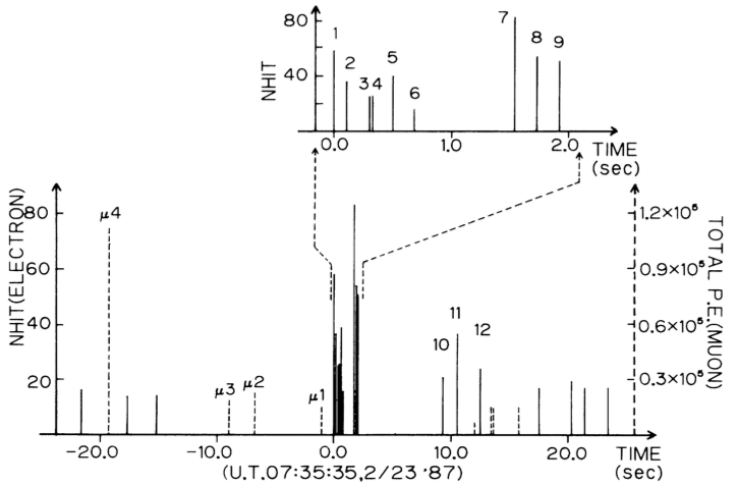


Figure 1.12 Readout of the Kamiokande-II events in a 45 s interval about the neutrino burst. The height of each line indicates the relative energy of the event. Solid lines represent electron events in units of the number of hit PMTs. Dashed fines represent muon events in units of the number of photoelectrons. [23]

200 tons of fiducial mass under 850 m.w.e. of rock [24]. The Baksan neutrino telescope is sensitive to neutrinos by inverse beta decay, or, if the neutrino energy is above 30 MeV, carbon capture:

$$\begin{aligned} \overline{\nu}_e + p &\rightarrow n + e^+ \\ \overline{\nu}_e + {}^{12}\mathrm{C} &\rightarrow {}^{12}\mathrm{N} + e^- . \end{aligned} \tag{1.50}$$

Baksan saw five neutrino events in 9.1 s. Interestingly, as noted by Baksan in Figure 1.13, the Baksan and Kamiokande-II signals appear to arrive in three bunches, while the IMB signal is more evenly distributed in time. The energy spectra do not show a bunched structure. The three-peak structure suggests the possibility of three neutrino masses, but the signal is not conclusive because the experiments were not clocked precisely enough.

1.3.1.9 DONUT, 2000

The discovery of the tau neutrino was not accomplished until the year 2000 by the DONUT experiment (Direct Observation of the NU Tau) [25]. The experiment collided an

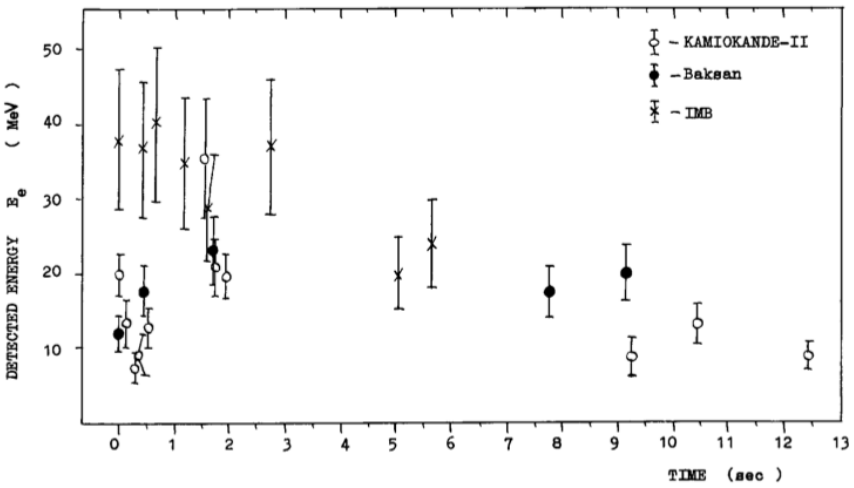


Figure 1.13 The timing and energy of the Baksan, IMB and Kamiokande-II experiments' detection of SN1987a neutrinos [24].

800 GeV proton beam into a tungsten beam dump, which in part created charmed mesons such as the D_s. This charmed meson can decay into a tau and tau antineutrino, after which the tau itself decays into a tau neutrino and other leptons. Some of the tau neutrinos interacted in the detector via charge current interactions, which create new taus. These taus traveled about 2 mm before decaying in the detector, exhibiting tracks characteristic of a tau neutrino.

The detectors were based on emulsion modules interleaved with scintillating fiber planes. Magnetic horns deflected charged background particles, and shielding and a scintillation counter veto were in place to further reduce backgrounds. If the trigger system of charged particle spectrometers and hodoscopes suggested a candidate tau neutrino event, the emulsion modules would be developed like photographs. Figure 1.14 shows a diagram of the experiment. DONUT identified 203 neutrino interactions in the nuclear emulsion targets from $3.54{\cdot}10^{17}$ protons incident on the beam dump. Four of these were identified as tau neutrinos against a background expectation of 0.34 events.

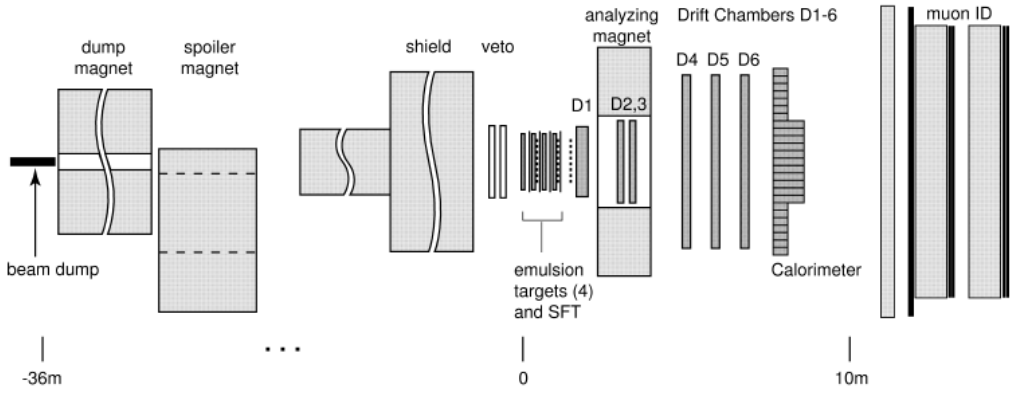


Figure 1.14 Diagram of the DONUT experiment [25].

1.3.2 Neutrino Oscillations

From the 1980s to the present day, several experiments brought the idea of neutrino oscillations from theory to observed phenomenon. Neutrino oscillations are now in a precision regime in which oscillation parameters are measured at the precision of percentage points [107]. The work of several experiments listed in this section built a quantitative understanding of neutrino oscillations that made Daya Bay conceivable in the first place.

1.3.2.1 Super Kamiokande

Super Kamiokande is a 50 kt water Cherenkov detector searching for atmospheric neutrino oscillations and nucleon decay since 1996 [26]. It was the first experiment to show that neutrinos have mass and oscillate.

The deep underground Super Kamiokande detector spans a cylinder 40 m tall and 40 m in diameter, as illustrated in Figure 1.15. This volume is divided into two optically separate zones outfitted with 50 cm PMTs providing 40% coverage. The inner volume, which contains the neutrino target, is half the diameter and most of the height of the entire detector. The outer detector tags charged particles such that all events seen only in the inner detector must be due to neutrinos and antineutrinos. Super Kamiokande can detect neutrinos over the energy range 4.5 MeV–1 TeV by way of charged current muon or electron production,

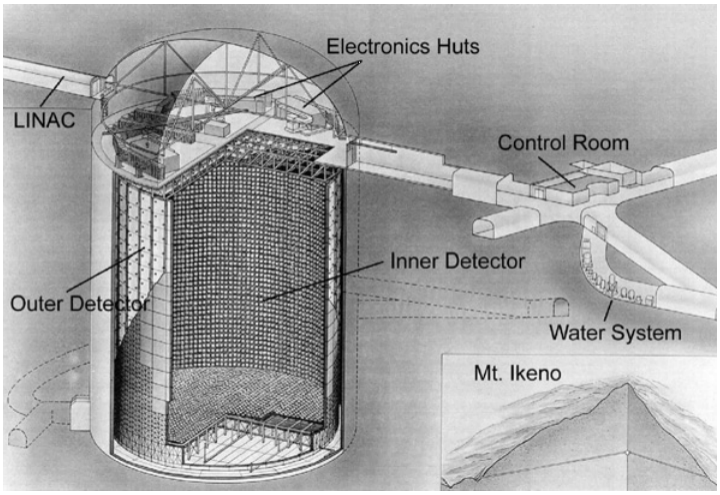


Figure 1.15 Drawing of Super Kamiokande detector [26].

depending on the flavor of the neutrino. The detector distinguishes the electrons and muons by the Cherenkov rings they produce. Muon rings are better resolved than electron rings because electrons are deflected by electromagnetic interactions with nuclei and other electrons, and the electrons emit bremsstrahlung photons that subsequently produce pairs of electrons and positrons

Super Kamiokande observed the first neutrino oscillations by studies of electron and muon flavor in atmospheric neutrinos. Atmospheric neutrinos are those that are generated in the Earth's atmosphere by cosmic ray interactions, which produce pions among other products. A pion usually decays into a muon and muon (anti)neutrino, after which the muon decays into an electron, an electron (anti)neutrino and a muon (anti)neutrino, for a ratio of two muon (anti)neutrinos to one electron (anti)neutrino [108]. However, the measured muon and electron neutrino rates revealed a ratio only two thirds of what was expected. The data to

Monte Carlo ratios of flavor ratios were:

$$R \equiv \frac{(\nu_\mu,\overline{\nu}_\mu/\nu_e,\overline{\nu}_e)_{\rm DATA}}{(\nu_\mu,\overline{\nu}_\mu/\nu_e,\overline{\nu}_e)_{\rm MC}}$$

$$R = 0.61 \pm 0.03(stat.) \pm 0.05(sys.) \qquad E_\nu < 1.33\,\text{GeV}\ [109] \tag{1.51}$$

$$R = 0.66 \pm 0.06(stat.) \pm 0.08(sys.) \qquad E_\nu > 1.33\,\text{GeV}\ [110]\,, \tag{1.52}$$

which indicates an excess of electron neutrinos or a deficit of muon neutrinos. The higher energy neutrino events were particularly informative because their directionality is easier to track. Neutrinos traveling upward traversed the Earth, while those going downward had a much shorter path. For electron and muon flavor events, and high and low energy events, the resulting flux as a function of angle (and thus distance traveled), seen in Figure 1.16, conclusively satisfied the oscillation hypothesis. This lead to contours of θ_{23} and Δm^2 shown in Figure 1.17, as well as the best fit values and allowed ranges below (Δm^2 is nearly equal to Δm^2_{23} but with small model-dependent inclusion of other mixing parameters):

$$\Delta m^2 = 2.1 \cdot 10^{-3}\,\text{eV}^2,\ \text{best fit} \tag{1.53}$$

$$\sin^2\theta_{23} = 0.50,\ \text{best fit} \tag{1.54}$$

$$\sin^2 2\theta_{13} = 0.0,\ \text{best fit} \tag{1.55}$$

$$(1.9 < \Delta m^2 < 2.6) \cdot 10^{-3}\,\text{eV}^2 \text{ at } 90\% \text{ CL for normal hierarchy} \tag{1.56}$$

$$(1.7 < \Delta m^2 < 2.7) \cdot 10^{-3}\,\text{eV}^2 \text{ at } 90\% \text{ CL for inverted hierarchy} \tag{1.57}$$

$$0.407 < \sin^2\theta_{23} < 0.583 \text{ at } 90\% \text{ CL} \tag{1.58}$$

$$\sin^2 2\theta_{13} < 0.04(0.09) \text{ at } 90\% \text{ CL for normal(inverted) hierarchy [28].} \tag{1.59}$$

1.3.2.2 Sudbury Neutrino Observatory

The Sudbury Neutrino Observatory (SNO) observed flavor oscillations in solar neutrinos, thus solving the solar neutrino problem, the deficit in expected solar electron neutrino flux observed at the Earth.

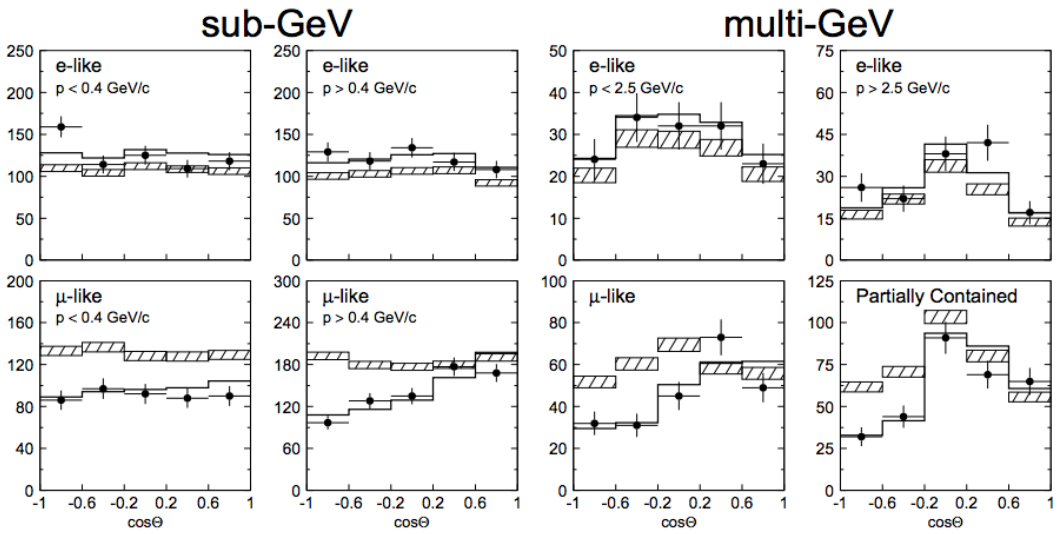


Figure 1.16 Zenith angle distributions of Super Kamiokande events associated with muon and electron neutrinos, grouped by energy: above or below 1.33 GeV. Events with $\cos\theta < 0$ are traveling upward, traversing a chord through the Earth in addition to traveling through the atmosphere. Such events show a greater deficit than neutrinos traveling through the atmosphere alone. This is the first evidence of neutrino oscillations [27].

The SNO detector was located at a 2 km deep underground laboratory. It consisted of 1 kt of heavy water (D_2O) housed in a 12 m spherical acrylic vessel. Another 7 kt volume of light water enveloped the detector to shield it against radiation from surrounding rock and support structures. In the detector, PMTs detected Cherenkov light emitted by charged particles at energies greater than 0.767 MeV from the following processes:

$$\nu + e^- \rightarrow \nu + e^- \quad \text{Elastic Scattering} \tag{1.60}$$

$$\nu + d \rightarrow p + n + \nu \quad \text{Neutral Current} \tag{1.61}$$

$$\nu_e + d \rightarrow p + p + e^- \quad \text{Charged Current} \tag{1.62}$$

The elastic scattering and neutral current reactions detector solar neutrinos regardless of flavor. The elastic scattering is powerful because the emitted electron is strongly correlated with the direction of neutrino motion. The reaction has a higher cross-section for ν_e because it can be mediated by both the W and Z, while ν_μ and ν_τ can only be mediated by Z. The neutral current reaction is also sensitive to all flavors, but with a cross-section an order of

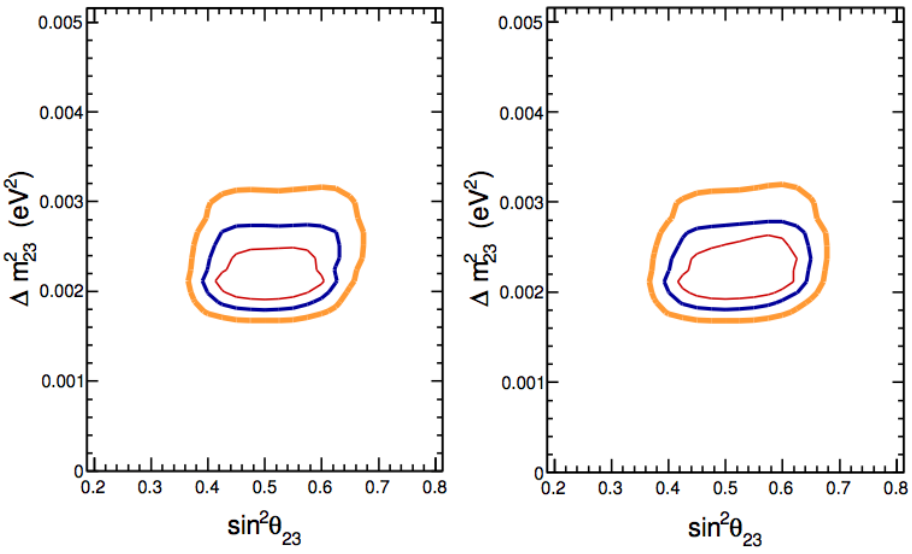


Figure 1.17 Super Kamiokande fits for $\sin^2\theta_{23}$ and Δm^2_{23} assuming normal hierarchy (left) and inverted hierarchy (right) [28].

magnitude larger. The remaining charged current reaction of Equation 1.62 occurs only for electron neutrinos. The charged current reaction provides a precise measurement of the solar neutrino spectrum because the recoil electron energy is well correlated with the incoming neutrino energy [29].

SNO went through three detector phases with different substances in the target to enhance the neutron signal. The first phase involved the use of D_2O to capture neutrons with 30% efficiency. Capture was indicated by the release of a 6.25 MeV gamma. Gammas in the SNO detector can be identified by their Compton scattering off electrons, and the subsequent Cherenkov radiation of the electrons. The final results from Phase 1 for the ^{8}B flux over the three reactions were [111]:

$$\phi_{CC} = 1.76^{+0.06}_{-0.05}(\text{stat.})^{+0.09}_{-0.09}(\text{sys.}) \cdot 10^6\,\text{cm}^2\text{s}^{-1} \tag{1.63}$$

$$\phi_{ES} = 2.39^{+0.24}_{-0.23}(\text{stat.})^{+0.12}_{-0.12}(\text{sys.}) \cdot 10^6\,\text{cm}^2\text{s}^{-1} \tag{1.64}$$

$$\phi_{NC} = 5.09^{+0.44}_{-0.43}(\text{stat.})^{+0.46}_{-0.43}(\text{sys.}) \cdot 10^6\,\text{cm}^2\text{s}^{-1}\,. \tag{1.65}$$

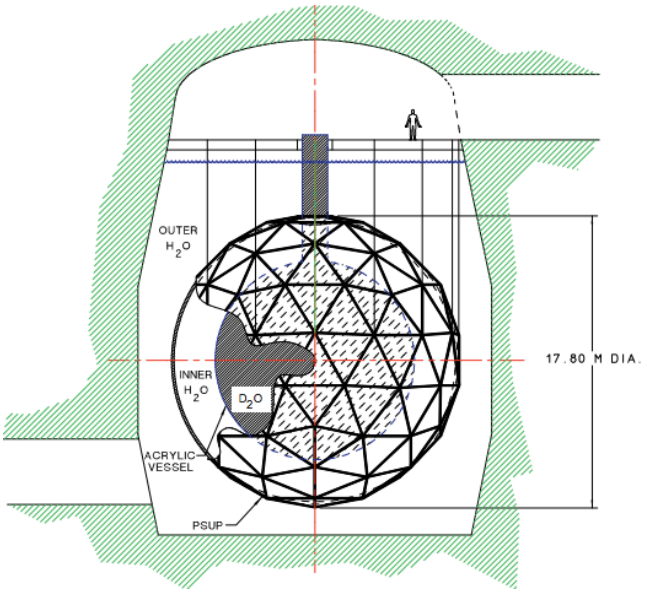


Figure 1.18 Diagram of the SNO detector [29].

Equation 1.65, the neutral current interaction sensitive to all flavors, is clearly larger than the other processes, which are only sensitive to electron neutrinos. The neutral current flux was consistent with solar models, proving that the electron neutrinos were only a fraction of the total neutrino flux and that flavor oscillation had occurred [107].

In the second phase, 2 t of sodium chloride was added to the detector to increase neutron capture efficiency by a factor of three, and increase the emitted light to 8.6 MeV. The results for the charged current and elastic scattering were largely unchanged, but the systematics of the neutral current reaction were halved [112, 113]:

$$\phi_{CC} = 1.68^{+0.06}_{-0.06}(\text{stat.})^{+0.08}_{-0.09}(\text{sys.}) \cdot 10^6\,\text{cm}^2\text{s}^{-1} \tag{1.66}$$

$$\phi_{ES} = 2.35^{+0.22}_{-0.22}(\text{stat.})^{+0.15}_{-0.15}(\text{sys.}) \cdot 10^6\,\text{cm}^2\text{s}^{-1} \tag{1.67}$$

$$\phi_{NC} = 4.94^{+0.21}_{-0.21}(\text{stat.})^{+0.38}_{-0.34}(\text{sys.}) \cdot 10^6\,\text{cm}^2\text{s}^{-1}\,. \tag{1.68}$$

In all, the best fit oscillation parameters measured by SNO are shown in Figure 1.19 and listed below:

$$\Delta m^2_{21} = 5.6^{+1.9}_{-1.4} \cdot 10^{-5}\,\text{eV}^2 \tag{1.69}$$

$$\tan^2\theta_{12} = 0.427^{+0.033}_{-0.029}\ [30]. \tag{1.70}$$

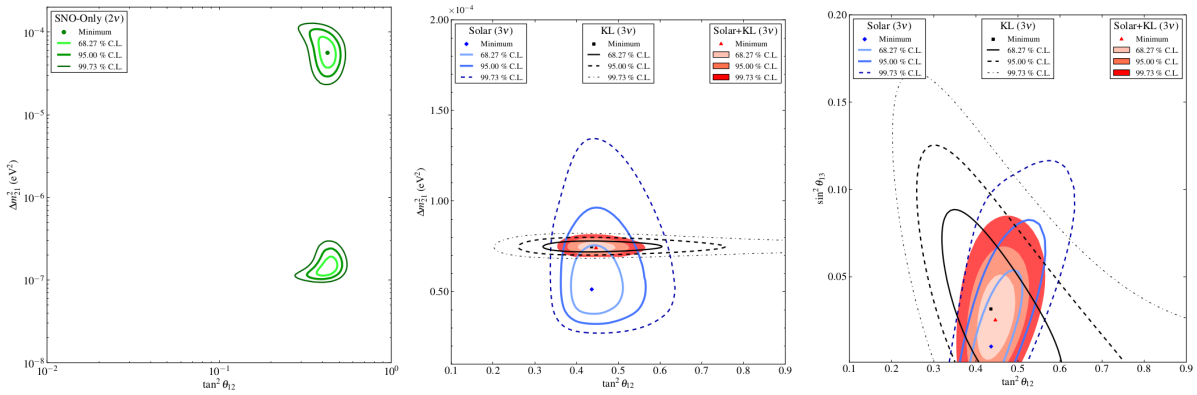


Figure 1.19 Left: SNO-only oscillation fits with Phase 1–3 data, including neutral current, charged current and elastic scattering events. Center and right: after the inclusion of KamLAND data [30].

The third phase of SNO implemented an additional neutron detector, the Neutral Current Detection array (NCD) [114]. These were proportional counters embedded in the detector. The NCD also improved neutron capture efficiency over the heavy water by a factor of three. Data from the third phase contributed to the measurements of Equations 1.69 and 1.70.

1.3.2.3 KamLAND

KamLAND is a reactor neutrino experiment detecting electron antineutrino from 57 reactors in Japan. Nuclear reactors produce a flux of pure electron antineutrino over energies less than about 10 MeV. Most of the reactors are located between 140–205 km away from the detector, and while distances vary, the flux from all of them can be combined into a total prediction for given oscillation parameters.

The KamLAND detector is located under 2700 m.w.e. of rock. The detector measures the flux and energies of electron antineutrino specifically, without sensitivity to muon or tau neutrino flavor. Incoming electron antineutrinos of energy greater than 1.8 MeV interact with free protons in the liquid scintillator to undergo inverse beta decay (IBD), as in Equation 1.39:

$$\overline{\nu}_e + p \;\rightarrow\; e^+ + n \tag{1.71}$$

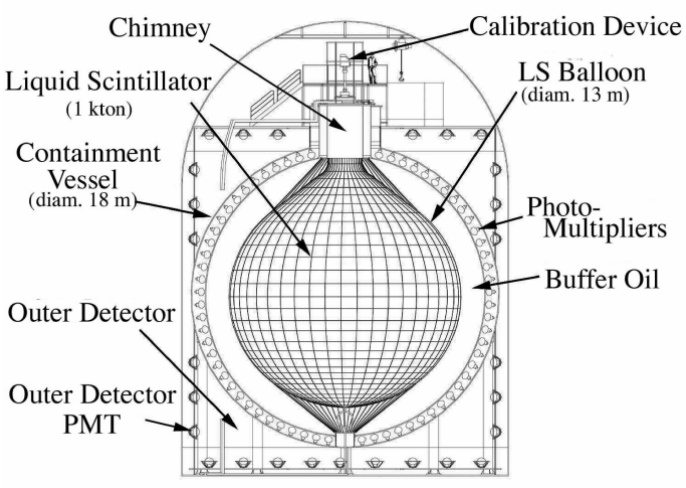


Figure 1.20 Diagram of the KamLAND detector [31].

The signal is formed when the positron annihilates promptly, then the neutron captures on a hydrogen nucleus about 200 μs later. The liquid scintillator and fluors absorb the gamma rays emitted and re-radiate more numerous lower energy photons that can be seen by PMTs. KamLAND's detector consists of a kiloton of liquid scintillator contained in a 13 m transparent balloon suspended in an oil buffer. Almost 2000 PMTs provide 34% coverage of the inner detector with the scintillator balloon, while an outer detector tags through-going charged particles by their Cherenkov emissions in water [31].

Figure 1.21 shows KamLAND's first results, demonstrating a conclusive deficit of reactor electron antineutrino flux as a function of distance. Previous reactor neutrino experiments measured electron antineutrino fluxes at baselines up to 1 km, exhibiting no deficits, but KamLAND's flux-weighted baseline of 175 km shows a deficit at the level of 3σ.

Subsequent data sets included energy-dependent oscillation signals for more discriminating power. Figure 1.22 shows the energy dependence over all reactors and the best fit oscillation parameters [32]. The best fits are:

$$\Delta m^2_{21} = 7.58^{+0.14}_{-0.13}(\text{stat.})^{+0.15}_{-0.15}(\text{sys.}) \cdot 10^{-5}\,\text{eV}^2 \tag{1.72}$$

$$\tan^2\theta_{12} = 0.56^{+0.10}_{-0.07}(\text{stat.})^{+0.10}_{-0.06}(\text{sys.})\,\sin^2\theta_{13} = 0.009^{+0.013}_{-0.007}\ [32,\ 115]. \tag{1.73}$$

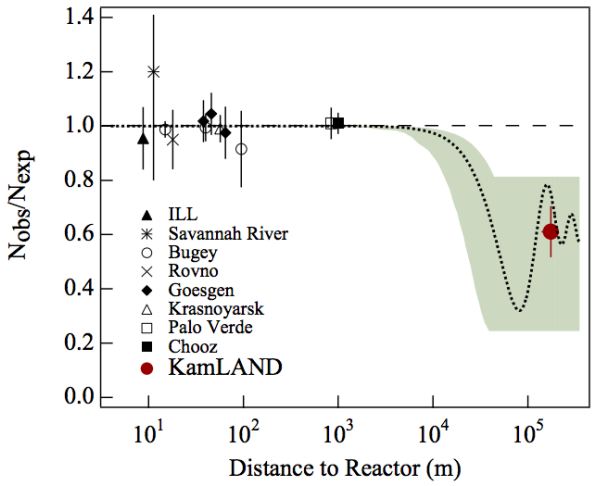


Figure 1.21 The ratio of detected electron antineutrino flux divided by expectation for KamLAND and previous experiments. The diameter of the KamLAND marker is indicative of the reactor distance uncertainty. The dashed line and shaded region indicate contemporary best fits on oscillation parameters and error margins; the dashed line represents no flavor mixing. [31]

1.3.2.4 K2K

The High Energy Accelerator Research Organization (KEK) to Kamioka Long-Baseline Neutrino Oscillation Experiment (K2K) directs a muon neutrino beam at two detectors. The Super Kamiokande water Cherenkov detector (Section 1.3.2.1) 250 km away serves as the far detector. The near detector 300 m away, built new for the experiment, characterizes the beam before the muon neutrinos undergo flavor oscillations. See Figure 1.23. The first of two segments of the near detector is a 1 kt water Cherenkov apparatus. It operates like a smaller Super Kamiokande detector with identical instrumentation. The second near detector consists of a scintillator fiber and water-target tracker, followed by a lead-glass calorimeter or additional scintillation detector, followed by a muon range detector. The scintillating fibers of the first segment were arranged at 90° rotation, read out by CCD

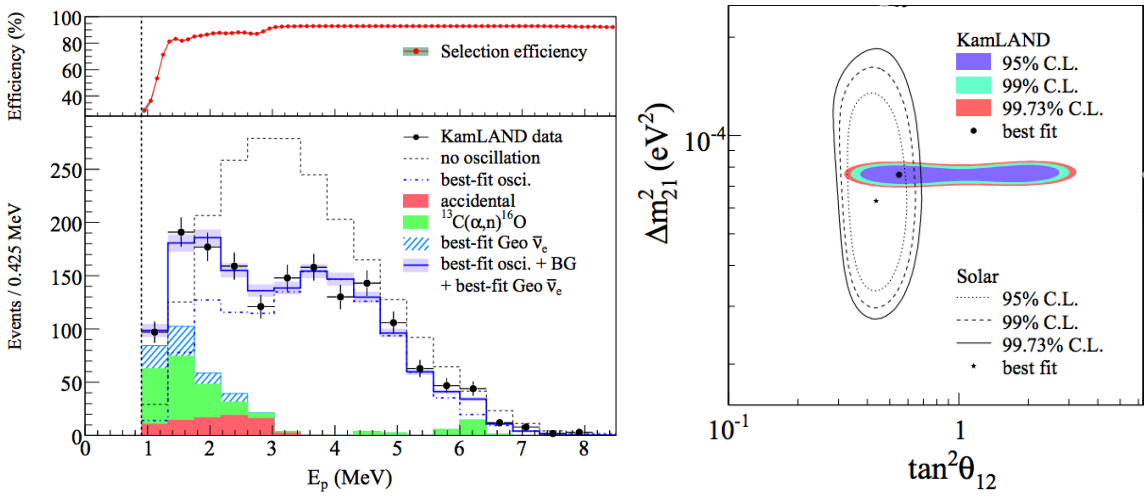


Figure 1.22 Left: KamLAND reactor electron antineutrino energy spectrum compared to both a no-oscillation hypothesis and the best fit oscillation. The no-oscillation hypothesis is ruled out at over 5σ. Right: Best fit contours for neutrino oscillation parameters θ_{12} and Δm^2_{21} [32].

cameras, to measure the neutrino spectrum and determine interaction rates [116]. The lead-glass calorimeter [117] or its replacement scintillation apparatus [118], discriminated between electrons and muons, or neutrino interactions with low-momentum daughters, respectively. The muon range detector [119] relied on alternating strips of iron absorbing layers and drift tubes to reconstruct muon tracks. The kinematics of the muons indicate the beam direction, profile, energy and stability.

Muon neutrinos in the K2K beam have energies between 1.0–1.5 GeV and oscillate primarily to tau neutrinos over the 250 km baseline. The beam is generated by bombarding an aluminum target with 12 GeV protons. This generates pions among other products, and the positively charged pions are directed by magnetic horns into a decay pipe. The pions decay into muon neutrinos and positive muons, but only the neutrinos survive to the far detector. 97% to 98% of the neutrinos in the beam initially are muon neutrinos, with small

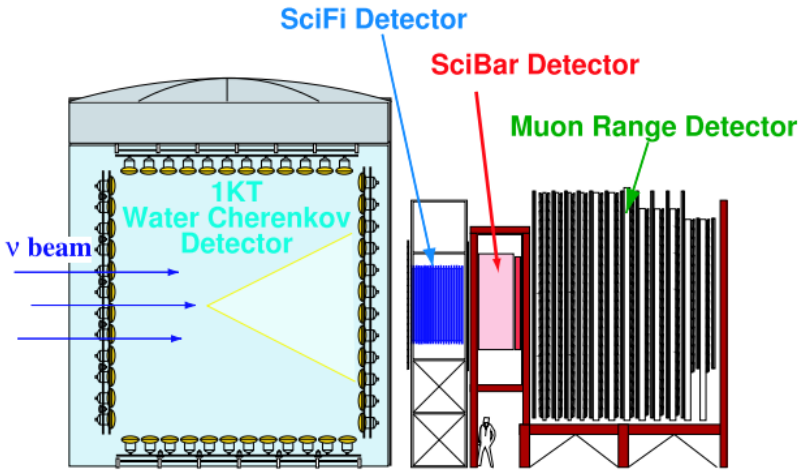


Figure 1.23 K2K near detector. From left to right: the water Cherenkov detector, the scintillator fiber and water-target tracker, the second scintillating apparatus, and the muon range detector. A lead-glass calorimeter was once in place of the second scintillator [33].

contamination of electron neutrinos (1%), muon antineutrinos (1%) and electron antineutrinos ($1{\cdot}10^{-4}$). Given the pulse timing of the beam, events at the far site can be correlated with beam activity to reject backgrounds.

K2K measures oscillations via disappearance of muon neutrinos and distortions in the energy spectrum. The muon neutrinos interact via the charged current quasi-elastic reaction:

$$\nu_\mu + n \;\rightarrow\; \mu + p, \tag{1.74}$$

where the muon alone is identified by its Cherenkov ring. After analysis of the data, K2K arrived at oscillation parameter best fits and allowed ranges of:

$$\Delta m^2 = 2.8 \cdot 10^{-3}\,\mathrm{eV}^2, \text{ best fit} \tag{1.75}$$

$$\sin^2 2\theta = 1, \text{ best fit} \tag{1.76}$$

$$1.9 \cdot 10^{-3}\,\mathrm{eV}^2 < \Delta m^2 < 3.5 \cdot 10^{-3}\,\mathrm{eV}^2 \text{ at } 90\%\text{ CL} \tag{1.77}$$

$$\sin^2 2\theta > 0.75 \text{ at } 90\%\text{ CL [34]}, \tag{1.78}$$

where Δm^2 is a mixture of Δm^2_{31} and Δm^2_{32}, and θ corresponds to θ_{23} with some model dependent reliance on other mixing parameters.

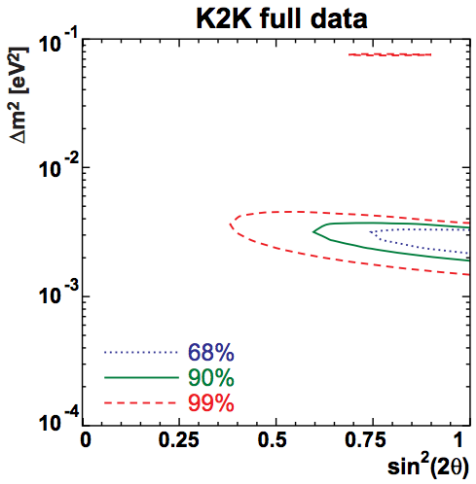


Figure 1.24 Best fit oscillation parameters from K2K [34].

1.3.2.5 Main Injector Neutrino Oscillation Search

Like K2K, the Main Injector Neutrino Oscillation Search (MINOS) is an accelerator neutrino oscillation experiment. Muon neutrinos generated at MINOS have energies up to 120 GeV, but mostly below 20 MeV. The muon neutrinos travel 735 km to the MINOS far detector, over which some oscillate into other flavors.

The NuMI beam (Figure 1.25), which is incident on the MINOS detectors, creates neutrinos by the bombardment of 120 GeV protons on a graphite target. Magnetic horns focus positive pions and kaons through a decay pipe toward the detectors. In flight, the pions and kaons decay into muon neutrinos among other particles, but all besides neutrinos are stopped by a beam dump [35].

The MINOS experiment consists of two functionally identical detectors, one near the beam and one 735 km away [4]. The detectors are magnetized panes of scintillating strips, where the strips are rotated 90° with respect to each other to read out position in two dimensions. Charged particles from the beam travel through as much as 484 successive panes, providing three dimensional tracking. MINOS detects muon neutrinos through the

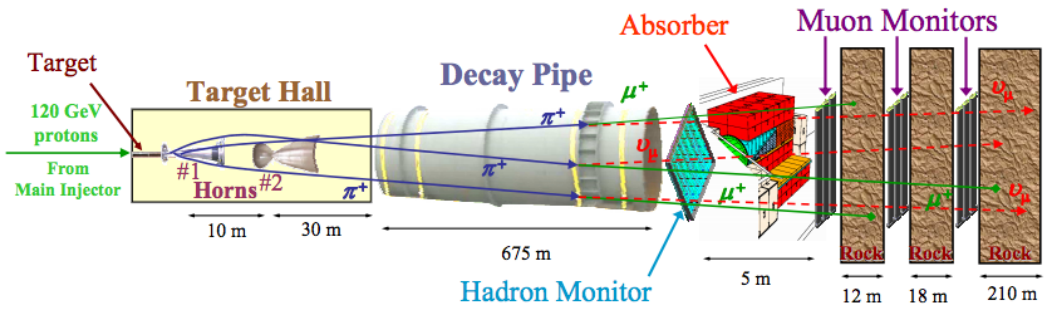


Figure 1.25 Diagram of the NuMI beam [35].

charged current interaction similar to Equation 1.74:

$$\nu_\mu(\overline{\nu}_\mu) + X \;\rightarrow\; \mu^-(\mu^+) + X', \tag{1.79}$$

and can identify particles and reconstruct their energies by tracking them through imposed magnetic fields.

MINOS currently holds the most precise measurements of Δm^2_{32} and θ_{23}:

$$\Delta m^2 = 2.41^{+0.09}_{-0.10} \cdot 10^{-3}\,\text{eV}^2 \tag{1.80}$$

$$\sin^2 2\theta = 0.950^{+0.035}_{-0.036}\ [4], \tag{1.81}$$

where Δm^2 and $\sin^2 2\theta$ are similar to Δm^2_{32} and $\sin^2 2\theta_{23}$, but with model-dependent relationships to other mixing parameters. The measurements are performed from muon neutrino and muon antineutrino disappearance, especially at lower energies (large L/E). From Figure 1.26, the observation is clearly inconsistent with a non-oscillated flux. MINOS is capable of running in both muon neutrino and muon antineutrino mode, and the recent measurement includes contributions from muon neutrinos at five times the rate of muon antineutrinos, with some muon antineutrino s naturally occurring from the muon neutrino flux.

1.3.2.6 Liquid Scintillator Neutrino Detector

The Liquid Scintillator Neutrino Detector (LSND) is another accelerator neutrino oscillation experiment, predating K2K and MINOS [36]. The LSND detector was a 167 t scintillator

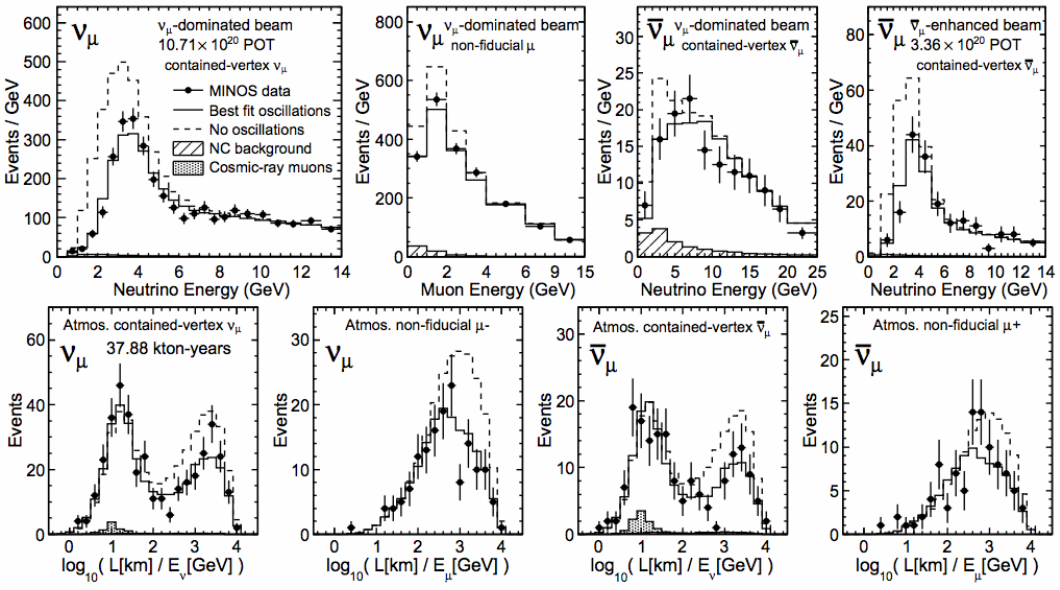


Figure 1.26 MINOS shows evidence of neutrino oscillations in muon neutrino and antineutrino data [4].

detector composed of mostly mineral oil and the addition of scintillator b-PBD. The low concentration of scintillator allowed for the detection of both scintillation and Cherenkov light by 1220 PMTs. LSND detected muon neutrinos generated by the 800 MeV LANSCE proton accelerator at a distance of 30 m. The production mechanism of ν_μ is the same as explained in Section 1.3.2.1.

The strategy of LSND was to search for muon antineutrino to electron antineutrino appearance through the inverse beta decay (IBD) reaction. Background rates of electron antineutrinos produced in either the beam or atmosphere were expected to be minuscule, and that any electron antineutrino appearance beyond 0.1% of the muon antineutrino flux would be due to oscillations. Additionally, a secondary search of muon to electron neutrino oscillation was performed for the muon neutrino also produced in the beam. To reduce background contamination, a neutrino energy cut of $20 < E < 200$ MeV is applied.

LSND reported an excess of electron antineutrino events well above background, 87.9 $\pm$22.4(stat)$\pm$6(sys) events. Figure 1.27 shows an excess versus energy compared to an oscillation hypothesis. The excess matched a neutrino oscillation hypothesis with $\Delta m^2 >$

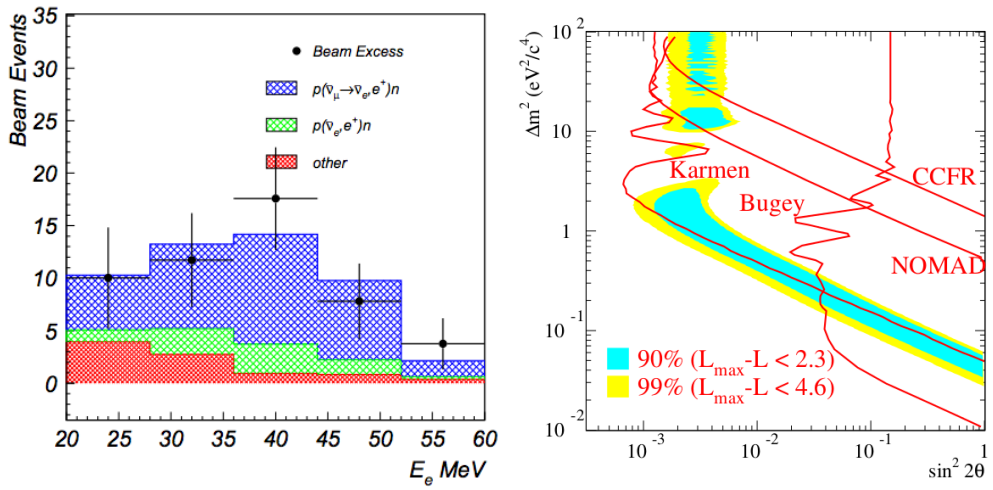


Figure 1.27 Left: LSND electron antineutrino excess versus energy. The shaded region shows the expected distribution from neutrino oscillations and backgrounds. Right: LSND-favored oscillation parameters compared to exclusion contours of previous experiments [36].

$0.2{\cdot}10^{-2}\,\mathrm{eV}^2$, but this contradicts other oscillation experiments, which is an unresolved discrepancy.

1.3.2.7 Mini Booster Neutrino Experiment (MiniBooNE)

The MiniBooNE experiment was devised to test the LSND result at the same distance over energy ratio, and hence similar neutrino oscillations, but at much higher energies and distance, with different systematics. The experiment directs a beam of muon neutrinos or antineutrinos from Fermilab to a 800 t mineral oil detector to search for muon neutrino disappearance and electron neutrino appearance [107, 37].

The MiniBooNE muon neutrino beam is generated from the collision of 8 GeV protons onto a beryllium target, which produces kaons and pions. A magnetic focusing horn directs the charged kaons and pions toward the detector. The polarity of the horn can be oriented to select positive mesons to produce a muon antineutrino beam, or can be reversed to create a beam of negative mesons, and hence muon neutrinos. These charged mesons decay in flight

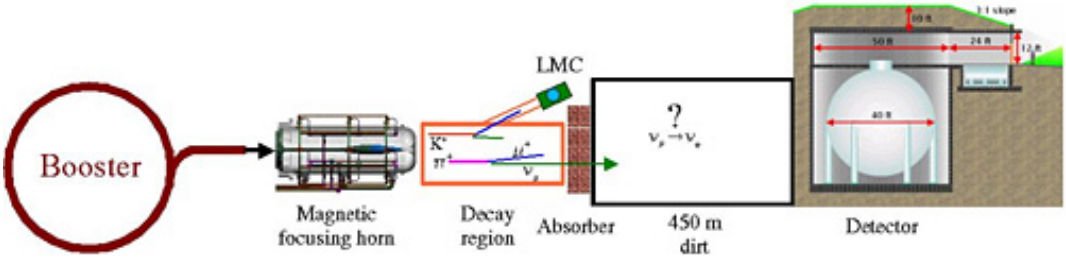


Figure 1.28 A diagram of the MiniBooNE beam and detector [37].

into muon neutrinos or antineutrinos, while other daughters are obstructed by an absorbing shield. The neutrino beam continues on to react in the detector.

The detector is positioned 541 m downstream, under 3 m of dirt overburden. It consists of a spherical vessel of mineral oil outfitted with PMTs to detect charged current interactions. The vessel is divided into inner and outer volumes, where the outer volume vetoes particles such as cosmic ray muons that pass through the detector, while the inner detector observes neutrino interactions that originate within.

MiniBooNE has reported partial agreement with LSND (see Figure 1.29), based on observations of excess electron (anti)neutrinos at low energies [120]. Running in muon antineutrino mode, the detector counted 78.4±28.5 electron antineutrinos over the energy range of 200–1250 MeV, a 2.8σ excess. In muon neutrino mode, the excess was 168±47.8, for 3.4σ. The antineutrino results were only consistent with antineutrino oscillations at the 66% level, with a Δm^2 between 0.01eV^2 and 1.0eV^2. The neutrino data were inconsistent with neutrino oscillations for any mass splitting and mixing angle values.

1.3.2.8 T2K

Tokai to Kamioka (T2K) is an accelerator neutrino experiment that directs a beam of muon neutrinos to the Super Kamiokande detector to observe muon neutrino disappearance and electron neutrino appearance [121]. The beam is generated at the Japan Proton

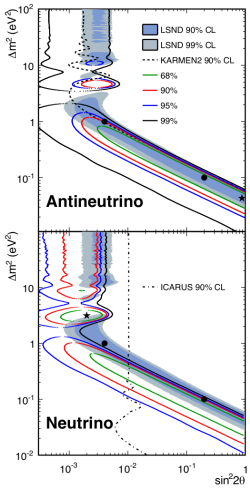


Figure 1.29 Allowed neutrino oscillation parameters at the indicated confidence limits for MiniBooNE compared to the LSND, KARMEN and ICARUS experiments. The stars indicate the MiniBooNE best fits, but although the best fit contours for neutrinos are shown, the absolute agreement of the neutrino data and oscillations are low. There is possible agreement between MiniBooNE and LSND for antineutrinos, but much less agreement for neutrino data.

Accelerator Research Complex (J-PARC) facility, where 30 GeV protons are collided into a graphite target, which generates kaons and pions. The kaons and pions are focused with magnetic horns, then decay into neutrinos that form the beam incident on the detectors. Other decay products are blocked by shielding. The neutrinos travel off-axis toward the Super Kamiokande detector 295 km away, and additional near detectors 280 m away. The near detectors monitor the beam before oscillations and provide a comparison point for the far detector. The beam impacting the detector off-axis rather than on-axis reduces the neutrino interaction rates, but narrows the energy spectrum of the muon neutrinos. The narrower range of energies permits more sensitive calculations of neutrino oscillation parameters.

The detectors determine the flux of muon neutrinos and electron neutrinos at the near and far detector by charged current interactions that produce muons and electrons. The muons and leptons are identified by Cherenkov rings, as discussed in Section 1.3.2.1. T2K reported observation of muon neutrinos oscillating to electron neutrinos, and in so doing have measured $\sin^2\theta_{23}$, the larger mass splitting Δm^2_{31} or Δm^2_{32}, depending on mass hierarchy,

and $\sin^2 2\theta_{13}$ [122, 123]:

$$\sin^2\theta_{23} = 0.514^{+0.055}_{-0.056} \text{ for normal hierarchy} \tag{1.82}$$

$$\sin^2\theta_{23} = 0.511 \pm 0.055 \text{ for inverted hierarchy} \tag{1.83}$$

$$\Delta m^2_{32} = 2.51 \pm 0.10 \cdot 10^{-3}\,\text{eV}^2 \text{ for normal hierarchy} \tag{1.84}$$

$$\Delta m^2_{31} = 2.48 \pm 0.10 \cdot 10^{-3}\,\text{eV}^2 \text{ for inverted hierarchy} \tag{1.85}$$

$$0.03 < \sin^2 2\theta_{13} < 0.28 \text{ for normal hierarchy, assuming } \delta_{CP} = 0 \tag{1.86}$$

$$0.04 < \sin^2 2\theta_{13} < 0.34 \text{ for inverted hierarchy, assuming } \delta_{CP} = 0. \tag{1.87}$$

1.3.2.9 Bugey

The Bugey experiment searched for electron antineutrino oscillations within meters of two nuclear reactors in the early 1990s [38]. Three detectors were installed at the Bugey Nuclear Power Plant at distances of 15 m, 40 m and 95 m from one reactor at a time (out of two total). One detector was deployed 15 m the first reactor, two detectors were located 40 m from the first reactor, and when the first reactor was offline, the near detector observed the flux from the second reactor at a distance of 95 m. The reactors generated 2.8 GW of thermal power each.

The detection principle is similar to the Savannah River experiment. Antineutrinos interact in the detector via inverse beta decay, which creates a positron and a neutron. The positron annihilates promptly and indicates the energy of the antineutrino, while the neutron captures on nucleus later, adding a subsequent deposition of energy. The deposited energy is measured by PMTs observing the reaction in liquid scintillator, which is doped with ^{6}Li to enhance neutron capture.

The experiment tested for neutrino oscillation by two approaches: the ratio of antineutrino rates and spectra at two detectors, and the normalized spectra compared to predictions. The data were thoroughly consistent with reactor flux predictions in the absence of neutrino oscillations, leading to the exclusion of oscillation parameter values in Figure 1.30.

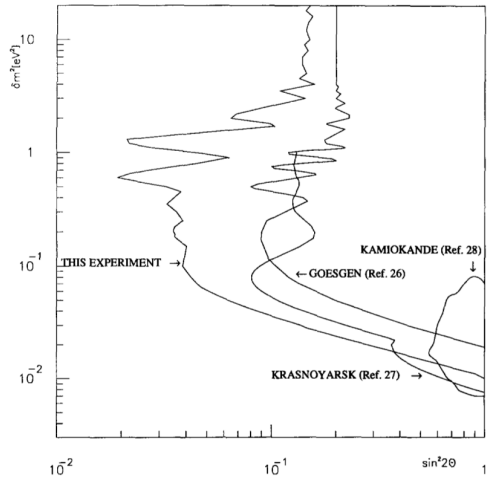


Figure 1.30 The reactor electron antineutrino oscillation parameters excluded by Bugey are shown, indicated by the label "THIS EXPERIMENT", along with exclusions from previous experiments at Goesgen and Krasnoyarsk [38, 39, 40]. The Kamiokande contour refers to a then-allowed region of oscillation parameters. The true mass-splitting for reactor antineutrinos is now known to fall below the range of the y-axis.

1.3.2.10 Palo Verde and Chooz

Palo Verde [41] and Chooz [94], were reactor antineutrino oscillation experiments in the late 1990s that served as predecessors to the ongoing RENO, Double Chooz and Daya Bay experiments (Sections 1.3.2.11 and 4). Their intent was to address the then-unexplained anomaly in Kamiokande atmospheric neutrino data, which turned out to be due to muon neutrino oscillations to tau neutrinos [27]. In the process, these experiments also provided limits on θ_{13} that stood until Daya Bay ten years later.

The Palo Verde experiment deployed a modular scintillator detector underground at the Palo Verde Nuclear Generating Station in Arizona, which housed three reactors that produced a total thermal output of 11.63 GW. The detector, 890 m from two reactors and 750 m from the other, consisted of gadolinium-doped liquid scintillator in separate acrylic cells. Separate oil and water buffers attenuated radioactive materials from the PMTs that detected neutrino interactions by deposited light. The antineutrino signal was produced in the same manner as in the Savannah River and Bugey experiments, via inverse beta decay, in

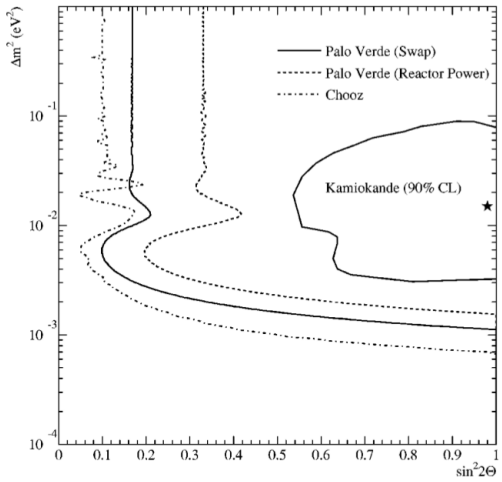


Figure 1.31 Values of $\sin^2 2\theta_{13}$ greater than the Palo Verde and Chooz contours were excluded at 90% confidence (the plot is from Palo Verde [41]). The Palo Verde result is shown for two analysis methods described in the reference. Also shown is the allowed space for muon neutrino to electron neutrino oscillations to explain the atmospheric neutrino anomaly reported by Kamiokande.

which the antineutrino produces a positron and a neutron. The positron annihilates promptly while the neutron captures on gadolinium shortly thereafter to produce a correlated signal.

At Chooz, the two reactors generate 4.25 GW of thermal power apiece. Like Palo Verde, the detection principle is inverse beta decay in gadolinium-doped scintillator. But, the Chooz detector was a single unit of two concentric volumes of scintillator, the inner volume containing gadolinium, the outer region without. The detector was located 1 km from both reactors, underground in a water Cherenkov muon veto.

The experiments ruled out the hypothesis that the atmospheric neutrino anomaly was due to muon neutrinos oscillating to electron neutrinos. Otherwise, electron antineutrino oscillations to muon antineutrino would have been observed in the reactor antineutrino flux. They excluded wide swaths of possible values of $\sin^2 2\theta_{13}$ and Δm^2_{32}, shown in Figure 1.31. Both Chooz and Palo Verde concluded a limit on $\sin^2 2\theta_{13} < 0.17$ at 90% confidence.

1.3.2.11 RENO and Double Chooz

The Reactor Experiment for Neutrino Oscillations (RENO) [74] in Korea and Double Chooz [47] in France are contemporary experiments to Daya Bay that rely on similar strategies and detectors. Both experiments deploy liquid scintillator detectors to two underground sites, one near their nuclear reactors and one at a site more sensitive to θ_{13}. RENO consists of four detectors at a six-reactor complex in Korea. Double Chooz is the successor experiment to Chooz, adding a near site to the existing far site with two new detectors to observe antineutrinos from two reactors. For each experiment, reactor power, detector masses, baselines and overburden are listed in Table 1.3.

The detectors for RENO and Double Chooz, like Daya Bay, are all multiple-volume constructions with a central target region that detects antineutrinos by way of inverse beta decay in gadolinium-doped liquid scintillator. Surrounding the target region in each detector is a scintillator volume without gadolinium that helps ensure that all neutron captures are surrounded by enough scintillator to convert emitted gamma rays to PMT-detectable light. Around this volume is a buffer that attenuates background radiation from detector materials. Additionally, Double Chooz detectors have a built-in muon veto volume, while RENO and Daya Bay build muon vetoes into the underground site. See Figure 1.32 for RENO and Double Chooz detector illustrations and Chapter 4 for Daya Bay.

Each of the experiments has published observations of θ_{13}, and continues to collect data. As seen in Table 1.4, Daya Bay and RENO have similar values of detector and reactor systematic uncertainties, with Reno's correlated uncertainties being about 30% smaller. However, Daya Bay has a much better handle on its backgrounds, reducing its background uncertainty by a factor of 3–4 compared to RENO. Double Chooz has not brought its new near detector online yet, so thus far has only determined the sum of the correlated and uncorrelated reactor and detector uncertainties for their far detector. Double Chooz's observations of θ_{13} have come from rate and shape analysis of antineutrino data compared to theory, while RENO

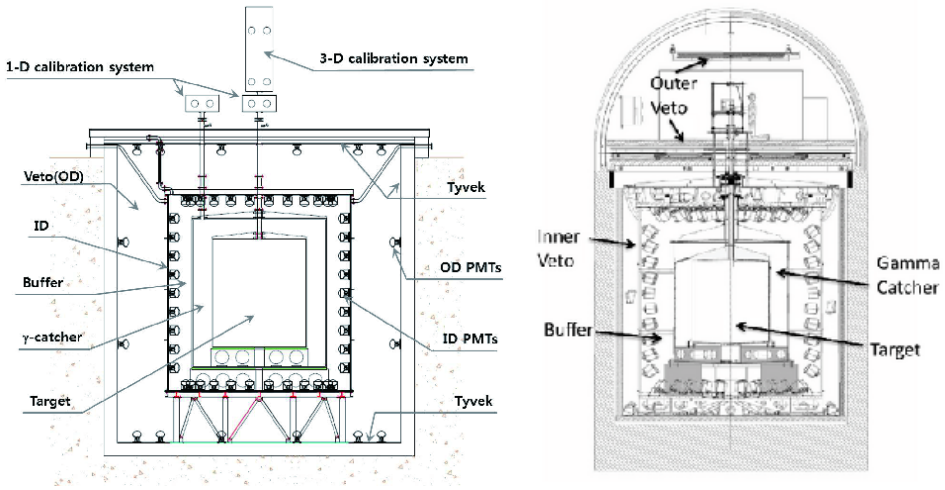


Figure 1.32 Detector diagrams for RENO, left, and Double Chooz, right [42, 43].

and Daya Bay compare near and far detectors. Most recently, the experiments have reported the following measurements of $\sin^2 2\theta_{13}$:

RENO	$\sin^2 2\theta_{13} = 0.100 \pm 0.010(stat.) \pm 0.015(sys.)$	December 2014 [124]
Double Chooz	$\sin^2 2\theta_{13} = 0.102 \pm 0.028(stat.) \pm 0.033(sys.)$	January 2014 [125]
Daya Bay	$\sin^2 2\theta_{13} = 0.090^{+0.008}_{-0.009}$	February 2014 [3]

1.3.3 Significance of the Measurement of θ_{13}

Measuring mixing angle θ_{13} is an important endeavor in its own right to understand neutrino oscillations, the nature of neutrino mass and physics beyond the Standard Model. But, it is also vital to future undertakings in neutrino physics. Before Daya Bay, θ_{13} was the largest hole in the understanding of neutrino oscillation. Now, the most significant questions in neutrino oscillation physics are the mass hierarchy and the CP-violating phase, both of which can be explored thanks to Daya Bay's elucidation of θ_{13}.

The long-baseline neutrino oscillation experiment program depends on knowledge of θ_{13}. If θ_{13} is smaller than about $\sin^2 2\theta_{13}$=0.003, the long baseline experiments like Noνa cannot measure δ_{CP} due to limited statistics; above this limit, the success of these experiments are proportional to θ_{13} due to the competition of signal and background [126]. Knowing

θ_{13} also determines the detector technology of the long baseline program. The capability of determining the neutrino mass hierarchy also depends on θ_{13} (and the value of δ_{CP}). For instance, at the now-known value of $\sin^2 2\theta_{13}$, Noνa should be capable of determining the hierarchy at the 2σ-level for half the δ_{CP} values. But, if $\sin^2 2\theta_{13}$ were less than 0.03, Noνa would be incapable of exploring the hierarchy.

Daya Bay has been indispensable in the effort to measure $\sin^2 2\theta_{13}$. Daya Bay is the most ambitious of the three contemporary reactor oscillation experiments because it pursued the tightest precision, which it accomplished by building the most numerous and most precise detectors. These detectors were installed at three underground sites rather than two, to observe the largest antineutrino flux. Figure 1.33 compares the measurements of $\sin^2 2\theta_{13}$ by the reactor and accelerator experiments since 2011 [44]. The world average is dominated by Daya Bay's latest result, and each of Daya Bay's published measurements are more precise than those from other experiments.

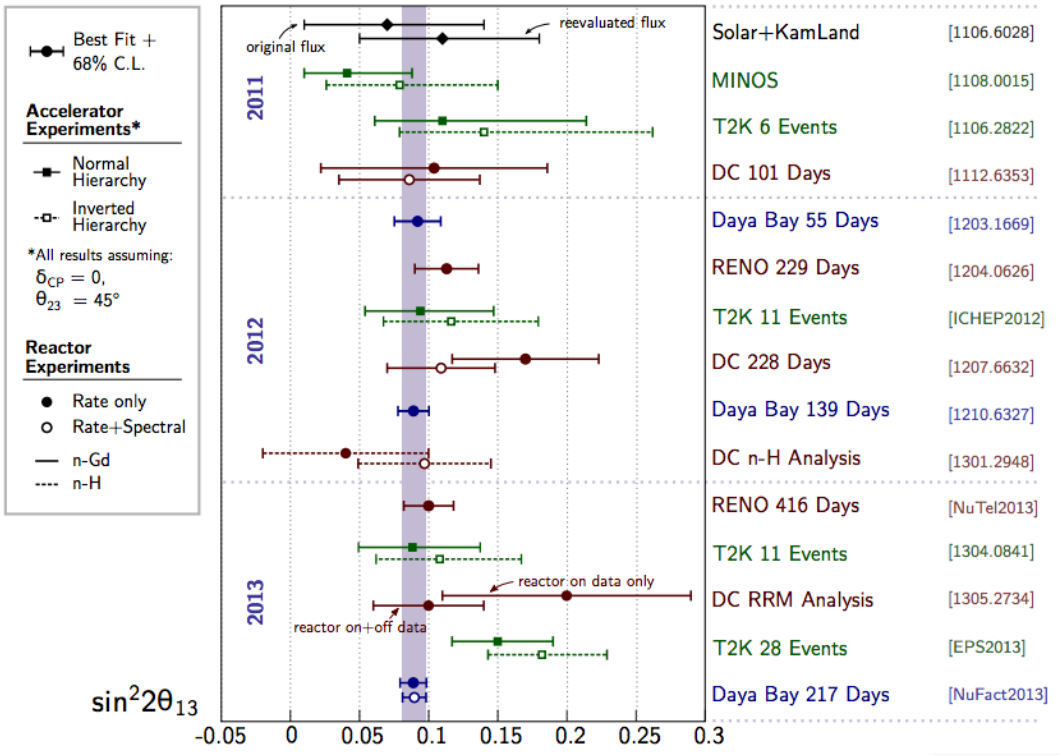


Figure 1.33 World measurements of $\sin^2 2\theta_{13}$ since 2011 [44].

Mixing angle	$\sin^2(2\theta)$	Dominant measurement
θ_{12}	$0.857^{+0.023}_{-0.025}$	Solar
θ_{23}	>0.95 (90% CL)	Super Kamiokande
θ_{13}	$0.090^{+0.008}_{-0.009}$	Reactor
Mass splitting	**Value**	**Dominant measurement**
$\lvert\Delta m^2_{31}\rvert \approx \lvert\Delta m^2_{32}\rvert$	$2.32^{+0.12}_{-0.08} \cdot 10^{-3}\,\mathrm{eV}^2$	Accelerator
Δm^2_{21}	$7.50^{+0.19}_{-0.20} \cdot 10^{-5}\,\mathrm{eV}^2$	KamLAND
$m_1 + m_2 + m_3$	$< 0.39\,\mathrm{eV}$ (95% CL)	Cosmic Microwave Background
$m_1 + m_2 + m_3$	$> 5.76^{+0.121}_{-0.0824}{\cdot}10^{-2}$ eV	Neutrino Oscillation
Phases	**Value**	**Dominant measurement**
δ_{CP}	$0 \leq \delta \leq 2\pi$	none
Majorana	$0 \leq \phi_1, \phi_2 \leq 2\pi$	none

Table 1.2 The state of knowledge of the neutrino mixing parameters from global data at the time of the analysis presented in this dissertation [1, 2, 3]. The value of $|\Delta m^2_{31}| \approx |\Delta m^2_{32}|$ has been more recently measured to be $2.41^{+0.09}_{-0.10}{\cdot}10^{-3}\,\mathrm{eV}^2$ [4]. In that case, $m_1 + m_2 + m_3 > 5.85^{+0.0895}_{-0.101}{\cdot}10^{-2}$ eV.

	Reactor Power	Detector Mass (t)		Baseline (m)		Overburden (m.w.e.)	
	(GW_{th})	Near	Far	Near	Far	Near	Far
RENO	16.5	16.5	16.5	409	1444	120	450
Double Chooz	8.5		8.2	400	1050	120	300
Daya Bay							
6 detectors	17.4	40, 20	60	470, 576	1650	250, 265	860
8 detectors	17.4	40, 40	80	470, 576	1650	250, 265	860

Table 1.3 Comparison of RENO, Double Chooz and Daya Bay experiments. Note that Double Chooz has not constructed its near detector yet, and that Daya Bay's published measurements are based on six-detector data [5].

	Detector		Reactor		Background/Signal	
	Corr.	Uncorr.	Corr.	Uncorr.	Near	Far
RENO	1.5	0.2	2.0	0.9	2.8 ± 0.8	5.8 ± 1.1
Double Chooz	1.0		1.7			5.5 ± 1.6
Daya Bay	1.9	0.2	3.0	0.8	1.9 ± 0.2	4.7 ± 0.4

Table 1.4 Systematic uncertainties in % (correlated and uncorrelated) for RENO, Double Chooz and Daya Bay. Since Double Chooz has only the far detector at the moment, Double Chooz uncertainties do not break down into correlated and uncorrelated [5].

Chapter 2

Daya Bay Strategy and Overview

The Daya Bay Reactor Neutrino Experiment ("Daya Bay") is a collaboration of American, Asian and European research institutions with the goal to perform the most precise measurement of neutrino mixing parameter $\sin^2 2\theta_{13}$, to achieve a sensitivity of $\sin^2 2\theta_{13}$=0.01 at 90% confidence [8].

The experiment operates underground at the Daya Bay Nuclear Power Complex [127] on the South China Sea, at Daya Bay, Guangdong Province, People's Republic of China. A map is shown in Figure 2.1. Eight 20 t liquid scintillator detectors, deployed to three underground sites, observe the antineutrino flux of six nuclear reactors by the inverse beta decay reaction (IBD). A near-far arrangement of functionally identical detectors measures the antineutrino flux and spectra at large and small oscillation probability due to θ_{13}, with little interference from the other mixing angles. The near-far comparison offers a more precise measurement than merely comparing detected flux to theory, and identical detectors increase the power of the measurement by greatly reducing systematic uncertainties.

At the conception of Daya Bay, the value of $\sin^2 2\theta_{13}$ was known only vaguely to be small. The then-limit was $\sin^2 2\theta_{13}$<0.17 at 90% confidence, with the allowed $\sin^2 2\theta_{13}$-Δm^2 space indicated in Figure 2.2. Most of the $\sin^2 2\theta_{13}$ parameter space had been excluded by the Chooz [94] and Palo Verde [41] experiments, but its value remained elusive.

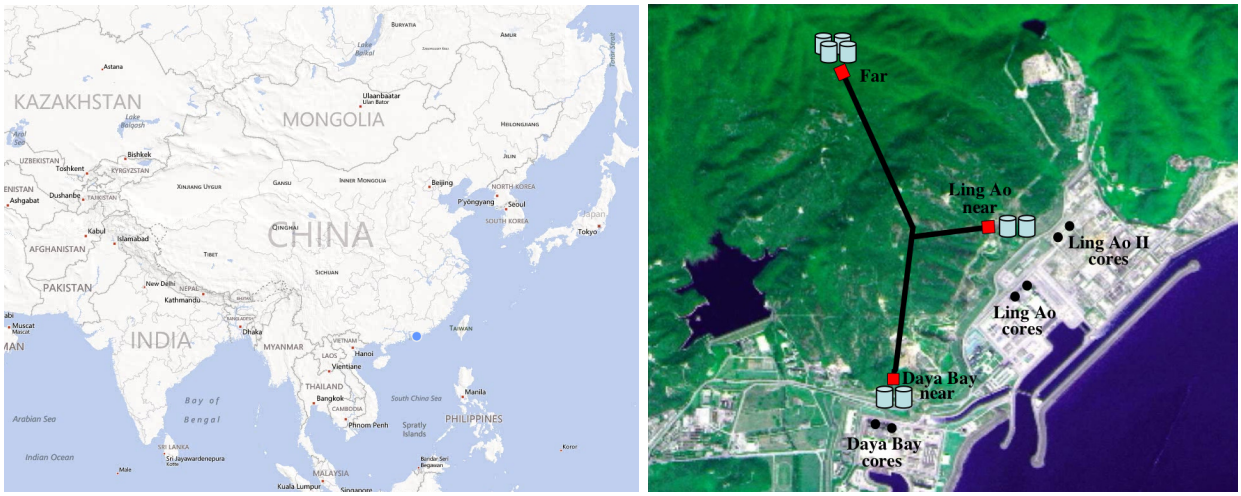


Figure 2.1 Left: Daya Bay is indicated by the blue marker on China's southern coast. Right: Daya Bay nuclear power station with detectors and reactors indicated [45, 46].

2.1 Antineutrinos at Daya Bay

The antineutrino flux at Daya Bay comes from six Pressure Water Reactors, each producing 2.9 GW of thermal power and about $6{\cdot}10^{20}\,\overline{\nu}_e$/s. Given the locations and cross-sections of the detectors, the experiment expects on order 100 antineutrinos per detector per day at the far site, and 1000 per day per detector at the near sites. The spectrum of these reactor antineutrinos, excluding detector effects, is shown in Figure 2.3. The antineutrino energies fall off exponentially from a sharp peak at zero to negligible rates beyond 12 MeV. 75% of the reactor antineutrino fall below the IBD energy threshold of 1.806 MeV, and thus cannot be detected at Daya Bay.

In total, eight antineutrino detectors are distributed to three underground sites, although for the existing oscillation data sets, the configuration is abbreviated to six detectors, omitting one each from the far site and Ling Ao near site. Each site is located underground to attenuate the flux of cosmic ray muons in order to avoid swamping the detector as happened at the Hanford Experiment (Section 1.3.1.1). Muons deposit so much energy that

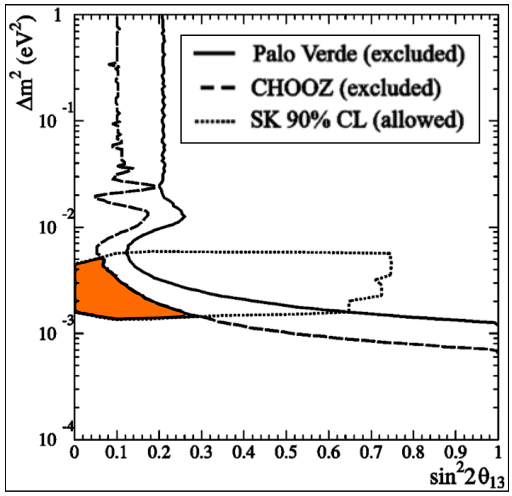


Figure 2.2 The available parameter space for $\sin^2 2\theta_{13}$ and Δm^2 at 90% confidence, prior to the construction of Daya Bay [47]. Δm^2 is the two-neutrino oscillation approximation to Δm^2_{31} and Δm^2_{32}. The goal of Daya Bay is to exclude the vast majority of this space; a line drawn demarcating Daya Bay's sensitivity would fall just inside the left minor tick marks.

they require a veto of up to 1.4 ms, which on the surface would force excessive dead time. Additionally, muons cause long-lived isotopic backgrounds for up to a second thereafter, which cannot be vetoed. At the near sites, the overburden is about 100 m of granite, while at the far site the overburden is 355 m. The larger overburden is necessary at the far site because the antineutrino flux is lower. The sites are equipped with a muon veto consisting of resistive plate chambers and a water pool outfitted with photomultiplier tubes to track and veto muons.

Half the detectors are installed at two near sites (the Daya Bay near site and the Ling Ao near site), while the remaining half are installed at the lone far site. The baselines from the detectors to reactors are indicated in Table 2.1, and range from 358 m to 1925 m. The flux-weighted average baselines from reactors sites to the Daya Bay near site, Ling Ao near site, and the far site are 493, 557 and 1634 meters respectively, with more detail shown in Figure 2.4. The role of the near site is to accumulate prolific statistics of the antineutrino flux before significant neutrino oscillations can occur, while the far site observes the flux near the maximal oscillation probability.

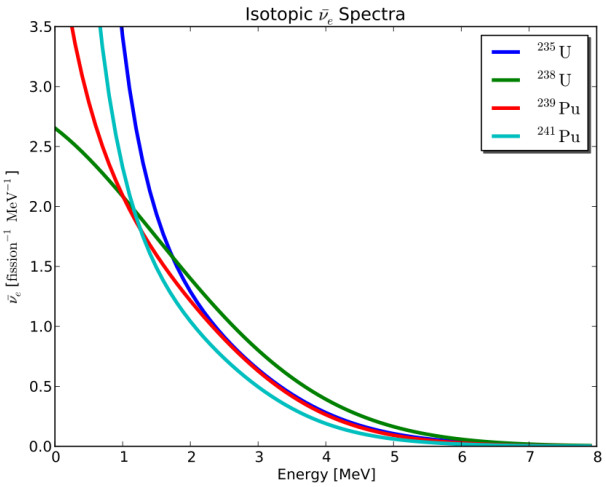


Figure 2.3 The antineutrino spectra for the top four reactor isotopes that comprise 99.9% of the reactor antineutrino flux [48].

The probability of antineutrino disappearance is plotted versus baseline in Figure 2.4, with the flux-weighted site baselines indicated. As seen from the figure, Daya Bay performs a clean measurement of $\sin^2 2\theta_{13}$, in that a measured antineutrino disappearance will be directly attributable to θ_{13}, but not the other mixing angles.

	Daya Bay NPP		Ling Ao I NPP		Ling Ao II NPP	
	1	2	1	2	1	2
Daya Bay 1	362.3804	371.7626	903.4664	817.1578	1353.6177	1265.3153
Daya Bay 2	357.9404	368.4142	903.3467	816.8962	1354.2293	1265.8861
Ling Ao 1	1332.4793	1358.1482	467.574	489.5774	557.5792	499.2072
Far 1	1919.6319	1894.3376	1533.1804	1533.6275	1551.3843	1524.94
Far 2	1917.5188	1891.9765	1534.9194	1535.0322	1554.7671	1528.046
Far 3	1925.255	1899.8607	1538.9301	1539.4683	1556.3439	1530.0787

Table 2.1 Detector to reactor baselines in meters for the six-detector configuration of the Daya Bay experiment [6]. At each nuclear power plant (NPP), the higher-numbered reactor core is west of the lower-numbered core. At the Daya Bay near site, detector 2 is east of detector 1, while at the Ling Ao near site, the detector is south of the open slot. At the far site, detectors 1 and 2 are closest to the reactors, while detectors 1 and 3 are east of detector 2 and the open slot.

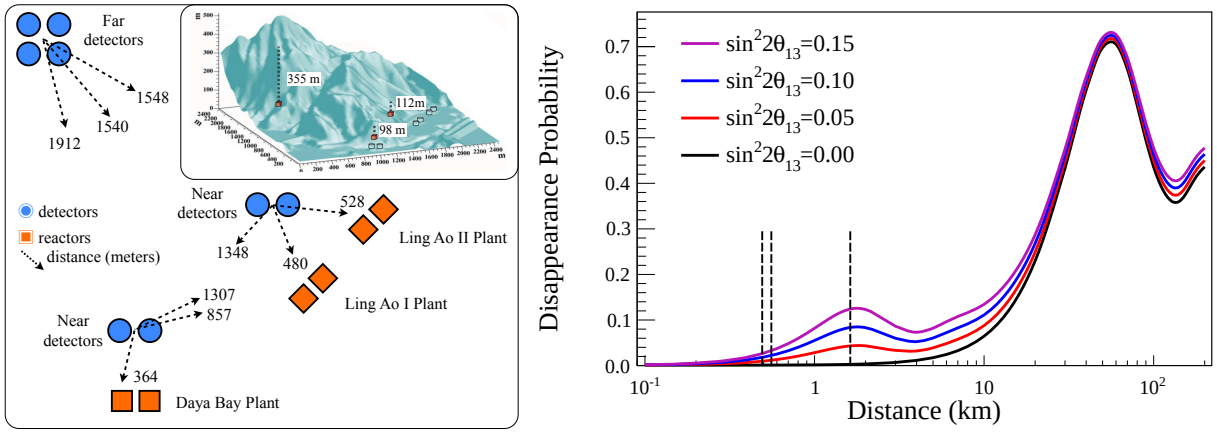


Figure 2.4 Left: The topography of the Daya Bay experiment. Eight detectors are deployed at three underground sites to observe the antineutrino flux from six reactors. The baselines between the detectors and reactors are indicated. The mountain overburden above the detectors is shown in the inset. Right: The oscillation probability for reactor antineutrinos. The near sites observe the antineutrino flux at little probability of oscillation, while the far site observes the flux at maximal sensitivity to $\sin^2 2\theta_{13}$ and minimal sensitivity to other mixing parameters. The vertical dashed lines indicate the flux-weighted average baselines of the three sites.

2.2 Relative Measurement

Daya Bay's precision is the consequence of a relative measurement of the antineutrino flux among detectors, first proposed by Mikaelyan and Sinev [128]. The ratio of the measured antineutrino rates between a pair of near and far detectors indicates a deficit caused by neutrino oscillation, which occurred while the antineutrino flux was propagating between them. For two given detectors, the relative rate measurement is described in Equation 2.1 [8].

$$\frac{N_f}{N_n} = \frac{N_{p,f}}{N_{p,n}} \frac{L_n^2}{L_f^2} \frac{\epsilon_f}{\epsilon_n} \frac{P_{sur}(\theta_{13}, \Delta m^2, L_f)}{P_{sur}(\theta_{13}, \Delta m^2, L_n)} \tag{2.1}$$

For multiple detectors, the relative measurement loses its simplicity. With several detectors at three sites, the simplest relative expression is to form a weighted sum of near and far detectors:

$$\frac{N_f}{N_n} \rightarrow \frac{N_{f1} + N_{f2} + N_{f3}}{\alpha(N_{n1} + N_{n2}) + \beta N_{n3}} \tag{2.2}$$

where α and β are the near site weights determined by unoscillated reactor flux and baselines [129]. Similar weighting is applied to the near site oscillation probability. More exact treatment requires a χ^2 analysis such as that presented in Chapter 8.

In Equation 2.1, N_n and N_f are the antineutrino rates at the near and far detectors respectively, N_p is the number of target protons in the detector, L is the baseline, ϵ is the detector efficiency and P_{sur} is the antineutrino survival probability. Oscillation parameter Δm^2 is the effective reactor mass splitting, a linear combination of Δm^2_{31} and Δm^2_{32} often used because reactor experiments cannot disentangle Δm^2_{31} and Δm^2_{32}. The energy dependences of ϵ and P_{sur} are integrated out over the common antineutrino spectrum in the rate measurement. Each of the measured quantities comes with associated uncertainties. These errors would combine in the case of a direct measurement:

$$N = \frac{N_p}{4\pi L^2} \int \epsilon(E)\, \sigma_{IBD}(E)\, S(E)\, P_{sur}(\theta_{13}, \Delta m^2, L, E)\,, \tag{2.3}$$

where $S(E)$ is the antineutrino rate and spectrum, and $\sigma_{IBD}(E)$ is the IBD reaction cross-section. The errors on a measured quantity such as ϵ for each detector consist of two

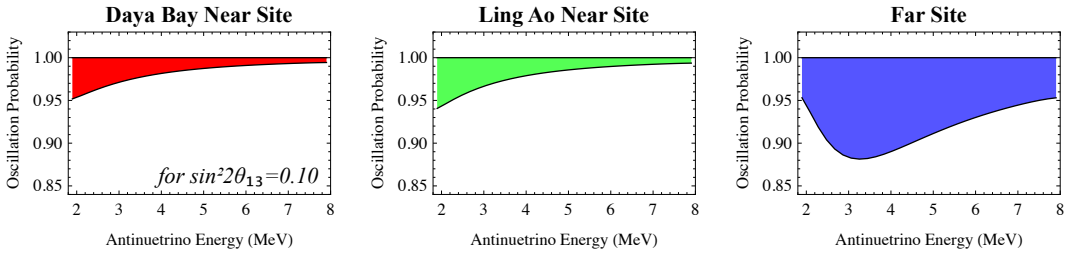


Figure 2.5 The electron antineutrino survival probability versus energy at the Daya Bay near site, Ling Ao near site, and far site, for the sample case of $\sin^2 2\theta_{13}$=0.10.

categories: correlated errors, which are common throughout the experiment, and uncorrelated errors, which are specific to the given detector or reactor. For a direct measurement, both the correlated and uncorrelated uncertainties contribute to the measured rate. For the relative measurement, the correlated uncertainties cancel out; any deviation common the ϵ_f and ϵ_n do not affect the ratio ϵ_f/ϵ_n. In other words, all detectors measuring rates off by -5% preserves the ratio ϵ_f/ϵ_n, but wrecks a direct comparison of the measured flux at one detector to the theoretical value at a given θ_{13} and Δm^2.

The discussion of the relative measurement thus far has involved the measurement of antineutrino rates, the dominant source of information on $\sin^2 2\theta_{13}$. Daya Bay is also sensitive to the energy dependence of the oscillation, forming a secondary, but important channel of information that can validate the rate measurement of $\sin^2 2\theta_{13}$ and provide the opportunity to measure Δm^2. At the near site, the oscillation manifests as a slight drop in survival probability in the low energy tail. At the far site, the loss is more pronounced and peaked at the middle of the energy range, about 3 MeV in antineutrino energy. Figure 2.5 illustrates the oscillation probability at each site, demonstrating the distinctive differences in magnitude and energy-dependence of the signal.

2.3 Detection Principle

The Daya Bay detectors observe incoming antineutrinos via the inverse beta decay reaction:

$$\overline{\nu}_e + p \;\rightarrow\; n + e^+ \,, \tag{2.4}$$

illustrated in Figure 2.6. The neutron and positron will interact subsequently: the positron will promptly annihilate with an electron, while the neutron will thermalize first, then capture on a gadolinium or hydrogen nucleus.

These interactions take place in the center volume of the detector, which contains a mixture of liquid scintillator, wave shifting chemicals, and an emulsion of gadolinium. Gadolinium has the highest thermal neutron capture cross-section ($4.9{\cdot}10^5$ barns) of any element by a factor of ten [130]. After neutron capture, the nucleus relaxes from an excited state back to ground level by the release of about 8 MeV of photons. This high cross-section and large release of energy enhances the signal greatly.

The energy release in the positron annihilation is indicative of the energy of the incoming antineutrino. Since the neutron mass is 2000 times larger than the positron mass, the positron carries almost all of the incoming energy. The characteristic time between the positron annihilation and the neutron capture is 28 μs, due to time required on average for the neutron to reach thermal equilibrium with the gadolinium. This energy and timing pattern is a powerful discriminant against backgrounds, which seldom mimic this pattern.

2.4 History

The Daya Bay experiment broke ground October 13, 2007, the commencement of tunneling into Mt. Pai Ya. After excavating the Daya Bay near site, and constructing, commissioning and installing the first two detectors, these detectors began collecting data September 23, 2011. Data was subsequently collected for exactly three months to validate the general performance of Daya Bay's detectors [67].

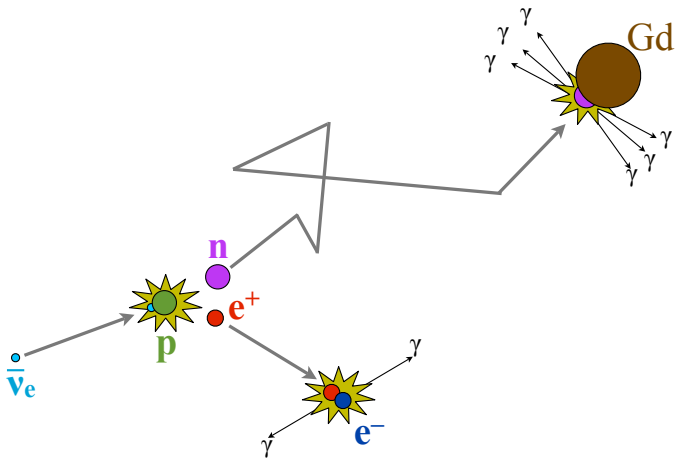


Figure 2.6 Diagram of inverse beta decay, $\overline{\nu}_e + p \rightarrow n + e^+$. An antineutrino enters the target volume, then interacts with a proton to generate a neutron and positron. The positron annihilates promptly while the neutron captures on a gadolinium shortly after. The energy released and timing provides Daya Bay with a unique signal of an antineutrino.

Meanwhile, the collaboration continued building Daya Bay's underground infrastructure, and producing and commissioning four more detectors. On December 24, 2011, Daya Bay transitioned to its six detector configuration and the start of its first oscillation data set. This resulted in two rate-based measurements of $\sin^2 2\theta_{13}$ published based on data sets concluding in February 17, 2012 [131] and May 11, 2012 [68], and one rate and spectrum measurement of $\sin^2 2\theta_{13}$ and Δm^2_{32} from the data set ending on July 28, 2012 [3]. As of October 19, 2012, all eight detectors have been collecting data.

2.5 Summary

The Daya Bay experiment exploits a powerful technique to measure neutrino oscillation parameters $\sin^2 2\theta_{13}$ and Δm^2. Eight functionally identical detectors are located underground at distances near to and far from six reactors (on the order of 100s of meters and 2 km respectively). The detectors determine reactor flux and spectra at positions of low and high oscillation probability. The comparison of the detected antineutrino flux and spectra

directly indicates $\sin^2 2\theta_{13}$ and Δm^2, while detector identicalness reduces the uncertainty of the measurement.

The detectors observe the reactor antineutrino flux by the inverse beta decay interaction of antineutrinos with protons in the target volume. The reaction produces a positron, which carries almost all of the antineutrino's energy and annihilates promptly, and a neutron that captures on a nucleus shortly thereafter. This combination of two punctuated depositions of energy offers an effective discriminant against backgrounds.

Chapter 3

Reactor Antineutrino Flux Prediction

An important ingredient in the measurement of oscillation parameters at Daya Bay is understanding the reactor antineutrino flux, which includes the not just antineutrino rates and spectra, but their associated uncertainties as well. The reactor predictions are half the input to an analysis that compares expected to measured antineutrino flux and spectra, but are also necessary for a near-far relative detector measurement, which still must take into account reactor uncertainties.

The reactor predictions are generated with data supplied by the power plant operators, including the power generated and calculated proportions of reactor fuel. The power plant data are in turn fed into the analysis efforts of several groups within the collaboration to generate antineutrino rates and spectra. My contribution to the flux analysis was small. I calculated rates and effective baselines for the initial detector comparison paper, I studied the propagation of reactor uncertainties, and I investigated the effect of reactor uncertainties on the oscillation measurement and sensitivity in detail.

3.1 Operation of Pressure Water Reactors

The Daya Bay, Ling Ao I and Ling Ao II Nuclear Power Plants (NPP) consist of pairs of Pressurized Water Reactors (PWR) produced by Framatome [127, 132]. The principle of operation of PWRs is that nuclear activity heats conduits of water, producing steam that drives a turbine. A diagram of a typical PWR is shown in Figure 3.1. Nuclear fission in the core heats the first of three loops of water, which is kept at high pressure to prevent

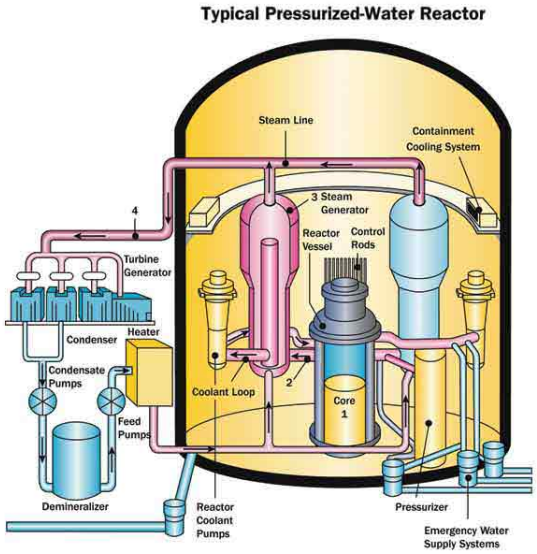


Figure 3.1 Diagram of a Pressurized Water Reactor [49].

boiling. It is circulated into a second closed loop of water that evaporates into steam to rotate the turbine, which in turn drives electrical generators. After that point, the steam is condensed back to liquid form by way of a third, open loop of water that carries the heat into the environment. In this manner, the second loop recirculates back into the core, and the volumes of water that interact with the core are isolated [49].

The heart of the reactor core is an assembly of fuel rods and moderators. A fuel rod consists of uranium oxide in pellet form, which is enriched to include a higher proportion of ^{235}U. The enrichment levels are 1.8–3.1% for Daya Bay NPP cores, and up to 4.45% for the Ling Ao cores. The pellets are assembled into thin fuel rods that are then combined into fuel assemblies. At Daya Bay and Ling Ao, 264 fuel rods combine with 24 guide tubes and one instrument tube for each assembly [48]. 157 fuel assemblies in total (72.5 MTU) comprise the core, with gaps between them to pass water to absorb the heat, and moderators that absorb neutrons to maintain steady operation [133, 48]. See Figure 3.2.

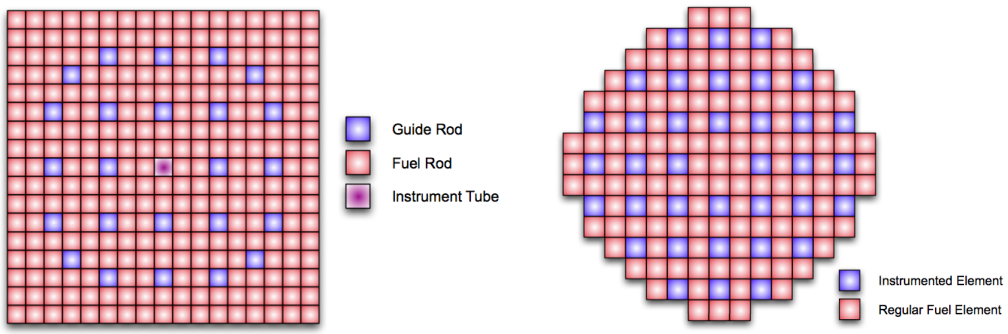


Figure 3.2 Left: diagram of a fuel assembly consisting of pure fuel rods, guide rods and an instrument tube. Right: the combination of fuel assemblies into a core, with regular and instrumented fuel rods [48].

3.2 Information Provided by the Power Plant

The predicted antineutrino flux is derived from two important sources of information supplied by the power plants: power production and fuel burn up simulation.

Three systems are deployed to measure the power generation of each reactor: RPN, KME and KIT/KDO [50, 134]. RPN is an online monitor, but is the least accurate. With detectors installed around the core, RPN tracks changes in the neutron flux, which is directly proportional to the power, but also depends on isotope. As the fuel cycle proceeds, and the isotopic proportions evolve, the conversion from neutron flux to power changes. Once RPN differs from the other systems by 1.5%, RPN is calibrated to match KIT.

In contrast, KIT/KDO and KME monitor power production by way of heat transfer in the primary and secondary loops. The KIT/KDO system determines the temperature, pressure and flow rate of water in the innermost water loop. It is slightly less accurate than the KME because KIT/KDO system flow meters are not allowed to restrict water flow. It is calibrated to within 0.1% of the more precise KME, which unlike the online KIT/KDO, is only activated monthly. KIT/KDO was chosen over KME to supply collaboration data, however, because the monthly period of KME prevents it from being the most precise means of providing daily antineutrino flux predictions. The KME system monitors the same parameters as KIT/KDO, but acts on the secondary loop instead, and accounts for heat transfer to the turbines and

pumps. The KME systems at all cores were cross-checked with an adjunct SAPEC system to measure its consistency across reactors. The result is a 0.5% reactor-uncorrelated power uncertainty, which is part of the reactor flux rate uncertainty quoted for the experiment.

The power is then provided to the collaboration at two precision levels [51]. The Daya Bay Reactor Working Group (RWG) receives daily averaged power at each reactor, integrated hourly over detector live-time. The RWG informs the collaboration of the predicted antineutrino rate and spectra based on this information (and the fuel cycle), but does not divulge the reactor data. The other source of information offered is the daily power produced, regardless of detector status. This is used in internal simulations of reactor fuel burn up.

In addition to the reactor power, the reactor operators keep track of the reactors' fuel isotopic compositions and provide this to the collaboration. This is important since the various isotopes in the reactor produce antineutrinos at different rates. The power plant uses simulation software to calculate the burn up parameter, which is the ratio of energy produced over fuel uranium mass:

$$B(t) = \frac{W \cdot t}{M_0}\,. \tag{3.1}$$

It is expressed in units of megawatt-days per metric ton of uranium (MWd/MTU). The fuel begins its life dominated by uranium isotopes, which decay into an assortment of other elements, predominantly plutonium. A typical fuel evolution versus burn up is shown in Figure 3.3. The burn up is a complex process dependent on not just time and power, but also neutron flux, fuel rod location, reactor control rods and more. The power plant provides to the RWG the burn up simulation at intervals of 1000 MWd/MTU, every two weeks, at 5% precision [52]. The RWG interpolates from the biweekly data to obtain the fuel composition daily.

Reactor fuel is a mixture of ^{235}U, ^{238}U, ^{239}Pu, and ^{241}Pu predominantly; these isotopes comprise over 99% of the antineutrinos emitted. The reactor fuel is initially very rich in ^{235}U, which burns into the other three isotopes and stable nuclei. Table 3.1 lists the proportions of the four isotopes throughout the fuel cycle.

Cycle	^{235}U	^{238}U	^{239}Pu	^{241}Pu
Beginning	73.78%	7.38%	15.99%	2.74%
Average	58%	7%	30%	5%
End	44.96%	7.70%	38.27%	8.82%

Table 3.1 The fractions of the top four isotopes in the reactors at the beginning and end of the fuel cycle [7], and on average [8].

3.3 Flux Modeling

The reactor power and fuel composition determine the antineutrino rate and spectra, because the number of fissions is proportional to the power generated, and each isotope decays with a characteristic antineutrino energy spectrum. The total rate of fissions in the reactor is equal to the quotient

$$N_f = W_{th} / \sum_{\iota} f_\iota E_\iota \,, \tag{3.2}$$

where N_f is the fission rate, W_{th} is the thermal power, f_ι is the proportion of the ι^{th} isotope in the reactor fuel and E_ι is the isotope's thermal energy per fission [51]. The thermal energy per fission is about 200 MeV, which accounts for the total energy released in the decay chain down to the stable daughter nuclei, neutrinos and neutrons [9]. For each isotope, E_ι is indicated in Table 3.2. On average, each decay chain yields around six antineutrinos.

Isotope	Thermal energy per fission
^{235}U	201.92 ± 0.46 MeV
^{238}U	205.52 ± 0.96 MeV
^{239}Pu	209.99 ± 0.6 MeV
^{241}Pu	213.60 ± 0.65 MeV

Table 3.2 Energy released as the given isotope fissions, and the fission products decay until stable nuclei remain [9].

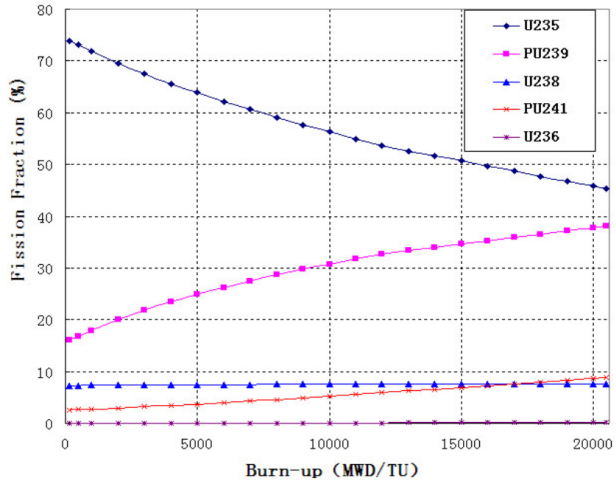


Figure 3.3 The composition of the reactor fuel as a function of burn up [50]. ^{235}U is converted to ^{239}Pu and ^{241}Pu as the burn up progresses.

The antineutrino spectra were calculated in the 1980s from Institut Laue-Langevin (ILL) reactor experiments [135, 136, 137] in the case of ^{235}U, ^{239}Pu, and ^{241}Pu, or from theory [138] for ^{238}U. Foils of ^{235}U, ^{239}Pu, and ^{241}Pu were exposed to a constant flux of thermal neutrons deep within an ILL reactor core for up to 44 h, after which the emitted beta particles were measured by a high precision magnetic spectrometer. The beta particles were sampled from all fission products and decay chains at once. Isotope ^{238}U was not investigated because it fissions only when activated by fast neutrons.

The beta spectra were then converted to antineutrino spectra by estimating the likely decay branches and daughter energies. The conversion to antineutrino energy is a complicated task since there are many combinations of possible beta decay branches available, and many have limited experimental data. The ILL analysis hypothesized 25–30 beta branches, then converted beta spectra to antineutrino spectra by conservation of energy with radiative corrections.

Two new flux models, "Mueller" [139] and "Huber" [140], improve the calculation of the antineutrino spectra by including thousands of beta branches with modern nuclear data [141], and improved the handling of systematics such as radiative corrections and weak magnetism corrections. All three reactor antineutrino flux models are tested in the oscillation analysis

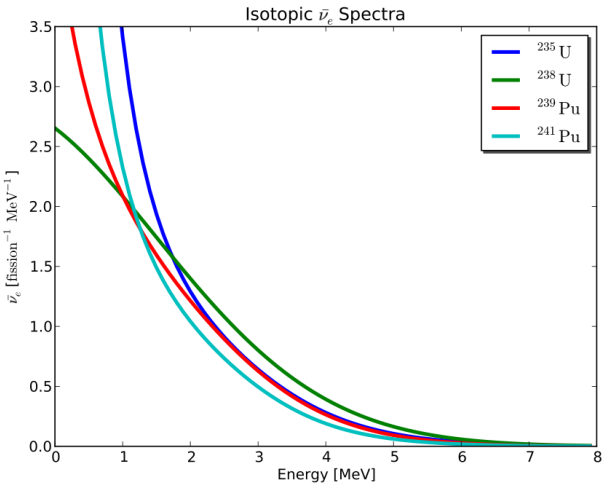


Figure 3.4 The antineutrino spectra for the top four reactor isotopes that comprise 99.9% of the reactor antineutrino flux [48].

of Daya Bay data, although Huber is chosen as the baseline in Chapter 9 since it is internal to the collaboration.

Besides the primary four isotopes that contribute to the antineutrino flux, spent nuclear fuel and off-equilibrium isotopes add to the mix as well. The baseline rate of antineutrinos from these sources are included in the flux predictions, while their uncertainty spectra are shown in Section 3.5.

Spent nuclear fuel is the collection of exhausted fuel rods removed from the reactor core. Typically the oldest one third of the fuel rods are removed at the end of the fuel cycle, but these are still too radioactive to transport off the reactor campus. Instead, the spent rods reside in cooling pools within 50 m of the core for several years, still emitting antineutrinos as long-lived nuclei decay. The contribution of spent nuclear fuel to the antineutrino flux drops precipitously over time as there is no neutron flux to activate the spent fuel. Averaged over the cooling period, its contribution is about 0.3% of the total antineutrino flux, entirely below 4 MeV.

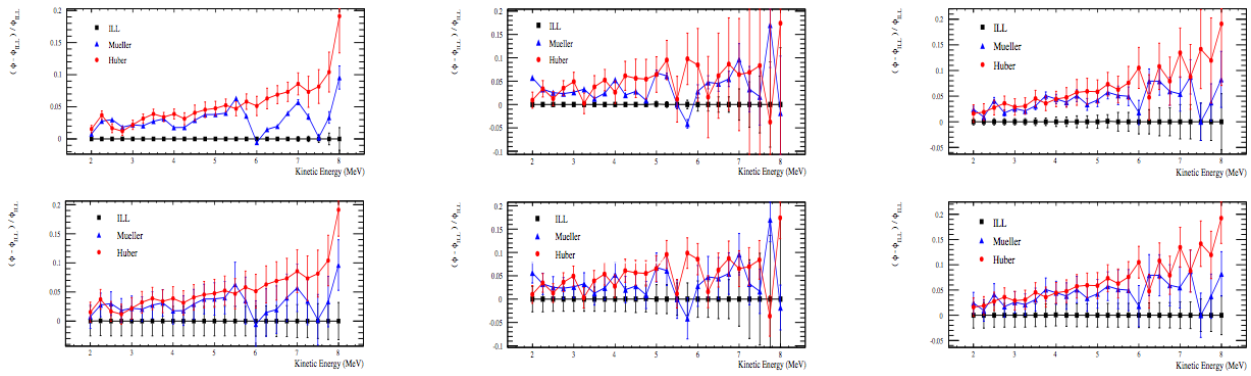


Figure 3.5 Comparison of the three flux models, ILL, Mueller and Huber [7]. From left to right, the plots show the flux predictions for ^{235}U, ^{239}Pu, and ^{241}Pu, relative to the ILL flux. The error bars of the top plot are uncorrelated in energy, while the error bars of the bottom plot are energy-correlated.

The nonequilibrium flux are the antineutrinos produced by the decay of long-lived isotopes that emitted far fewer antineutrinos in the ILL experiments than they do in the reactor core. The discrepancy is a consequence of the short irradiation time at ILL and the half-lives of some daughters. The exposure at ILL was less than two days, compared to years in the reactor. Over this time, about 10% of the nuclei in the decay chains of ^{235}U, ^{239}Pu, and ^{241}Pu have not yet come into equilibrium [139]. Furthermore, the decay chains are affected by fast neutrons that are present in commercial reactors, but not at ILL. Hence, the true long-lived isotope production must be predicted and accounted for; about a dozen candidate isotopes [142] have lifetimes longer than 10 h and either these isotopes, or their daughters, decay at energies beyond the IBD threshold of 1.8 MeV. The nonequilibrium flux, like the spent nuclear fuel, is entirely below 4.5 MeV, and accounts for about 0.6% of the total antineutrino flux. An energy-dependent correction factor of magnitude 6% or less must be applied to the antineutrino spectra of ^{235}U, ^{239}Pu, and ^{241}Pu to augment the low energy bins. These corrections are also dependent on time within the fuel cycle, since around 100 days are required for all the long-lived isotopes to come into equilibrium. See Table VII of [139] for corrections as a function of time and energy.

3.4 IBD Prediction

For the contribution of a given reactor to the antineutrino flux at a given detector, the detected antineutrino rate is predicted, excluding neutrino oscillations, according to Equation 3.3, which combines the flux prediction, detector response and distance propagated [51]:

$$\frac{dN_{IBD}}{dE}(E, L, t) = \frac{N_p(t)}{4\pi L^2}\,\epsilon(E, t)\,\sigma_{IBD}(E)\,S(E, t)\,. \tag{3.3}$$

For a given detector and core:

- $N_p(t)$ is the number of target protons, which varies with temperature and pressure in the experiment halls, and is a function of time.
- L is the baseline, the distance between the given detector and reactor core
- $\epsilon(E, t)$ is the efficiency of the detector, which is a function of energy and weekly calibrations.
- $\sigma_{IBD}(E)$ is the cross-section of the IBD reaction
- $S(E)$ is the antineutrino flux at the reactor core

Note that the natural energy domain of the reactor flux prediction and IBD cross-section is $E_{\bar{\nu}}$, whereas the detector response is a function of the detected visible energy E_{vis}, the amount of light generated by a IBD reaction involving the antineutrino. Refer to Chapter 8: by convention in the oscillation analysis, quantities in the $E_{\bar{\nu}}$ domain are converted to the E_{vis}. Also note that the time variation of the flux and detector properties are gradual and well understood, so all time-dependent parameters are integrated over the data set. The small uncertainties associated with the integration are accounted for in any quoted uncertainty values [143].

The flux at the reactor $S(E)$ takes the form below [51] based on the flux modeling explained in Section 3.3:

$$S(E, t) = \sum_{\iota} \left(N_f(t)\, f_\iota(t)\, S_\iota(E)\, \left(1 + C_\iota^{NEQ}(E, t)\right)\right) + S^{SNF}(E, t)\,, \tag{3.4}$$

where N_f is the total fission rate, f_i is the fraction of the i^{th} isotope in the core, $S_i(E)$ is the spectrum and rate of antineutrino from isotope i, C^{NEQ} is a small correction for nonequilibrium isotope antineutrino production, and S^{SNF} is the antineutrino flux from spent nuclear fuel. The antineutrino spectra fall sharply as energy increases, with most antineutrinos falling below the IBD reaction threshold of 1.806 MeV.

The IBD cross-section is calculated from the $1/M$ order expression from [144], where M is the proton mass for the case of Daya Bay. For comparison, at zeroth order in $1/M$, the total cross-section is:

$$\begin{aligned}\sigma_{IBD}(E) &\simeq \sigma_0 \left(f^2+3g^2\right)(E_\nu - m_n + m_p)\sqrt{(E_\nu - m_n + m_p)^2 - m_e^2} \\ &= 9.52\cdot 10^{-44}\,\frac{\mathrm{cm}^2}{\mathrm{MeV}^2}\,(E_\nu - m_n + m_p)\sqrt{(E_\nu - m_n + m_p)^2 - m_e^2}\,, \end{aligned} \tag{3.5}$$

where $\sigma_0 = 1.024\,G_F^2\cos^2\theta_C/\pi$ and f and g are the vector and axial vector coupling constants. At first order in $1/M$ the positron energy depends upon the scattering angle, and other corrections are implemented to obtain the form:

$$\sigma_{IBD}(E) = \sigma_0\left(\alpha_1 + \beta_1\frac{m_n - m_p}{M} + \gamma_1\frac{E_\nu - m_n + m_p}{M}\right)(E_\nu - m_n + m_p)^2\,, \tag{3.6}$$

where α_1, β_1 and γ_1 are functions of f, g and particle masses explained in [144]. The IBD cross-section rises with energy above the reaction threshold. Together with the falling energy spectrum of $S(E)$, the spectrum of detected antineutrinos is a peak centered at approximately 4 MeV, shown in Figure 3.6.

3.5 Antineutrino Prediction Uncertainties

The uncertainties associated with the antineutrino prediction split along several lines. Uncertainties can influence event rates, energy spectra or both. They can be correlated or uncorrelated among reactors or energy bins (reactor-correlated uncertainties are those that affect all reactors identically, whereas uncorrelated uncertainties affect each reactor

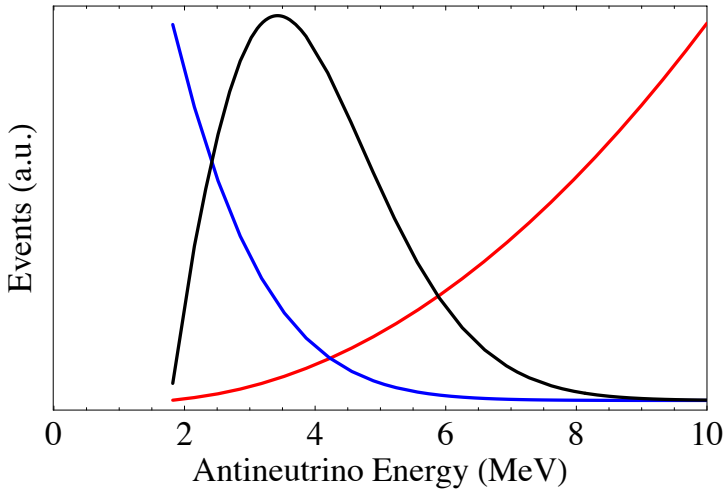


Figure 3.6 The black line shows a toy model of the detected antineutrino spectrum, in arbitrary units, which is a product of the antineutrino flux and IBD cross-section. The red increasing line shows the IBD reaction cross-section as a function of antineutrino energy, while the blue decreasing line shows a typical antineutrino flux [8].

independently; the same holds for energy bins). Finally, the uncertainties can emanate from either the reactor flux prediction or the inverse beta decay (IBD) cross-section. Detector-related uncertainties are discussed in Chapters 6 and 8.

The flux rate uncertainties stem from reactor power monitoring and nuclear physics. As discussed in Section 3.2, the reactor power levels are read equally to each other within 0.5% from instrumentation precision. This is the primary contributor to the reactor-uncorrelated rate uncertainty. By the same instrumentation, the correlated uncertainty on the reactor flux is also 0.5% [50, 51], which is negligible compared to larger uncertainties up to 3% discussed below [68].

The primary contributions to the correlated reactor rate uncertainty are from the IBD cross-section and the energy released per fission. The IBD cross-section uncertainty is driven by the fuel composition and the neutron live-time. Since the cross-section is energy-dependent, and each isotope emits antineutrinos at different energy spectra with uncertainties, the IBD cross-section is therefore isotope-dependent, and the isotopic energy spectra

uncertainties translate directly to cross-section uncertainties. Additionally, the IBD cross-section is scaled by the neutron lifetime uncertainty, which is currently 0.1% [1]. The uncertainty in the energy released per fission, described in more detail in Table 3.2, is approximately 0.2% and isotope-dependent.

Additional sources of reactor-uncorrelated uncertainties are supplied by the spent nuclear fuel and nonequilibrium isotopes, for which the rate uncertainties are discussed in Section 3.3, as well as the fission fraction uncertainty, discussed later in this section, which confers a 0.6% rate uncertainty. However, these three sources of uncertainty are incorporated in to the flux predictions as spectra during the oscillation analysis, rather than straight normalizations.

Further spectral shape uncertainties arise from the modeling of the isotopic antineutrino fluxes. These spectral shape uncertainties are decomposed into two categories— energy-correlated, in which the systematic affects each energy bin in a manner dependent on the effect at other energies— and energy-uncorrelated, in which the impact on one energy bin is independent of all others. In all cases, reactor spectral shape uncertainties are reactor-correlated, because the physical processes are the same at all reactors, and are isotope-dependent.

In all three flux models, the statistical uncertainty of the underlying ILL-measured spectra contributes to an unavoidable energy-uncorrelated uncertainty. Per the ILL and Mueller models, the statistical uncertainty is computed from the ILL beta spectra. Meanwhile, Huber converts the beta spectra to antineutrino spectra first, then bases the uncorrelated uncertainty on the statistics of the antineutrino spectra, plus an additional factor for potential bias uncertainty of the conversion. Each model incorporates an energy-correlated uncertainty from the $\beta \rightarrow \bar{\nu}$ conversion procedure, consisting of corrections for nuclear charge and weak magnetism, and uncertainties on the extrapolation of the antineutrino spectrum from less than 10 MeV out to 12 MeV.

Isotope ^{238}U has larger uncertainties than the other nuclei, with less understanding of how to treat them, because its spectrum is more theoretical. Quoted uncertainties in the

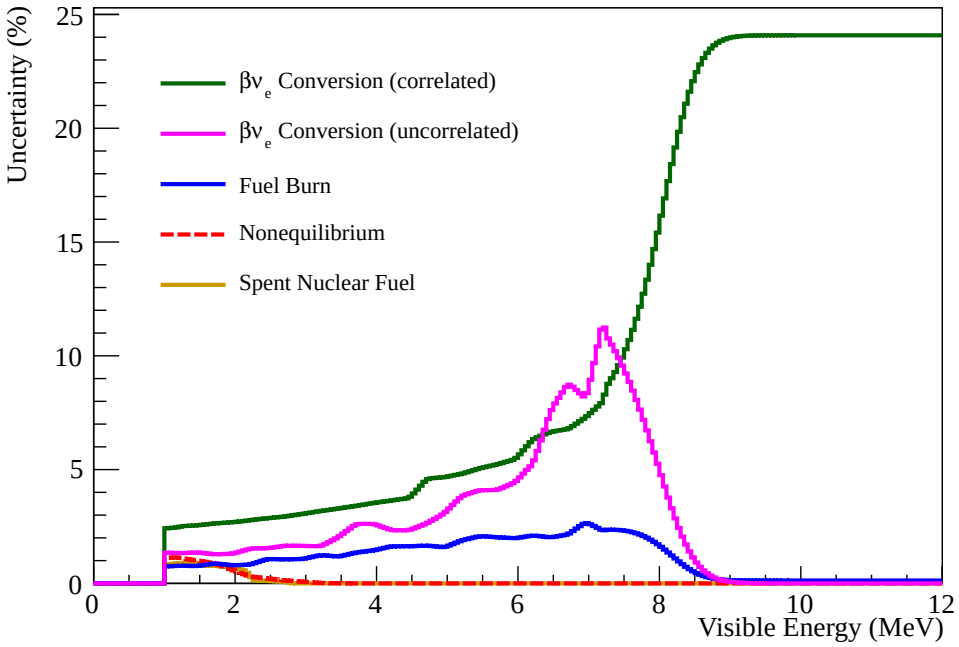


Figure 3.7 The five reactor uncertainty spectra, which can be added to, or subtracted from the flux prediction, normalized by the associated uncertainty [51, 52]. The small contributions at low energies are uncertainties from spent nuclear fuel and the nonequilibrium corrections. The medium-sized uncertainty is from the fission fraction, which has a linear trend from 2–8 MeV. The largest two uncertainties are the energy-correlated, and energy-uncorrelated components of the $\beta \rightarrow \bar{\nu}$ conversion uncertainty. The ^{238}U is modeled as part of the energy correlated uncertainty in this case.

nuclear databases provide to the ^{238}U uncertainty a contribution that ranges from 1% to 13% over energies of 2 MeV to 8 MeV. Meanwhile missing data uncertainties grow from 10% at low energies to greater than 20% at high energies [51]. These uncertainties are combined in quadrature, but whether they are energy-correlated, uncorrelated, or in between, is not understood. Thus, extreme cases of fully correlated and fully uncorrelated treatments are compared in the oscillation analysis of Chapter 9.

The final component to the spectral shape uncertainty is the fuel composition. As discussed in Section 3.2, the simulation of the fuel composition is precise to 5% [52]. To be conservative, the uncertainty spectrum is constructed from a shift in fuel fractions by 5% in the manner that produces the largest effect. This happens to be a shift between ^{235}U and ^{239}Pu, and its resulting spectrum is seen in Figure 3.7. The shape of the uncertainty spectrum is a linear increase with energy over 2–8 MeV. Since it is added or subtracted from the prediction within the uncertainty value, it represents an increase in the high energy portion of the spectrum relative to the low energy, or vice versa. The uncertainty vanishes for energies above 8 MeV because antineutrinos at 8 MeV and higher come only from ^{238}U, which remains approximately constant in proportion over the fuel cycle.

3.6 Summary

Nuclear reactors are a prodigious source of antineutrinos. The power produced by nuclear reactors is well measured and regulated, and the proportions of the isotopes in the fuel are tracked by simulation and verified physically. The reactor power and composition are converted to antineutrino flux and spectra by taking account of the calculated antineutrino yields and energies of the reactor isotopes and their daughter nuclei. The precision of the reactor inputs, and new techniques in extracting antineutrino information from nuclear data, enable Daya Bay to measure neutrino oscillation parameters with world leading precision.

Chapter 4

Daya Bay Detector Construction

The Daya Bay experiment relies on inverse beta decay (IBD) to identify antineutrino interactions in eight detectors at three underground sites. An antineutrino interacts with a proton in the target volume, which generates a positron and neutron. The positron annihilates promptly, depositing energy indicative of the antineutrino energy. The neutron captures on a gadolinium nucleus after 28 μs, depositing about 8 MeV. This distinct pattern, along with the rock overburden and muon veto system, allows Daya Bay to identify antineutrinos to better than 99% precision.

The core of a Daya Bay antineutrino detector is a 20 t target of gadolinium-doped liquid scintillator. The scintillator provides the protons for the IBD reaction while converting gamma rays to ultraviolet light; the gadolinium increases the neutron capture cross-section and deposited energy. Enveloping this central target zone are two more volumes of liquid: a gadolinium-free scintillator gamma catcher that surrounds every gadolinium neutron capture with enough scintillator to convert its gamma rays to ultraviolet, and an outermost buffer zone of non-scintillating mineral oil that attenuates radiation from detector instrumentation and support structures. An arrangement of 192 photomultiplier tubes (PMTs) surround the inside of the detectors to capture light from the antineutrino IBD interactions. Calibration and monitoring systems reduce systematic uncertainties

The collaboration has taken great care to produce eight detectors to be as identical as possible, determined by the performance of the detectors in measuring event rates and

antineutrino energies after calibration. The goal of the collaboration was 0.38% detector-to-detector uncertainty in event rates, 12% energy resolution and 1% energy scale [8]. As discussed in the following sections, these targets were surpassed using several techniques including consistent construction of detectors in a clean room environment over short time spans, and choice of inert and non-radioactive construction materials from the same batches of material where possible [145].

My contribution to the detector hardware lies primarily in the detector monitoring camera system, which I designed, tested and implemented. The camera system, and my contributions to the experiment from its use are described later in Chapter 5. I also contributed to the general detector development in separate ways, some of which follow. I cleaned, inspected and helped repair acrylic vessels. I participated in several of the filling campaigns by manning the filling station that kept track of and controlled liquid filling, and by inspecting and assembling equipment. I helped test and install liquid level sensors and assisted in the set up of the cover gas and calibration systems. I participated in the study that lead to the adoption of a radial absorber rather than a reflector, and helped install it on site.

4.1 Detector Construction

The Daya Bay detectors consist of three volumes of liquid, three vessels to contain them, PMTs and calibration and monitoring systems. An illustration of the detecctor with labeled components is shown in Figure 4.1. In total the cylindrical detectors measure 5 m in diameter and height and weigh a total of 110 t. An outer stainless steel vessel provides support for the PMTs, monitoring devices, and two nested acrylic vessels that separate the fluid volumes. Within these vessels are three concentric volumes of liquid. The inner most volume is 20 t of gadolinium-doped liquid scintillator (GdLS), the antineutrino target, and surrounding that is a volume of liquid scintillator (LS) without gadolinium to enhance light collection. The outermost volume is a non-scintillating buffer of mineral oil (MO), which separates the support structures and instruments from the LS to reduce backgrounds.

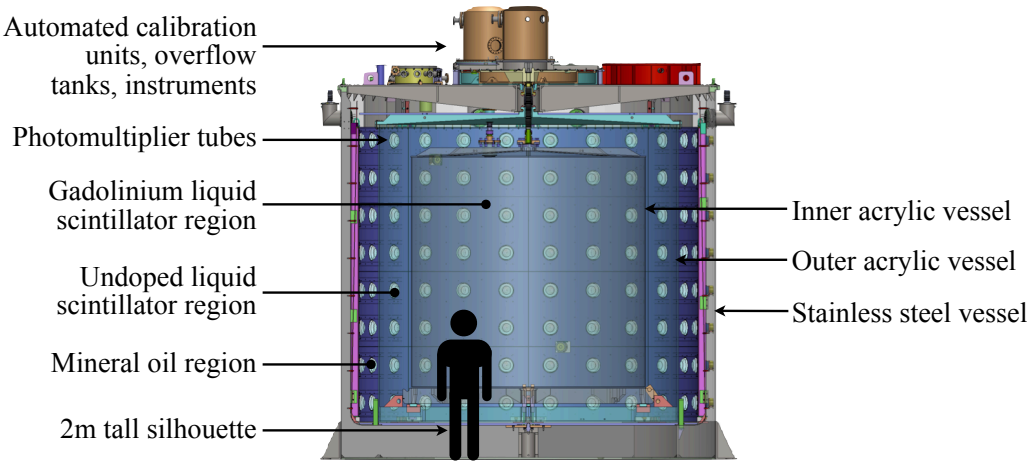


Figure 4.1 A diagram of a detector with several components labeled [53].

4.1.1 Liquid Composition

The target volume is 20 t of the liquid scintillator linear alkylbenzene (LAB) with chemical formula $C_5H_6C_{2n}H_{2n+1}$, where n is typically 10–13 [146]. LAB was chosen as the scintillator for Daya Bay due to its relative ease of gadolinium dissolution, safety and chemical inertness [147]. The target scintillator is doped to 0.1% by mass with gadolinium, the element with the greatest neutron capture cross-section, 49000 b, by an order of magnitude [130]. The chelating ligand 3,5,5-trimethylhexanoic acid (TMHA) forms a complex with gadolinium that is stable and easy to produce, which allows it to be reliably dissolved in the scintillator. The scintillator also contains 3 g/L of 2,5-diphenyloxazole (PPO) as the fluor and 15 mg/L p-bis-(o-methylstyryl)-benzene (bis-MSB) as the wavelength shifter, which help convert the wavelength of deposited light to that which is more suitable for PMTs.

When an antineutrino interacts in the target volume, it is observed via the IBD reaction $\overline{\nu}_e + p \rightarrow n + e^+$. The positron annihilates promptly, releasing approximately 0.7–12 MeV of energy in gamma rays, depending on the energy of the antineutrino. This is discussed further in Chapter 8. The neutron captures on gadolinium to deposit about 8 MeV 28 μs later. The scintillator provides the target protons for the IBD reaction, and it absorbs the gamma

radiation then re-emits light in the near ultraviolet, which is detected with photomultiplier tubes distributed around the outer volume of the detector.

A second volume of scintillator, without gadolinium, surrounds the target volume to ensure that each positron annihilation and neutron capture vertex are enveloped by at least 50 cm of scintillator. This ensures there is enough scintillator to reliably convert the gamma rays to ultraviolet, lest some of the deposited energy escape the detector. Otherwise, the antineutrino energy may be underestimated, or the neutron capture energy may fail below analysis cuts.

The outermost fluid volume is a mineral oil buffer. While the detectors are low in background, some unavoidable materials in the outer detector region emit radiation, such as PMT glass, monitoring devices and tons of steel. The mineral oil provides a dead volume that attenuates radiation before it gets to the target region. It also provides structure by filling the space between the scintillator and the walls of the detector while maintaining a continuous index of refraction from the target region to the PMTs.

4.1.2 Acrylic and Steel Vessels

The stainless steel vessel (SSV) is constructed out of 304L stainless steel and non-radioactive welds due to the chemical compatibility, low radioactivity and strength of these materials [8]. A model of the SSV is shown in Figure 4.2. The floor and lid of the SSV have eight radial and one circular rib each to guarantee stability during lifting and to support the acrylic vessels inside. The lid forms a leak-tight seal to the top of the SSV with a pair of Viton o-rings [148]. The SSV contains four fixtures for lifting around the outside, constructed of boxed beams and flanges around the base. Around the inside perimeter are fixtures for securing PMTs and monitoring devices, and dry-box flanges to conduct signal and power cables to the electronics halls. Coaxial cables for the PMTs and monitoring devices pass through a leak-tight feed-through then connect to a wall of sockets in the dry box that connects them to external cables. Of the liquids inside the detector discussed below, only mineral oil is in contact with the SSV.

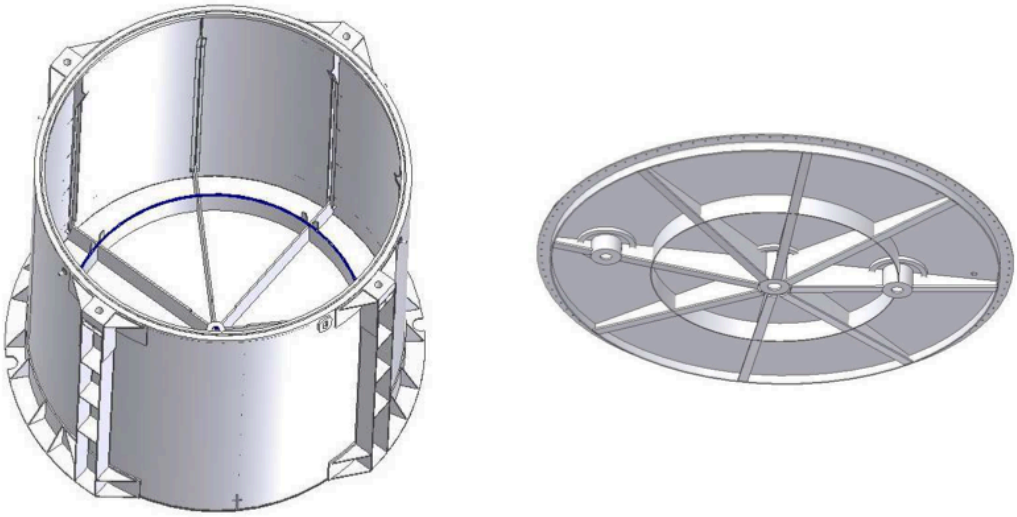


Figure 4.2 Illustration of the stainless steel vessel, with lid at right [8].

The scintillator volumes are contained by two nested acrylic vessels (AVs) inside the SSV [54]. See Figure 4.3. The inner acrylic vessel (IAV) is one contiguous piece produced by bonded acrylic sheets 10 mm thick. The top is conical in shape to collect and pass gas bubbles, and has built in openings on top for calibration ports and an overflow tank. The outer acrylic vessel (OAV) is similarly constructed out of 18 mm sheets, but the lid is detachable to permit the insertion of the inner vessel.

Both AVs are made of ultraviolet transmitting acrylic, where the wall thicknesses are optimized for both structural integrity and minimal attenuation of scintillation light. The AVs have the same index of refraction as the detector liquids, have radiation levels consistent with zero [149], and are compatible with detector fluids.

The bases of both AVs contain reinforcing ribs like the SSV, as well as hold-down clasps to secure the inner vessel to the outer vessel, and lifting hooks. Atop the vessels on the stainless steel lid are overflow tanks that keep the scintillator volumes full inside the detector regardless of temperature and pressure. Connecting all three vessels are bellows that pass calibration sources without contamination from the lid of the SSV down through the scintillator volumes.

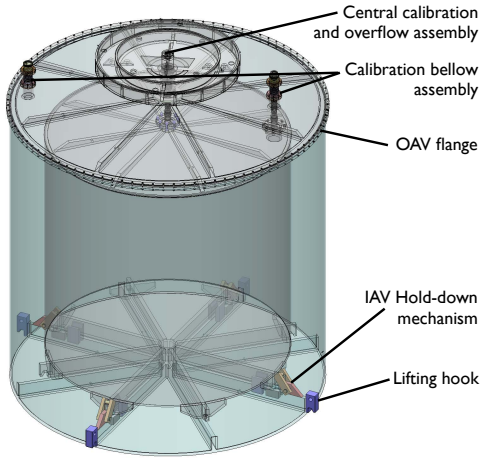


Figure 4.3 Illustration of the inner and outer acrylic vessels with key features labeled [54].

4.1.3 Light Collection

Light collection in the detectors is achieved with 192 PMTs distributed along the SSV walls facing inward, providing 12% effective coverage [8]. These Hamamatsu R5912 8 in. PMTs [64] have sensitivity to photons in the range of 300–700 nm, with a quantum efficiency up to 20%. The PMTs are installed onto eight ladder-like support structures that slide into rails mounted in the SSV. The bulbs of the PMTs protrude through black absorbing panels to 20 cm from the OAV wall. The black panels are in place to reduce reflections from the scintillation light, which might otherwise cause difficulty in reconstructing the antineutrino energy. Behind the absorber, the PMTs are covered by a conical magnetic shield. Their SHV cables are potted into the epoxy base and run along the PMT ladders out to the dry box.

Specular reflectors are installed in the detectors above and below the OAV rather than PMTs. The 4.5 m diameter reflectors reflect 98% of incident scintillation light and are located beyond the target and gamma catcher volumes in the mineral oil. They are produced from a reflective film sandwiched between two 1 cm thick acrylic panes. The reflectors improve the

uniformity and energy and position resolution of the cylindrical detectors because all PMTs are equally spaced from the gamma catcher in this scenario, whereas without the reflector, the PMTs along the tops, bottoms and corners would be at inconsistent distances. A spherical or ellipsoidal detector would not share this drawback, but would be more expensive and difficult to build. The reflectors have been shown to not complicate antineutrino event reconstruction [150].

4.1.4 Detector Monitoring

Monitoring devices inside and outside the detector are deployed to provide information about each detector's liquid level, temperature and cover gas, or to provide visual images.

The detectors are more accurate and identical to one another when completely full of scintillator and mineral oil. Pockets of air would disrupt the optical uniformity inside the detector, interfering with the reconstruction of the antineutrino spectrum. Gas could reflect the scintillation light, altering the timing of the event, or absorb or scatter light without scintillating, altering the reconstructed energy. Additionally, understanding the neutrino flux from the detected event rate requires precision knowledge of the number of target protons in the target volume— GdLS outside the target volume, or gas inside the target volume, do not contribute to the target mass because light produced by an antineutrino event in either does not reach the PMTs. The overflow tanks on the lid allow the detectors to be filled past capacity. This way, fluctuations in temperature and pressure within experimentally maintained margins do not cause the liquid levels to drop into the detector. The target mass is thus the total poured into the detectors minus the mass in the overflow tanks and that calculated to be in the bellows above the top reflector.

Three systems monitor the liquid height in the overflow tanks: ultrasonic, capacitive, and visual [55]. The two scintillator overflow tanks are each instrumented with an ultrasonic liquid level sensor and a capacitive liquid level sensor for redundancy, while the less critical mineral oil volumes are monitored by a capacitance sensor alone. Cameras in the scintillator

regions are activated periodically to photograph the levels against a graduated strip. Additionally, the overflow tanks and detectors are outfitted with precision thermometers, and the lid contains a two dimensional inclinometer, both to more accurately convert the recorded height into the mass present in the overflow tanks. An overflow tank, liquid level sensors, thermometer and inclinometer are shown in Figure 4.4.

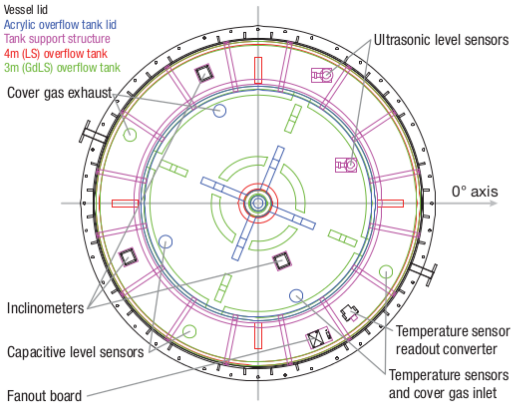
Additionally, cover gas is provided in the overflow and calibration tanks to maintain an interface of the detector fluids with inert dry nitrogen, where sensors measure the humidity and flow rate of the gas to guarantee performance [151]. Exposure to oxygen and water vapor can degrade the scintillators, and the accuracy of the ultrasonic and capacitance sensors depends on correct knowledge of, and consistent, gas in between the liquid level and the instrument [8].

Lastly, two internal monitoring cameras are installed inside the detector, on PMT ladders in the mineral oil. These cameras, my primary contribution to the detector hardware, discussed in depth in Chapter 5, provide visual images for the filling process, monitoring for processes like detector movement, troubleshooting for calibration and general inspection.

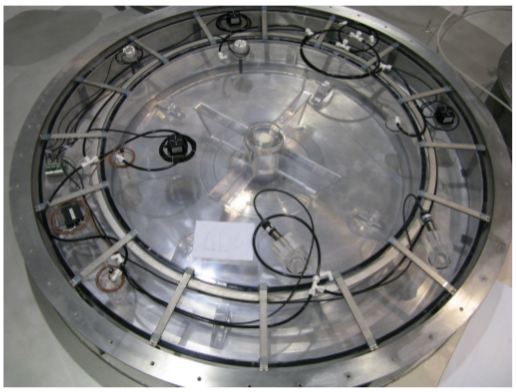
4.1.5 Detector Filling

Detector filling is a sensitive step in detector construction [152]. The requirement of the detector filling process is to protect the integrity of the AVs while precisely measuring the total mass of inserted GdLS. If the filling procedure had not met these goals, the AVs could have been ruptured by the pressure from inconsistent liquid levels across an acrylic wall, or the precision in measuring $\sin^2 2\theta_{13}$ could have been much worse due to detector non-identicalness.

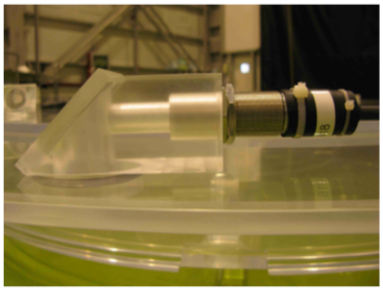
Detectors are constructed in pairs on the surface in a class 10,000 clean room (no more than 10,000 particles larger than 0.5 μs per cubic foot of air). The dry construction phase involves the assembly of AVs, PMTs, monitoring devices, reflectors and lids. Upon completion detectors are transported empty to the underground filling hall, where they are filled



(a) Top view of the central overflow tanks, showing the mounting locations of the sensors and the support structure of the tanks. The tank's outer diameter is 1.8 m.



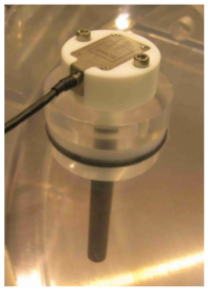
(b) A central overflow tank lid shown at the end of assembly, with all instrumentation installed. (Note that the detector 0° axis faces the camera in this image.)



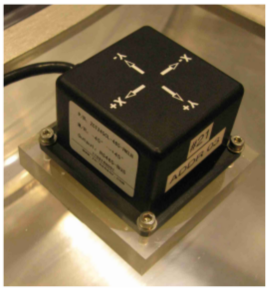
(c) Ultrasonic liquid level sensor.



(d) Temperature sensor.



(e) PTFE capacitive liquid level sensor.



(f) Two-axis inclinometer.

Figure 4.4 Explanation of detector overflow tanks (top) and lid sensors contained therein (bottom) [55]. The overflow tanks can be seen in context on the detector in Figure 4.1.

in quick succession through openings in the overflow tanks that lead to the three empty volumes. After filling they are then transported to their destined experimental site.

The first goal of filling, to protect the integrity of the AVs, is achieved with a system of metered pumps, scales, height sensors and cameras. The metered pumps convey a precise flow of fluid to the detector, and the flow rate is confirmed by scales on the GdLS holding tank and flow meters. The operator sets the flow rate to provide even liquid levels as the fill progresses because levels mismatched more than a few centimeters can apply enough pressure against the AVs to rupture the thin acrylic walls.

The user first fills the lower mineral oil volume, below the OAV, at maximum speed. When the height reaches the OAV bottom, fluid flow is slowed to fill the mineral oil and LS regions evenly, until the IAV bottom is reached. Any mismatches detected by the camera system or liquid level sensors are corrected by stopping flow and filling one volume until the levels match. The same strategies are applied at any change in detector cross-section as the fluid level rises.

The other goal of the filling system is to determine the target mass of GdLS in the detectors to a relative uncertainty of 0.1% or better (the actual uncertainty achieved was 0.02%). Prior to filling, about 40 t of GdLS is transferred to a holding tank, which is weighed precisely before and after each fill. The GdLS mass measurements were taken with four load cells calibrated before each fill. These load cells have a precision of 0.015%, dominated by a drift of ± 3 kg due to electronic noise. The mass of LS and MO in the detectors is not necessary to understand to meet Daya Bay's physics goals. Coriolis mass flow meters measure the dispensed LS and MO masses and are used to provide a redundant mass measurement for the GdLS. The Coriolis flow meters have a relative precision of 0.05% for the LS and GdLS from detector to detector, and 0.2% uncertainty for the MO.

4.2 Calibration

Fundamentally, the detectors merely report a series of electrical signals corresponding to photons triggering PMTs. A photon knocks an electron free from the photocathode of

the PMT due to the photoelectric effect, which is then accelerated by high voltage into a succession of anodes and dynodes. A pulse of electric charge, measured in photoelectrons, (PEs) is generated, with the amplitude of the pulse, and the number of PMTs triggered, indicating the energy deposited in the detector. The calibration system is necessary to convert PMT signals to deposited energy. The calibration system consists of a weekly automated calibration, and an occasional manual calibration.

4.2.1 Automated Calibration

The goals of the automated calibration system are to convert the number of PEs counted by the PMTs to deposited energy accurately over the range of 1–8 MeV, to calibrate PMT gains and timing, to correct position dependence of the detector response, and to detect changes in any of these properties over time [56]. All the while, the calibration system is designed not to interfere with the detector through either electrical noise, radioactive backgrounds or materials incompatibility.

The calibration instruments are encased in three stainless steel bells atop each detector. Inside are several calibration sources, shielding, motion mechanisms, and monitoring systems, depicted in Figure 5.14. The three calibration bells deploy sources to several heights at the center of the target volume, at the edge of the target volume near the IAV wall, and in the LS region. Calibration at all these positions determines and corrects the position-based detector response.

Three deployment axes in each calibration bell can deploy the following sources: LEDs, ^{241}Am^{13}C, ^{60}Co, or ^{68}Ge. Each source can be lowered one at a time except the ^{241}Am^{13}C and ^{60}Co, which are paired together. The LEDs pulse light on command with a controllable intensity, while the nuclei emit gamma radiation at known energies: 1.022 MeV for ^{68}Ge, 2.506 MeV for ^{60}Co, and 8 MeV for ^{241}Am^{13}C.

The LED emits 430 nm light in 10 ns pulses, and is pocketed in a white nylon ball to diffuse its light. The LEDs' purpose was simulate scintillator light in a dry detector. The

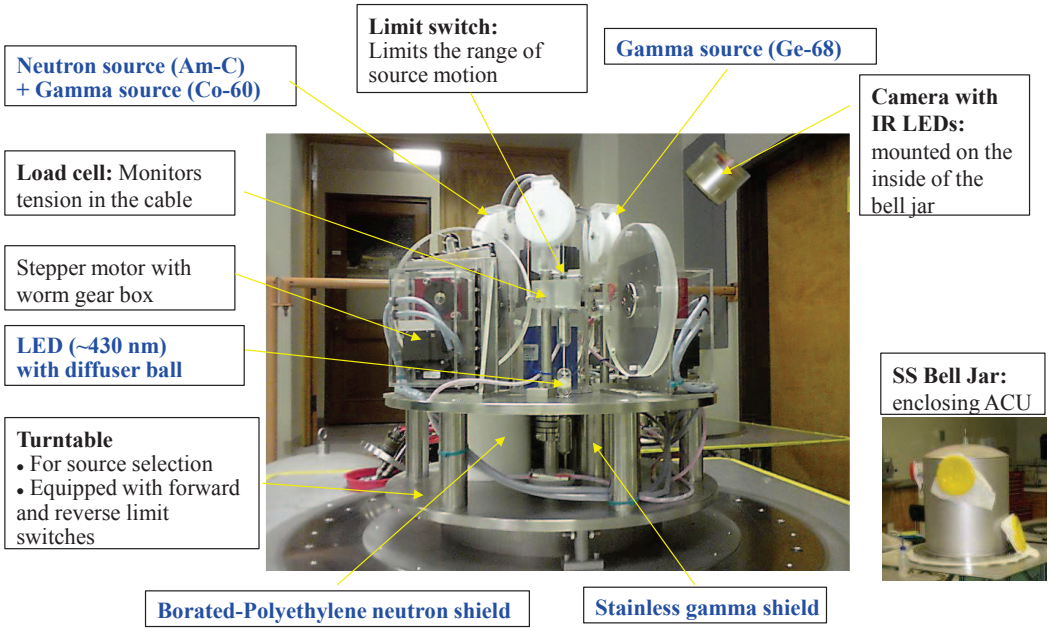


Figure 4.5 Automated calibration unit open to the inside [56]. Calibration sources and motion and monitoring devices are labeled.

conversion from LED voltage to PEs is shown in Figure 4.6. The LEDs were pulsed to simulate low energy antineutrino events in the detector in order to determine PMT gains, while high energy pulses, similar to those from muons, tested the PMT recovery from high energy events.

The ^{60}Co source emits two gammas together at energies of 1.173 MeV and 1.332 MeV, for a total deposited energy of 2.506 MeV at about 100 Hz. This source calibrates the energy linearity, stability, resolution, scintillator quenching and detector spatial and temporal variations. The ^{60}Co is paired with ^{241}Am^{13}C, a neutron emitter, to mimic IBD events. The ^{241}Am releases an α into the ^{13}C, which emits neutron at 0.7 Hz. The neutron captures just as an IBD neutron would, so this calibrates the detector response to neutrons. ^{68}Ge is also a gamma emitter. The ^{68}Ge decay chain results in the release of a positron at 10 Hz, which annihilates in the source enclosure, depositing 1.022 MeV. This calibrates the energy scale, trigger threshold, and relative PMT quantum efficiency.

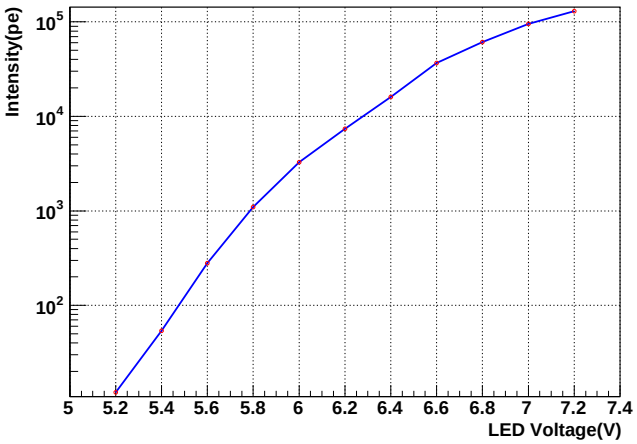


Figure 4.6 Conversion from LED voltage to photoelectrons using the calibration LED and diffusing ball apparatus in a dry detector [56].

4.2.2 Manual Calibration

In addition to the weekly automated calibration, a manual calibration system can be deployed electively, with similar goals as the automated calibration [57]. The system is designed to calibrate the energy non-linearity, detector position non-uniformity, neutron capture time, the ratio of captures on gadolinium to hydrogen, and the behavior of neutron captures at the edge of the target volume.

The manual calibration system consists of a tower that is mounted to the center of the detector lid. It drops a retractable arm with a source down into the target volume. The arm folds out at 90°, and can extend or rotate to cover any position in the target volume to an uncertainty of 2 cm. For a schematic, see Figure 4.7.

The sources deployed by the manual calibration system are the aforementioned ^{60}Co and ^{238}Pu^{13}C. The ^{238}Pu^{13}C tandem is a neutron emitter like the ^{241}Am^{13}C of the automated calibration. Additionally, ^{238}Pu^{13}C emits 6.13 MeV of gamma radiation, which offers a good calibration point for the 6 MeV analysis cut on the IBD neutron capture energy.

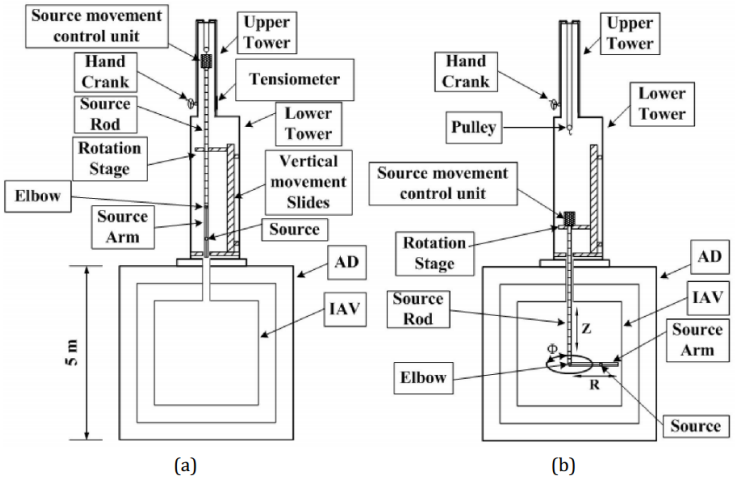


Figure 4.7 Schematic of the manual calibration system: (a) before source rod insertion into the detector, and (b) after insertion and deployment of the source arm [57].

4.3 Underground Sites

The Daya Bay antineutrino detectors must be shielded from muons because muons deposit so much energy in the detectors that they distort the PMT responses for a short time after. Muons also generate backgrounds such as spallation particles like neutrons and long-lived isotopes such as ^{9}Li/^{8}He, that trigger the detector for up to a second after the muon has passed. For this reason, the muons must be reduced in freuency and detected by a dedicated muon tagging system. The time shortly before and after muon passage must be vetoed from the data set, which is detailed in Chapter 6. If the detectors were on the surface, the frequent muon vetoes would render the detector ineffective, as Reines and Cowan learned at Hanford, so Daya Bay's detectors are placed underground to reduce muon rates to manageable levels.

The rate of muons passing through the granite overburden (density 2.6 g/cm^3) and reaching each detector is indicated in Table 4.1. The overburden not only attenuates the rate of muons, but also alters their energy spectra because the rock is more effective at obstructing lower energy muons. Average muon energies are provided in Table 4.1 and spectra are shown in Figure 4.8 for each site [153].

The identification and vetoing of muons is performed by a system of water pools and resistive plate chambers (RPCs). The water pool, divided into inner and outer volumes, tags muons at a rate of 99.7% for the IWS, and 97% for the OWS, with an uncertainty of 0.25%. The RPCs provide additional muon tagging, but have not been introduced into the data stream at the time of the analysis discussed here. The water pool and RPC systems are discussed in the sections below.

Site	Overburden (m/m.w.e.)	Flux (Hz/m^2)	Average Energy (GeV)
Daya Bay near site	93/241	0.88	57.0
Ling Ao near site	100/260	0.69	57.9
Far site	324/842	0.039	136.5

Table 4.1 The rock overburden in meters and meters of water equivalent (m.w.e.), and muon rates and energies incident on the detectors, at each underground site.

4.3.1 Water Pool Muon Veto

The water pool is responsible for muon vetoes and attenuation of neutrons and from surrounding rock. Each detector is surrounded in all directions by at least 2.5 m of water, which reduces the frequency of radiation from the rock by a factor of 10^6. The water pool is capable of tracking passing muons and determining the muon energy by the timing of the PMT hits and the number of photoelectrons. Figure 4.10 provides the floor plan of the near and far halls. The corners are chamfered to improve the muon identification efficiency because muons that would just pass through the corner of water pool would not deposit enough energy to identify, but might still release neutrons from interactions with the water.

The water pool is outfitted with PMTs to detect the Cherenkov radiation from passing muons. The water pool is divided into two regions, both with PMTs, to improve muon tracking: an outer water shield (OWS) and inner water shield (IWS), which are separated by reflective and opaque Tyvek.

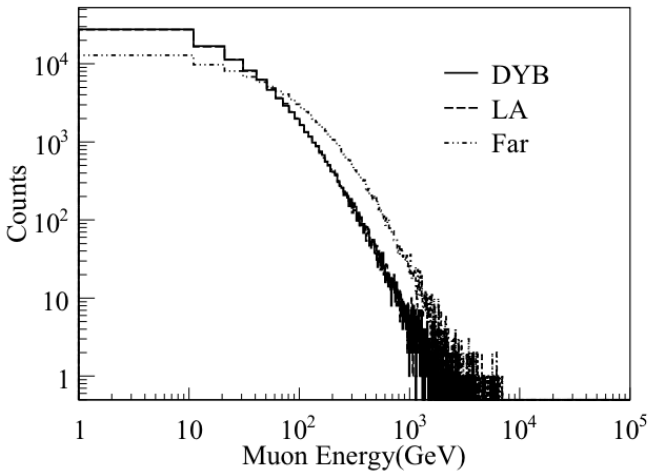


Figure 4.8 The energy spectra for muons passing through the overburden at each site. The two near site spectra are indistinguishable on this plot. The overburden is higher at the far site, which disproportionately attenuates lower energy muons.

At the smaller near halls 288 PMTs comprise the water pool muon veto, 121 for the IWS and 167 for the OWS. The far site water pool contains 384 PMTs: 160 IWS and 224 OWS. About two thirds of the PMTs are new Hamamatsu R5912 [64] models; the rest are recycled from the MACRO experiment [154].

4.3.2 Resistive Plate Muon Veto

Above the water pool at each site is an array of resistive plate chambers (RPCs) [155, 1] that track through-going muons. RPCs are devices made of alternating conductive layers at high voltage, dielectric layers and insulating gas. A passing charged particle creates a spark that is traced to a location because the conductors are laid out in strips. Alternation of strips by 90° provides a two dimensional point of entry for the particle, and multiple layers of strips will indicate the particles trajectory. Daya Bay's RPCs [59] cover an area wider than the water pool by 1 m each direction, offer a spatial resolution of 8 cm, and are installed a few meters above. A cross-section of one plate within the RPC assembly is shown in Figure 4.11.

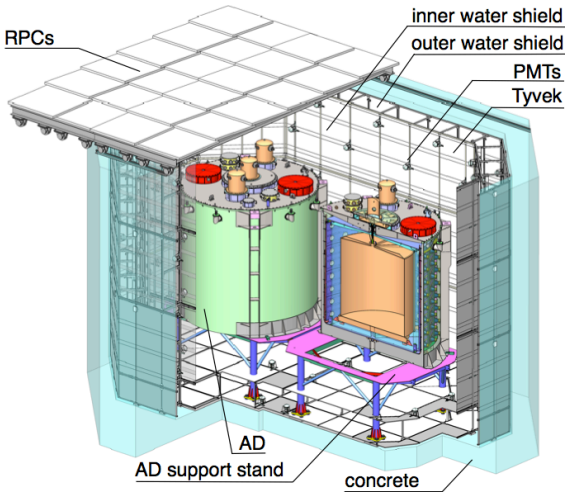


Figure 4.9 Diagram of two detectors in a near site muon veto consisting of a water pool and RPCs [58].

4.4 Summary

The Daya Bay detectors consist of three zones of liquid: a central target scintillator, a second layer of scintillator, and a buffer of mineral oil. Antineutrinos are observed in the target scintillator volume when they produce positron-neutron pairs via inverse beta decay. The positron annihilates promptly and the scintillator converts its light to ultraviolet, whereupon it is measured by PMTs. The neutron captures on a gadolinium or hydrogen nucleus soon after, and the light is again read out by the PMTs with the second scintillator providing additional coverage of the neutron capture.

The liquids are contained by two acrylic vessels and a stainless steel tank. Calibration units are deployed to understand the conversion of deposited energy to observed photons, and various monitoring devices, such as liquid level sensors and monitoring cameras for example, aid in the construction and maintenance of the detectors. The detectors are located

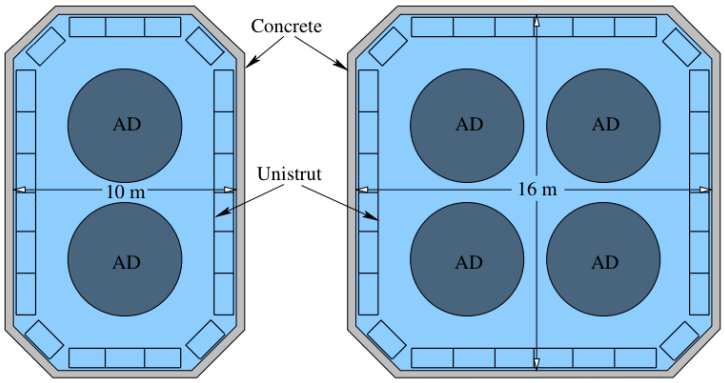


Figure 4.10 Diagram of detectors in a near site pool (left) and four detectors in a far site water pool (right) [59].

underground to shield them from cosmic ray muon backgrounds, in a water pool and RPC muon veto system.

By careful design, construction calibration and monitoring, the detectors have exceeded the identicalness goals set forth in the Daya Bay proposal.

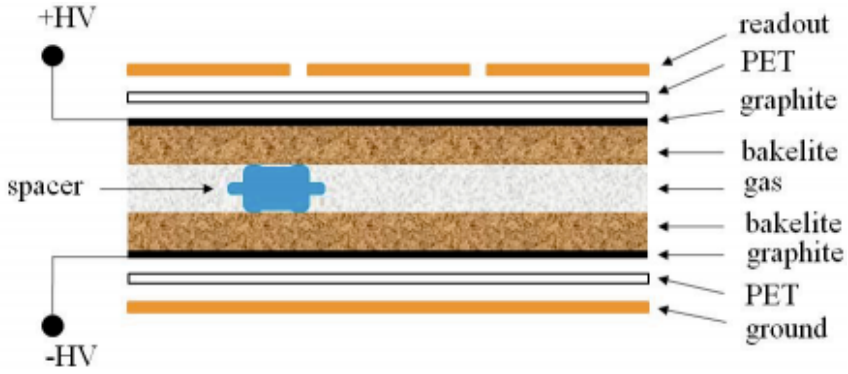


Figure 4.11 A cross-section of a single RPC plate [59]. Narrow strips in this plate read out the position of a passing charged particle in one dimension. An assembly of four of the plates provide the location and trajectory of a through-going muon.



Figure 4.12 The far site with all four detectors during the filling of the muon veto water pool [60].

Chapter 5

Detector Monitoring Cameras

Daya Bay's montioring camera system has proven to be a vital component in building and maintaining the antineutrino detectors for the Daya Bay experiment [156]. All together they have captured over 10,000 photographs during the detector filling, transportation and calibration, without interference with data collection. The system was effectively designed around several constraints imposed by the arrangement of features within the detector, materials compatibility, radioactive backgrounds, and electronics and light interference.

This system represents my primary contribution to the Daya Bay hardware. With my assistance the monitoring camera system proved a vital source of information for fluid levels during filling, thus helping the filling process to be a success. The cameras verified the integrity of the detector during transportation from the surface to underground. Additionally, I integrated my camera system into the plans for the manual calibration system, and in one case investigated a failure of that system, as well as helped troubleshoot the automated calibration.

5.1 Goals and Design Requirements of the System

Several photographs of the cameras are shown in Figure 5.2, and the cameras are depicted in the detector in Figure 5.1. The system is designed to monitor many processes, including detector filling, transportation, installation and calibration, as well as to provide a flexible, on-demand investigative tool. These processes dictate the system design goals.

One of the principal uses of the camera is the monitoring of the detector liquids during filling. One critical requirement of detector filling is to maintain equal liquid levels within 5 cm at all times as all three fluids are pumped in simultaneously, at different speeds. Although there are a variety of instruments measuring the fluid mass flow, the cameras offer the only visual verification. The system must be capable of providing live confirmation of all three fluid levels inside the detector, especially when the liquids reach the tops and bottoms of the acrylic vessels.

Similarly, transportation of the detectors, which occurs before and after filling, is a process that requires careful monitoring to avoid damage. The cameras must help ensure the safety of the move by displaying the position of various detector elements in real time. In addition, the system must provide a photographic record of the positions of internal components before and after filling, transport and installation, especially of the bellows that attach the inner acrylic vessels to the top of the detector, a representative sample of PMTs, the reflectors, and the connections at the bases of the acrylic vessels.

Detector calibration is another process of interest. The automated calibration, whereby a radioactive source is periodically lowered under gravity though the detector volumes, is a well-regulated process that nonetheless benefits from the availability of the cameras on demand. Less frequent is the manual calibration, whereby a source is inserted along an extendable, rotatable arm from a platform atop the detector. Either calibration procedure poses the risk of inserting an active source of radiation into the detector, and while the likelihood of an error is low, the consequence would be high. The camera must be capable of cross-checking the source deployment whenever desired.

Finally, the cameras must offer an effective general-purpose inspection tool. They have to satisfy the explicit list of monitoring requirements while remaining as versatile as possible, able to provide a wide, detailed view on limited notice.

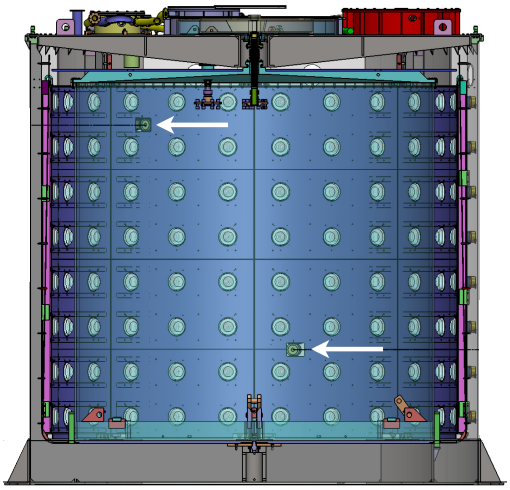


Figure 5.1 The monitoring cameras, indicated by the white arrows, in the context of the detector [53].

5.1.1 Design Specifications

The cameras' visual requirements are established by the critical features of the detector that may need to be photographed. Critical features are those that are pertinent to the monitoring tasks described in Section 5.1. This list includes liquid levels during filling, bellows connecting the tops of the acrylic vessels with the lid of the detector through which calibration and filling devices pass, the connections among the acrylic vessels, reflectors, and other interfaces among components. From the closest bellow to the fluid levels across the detector, the depth of field required of the cameras is 75 cm to 450 cm, and the required field of view is at least 30° horizontally and vertically. The design field of view is shown in Figures 5.3 and 5.4. A goal of 1 mm resolution throughout the detector is established from the features that need to be resolved finely, such as bond gaps in the acrylic, or crazing that could develop. These requirements compete with one another and force compromise. For instance, a deep field generally requires a large f-stop (a narrow aperture), but the limited available light necessitates a wide aperture. This all must be reconciled empirically.

A clear requirement of this system is that it provide its own light, since the detector is light-tight by necessity. Furthermore, this light must not interfere with the PMTs, or

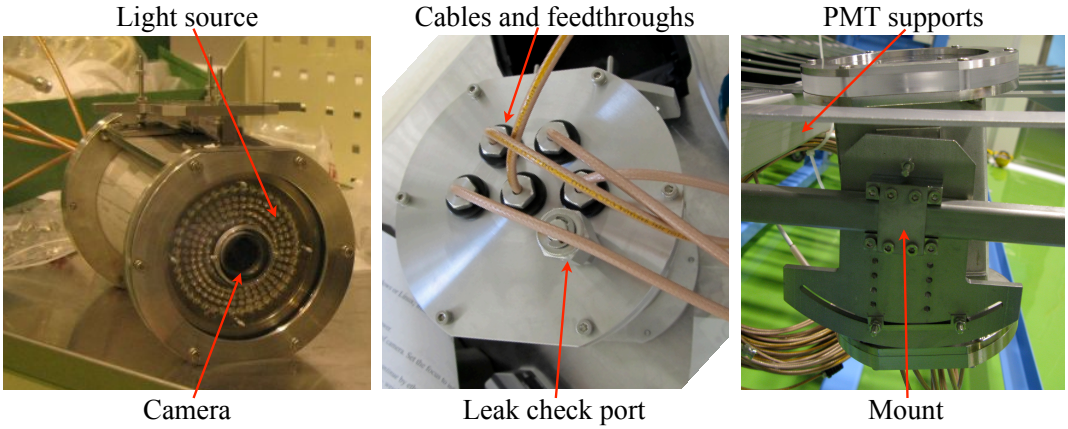


Figure 5.2 Left: front of camera on bench during preparation for installation. The camera opening and light source are prominent. Center: back of camera during assembly with power and readout cables, leak-tight feed-throughs and leak check port are visible. Right: camera on PMT support ladder showing the adjustable mount that attaches it in place. The components and system design are explicated in the sections to follow.

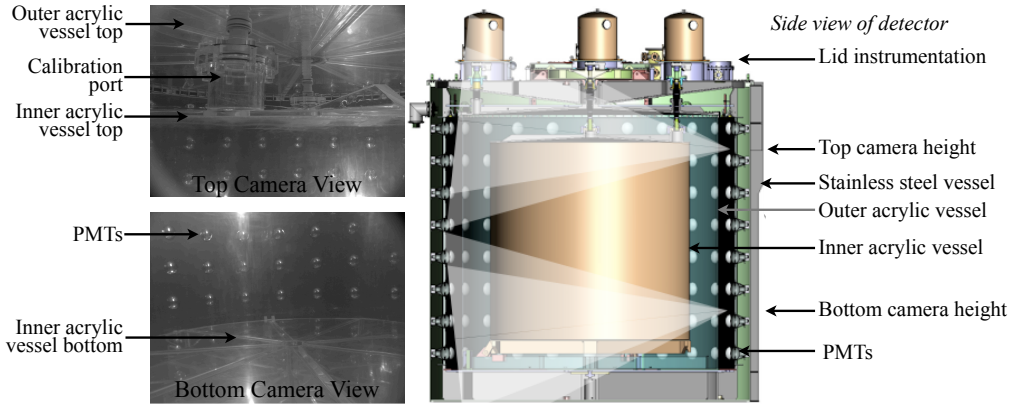


Figure 5.3 Left: Views from the cameras in an empty detector with some features labeled for reference. Right: Cutaway view of the detector with opaque inner acrylic vessel. Shaded triangles show design vertical field of view, which is 43° in an empty detector and 30° when filled with liquid scintillator. Cameras are installed with a 6° tilt away from the center of the detector to provide a better view of critical features.

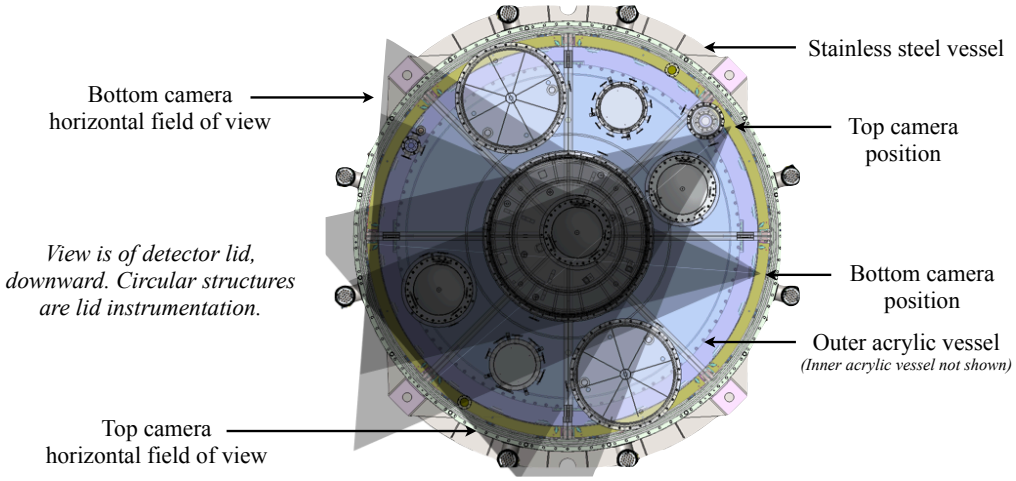


Figure 5.4 Top-down view of detector lid schematic, with camera locations and detector features indicated. Shaded regions show design lateral field of view: 56° in an empty detector and 37° after filling. Both cameras are panned 7° counterclockwise with respect to this view axis in order to photograph more critical features.

otherwise with data taking. As a result, the system must provide both normal white light and infrared light well outside the PMTs' wavelength domain, and usage of both must be carefully controlled.

Equally vital, the system must meet these requirements without interfering with the operation of the detector. The materials chosen for the project must not introduce excessive radioactive backgrounds, nor chemically interact with the mineral oil buffer. The collaboration has established a radioactivity goal of 50 Hz or less per detector for energies greater than 1 MeV. Any more radioactivity risks increasing systematic uncertainties and detector dead time. Failure to use compatible materials may cause increased opacity in mineral oil or acrylic over time. The construction of the system therefore uses materials found elsewhere in the detector, assembled in a clean environment such as a nitrogen bag or a class 10000 or better clean room.

Finally, the camera system must be robustly constructed to be operable throughout the five-year expected lifetime of a detector. Repairs are impossible once the detectors are filled, so the design must be simple and resilient. Mechanical motion and unnecessary electrical components are discouraged, data lines must be reliable, and the enclosure must be leak-tight.

5.2 Design of the Monitoring Camera System

Figure 5.5 shows a single camera installed on a PMT ladder, the structure of vertical and horizontal beams that secure the PMTs. The visible components are labeled and discussed in this section. Together, Figures 5.1–5.5 portray the camera system in the context of the detector.

5.2.1 Camera and Optics

The camera chosen for this project is the small machine vision camera *UI5480SE-MGL* manufactured by IDS Imaging Development Systems [61], shown in Figure 5.6. The *UI5480SE-MGL* is compact and offers 5 MB resolution, infrared sensitivity, and Ethernet connectivity.

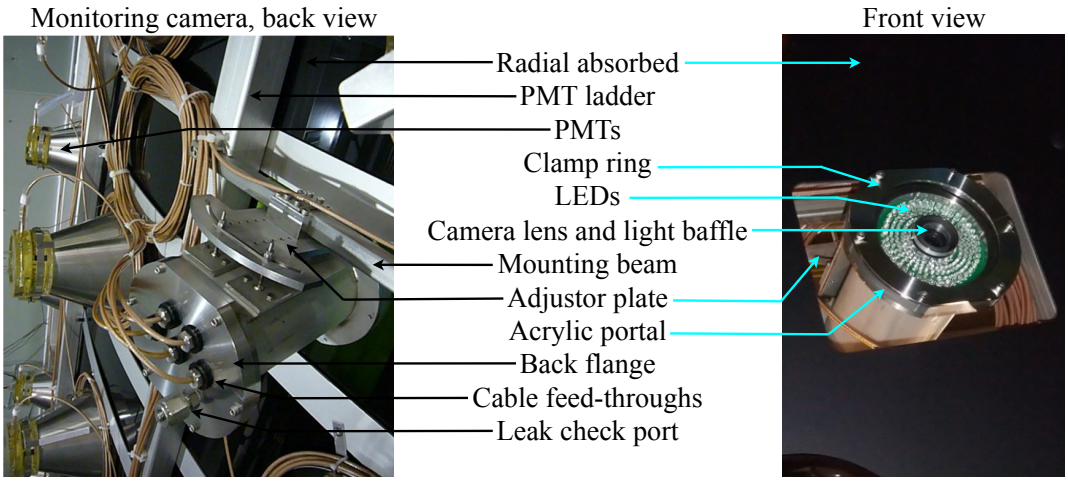


Figure 5.5 Left: Back view of camera installed on a PMT ladder. Right: Front view of camera installed on a PMT ladder. Major features of the camera assembly and PMT ladder are labeled.

At 5 megapixels per image, the camera achieves the goal of 1 mm resolution across the detector with a lens of focal length 6 mm or longer. As such, the camera is not the limiting factor in resolution, but rather the dim light and the polish grade of the acrylic vessels. The camera's infrared sensitivity [62] is sufficient to photograph the detector without white light, which Figure 5.6 demonstrates. In the 900 nm-1000 nm range where the quantum efficiency is not shown in Figure 5.6, the relative quantum efficiency is approximately half the value at 900 nm [157]. Choosing the monochrome model improves the overall sensitivity by omitting unnecessary color filters.

Since video cameras are typically not constructed for low radioactivity measurements, they can include materials otherwise too radioactive for the detectors. For instance, materials such as glass and aluminum are typically not used in low-background detectors, but are difficult to avoid in cameras and lenses. The solution is a camera with little mass enclosed in a low-radioactivity housing. At only 108 g and 40 mm a side, the *UI5480SE-MGL* minimizes the introduction of potentially radioactive materials and allows the housing to be small.

Since the camera is more than 50 m from the control electronics, care must be taken in the choice of readout technology for robust and reliable operation. The data are conveyed

over Ethernet, which is reliable and easy to integrate into the experimental halls at adequate bandwidth. This is superior to other options like USB and analog coaxial models. USB camera signals would require repeaters in sensitive locations, while cameras with analog coaxial readouts tend to offer lower resolution.

Other types of consumer and scientific cameras were considered but found unsuitable for this application. Customized versions of commercial, consumer-grade cameras have been used in other neutrino detectors such as Borexino [158, 159]. However, hand-held consumer cameras generally have infrared cut filters integrated directly onto the sensor, are not equipped for Ethernet transmission, and are not designed to run for long periods in isolation. Pan-tilt-zoom security cameras meet these requirements, but rely on motors that cannot be serviced in the event of mechanical failure. Finally, cameras for laser applications were highly sensitive to infrared but low in resolution.

The lens chosen for this system was the *HFA0612* from Senko Advanced Components [160]. The *HFA0612* is a megapixel-quality lens with an infrared transmission at 60% [161]. It is not specially constructed for infrared focus, but testing shows that the focus is adequate. A lens that is constructed for both megapixel quality and infrared light is much more expensive; in this application megapixel quality is far more important so long as infrared transmission is satisfactory. The reduced transmission is offset by the ability to take long exposures; all processes of interest are very slow, or static. The *HFA0612* focal length is 6 mm, which offers both the resolution and field of view desired, while the lens has an adjustable iris that allows the f-stop to be optimized experimentally. Due to the counterplay between the wide depth of field desired and the limited light, finding the best iris diameter empirically is crucial. Lens types that were considered but rejected include varifocal and plastic varieties. Varifocal lenses, for which the focal length can be adjusted electronically, have mechanical parts that risk failure. Plastic lenses, which would have been less radioactive, were not available at the desired resolution.

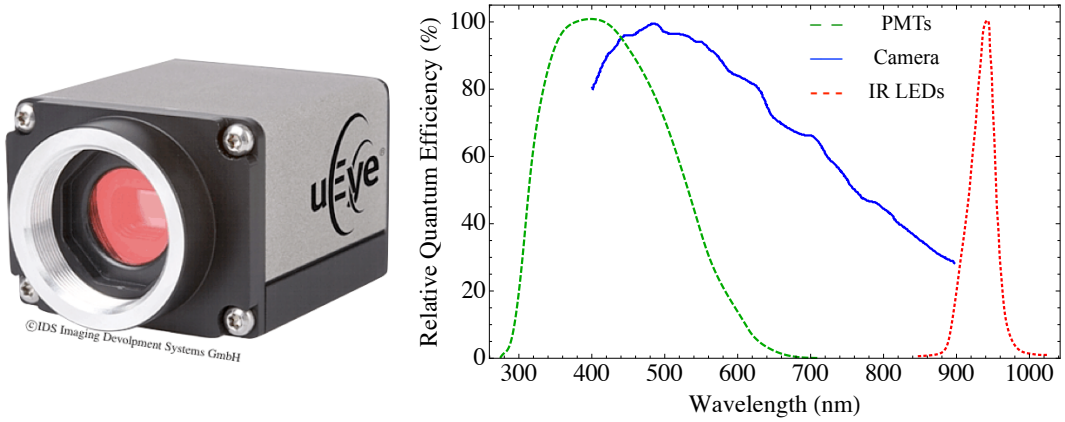


Figure 5.6 Left: The IDS *UI5480SE-MGL*, the camera chosen for this system. Right: The relative quantum efficiency of: the camera (blue solid line) [61, 62], the emission spectrum of the infrared LEDs (red dotted line) [63], and the Hamamatsu *R5912* PMTs used in the detectors (green dashed line) [64]. The LED spectrum overlaps with the camera sensor spectrum, while overlapping minimally with the PMTs.

5.2.2 Lighting

Since Daya Bay's antineutrino detectors detect single photon signals, the detectors must be light-tight, and the camera system must supply its own controllable source of illumination. This source must not interfere with the PMTs, but must provide sufficient light to resolve important features across the detector. It must also be regulable so that a user can optimize the illumination to resolve a particular feature. Finally, the light must not backscatter off the acrylic into the camera, cause blinding fluorescence in the scintillator, nor create more heat than can be dissipated by the enclosure.

In this system, the light is provided by an array of 120 infrared and 60 white LEDs encircling the lens, shown in Figure 5.7. The infrared LEDs are the model *VSLB3940* from Vishay [63], which shine at central wavelength 940 nm. Figure 5.6 juxtaposes the LED spectrum with the quantum efficiency of the PMTs [64] and camera. Infrared LEDs allow the camera system to run in a manner compatible with PMTs, as required anytime the detector will be operated soon after illumination, or could be powered by user error. The consequence of running the infrared LEDs when the PMTs are powered is minimal because

the PMT response drops sharply at about 700 nm. The hit rates will increase, as shown in Figure 5.8, but will return to their normal baseline quickly. Data is not taken when the infrared LEDs are on, and the data acquisition system is stowed out of precaution. It is worth noting that dark box tests of infrared LEDs and PMTs differ from tests in the detector. The dark box PMTs do not show this increase in hit rates from infrared light, so it is suspected that the hit rate increase is influenced by surrounding material.

The effect of white light on PMTs is understandably greater. When the PMTs are unpowered, illumination with the white LEDs is preferable. White light shone on unpowered PMTs still causes an increase in dark rates for a period of time less than 24 hours afterward, but no long-term effects. The 60 white *C513A-WSN* LEDs from CREE [162] are brighter, more efficient and illuminate within the optimal quantum efficiency of the camera and lens. They therefore generate less heat than the infrared LEDs. At maximum luminosity, the 60 white LEDs draw 5 W of power while the infrared LEDs draw 16 W.

The white LEDs easily illuminate the detector. The attenuation length in the visible-near infrared range of each optical medium is longer than 10 m, and the liquid scintillator only absorbs in the near ultraviolet range. Thus the liquids and acrylic neither obstruct much light nor fluoresce back into the camera. The indices of refraction off the acrylic vessels and liquids are constant from the near ultraviolet to the near infrared, so the passage of light through the acrylic and scintillating media is unimpeded

The LEDs shine through a specially designed portal that passes light without any reflections back into the lens, shown in Figure 5.7. When the detector is unfilled, backward reflections of the LED light of the enclosure's acrylic portal would decrease the cameras' effectiveness. To prevent glare, two baffles are embedded into the acrylic portal, and the lens is pressed into a black foam annulus perpendicular to them. The arrangement successfully obstructs all glare from the lens.

Finally, both white and infrared LEDs are interlocked in software to prevent them from being activated when the PMT high voltage is on, and the LED power cables are unplugged and locked out when not in use. This is discussed in Section 5.2.4.

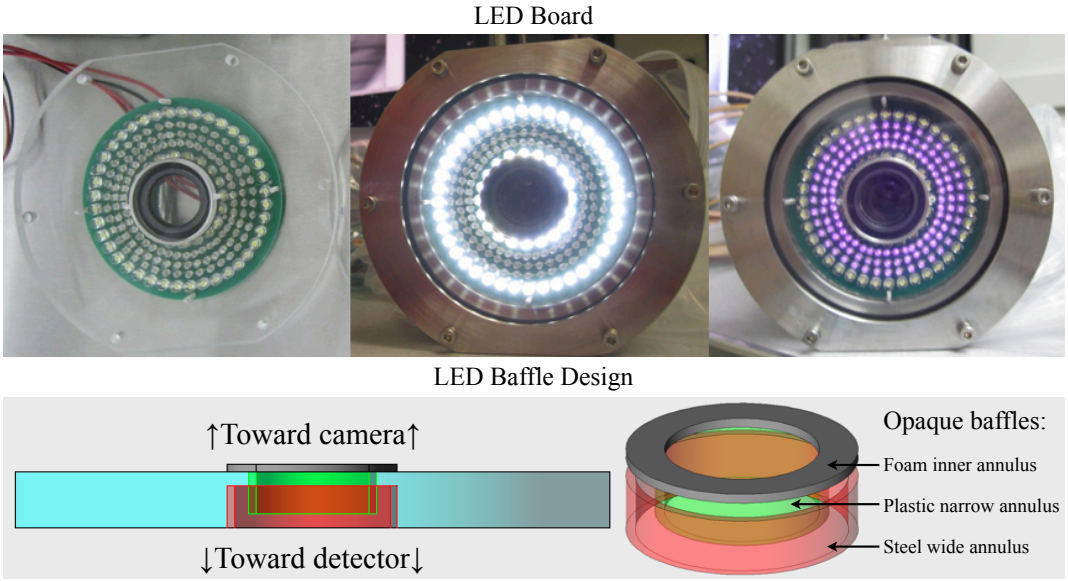


Figure 5.7 Top: The LED illumination element at the front of the camera assembly. The assembly includes five rings of LEDs, of which the outer and inner rings are white LEDs and the middle three are infrared. The camera peers through a light baffle at the center of the portal. Bottom: Diagram of the light baffle consisting of two opposing rings and a perpendicular annulus. The baffle prevents the backward reflection of LED light into the camera.

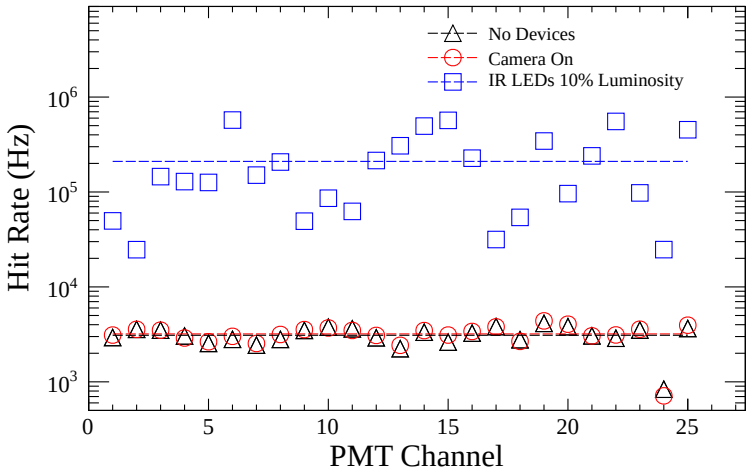


Figure 5.8 Hit rates of an empty detector with camera and infrared LEDs off (black triangles), camera on and infrared LEDs off (red circles), and camera off and infrared LEDs at 10% luminosity (blue squares). The infrared LEDs cause an increase in hit rates in a dry detector. Dashed lines represent averages [65].

5.2.3 Integration into Detector

The camera housings mount onto the PMT ladders that supports the detectors' PMTs, black absorbing shields and some sensors. The housings are fixed within an adjustable, stainless steel mount that permits three translations and two rotations. At the front of the enclosure is an acrylic portal through which the camera and LEDs face the detector. At the back, a leak-tight flange conducts five cables. All materials that contact the mineral oil buffer in which the system resides are either stainless steel, acrylic, nylon, Viton, or Teflon: compatible materials used elsewhere in the detectors. The enclosure and mounting are illustrated in Figure 5.9.

The front portal allows clear imaging and illumination of the detector while withstanding its fluid pressure. The half-inch thick acrylic presses against two o-rings and the front flange of the enclosure body. A clamp ring in front of the acrylic maintains pressure on the o-rings without damaging the acrylic. The portal is not a perfect circle: two short chords are cut off the top and bottom of the flanges to improve clearance for installation. The two concentric,

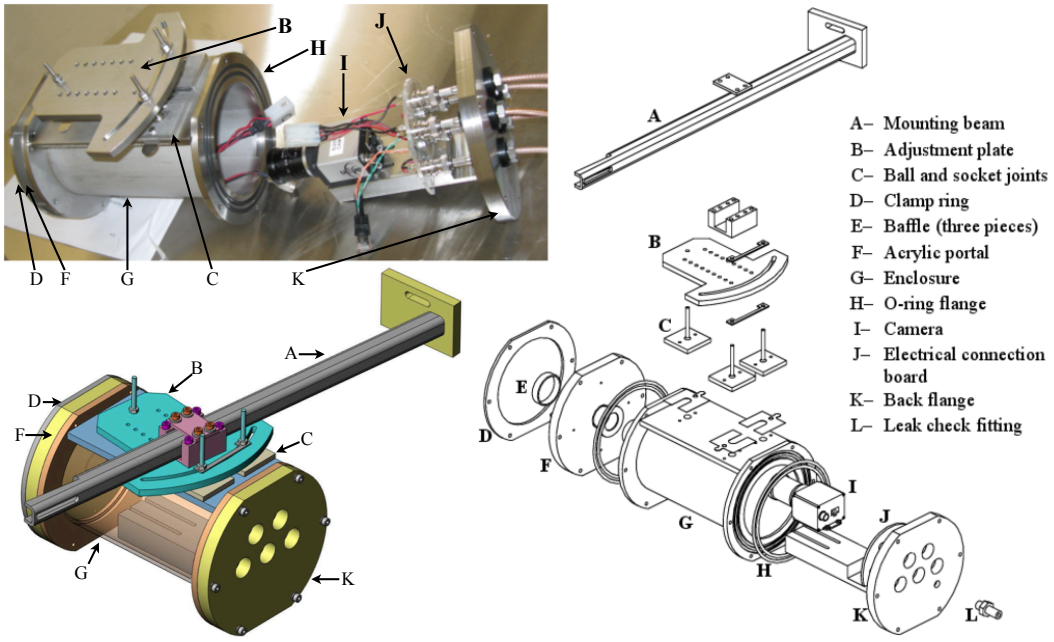


Figure 5.9 Right: Assembly of camera components. Top Left: A camera during assembly. The front portal and LEDs have been attached; the cables have been connected, passed through the back flange and secured; the adjustor plate has been connected and positioned and the camera awaits connection with internal electrical components, followed by vessels closure. Bottom Left: Rendered model showing the camera enclosure assembled and adjusted, as though installed in a detector [53].

opaque light baffles described in Section 5.2.2 sit tightly in opposing grooves cut 3/8” deep and 1/16” wide.

The camera itself is positioned against the portal along a rod that attaches to the back flange. The rod offers adjustability of the camera position and effectively dissipates heat into the mineral oil buffer and PMT ladder. The back flange attaches to the enclosure like the portal, and passes five coaxial cables that conduct electrical power and data to and from the camera and LEDs, as discussed in Section 5.2.4.

The cables are sealed by a feed-through plug that is identical to that used for the PMTs. Each cable is produced with captured seal plugs on both ends. Within each seal plug, a hollow bolt compresses two o-rings against the cable and inner seal plug. Two more o-rings compress against the seal plug and matching hole in the flange when the plugs are pushed into place and captured by a retaining ring. Overall, the enclosure contains the camera, LEDs and electronics in a leak-tight volume.

The enclosure attaches to the PMT ladder by way of an adjustable mount that allows several degrees of freedom. The mount and enclosure are connected by three ball and socket joints formed from round indentations on a flat plate welded onto the enclosure. Three threaded rod-ball bearing assemblies sit in these indentations, held by three smaller capture plates and shims, with the threaded rods extending through an adjustor plate. The capture plates and shims hold the threaded rods fast, but allow slight movement of the joints to prevent tension. The adjustor plate has one clearance hole serving as a pivot point, and one continuous arc. The arc permits the camera to pan, while nuts on the threaded rods allow independent pitch and height adjustment. Once the position is set, pairs of nuts lock the configuration into place.

The cameras are installed on adjacent ladders in voids between rows of PMTs, one just below the top row, the other above the second row from the bottom. These positions are indicated in the detector diagrams of Figures 5.3 and 5.4. The positions and orientations of the cameras are chosen to maximize the usefulness of the view. The top camera is pitched upward 6° and panned 7° counterclockwise relative to a vertical downward axis, to visualize

the most critical features, such as the bellows and liquid levels at the tops of the acrylic vessels. The bottom camera is pitched downward to view more low lying features of the detector such as the bottom reflector and acrylic vessel connections. The cameras are shown at various stages of installation in Figure 5.10.

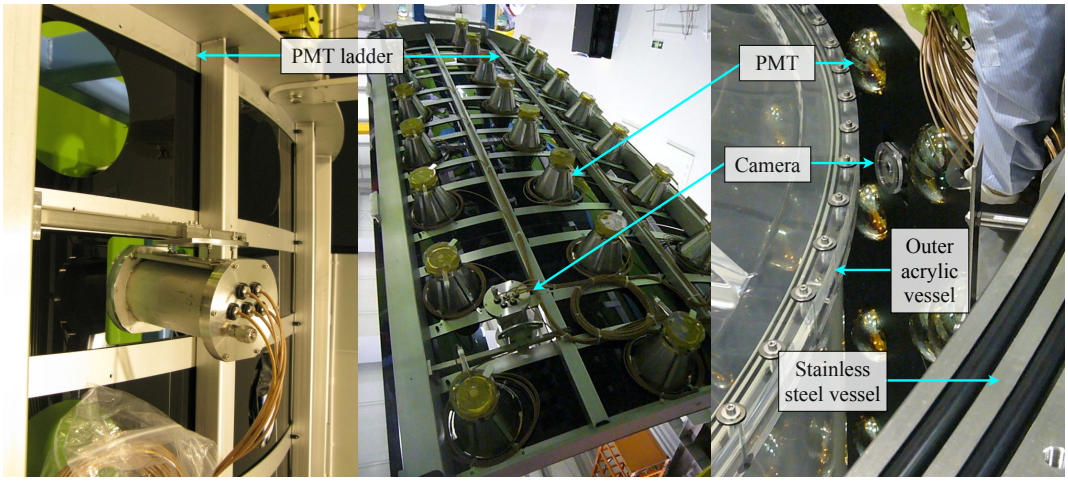


Figure 5.10 Left: Back view of top camera newly installed on a PMT ladder, awaiting installation of PMTs. Center: Back view of top camera installed at the top of a PMT ladder loaded with PMTs, awaiting installation into a detector. Right: Front view of top camera installed in a detector. Key detector features are labeled.

5.2.4 System Readout and Control

The control system is designed amid constraints imposed by the detectors and other electronics, particularly regarding materials compatibility, leak-tightness, electronic noise and inaccessibility. The camera requires an Ethernet data connection and direct current power, while the LEDs also require direct current power. Typical cables for power and Ethernet are barred from the detectors due to materials compatibility, so the system uses BNC coaxial cables identical to those of the PMTs for these purposes. These cables are Teflon coated and form leak-tight seals with the existing Daya Bay seal plugs. Many non-coaxial cables, especially Ethernet, lack the uniform surface required for this seal to be leak-tight.

Signals sent to and from the camera are converted between Ethernet and coaxial cables by way of balun transformers. The baluns have a 2:1 impedance ratio to match the 50 Ω coaxial cable to the 100 Ω Ethernet. Inside the enclosure two baluns convert two Ethernet twisted pairs to two coaxial cables, while another pair inside the readout box reverses the conversion (Figure 5.11). A balun creates an unbalanced signal from the balanced, positive and negative pulses along the Ethernet. While the unbalanced signal is inherently more susceptible to noise, the coaxial cable is sufficiently shielded. The camera itself possesses great noise filtering, so additional capacitive high-pass filters on the Ethernet line are unnecessary. The bandwidth is reduced from the 1 Gbps maximum of the camera to 100 Mbps, but this is more than sufficient to operate the camera within demands. Since the subjects of the camera are very slow processes or stationary objects, and since the camera operates in a low light environment, the frame rate is set as low as permitted– 0.29 fps– and the bandwidth used is far lower than 100 Mbps.

In total there are five coaxial cables: three conducting power to the camera, white and infrared LEDs, and two transmitting data to and from the camera. Alternatives for fewer cables were considered and rejected for fear of superfluous components inside the detector, which increase the risk of radioactive backgrounds, heat production, and inaccessible component failures.

In addition to converting the signal to Ethernet, the readout system contains an Ethernet-controlled relay bank and power supplies managing a total of four cameras. DC power to all cameras and LEDs passes through the 16-switch relay bank, model *NER165PROXR* [163] from National Control Devices, which selects one camera and one light source to operate. The power supply for the LEDs is a single programmable Sorenson *XEL 60-1.5P* [164], and the power source for the cameras and relay bank are AC:DC converters provided by the manufacturers. The readout box also contains an array of fuses and indicator lights for safety. The relay bank and power supply were chosen for their Ethernet connectivity, programmability, and ease of integration into the control software.

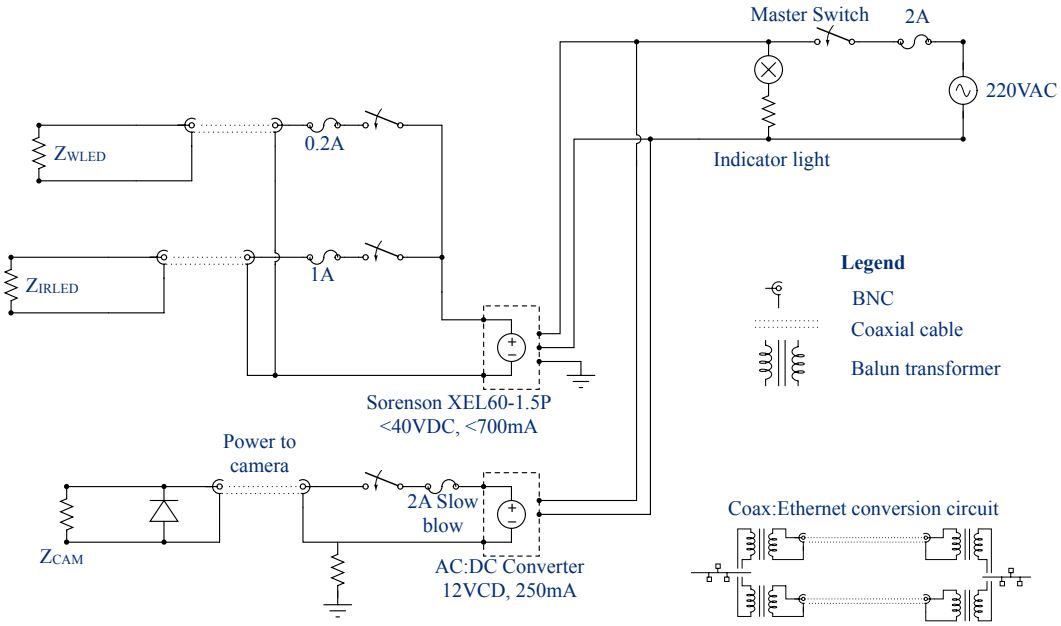


Figure 5.11 Schematic of the readout system. The center and top left of the diagram describes the readout system in the electronics rack outside the detector. To the left, separated by a double dotted line (coaxial cable) are the loads: the camera and LEDs inside the detector. To the bottom right is an Ethernet to coaxial cable conversion circuit using balun transformers. This simplified schematic depicts one camera control; each readout box controls four cameras in parallel. An Ethernet-controlled relay selects one camera and light source to power at a time.

The operating software plays an important role in both running the cameras and protecting the detector and camera system. The LabView-based [165] interface operates the system by controlling the relay card, power supply and camera over the network. The power supply and relay are represented in software as Virtual Instrument Software Architecture (VISA) resources. Custom LabView code was written for the camera system using drivers provided by the devices' manufacturers, which allows real-time operation. The code is integrated into the experiment's comprehensive control framework, *Detector Control System* [166].

The user is permitted to operate one of four cameras in a pair of detectors at a time, within the built-in safety constraints. The system is configured to preclude the operation of the wrong camera, and will not summon power to LEDs outside acceptable voltage and current ranges. Meanwhile, if the PMT high voltage is active, the LEDs are interlocked. Also, since the infrared LEDs generate 16 W of power pressed against the poorly dissipating acrylic surface, the user is time-limited in their usage. Otherwise, the user has control over LED brightness and camera gain, and can select one camera out of four connected with either type of LED at either position in the same detector. Only one LED strand is permitted power at a time to prevent too large a current through the system. For best results, when the detector is dry, the user relies on the LEDs from the opposite camera position, taking advantage of the light scattering about the acrylic and reflectors. After filling, the user should illuminate the LEDs of the same camera. The user can capture images manually or automatically at a selected rate, and the images are immediately uploaded to a central database.

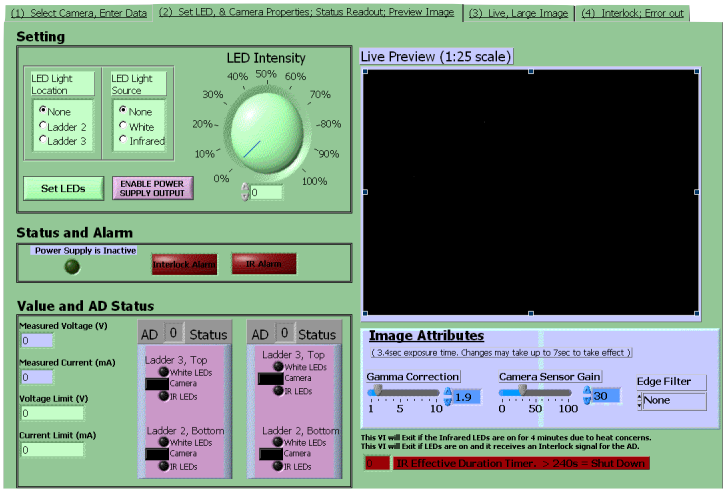


Figure 5.12 One panel of the control software. The user can operate the LED light source in the upper left, readout power supply and relay bank statuses in the lower left, adjust camera settings in the lower right, and check a preview of the image in the upper right. Functions not shown include: device connection, network monitors, image saving, image autosaving, image commenting, interlocks and some alarms.

5.3 Background Levels

The radioactivity of one complete camera assembly was measured, and the activity from most isotopes is consistent with zero (Table 5.1, Figure 5.13). Those isotopes with nonzero activity are members of the ^{232}Th decay chain, primarily ^{228}Ac. In total, one camera assembly has a similar level of activity to one Hamamatsu *R5912* PMT, and the largest sources of activity are presumed to be the glass in the lens and circuit board, and the aluminum comprising the camera case [10, 167].

Chain	Nuclide	Line (keV)	Camera Activity (Bq)	PMT Activity (Bq)
	^{40}K		0.66 ± 2.05	3.9
^{232}Th	^{228}Ac	911.07	2.5 ± 0.77	
		968.97	0.737 ± 1.13	
	^{212}Pb	238.63	0.825 ± 0.43	
	^{208}Tl	583.14	0.0957 ± 0.216	
		2614.47	0.408 ± 0.315	
	Total		0.912 ± 0.57	0.6
^{238}U	^{214}Bi	608.81	< 0.45	
		1764.24	< 1.37	
	^{214}Pb	294.83	< 0.82	
		352.59	< 0.52	
	Total		< 0.79	1.9

Table 5.1 Total radioactivity level of one camera assembly. The activity of an assembly is dominated by ^{232}Th-chain decays, and the total activity is lower than a typical PMT [10].

5.4 Performance

The cameras have proven very useful and reliable, providing an average of 2,000 images per detector. Most of these images were taken during the filling process, followed by monitoring of detector transportation. Figures 5.14 and 5.15 show annotated photographs taken using the bottom camera and white light from the top camera, during an automated

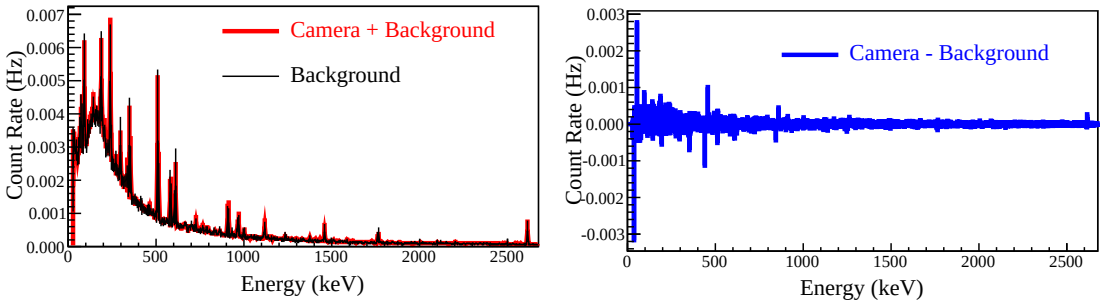


Figure 5.13 Left: Gamma spectrum of one assembled camera [10]. Black, thin peaks denote the measurement chamber alone; thick red denotes the measurement of the camera system and chamber. Right: Difference between camera and background radiation. The camera activity is typically consistent with background. The sharp, upward and downward fluctuations in adjacent energy bins near radioactivity peaks result from a small energy calibration difference between the source and background measurements.

calibration test, and detector filling respectively. The calibration source and liquid levels appear very clearly. Figure 5.16 shows a photograph taken from the top camera in a dry detector with white light from the bottom camera, while Figure 5.17 shows a photograph taken after filling, using white light from the same camera. As an example of infrared light photography, Figure 5.18 displays a photograph of the inside of a dry detector taken with the bottom camera under infrared light from the opposite camera. Finally, Figure 5.19 shows an image of a manual calibration mechanical test in a partially assembled detector, taken under with the bottom camera white light from the top camera.

5.5 Summary

Two cameras in each detector provide visual coverage of most of the features atop the acrylic vessels such as calibration bellows and ports, almost full coverage vertically, and a sample of PMTs and acrylic vessel bases. The cameras are installed alongside the PMTs, are leak tight, offer 1 mm resolution across the detector and provide their own light source.

The cameras were vital to the construction of Daya Bay's detectors. The camera system enabled the detector filling to proceed safely, troubleshot the automated and manual calibrations, and was incorporated into manual calibration procedures. The cameras recorded

over 10,000 images without interfering with the data taking either electronically or by the introduction of radioactive materials.

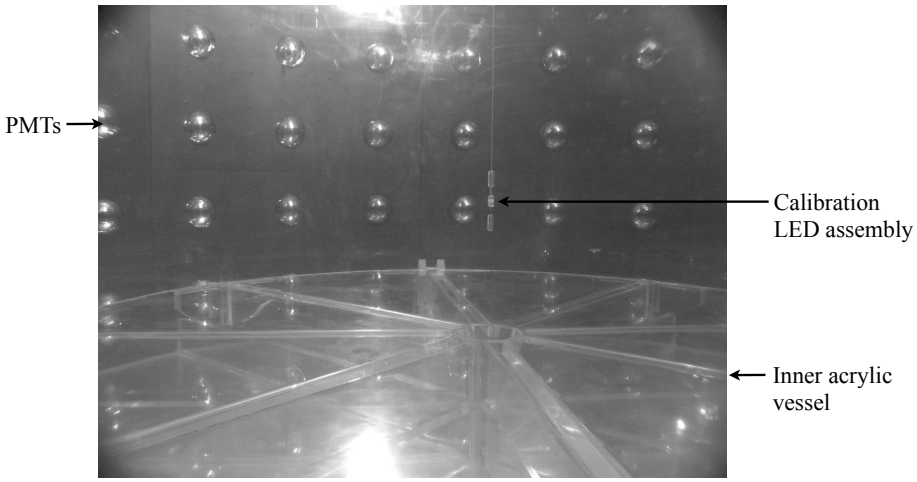


Figure 5.14 Photograph of the deployment of a calibration LED photographed by the bottom camera. The detector has not been filled yet. The light source is the white LEDs of the top camera.

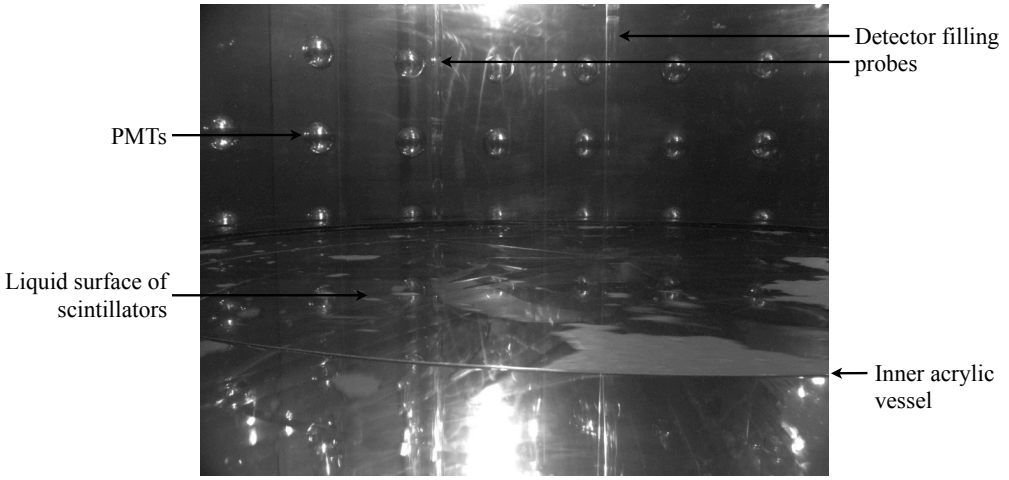


Figure 5.15 Photograph from the bottom camera during filling. Gadolinium-doped liquid scintillator is visible in the center of the detector, while undoped scintillator is visible at the bottom of the image. The boundary between them is formed by the inner acrylic vessel. The light source is the white LEDs of the top camera.

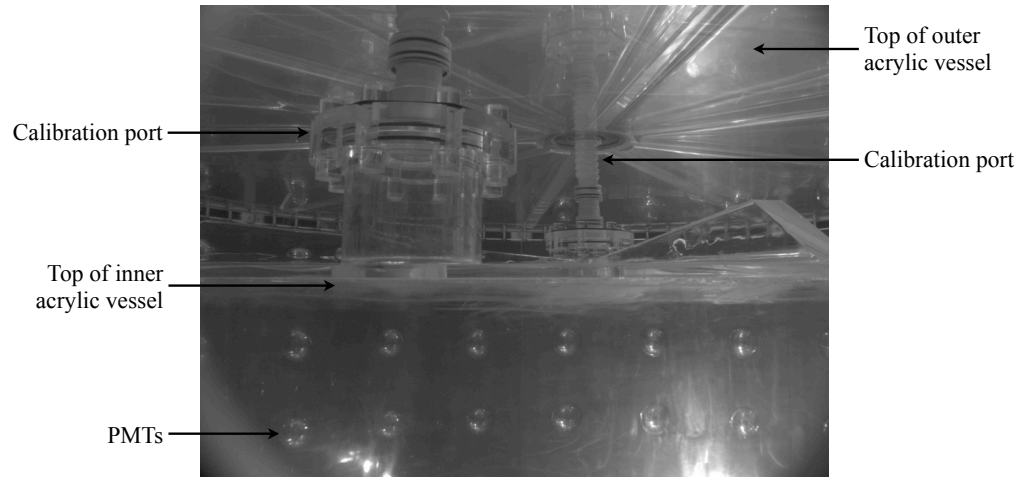


Figure 5.16 View from the top camera in a dry detector. Calibration ports and acrylic vessel lids are prominent above the midline of the image, while below, several rows of PMTs can be seen. The light source is the white LEDs of the bottom camera.

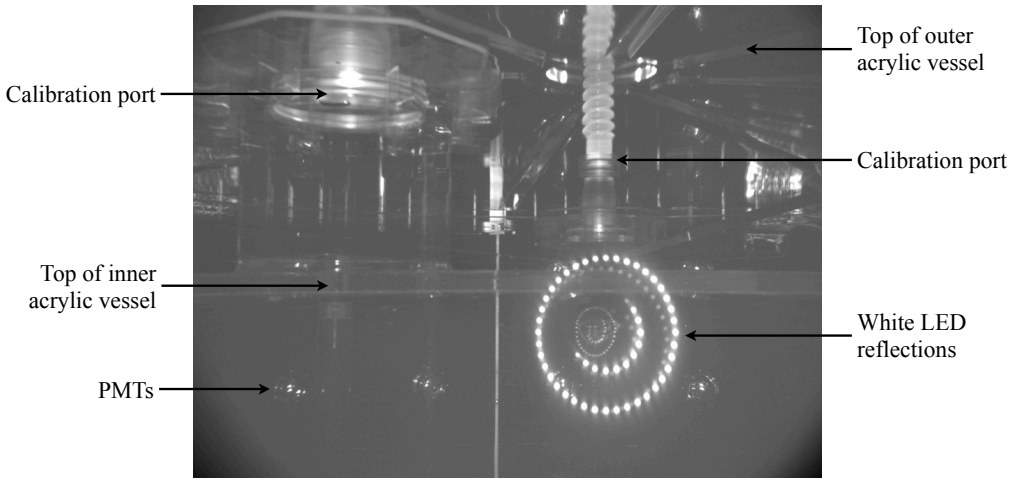


Figure 5.17 Photograph from the top camera after filling completion. The light source is the white LEDs from the same camera. The reflections of the LEDs are visible at the bottom left, where the missing LED reflections are due to the curvature of the acrylic vessels. The photograph appears magnified relative to Figure 5.16 because the scintillator and mineral oil have a higher index of refraction than air.

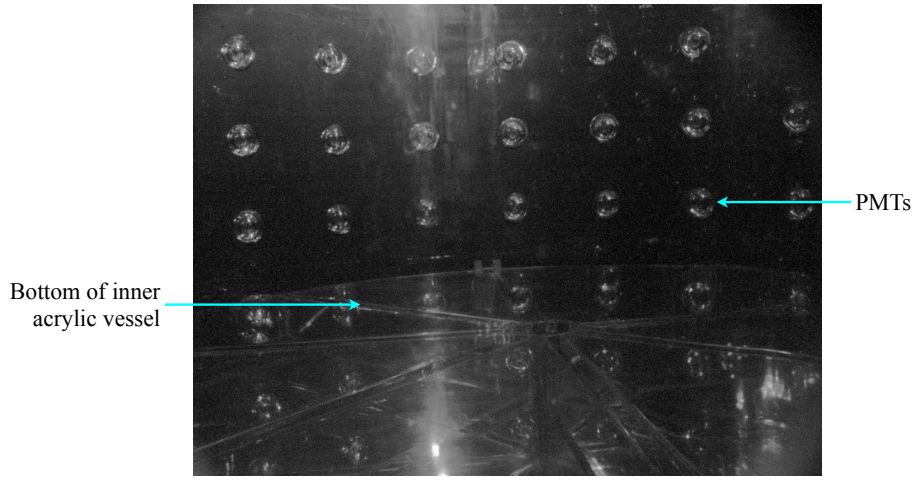


Figure 5.18 Left: A photograph taken with the bottom camera under infrared light from the top camera. The acrylic vessels and PMTs are visible in this detector waiting to be filled. The quality is lesser compared to white light, but still effective.

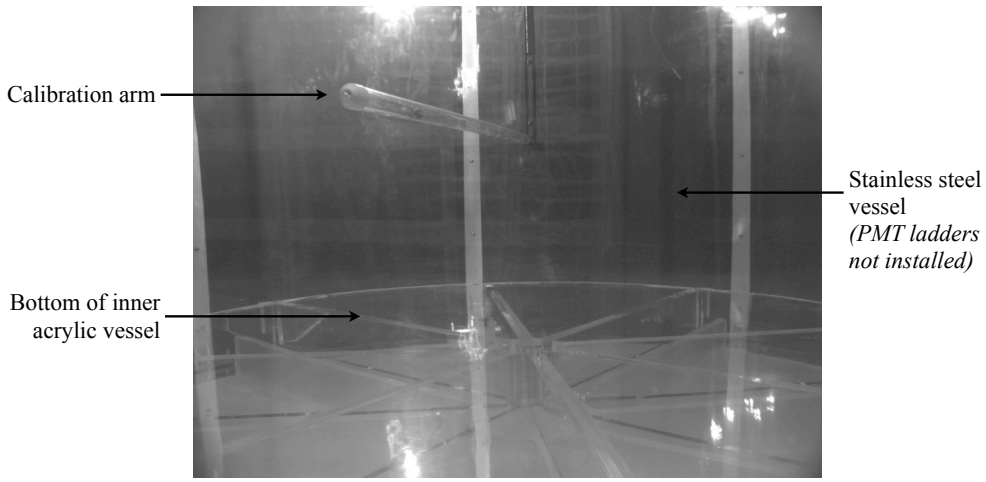


Figure 5.19 A photograph taken of the manual calibration test in a partially constructed detector, under white light from the top camera. The manual calibration arm is seen extended from the center of the detector toward the camera to the left. In the background, only the outer acrylic vessel and stainless steel vessel are present; the PMT ladders were not installed at the time of this test.

Chapter 6

Daya Bay Detector Analysis

The Daya Bay detectors report the electronic pulses and timing of PMT hits triggered by light emitted during particle interactions. These pulses are converted to deposited energy by calibration, but further effort is necessary to understand the deposited energy in terms of physical processes occurring in the detector. Inverse beta decay (IBD) events caused by antineutrinos are identified by a progression of analysis cuts that eliminate backgrounds such as those from muons or environmental radiation. The cuts are predicated on the characteristic IBD interaction in the detectors, in which the antineutrino generates a positron and a neutron, which then deposit a limited range of energy with distinct timing (positron annihilation followed by neutron capture). The cuts are developed on Monte Carlo then applied to the data with the goal to jointly optimize IBD statistics and systematic uncertainties.

The next few sections characterize the data sets, analysis cuts and resulting efficiencies and uncertainties. The analysis is a product of efforts by the whole collaboration, which I played a part in. My primary contribution was investigating the relationship of the oscillation measurements and analysis assumptions such as the systematic uncertainties or energy binning. and organizing oscillation analysis groups regarding the values we would use in our calculations. I also offered helpful discussions with others regarding the energy scale and conversion of antineutrino energy to detector visible energy, for instance. These discussions helped validate and debug analyses.

6.1 Data Sets

Over the course of data analysis from December 24, 2011 until the present, three data sets have been defined for the purpose of neutrino oscillation analyses. And, prior to the oscillation analyses, a three month data set was designated to evaluate the identicalness of the first two detectors [67]. The multiple oscillation data sets were defined to maximize communication of neutrino measurements to the physics community. Data Set 1 represented the fastest Daya Bay could offer a reliable measurement of $\sin^2 2\theta_{13}$ [131] while Data Set 2 enabled a substantial update and the opportunity to explain more details of the analysis [68]. Most recently, Data Set 3 provided for the analysis of rate and spectral data, whereas the previous analyses were rate-only [3]. Thus far, all oscillation data sets have been limited to the initial six detectors, but future data sets will include all eight detectors. These sets are summarized in Table 6.1.

While Data Set 3 is the basis of the most recent oscillation analysis, many general details of Daya Bay's antineutrino analysis such as IBD selection efficiencies and uncertainties were discussed most thoroughly in [68] using Data Set 2. As a result, all data sets are relevant to the discussion that follows.

Data Set	Start Date	End Date	$N_{det.}$	$\sin^2 2\theta_{13}$	Δm^2_{ee}	Remark
0	Sept 23, 2011	Dec 23, 2011	2	—	—	Det. 1 & 2 comparison [67]
1	Dec 24, 2011	Feb 17, 2012	6	0.092±0.017	—	Rate only [131]
2	Dec 24, 2011	May 11, 2012	6	0.089±0.011	—	Rate only [68]
3	Dec 24, 2011	July 28, 2012	6	$0.090^{+0.008}_{-0.009}$	$2.59^{+0.19}_{-0.20}$	Rate and spectrum [3]

Table 6.1 Daya Bay's data sets from the installation of the first two detectors to present. The first data set was used to assess the identicalness of the detectors; the rest were dedicated to oscillation analyses with published results indicated. The quantity Δm^2_{ee} is a linear combination of Δm^2_{31} and Δm^2_{32}, which are indistinguishable at Daya Bay because their difference is much smaller than the precision at which they can be measured.

6.2 Reconstructed Energy and Position

Detector calibration converts the PMT detected charge and timing into a relationship between deposited energy and the magnitude of the PMT signal measured in photoelectrons (see Section 4.2). However, small linear differences among detectors remain after calibration, which are referred to as the energy scale, discussed below. That the energy scale is linear is an empirical fact and due to the slightness of the differences among detectors. The energy scale contributes to the efficiencies and systematic uncertainties because many cuts on the data set are functions of energy.

The collaboration developed two algorithms to understand the energy scale and event interaction locations, AdSimple [66] and AdScaled [168]. Both operate on similar principles, but differ in that AdSimple relies on calibration and spallation neutrons, while AdScaled is based more heavily on calibrations. AdSimple is discussed in more detail in Section 6.2 because it is incorporated into the oscillation analysis of this dissertation.

The calibration system and spallation neutrons from muons both determine the energy response of the detectors— the calibration determines the approximately linear relationship between the deposited energy and PMT response to scintillation light, while the spallation neutrons improve detectors comparison. The calibration system has the advantage of being operated on demand and offers several independently determined energy levels, while the spallation neutrons are uniform over the detector volume and are nearly uniform among detectors. The uniformity of spallation neutrons throughout a detector is crucial for understanding the position-dependence of the energy reconstruction, and in turn, the identicalness of the detectors.

6.2.1 Position Reconstruction

Fiducial cuts are not necessary for Daya Bay's detectors because all antineutrino events are detected in part by neuron capture on gadolinium, which can only occur in the target

volume (the alternative neutron-hydrogen capture analysis notwithstanding). It is nevertheless important to understand the IBD event positions because this still factors into the energy reconstruction and background validation.

The timing and charge distributions of the PMT hits is a direct indicator of the location of the event. The vertex location is calculated by comparing the PMT hit timing to Monte Carlo samples produced for every position in the detector. This is more reliable than the simplest method of comparing the order in which PMTs are hit. The resolution in the position calculation in polar coordinates is 7 cm in radius r and 9 cm in height z, with no evident biases.

6.2.2 Energy Reconstruction

The energy reconstruction algorithm is more complicated, and consists of four steps:

1. Determine the total charge deposited in the detector as seen by the PMTs, in units of photoelectrons (PE).
2. Convert the total charge to a physical energy scale based on the muon-induced spallation neutron captures on gadolinium.
3. Correct the energy scale for the differences between muon and antineutrino events.
4. Correct for position within the detector.

To obtain the total charge deposited in the detector for an event, the hits to all PMTs are included. However, the fact that PMTs can be hit multiple times in an event presents an ambiguity. For a time window defined around an event, summing all the hits therein has been found to be inaccurate. Instead, two methods— selecting only the first PMT hit, or only the largest PMT hit— yield equivalent and accurate deposited energy measurements. The AdSimple algorithm selects the first hit. For each PMT hit, the pedestal, which is the baseline PMT readout in the absence of activity, is subtracted before the charge is recorded. Failed PMTs are removed from the data stream, and the total charge deposited in the

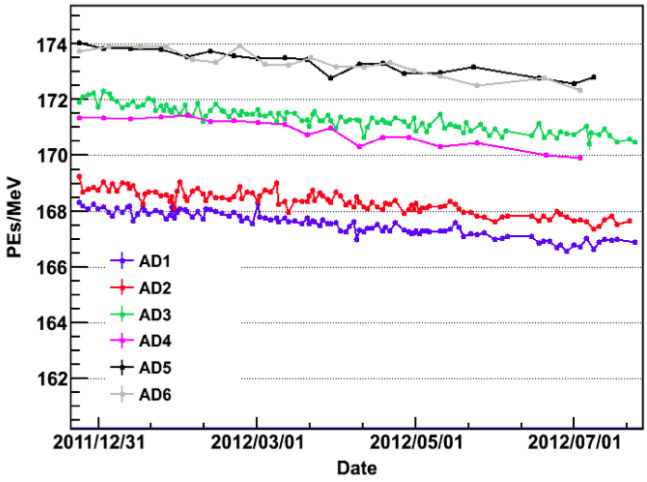


Figure 6.1 The conversion of photoelectrons per 1 MeV versus time determined by AdSimple from spallation neutrons [66]. "AD" refers to antineutrino detector.

detector for an event is scaled by the ratio $192/N$, where N is the count of functional PMTs and 192 is the total installed.

The total charge deposited in the detector must then be converted to a physical energy value, with differences among detectors accounted for. This is accomplished by relating the count of PEs to deposited energy from calibration sources and spallation neutrons. Spallation neutrons are those created by energetic muons interacting with materials surrounding the detectors. The neutrons then thermalize (lose energy via scattering) and capture on gadolinium as IBD neutrons would. Spallation neutrons have several advantages: they are abundant, they interact throughout the target volume like IBD neutrons, and interact in detectors equally. The number of PEs corresponding to the neutron capture peak is divided by the peak energy of 7.94 MeV. The typical conversion ranges from 167–174 PE/MeV depending on the detector, as seen in Figure 6.1. The conversions for detectors pairs differ by less than 1 PE/MeV, and the conversions for all detectors trend downward slowly by 2 PE/MeV/yr for unknown reasons. The time dependence and detector to detector variation (the energy scale) are corrected.

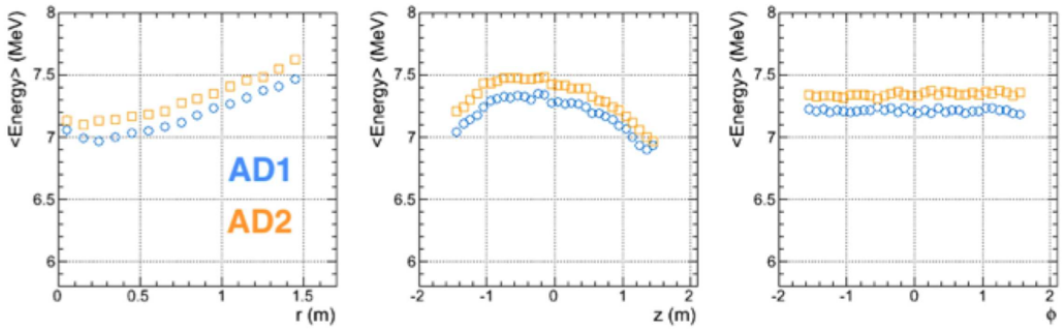


Figure 6.2 Visible energy of nGd captures in detectors 1 and 2 at the Daya Bay near site versus position in polar coordinates r, z and ϕ [66]. From the reference, "AD" means antineutrino detector.

Since the spallation neutrons follow a muon while IBD neutrons do not, and muons have a wide range of energies, a small distortion occurs in the detector response for some spallation neutron captures. The correction to the measured energy for this effect is a linear function of muon energy, at the level of 0.7–1.0%. The correction depends on near versus far site: due to the overburden, the muon spectra at the sites differ.

Finally, there is a correction required for the detector position dependence of the reconstruction. As Figure 6.2 demonstrates, the energy response varies as much as 7% as a function of r and z in polar coordinates, although not at all as a function of ϕ. Additionally, there is slight asymmetry in z, which is attributable to the differences in the acrylic structures top to bottom. At the top of the acrylic vessels are ports and Teflon bellows for the calibration sources and overflow tanks, while at the bottom the acrylic vessels are thicker for support.

6.3 Selection Cuts for Antineutrino-Induced IBD Events

Several cuts are imposed on the recorded data to distill a list of electron antineutrino candidates that is optimized for high antineutrino statistics, minimal systematic uncertainties, and few backgrounds. Not all antineutrino events can be recovered by these cuts, so

the proportion retained, the efficiency, is calculated per detector. These cuts are enumerated below, and described in more detail in the following subsections:

1. Only data from good runs are considered.
2. The prompt energy E_p must satisfy $0.7\,\mathrm{MeV} < E_p < 12\,\mathrm{MeV}$.
3. The delayed energy E_d must satisfy $6\,\mathrm{MeV} < E_d < 12\,\mathrm{MeV}$.
4. The time delay between the prompt and delayed energy deposition $\Delta T = T_d - T_p$ must satisfy $1\,\mu s < \Delta T < 200\,\mu s$.
5. The event must pass a PMT flasher veto.
6. The event must pass a muon veto.
7. The event must pass a multiplicity cut.

6.3.1 Good Run Selection

There are several data periods ascribed for analyses that were discussed in Section 6.1. The analysis of Chapter 9 utilizes Data Set 3, from December 24, 2011 – July 28, 2012, although previous data sets are discussed below to evaluate the effects of cuts.

Data sets are formed from the concatenation of a series of runs, typically lasting 48 hours and dedicated to physics analysis. Some runs are designated for calibration or other diagnostics, and these are excluded from the oscillation data set. Additionally, physics runs without all active detectors taking data, or in which an experimental problem is found, are omitted. A survey of run rejections from EH1 and EH2 from September 23, 2011 – December 24, 2011 indicates experimental disruptions such as: data acquisition system (DAQ) errors; abnormal trigger rates in the detectors, water pools or RPCs; mislabeled runs or missing data. This resulted in a rejection rate of 12% at EH1. Table 6.2 summarizes the rejections over this period. The efficiency of the data quality veto is by definition 100%, because bad data does not belong in the analysis in the first place.

Category	Run time (h)
Total calendar time	2194.3
Total DAQ up time	2092.5
Physics data taking	1905.2
Good runs	1684.2
Bad runs	221.0
Rejection reason:	
Systematic check run	126.8
Abnormal detector, water pool, flasher rate	86.6
DAQ, Electronics, high voltage errors or miscellaneous problems	7.58

Table 6.2 Summary of detector runs during the three month Data Set 0. Proportion of rejected runs and reasons are indicated [11].

6.3.2 Prompt Energy Cut

The prompt energy cut is applied to the visible energy, which is offset from the antineutrino energy by approximately 0.8 MeV:

$$E_{vis} = E_\nu - (m_n - m_p) + m_e \approx E_\nu - 0.8\,\text{MeV}. \tag{6.1}$$

The relationship between visible and antineutrino energy is explained in more detail in Section 8.1.1.1. The threshold for the IBD reaction is 1.806 MeV, below which no interaction can occur. In visible energy, the threshold is about 1 MeV, but energy loss due to detector effects described in Section 6.4 push this down to about 0.7 MeV. The antineutrino event rates at the high and low ends of the spectrum are nearly zero, so the cut

$$0.7\,\text{MeV} < E_p < 12\,\text{MeV} \tag{6.2}$$

has a high efficiency. From Monte Carlo studies the efficiency been determined to be 99.88% with an uncertainty of 0.1% correlated among detectors and 0.1% uncorrelated among detectors [169]. Figure 6.3 shows a plot of the prompt and delayed energies, where regions of IBD events and backgrounds are clearly discernible.

6.3.3 Delayed Energy Cut

The neutron released from an IBD interaction captures on gadolinium 83.8% of the time, and hydrogen the balance. The hydrogen capture (nH) releases 2.2 MeV of gamma radiation, and an analysis based on hydrogen capture is in preparation to be published [170]. However, the accidental background deposits energy in that range as well, so the analysis is more difficult and is subject to higher systematic uncertainties. The analysis of this dissertation relies only on the neutron captures on gadolinium (nGd), for which the energy released is 7.94 MeV and 8.54 MeV for the isotopes ^{157}Gd and ^{155}Gd respectively. The neutron is 4.5 times as likely to capture on ^{157}Gd than ^{155}Gd by abundance. A cut of

$$6\,\text{MeV} < E_d < 12\,\text{MeV} \tag{6.3}$$

illustrated in Figure 6.3 excludes the nH captures while yielding an nGd efficiency of 90.9%.

The uncertainty on the delayed energy cut is almost entirely from the cut at 6 MeV as there are few events at 12 MeV. Two effects contribute to the uncertainty: the shape of the nGd spectrum and the precision of measuring 6 MeV in the detector. As seen from Figure 6.4, the 6 MeV cut occurs at the tail of the nGd distribution. The tail is fit to a line to determine the efficiency of the cut, and the small uncertainty in the linearization is propagated to the cut uncertainty [171]. The precision of 6 MeV is determined by the energy scale, which is the small linear uncertainty on the conversion process of photoelectrons to visible energy described in Section 6.2.2. The detector-uncorrelated uncertainty on the delayed energy cut is 0.12%, to which both effects contribute equally. The detector-correlated uncertainty of 0.6% is determined through Monte Carlo studies [172, 173]. Overall the uncertainty is small because the event rate near 6 MeV is low.

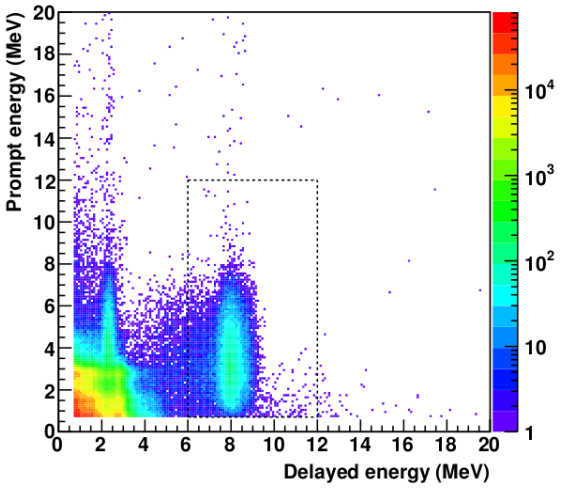


Figure 6.3 Prompt and delayed energies deposited in the two Daya Bay near detectors during Data Set 0 [67]. The boxed region indicates events passing the IBD selection cuts for nGd capture. The peak at $E_d = 2.2\,\text{MeV}$ corresponds to IBDs with nH capture. The peak of $E_d < 4\,\text{MeV}$ and $E_p < 4\,\text{MeV}$ is from accidental background.

6.3.4 Prompt-Delayed Time Cut

Background singles, the dominant background by rate, occur at approximately 70 Hz. This amounts to one single every 14 ms on average, while gadolinium and hydrogen have characteristic neutron capture times of 30 μs and 200 μs respectively. Since the characteristic capture time of gadolinium is much shorter than hydrogen, and the cross-section larger, most neutrons capture on gadolinium. Those neutrons that do capture on hydrogen capture on the same time frame as the gadolinium captures because few neutrons are still free within 200 μs.

The prompt-delayed timing cut of

$$1\,\mu s < \Delta T < 200\,\mu s \tag{6.4}$$

thus reduces backgrounds greatly, but does not eliminate many nGd or nH captures. The nH capture is removed by the delayed energy cut. The upper limit of 200 μs is based on a distribution of neutron capture times such as the one shown in Figure 6.4. Figure 6.4 exhibits a clear trend in which the capture times are elevated for $\Delta T < 200\,\mu s$, but return to a flat baseline afterward. The lower limit of the cut is imposed to prevent possible ambiguity in

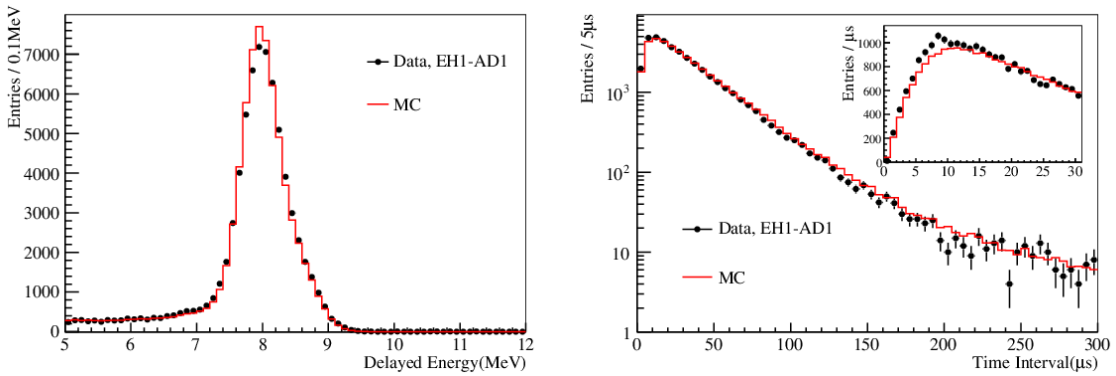


Figure 6.4 The delayed energy E_d (left) and neutron capture time ΔT (right) in detector 1 over Data Set 2 [68]. The peak at 8 μs corresponds to the neutron thermalization time.

the electronics trigger window. It is not influenced by the neutron thermalization timescale, which is about 8 μs.

The efficiency of the timing cut is 98.6%, dominated by the $\Delta T < 200\,\mu s$ upper limit. The uncertainty is 0.01% detector-uncorrelated and 0.12% detector-correlated. The efficiency and uncertainties are determined from simulation [174].

6.3.5 PMT Flasher Cut

PMT flashing is a phenomenon in which the PMTs emit light through a spontaneous electric discharge in the PMT dynode. About 5% of PMTs have flashed, and the perceived energies of flashes range as high as 100 MeV. Flashers occur within the neutron capture energy cut of 6–12 MeV at a rate of 0.7 Hz; when such flashers occur, they can combine with singles in the time window to mimic an IBD.

Flashing PMTs have unique characteristics that allow for effective vetoing [175, 69]. As seen from Figure 6.5, flashers deposit a large fraction of their charge in a single PMT, and another outsized fraction in the PMTs directly across. Based on these characteristics two variables, Q_{max} and Q_{quad}, are defined to discriminate against flashers. Q_{max} is the largest fraction of charge deposited in a single PMT. For Q_{quad}, the PMTs are divided into four quadrants circumferentially, where a quadrant is defined as six consecutive columns of eight

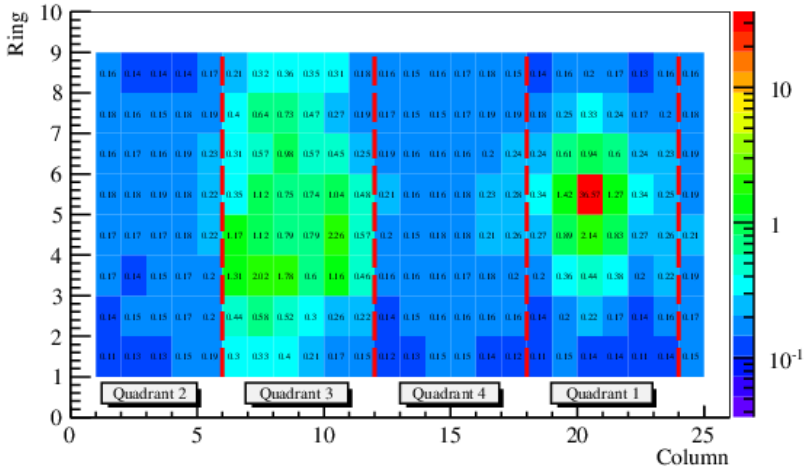


Figure 6.5 Deposition of energy from a flashing PMT. The high fraction of energy deposited in one PMT, and the disproportionate deposition of energy in the columns of PMTs adjacent to and facing the flasher, are distinct characteristics of PMT flashers [69].

PMTs (there are 24 columns total). The ratio Q_{quad} is defined as

$$Q_{quad} \equiv Q_3/(Q_2 + Q_4)\,, \tag{6.5}$$

where Q_1 is the quadrant with the largest charge deposition, Q_3 is the quadrant directly across, and $Q_{2,4}$ are the adjacent quadrants. The variables Q_{max} and Q_{quad} are combined into a variable FID:

$$FID \equiv \log_{10}[(Q_{max}/0.45)^2 + (Q_{quad})^2]\,. \tag{6.6}$$

The discriminant FID is defined in such a way that values of $FID < 0$ for an event indicate the event is IBD, while $FID > 0$ indicates a flasher. The distribution for Data Set 1 is shown in Figure 6.6.

The efficiency of the flasher cut is close to 100% because the vast majority of vetoed events are not IBDs. Potential IBD events that were vetoed by the cut were on the boundary ($FID \sim 0$) and reduce the efficiency to 99.98%. Contamination from flashers passing the cut was negligible because the small quantity of flashers passing the cut fail the coincidence

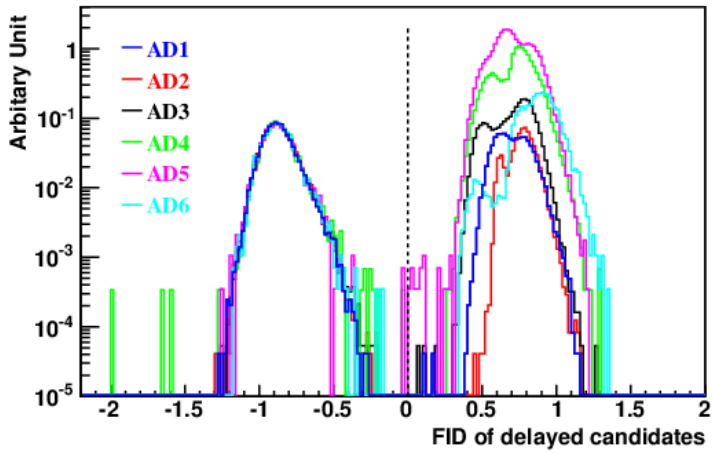


Figure 6.6 Flasher discriminant variable FID from Data Set 1. Values of $FID > 0$ indicate a flasher [69].

cut for lacking both prompt and delayed deposited energy. The uncertainty on the cut is 0.01%, for both the correlated and uncorrelated components.

6.3.6 Muon Rejection

The period of time after a muon passes through the detector or water pool exhibits an increased chance of background events due to muon interactions. Muons free neutrons as spallation products, release energy via recoils or Cherenkov radiation, and create long-lived unstable isotopes such as those described in Section 6.5. As a result, a period of time must be vetoed after each muon depending its kinematics.

Three types of muons are defined based on trajectory and energy: detector muons, water pool muons and showering muons:

- Detector muon— Passes through the detector depositing at least 3000 PE of light (∼18 MeV)
- Water pool muon— Passes through the water pool and triggers 12 PMTs in either the IWS or OWS

- Showering muon— Passes through the detector depositing at least 300000 PE of light ($\sim$1.8 GeV)

To reduce the muon-induced backgrounds, the following vetoes are imposed:

- All events 600 μs after a water pool muon
- All events 1400 μs after a detector muon
- All events 0.4 s after a showering muon
- All events 2 μs before any muon

More energetic showering muons are treated more carefully because they introduce more and longer-lived backgrounds. The veto of events 2 μs before the muon is imposed due to possible non-synchronicity among the detectors and water pools.

The efficiency of the muon cuts depend on muon rates primarily, and muon spectra secondarily, which differ among the underground sites. Per Table 6.5, the efficiencies range from approximately 82–98% and are almost identical for all detectors at a site.

6.3.7 Multiplicity Cut

The multiplicity cut ensures that prompt-delayed pairs are unambiguous. The designations of prompt and delayed are relative, and if a third deposition of energy occurs, then the true IBD pair is unknown. By necessity, the multiplicity cut is implemented last in the progression to exclude consideration of non-IBD events, and thus preserve as many true IBD events as possible. Every candidate prompt-delayed pair is subject to the following requirements:

- Only one possible prompt event can occur 200 μs before a delayed candidate.
- There can be no other prompt candidate (to a different delayed candidate) 400 μs before the given delayed candidate.
- No other delayed candidate can occur within 200 μs of the given delayed candidate.

The efficiency of this cut is high since background events occur on the order of 0.01 Hz per detector, and antineutrino events on the order of one per minute or less. The efficiency is 97.4% averaged over the detectors as shown in Table 6.5.

6.4 Corrections for Detector Effects

Two geometry-based detector effects further influence the implementation of the analysis cuts and contribute to the efficiencies and uncertainties. These are referred to as spill in or spill out, and the IAV correction (inner acrylic vessel).

The spill-in and spill-out effects concern the boundary between the target gadolinium liquid scintillator (GdLS) and the surrounding liquid scintillator (LS) volumes. A small fraction of detected IBD events will occur in the LS region in which the neutron wanders in to the target volume and captures on gadolinium. This is the spill-in effect, and such events are indistinguishable from events confined in the target volume. The converse is spill-out, in which an IBD reaction occurs in the target volume, but the neutron wanders into the LS, where it cannot capture on gadolinium. Since the spill-out events cannot capture on gadolinium, this reduces the nGd capture fraction efficiency discussed earlier [174].

Another geometric effect is the IAV correction, which is necessary because the inner acrylic vessel absorbs deposited energy, but does not scintillate [176, 177]. If a positron annihilation or neutron capture occurs within 6 cm of acrylic, some of the deposited energy may be lost. The distortion applies to few events and affects high and low energy photons differently. High energy photons will pass through the IAV more easily and deposit ~ 2 MeV of energy into it. Low energy photons incident on the IAV will lose a larger fraction of their energy, potentially as much as half since the annihilation photons are emitted back to back.

The effect on the prompt signal is a small downward shift in the antineutrino spectra. This is the reason that the lower bound on the prompt energy is $E_p > 0.7$ MeV rather than $E_p > 1$ MeV. The IAV effect contributes to a tail in the nGd capture spectrum, causing some otherwise good events to fail the $E_d > 6$ MeV delayed energy cut. The impact of

the IAV on the efficiency of the nGd capture is factored in to the calculation discussed in Section 6.3.3, while the uncertainty in the prompt spectrum is discussed in Section 8.1.1

6.5 Backgrounds

Backgrounds are non-antineutrino events that pass all the IBD selection cuts. In each case their rate and spectra can be measured or calculated, then subtracted from the antineutrino events with an uncertainty. The sources of background contamination are muon-induced particles or radioactive detector materials. Background rates and rate uncertainties are listed in Table 6.3, and are described in more detail in the rest of this section.

6.5.1 Accidental Background

Materials in the detector, especially ^{40}K, ^{208}Tl, ^{60}Co and ^{210}Po, generate radioactive backgrounds that are recorded as single events at 64–71 Hz the energy range of $0.7\,\text{MeV} < E < 12\,\text{MeV}$ [178]. If two singles coincide within the $200\,\mu s$ timing cut window, and pass the cuts on prompt and delayed energy, the event can mimic an IBD and is referred to as an accidental background.

The rate, spectrum and rate uncertainty of the accidental background are computed from the rate and spectrum of singles, using statistics to determine the probability of coincidence of two singles that pass the energy and timing cuts [179]. The accidentals occur at a rate of about nine per day at the near detectors and three per day at the far detectors, with detailed rates listed in Table 6.3. The accidentals have the spectra shown in Figure 6.4: besides the nGd captures with delayed energy 8 MeV and the nH capture with delayed energy 2.2 MeV, nearly every other event is an accidental background.

6.5.2 Muon-Induced ^{9}Li and ^{8}He Background

Muons passing through the scintillator volumes of the detector, especially those of GeV-order energy, can break up a carbon nucleus to produce ^{9}Li and ^{8}He nuclei. Both ^{9}Li and ^{8}He decay by the emission of an electron and a neutron with total energies (Q) and half-lives

($\tau_{1/2}$) of:

$$^{9}\text{Li}: \quad \tau_{1/2} = 178\,\text{ms}, \quad Q = 13.6\,\text{MeV} \tag{6.7}$$

$$^{8}\text{He}: \quad \tau_{1/2} = 119\,\text{ms}, \quad Q = 10.6\,\text{MeV}. \tag{6.8}$$

These decays mimic the IBD signal because the neutron capture creates a delayed signal while the recoil of the electron provides a prompt signal. The half-lives of ^{9}Li and ^{8}He are much longer than the muon veto time, but extending the veto time to exclude these nuclei would reduce the efficiency to unacceptable levels.

The combined rate of ^{9}Li and ^{8}He, which are not separable in data, are calculated from muon timing to be 0.22 per day at the far site and approximately two per day at the near sites [68, 180]. See Table 6.3. Figure 6.7 shows energy deposition in coincidence with muons of energy $E_\mu > 4.5\,\text{GeV}$. Most events are uncorrelated with the muon, showing a flat distribution for times $t > 1\,\text{s}$. But, for $t < 1\,\text{s}$, there is an exponential decay that indicates the production of ^{9}Li and ^{8}He. The rate of events in this peak minus the flat rate provides the rate of ^{9}Li and ^{8}He.

There are too few ^{9}Li and ^{8}He background events in Data Set 3 to precisely measure their spectra. Instead, the spectra are estimated from theory [70]. Figure 6.8 [70] shows the ^{9}Li and ^{8}He spectra predicted from kinematics, Fermi theory of beta decay, known branching ratios and widths of intermediate states. In the data analysis, these spectra are assumed and scaled according to the ^{9}Li/^{8}He rate.

6.5.3 Fast Neutrons Background

The fast neutron background is produced by muons passing through the rock surrounding the water pool. These muons do not pass through the water, hence do not get tagged and vetoed. They can, however, impact nuclei to produce high energy neutrons which then

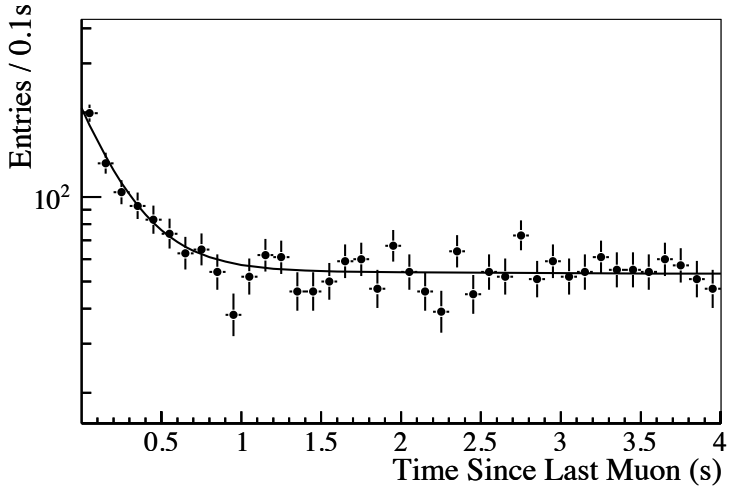


Figure 6.7 Energy deposits for a given time after muon for a subset of Data Set 2. The peak below 1 s corresponds to decays of muon-induced ^{9}Li and ^{8}He, which decay with a half-life of about 0.1 s [68].

scatter into the detector. Such a neutron will lose energy via collisions with other particles and may subsequently be captured on gadolinium. If the fast neutron collides with a proton in the detector before capture, the recoil energy may generate a prompt signal while the nGd capture will provide the delayed energy.

As shown in Figure 6.9, the neutron energies range as high as over 100 MeV and their spectrum is nearly flat between 12 and 100 MeV [68]. Thus, the rate of fast neutrons is calculated by observing the number of IBD-like events at energies from 12–100 MeV, and extrapolating that rate below 12 MeV linearly. The resulting fast neutron background rates are less than one per day at the near and 0.04 per day at the far site. The uncertainty on the rates are calculated from the fit parameters. Further rate details are indicated in Table 6.3.

6.5.4 Americium Carbon and Carbon Alpha Backgrounds

One of the calibration sources that sits atop the detector is AmC, described in Section 4.2.1. The americium emits an alpha particle that captures on the carbon. This creates

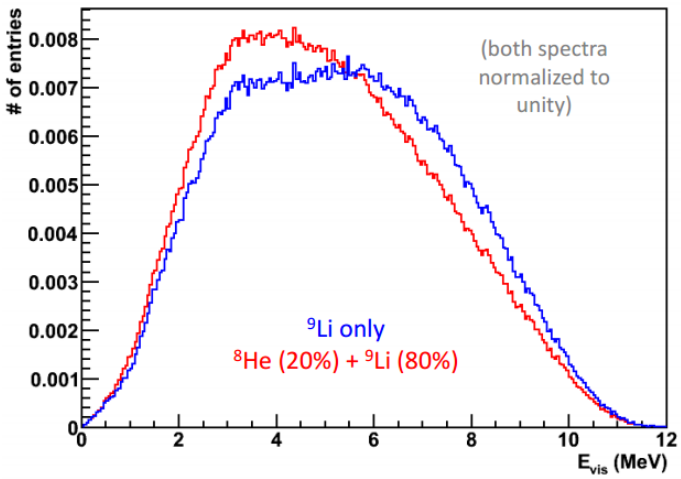


Figure 6.8 The spectra of ^{9}Li and ^{8}He background predicted from theory [70]. The expected ratio of lithium to helium among the background events is 4:1.

an oxygen and emits a free neutron:

$$\alpha + {}^{13}\mathrm{C} \;\rightarrow\; {}^{16}\mathrm{O} + n\,. \tag{6.9}$$

The neutron can scatter off of materials in the source shielding and capture on a nucleus, releasing gamma rays multiple times. If multiple gamma rays are emitted in this manner and reach the scintillator, the result may mimic an IBD signal. Since the calibration sources are on top of the detector, the rate of this background is determined from the top-bottom asymmetry to be 0.2 events per day per detector [68]. The uncertainty was determined by Monte Carlo studies to be 50% of this rate correlated at all sites. The uncorrelated AmC uncertainty is much smaller and absorbed into the accidentals.

The carbon alpha background is generated in a similar manner as the AmC background, except that the α particles emanate from ^{238}U, ^{232}Th, ^{227}Ac and ^{210}Po in detector materials. The neutron recoil tends to deposit 3 MeV or less in the detectors while the neutron capture tends to release 2 MeV or lower. The carbon alpha background rate is determined from observation of α decay in the detector plus Monte Carlo studies to determine the neutron yield and spectra based on all possible decay chains. The daily rate was determined to be 0.04–0.08 at the far site and near sites respectively. The uncertainty on this rate was

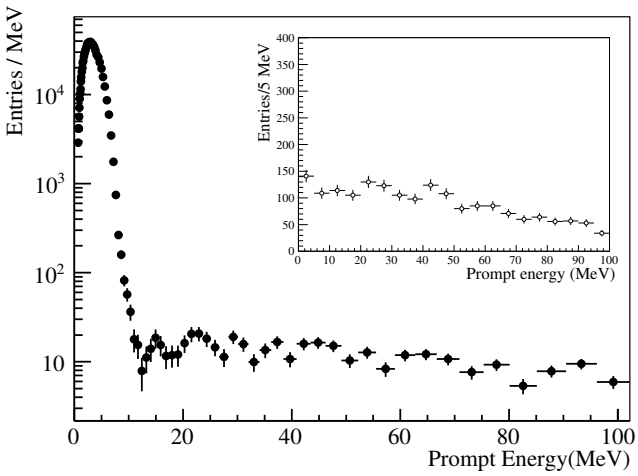


Figure 6.9 Events passing all IBD selection cuts except $E_p < 12\,\text{MeV}$ [68]. The $E_p > 12\,\text{MeV}$ events are ascribed to the fast neutrons. The fast neutron background rate in the IBD energy window is deduced from extrapolating the rate of fast neutrons above 12 MeV. The inset shows the subset of fast neutron-like events following a muon tagged by the veto as a cross-check.

estimated to be 50% based on contributions from Monte Carlo uncertainties and scintillator purification processes [68].

6.6 Summary

A series of analysis cuts are imposed on the Daya Bay data to extract a collection of antineutrino events that is optimized for high statistics but low uncertainties and backgrounds. The cuts take advantage of the unique pattern of two depositions of energy, and the timing between them, caused when an antineutrino interacts in the target volume of a detector.

Almost every analysis cut imposes upon the data set an efficiency and a contribution to the systematic uncertainties. The candidate antineutrino-induced IBD event rates, and background rates and uncertainties, are listed in Table 6.3. Tables 6.4 and 6.5 summarize the efficiencies and uncertainties of the analysis cuts.

	Detector 1	Detector 2	Detector 3	Detector 4	Detector 5	Detector 6
IBD candidates	101290	102519	92912	13964	13894	13731
DAQ live-time (days)	191.001		189.645		189.779	
Accidentals (per day)	9.54±0.03	9.36±0.03	7.44±0.02	2.96±0.01	2.92±0.01	2.87±0.01
Fast-neutron (per day)	0.92±0.46		0.62±0.31		0.04±0.02	
^{9}Li/^{8}He (per day)	2.40±0.86		1.2±0.63		0.22±0.06	
Am-C correlated (per day)	0.26±0.12					
Carbon α (per day)	0.08±0.04	0.07±0.04	0.05±0.03	0.04±0.02	0.04±0.02	0.04±0.02
IBD rate (per day)	653.30±2.31	664.15±2.33	581.97±2.07	73.31±0.66	73.03±0.66	72.20±0.66

Table 6.3 Rates of antineutrino candidate IBD events and various backgrounds and uncertainties for Data Set 3 [3].

Cut	Efficiency	Correlated	Uncorrelated
Target protons	—	0.47%	0.03%
Live-time	—	0.002%	<0.01%
Delayed energy cut	90.9%	0.6%	0.12%
Prompt energy cut	99.88%	0.10%	0.01%
Multiplicity cut	—	0.02%	<0.01%
Capture time cut	98.6%	0.12%	0.01%
Gd capture fraction	83.8%	0.8%	<0.1%
Flasher cut	99.98%	0.01%	0.01%
Spill-in	105.0%	1.5%	0.02%
Spill-out	98.6%	—	—
Combined	78.8%*	1.9%	0.2%

Table 6.4 Summary of detector-independent absolute efficiencies, and correlated and uncorrelated systematic uncertainties for Data Set 3 [3]. *The total efficiency listed does not include the detector-dependent components from the muon and multiplicity cuts that are shown in Table 6.5.

Cut	Efficiency						Data Set
	Detector 1	Detector 2	Detector 3	Detector 4	Detector 5	Detector 6	
Muon	0.8231	0.8198	0.8576	0.9813	0.9813	0.9810	2 [68]
Multiplicity	0.9738	0.9742	0.9753	0.9737	0.9734	0.9732	2 [68]
Combined	0.7957	0.7927	0.8282	0.9577	0.9568	0.9566	3 [3]

Table 6.5 Detector-dependent efficiencies for the muon and multiplicity cuts reported for Data Sets 2 and 3.

Chapter 7

Prediction and Modeling of Daya Bay Sensitivity to θ_{13}

Before the first detector was built, I developed a χ^2 model to project Daya Bay's ability to measure $\sin^2 2\theta_{13}$ over a given period of time. The goals were to understand the capability of the experiment given a range of circumstances, such as how well the experiment would perform given different systematic uncertainties or alternate detector configurations, and the quantitative dependence of the measurement precision on various analysis parameters like Δm^2_{32}, baselines and uncertainties. My investigation was helpful to the collaboration in quantifying targets for systematic uncertainties and pivotal in motivating Daya Bay to pursue a measurement of $\sin^2 2\theta_{13}$ before completing all eight detectors or finishing three years of operation.

Given a set of assumptions including uncertainties, baselines, reactor antineutrino flux and spectra for instance, the simulation calculates the sensitivity, which is defined as the lowest possible value of $\sin^2 2\theta_{13}$ that Daya Bay could exclude at 90% confidence if the actual value of $\sin^2 2\theta_{13}$ were zero. The sensitivity was chosen as the figure of merit because prior to Daya Bay's initial measurement, θ_{13} was consistent with zero. Whether θ_{13} really was nonzero— and how soon that fact could be confirmed or refuted— was critical to future particle experiments. For example, the long-baseline neutrino program must know θ_{13} to plan to measure the CP violation phase and mass hierarchy [126]. As the strength of Daya Bay was realized, the discovery limit, which is set at a higher confidence limit of 3σ or 5σ, came into favor as well. By definition, above the discovery limit, Daya Bay is expected to establish a double-sided measurement of $\sin^2 2\theta_{13}$, exclusive of $\sin^2 2\theta_{13}$=0.

The sensitivity was calculated using the General Long Baseline Experiment Simulator (GLoBES), a software package for neutrino oscillation experiments [181, 182]. GLoBES provides tools to model experiments, systematic uncertainties and neutrino oscillations quantitatively in the C programming language. Given a flux of neutrinos and a detector, it calculates an expectation value for the antineutrino rates and spectra that detector should measure, as though the experiment were run a large number of times and the median result were observed. GLoBES can then predict a measurement precision based on the statistics, systematic uncertainties and running time.

7.1 Daya Bay Experiment Modeling

The sensitivity model was devised before the first detector had been built, so it was based upon information specified in the Daya Bay Technical Design Report (TDR) [8]. The TDR provides expectations of Daya Bay's uncertainties and reactor flux.

Figure 7.1 illustrates the layout of the reactors and detectors assumed in the model. The model baselines differ from the true baselines because during civil construction the collaboration decided to install the far site 80 m closer to the reactors to avoid cracked rock discovered during excavation. The effect of this discrepancy on the sensitivity is merely a 2% loss [183]. As with the data analysis, each detector and reactor core are simplified to point objects for the purpose of calculating oscillations and reactor flux.

Each detector is assumed to contain a fiducial target mass of 20 t of gadolinium-doped liquid scintillator consisting of 99.5% linear alkylbenzene (LAB) with 0.1% gadolinium. Since the detectors are built in rapid succession from the same materials and filled with scintillator from common storage tanks, the detectors are assumed to be identical within a systematic uncertainty, after calibrations. The systematic uncertainties effect any differences among detectors in terms of efficiency or energy dependence.

The energy spectrum of reactor antineutrinos depends on the time-dependent fuel composition of the reactors as discussed in [184, 47, 185] and Chapter 3. In modeling the Daya

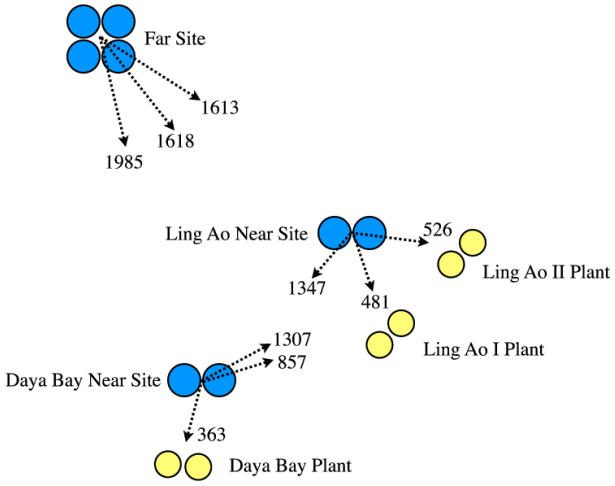


Figure 7.1 Layout of Daya Bay with eight identical detectors and six identical reactors assumed for the sensitivity model. Antineutrino propagation lengths (baselines) are indicated in meters by the arrows.

Bay experiment, the same time-averaged antineutrino flux is assumed for all reactors, parameterized according to [186], and detected via the inverse beta decay (IBD) cross-section parameterized in [144]. The reactor fuel composition is taken from the technical design report, in which 58% of fissions are from ^{235}U, 30% from ^{239}Pu, 7% from ^{238}U and 5% from ^{241}Pu, on average. Like the detectors, reactors are assumed to be identical to each other, and any differences in normalization or spectrum are applied by way of systematics uncertainties.

The oscillation probabilities are applied from a three neutrino framework with the then-best measured oscillation parameter values. At the creation of this sensitivity model, solar and long-baseline reactor experiments gave a best fit value of $\sin^2\theta_{12} = 0.304^{+0.022}_{-0.016}$, while atmospheric and long-baseline accelerator experiments measured $\sin^2\theta_{23} = 0.50^{+0.07}_{-0.06}$. As for the mass splittings, the global fit of the solar and KamLAND data indicated $\Delta m^2_{12} = 7.65^{+0.23}_{-0.20}\cdot 10^{-5}\,\mathrm{eV}^2$, while the analysis of atmospheric and accelerator experiments indicated $\Delta m^2_{23} = 2.40^{+0.21}_{-0.20}\cdot 10^{-5}\,\mathrm{eV}^2$ [72]. The best limit on $\sin^2 2\theta_{13}$ was the original CHOOZ result of $\sin^2 2\theta_{13} < 0.19$ at 90% confidence limit (CL) [47, 187]. However, global fits suggested a slightly nonzero best-fit value of $\sin^2\theta_{13} \simeq 0.02 \pm 0.01$ [188, 189].

7.1.1 IBD Event Rates and Detector Efficiencies

The GLoBES model treats the Daya Bay experiment as 6×8 experiments with inter-related systematic uncertainties. The differential IBD rate from one reactor site at one detector, without neutrino oscillations, is given by

$$\frac{dN}{dE} = \sum_{\iota} \frac{C_\iota}{E_\iota} \cdot \frac{\Phi_\iota}{4\pi L^2} P \cdot \sigma \epsilon T \,, \tag{7.1}$$

where C_ι, the fraction of fissions from the ι^{th} isotope, depends on the average fuel composition, Φ_ι is the differential flux from the ι^{th} isotope, and E_ι is corresponding energy per fission, all noted in Section 7.1. The reactor power $P = 2.9\,\text{GW}_{\text{th}}$ per core, the baselines L are given in Figure 7.1, and the efficiencies ϵ are given in Table 7.2. Finally, T, the number of target protons, is taken to be $7.31 \cdot 10^{28}$ protons/metric ton for the 20 t target region, which assumes the hydrogen in LAB (approximate chemical composition $C_{18}H_{30}$) accounts for all free protons.

The number of unoscillated IBD events per day at each detector is calculated by integrating Equation 7.1 over 1.8–8 MeV, which yields the rates provided in Table 7.1. The rates in Table 7.1 are listed with and without the detector efficiencies. An effective detector target mass of 90% includes nGd contributions (87% of IBD events), rejects nH captures (the remaining 13%) and includes the spill-in/spill-out efficiency of 104% discussed in Chapter 6. Spill-out refers to IBD events that occur inside the target volume, but in which the neutron wanders out, unable to capture on gadolinium nucleus. Spill-in is the opposite effect, in which an IBD event occurs outside the target volume, but the neutron fortuitously wanders into the target volume to capture on gadolinium. The spill-in rate is larger than the spill-out, hence the efficiency is greater than 100%. Accounting for anticipated reactor up time, detector downtime, and other operational aspects of the experiment, a year of running at Daya Bay is estimated to be equivalent to 300 full days per year.

Reactor Contributions	Event Rates Per 20 Ton Detector		
	DYB Near	LA Near	Far
Daya Bay	814	59	27
Ling Ao I	146	463	41
Ling Ao II	63	387	41
Total events/day	1022	910	109
Total events/day (with detection efficiencies from Table 7.2)	603	610	85
Total events/year (with live-time correction of 300/365 days)	181000	183000	25500

Table 7.1 IBD event rates per day per 20 ton detector given the baselines in Figure 7.1. Also provided are the event rates including detection efficiencies from Table 7.2, and with a live-time of 300 days per year. The simulated event rates are within 10% of the latest detected rates (Table 6.3).

7.1.2 Backgrounds

The model considers three backgrounds: accidentals, fast neutrons and cosmogenic ^{8}He/^{9}Li. Spectra for each are presented in Figure 7.2. The remaining backgrounds, AmC and C(α,n)O, were not realized until data taking started.

Natural radioactivity from ^{238}U, ^{232}Th, ^{40}K, ^{60}Co, ^{222}Rn, and ^{85}Kr found in the detector materials and surrounding rocks were considered as sources of the accidental background. These isotopes emit gamma rays with an energy spectrum rapidly falling with energy, so the accidentals spectrum is simplified as an exponential decay without peaks. The rate of individual radiation was predicted to be 50 Hz [8], which limits the accidental backgrounds to less than 0.2% of the IBD event rate. Based on a muon tagging efficiency of 99.5%, the fast neutron background rate is estimated to be 0.1% of the IBD rate, with a flat spectrum. The ^{8}He/^{9}Li background rate is presumed to be as high as 0.3% of the IBD rate for the near sites and 0.2% at the far site, with a spectrum modeled on past Double Chooz studies [71].

Since the experiment had not yet begun operation, background rates were conservatively assigned values of 0.3% of the IBD signal per species at each detector. The uncertainties on these background rates were further conservatively taken to be 100%, and while the

Efficiency Factors	Efficiencies in Detectors (%)		
	DYB Near	LA Near	Far
Positron detection	98	98	98
Neutron detection	91	91	91
Prompt-delayed coincidence	98	98	98
nGd fraction	87	87	87
Spill-in/spill-out	104	104	104
Muon veto	75	85	99
Total detection efficiency	59	67	78

Table 7.2 Summary of all detection efficiencies in the simulation model based on the Technical Design Report and detector simulations [12].

muonic backgrounds are site-dependent, their rate uncertainties are modeled as detector-uncorrelated.

7.2 Daya Bay Experiment Model

7.2.1 Daya Bay Model χ^2

The basis of the model is a χ^2 function that quantifies the comparison between reactor antineutrino flux at arbitrary oscillation parameters to a non-oscillated flux, as seen by the detectors. Equation 7.2 describes the χ^2 for D=8 detectors, S=3 sites, C=6 cores, I=4 fluxes and B=62 energy bins between 1.8–8 MeV:

$$\begin{aligned}\chi^2(\theta_{13},\theta'_{13},\Delta m^2_{31}|\vec{\eta}) \;=\; & \sum_{d=1}^{D}\sum_{b=1}^{B}\frac{\left(f_b^d(\vec{\eta})-o_b^d\right)^2}{o_b^d+(o_b^d\sigma_{\mathrm{b2b}})^2}+\left(\frac{\mathcal{H}}{\sigma_{\mathcal{H}}}\right)^2+\sum_{b=1}^{B}\left(\frac{\eta^b_{\mathrm{shape}}}{\sigma^b_{\mathrm{shape}}}\right)^2 \\ & +\sum_{c=1}^{C}\left[\left(\frac{\eta^c_{\mathrm{core}}}{\sigma^c_{\mathrm{core}}}\right)^2+\left(\frac{\eta^c_{^{241}\mathrm{Pu}}}{\sigma^c_{^{241}\mathrm{Pu}}}\right)^2+\left(\frac{\eta^c_{^{238}\mathrm{U}}}{\sigma^c_{^{238}\mathrm{U}}}\right)^2+\left(\frac{\eta^c_{^{239}\mathrm{Pu}}}{\sigma^c_{^{239}\mathrm{Pu}}}\right)^2\right] \\ & +\sum_{d=1}^{D}\left[\left(\frac{\eta^d_{\mathrm{det}}}{\sigma^d_{\mathrm{det}}}\right)^2+\left(\frac{\eta^d_{\mathrm{scale}}}{\sigma^d_{\mathrm{scale}}}\right)^2\right] \\ & +\sum_{d=1}^{D}\left[\left(\frac{\eta^d_{\mathrm{acc}}}{\sigma^d_{\mathrm{acc}}}\right)^2+\left(\frac{\eta^d_{\mathrm{fast}}}{\sigma^d_{\mathrm{fast}}}\right)^2+\left(\frac{\eta^d_{\mathrm{iso}}}{\sigma^d_{\mathrm{iso}}}\right)^2\right]. \end{aligned} \tag{7.2}$$

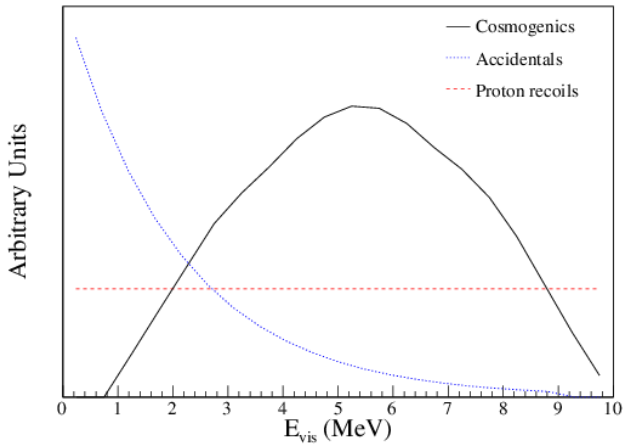


Figure 7.2 Background energy spectra with arbitrary normalization for fast neutrons (red dashed line), accidentals (blue dotted line) and ^{8}He/^{9}Li (black solid line), as assumed in the sensitivity model. The energy spectra follow the description in [71].

Here, o_b^d is the observed number of events in energy bin b of detector d, accounting for the flux from all reactors and the true-analog oscillation:

$$o_b^d(\theta_{13}, \Delta m^2_{31}) \equiv \sum_c \sum_\iota N_{c,\iota}^{d,b}\, P_{surv}^{b,c,d}(\sin^2 2\theta_{13}, \Delta m^2_{31}) + N_{acc}^{b,d} + N_{fast}^{b,d} + N_{iso}^{b,d}\,. \tag{7.3}$$

$N_{c,\iota}^{d,b}$ is the total number of events in energy bin b of detector d due to isotope ι in core c, and P_{surv} is the survival probability of the $\overline{\nu}_e$ flux, which is a function of oscillation parameters $\sin^2 2\theta_{13}$ and Δm^2_{31}, antineutrino energy and the reactor-detector baseline. The terms involving $N_{acc}^{b,d}$, $N_{fast}^{b,d}$ and $N_{iso}^{b,d}$ represent accidental, fast neutron and cosmogenic backgrounds respectively, of which o_b^d contains expectation values in addition to antineutrinos. For most cases of o_b^d, $\sin^2 2\theta_{13}$=0. The quantity f_b^d is the expected number of signal events with systematic uncertainties considered:

$$\begin{aligned} f_b^d(\theta'_{13}, \Delta m^2_{31}|\vec{\eta}) \;\equiv\; & \left(1 + \mathcal{H} + \eta^d_{\rm det} + \eta^b_{\rm shape}\right) \sum_{c=1}^{C} \left(1 + \eta^c_{\rm core}\right) \left(N^{d,b}_{c,\iota=1} + \sum_{\iota=2}^{I} \left(1 + \eta_{{\rm c},\iota}\right) N^{d,b}_{c,\iota} \right) \\ & \times P^{b,c,d}_{surv}(\sin^2 2\theta'_{13}, \Delta m^2_{31}) \\ & + \left(1 + \eta^d_{\rm acc}\right) N^{b,d}_{acc} + \left(1 + \eta^d_{\rm fast}\right) N^{b,d}_{fast} + \left(1 + \eta^d_{\rm iso}\right) N^{b,d}_{iso}\,, \end{aligned} \tag{7.4}$$

f_b^d is similar to o_b^d except for the variable, rather than constant, value of $\sin^2 2\theta_{13}$, and the nuisance parameters. The reactor and isotope contributions are summed internally within f_b^d, where the isotope summation is handled specifically so that the sum is 100%, hence the broken sum.

The nuisance parameters η_ι seen in Equations 7.2 and 7.4 represent the effect of systematic uncertainties on the flux, and are used to minimize the χ^2. The minimization of the χ^2 is crucial to understanding the space of oscillation parameter values allowed at the given sensitivity. The χ^2 compares a flux with test oscillation parameters (θ'_{13} and Δm^2_{31} in Equation 7.4) to a reference flux with set oscillation parameters (θ_{13} and Δm^2_{31} in Equation 7.3). The lower the minimized χ^2 for the test oscillation parameters, the better the test values reflect the reference oscillation values. In practice, the χ^2 most often compares a detected reference flux at $\sin^2 2\theta_{13}$=0 to test fluxes at arbitrary oscillation values; in that case, after minimization, the test value of $\sin^2 2\theta_{13}$=0 leads to the absolute minimum χ^2 value. Test oscillation parameter values that lead to a minimized χ^2 within a defined tolerance of the absolute minimum, ascribe the sensitivity.

The η_ι parameters are small by construction, $\eta_\iota << 1$, and are typically normalizations of the form $(1 + \eta_\iota)$ that scale existing contributions such as background species or reactor powers. This is evident from Equation 7.4. They can also be more complicated, such as in the case of the energy scale, which is implemented following Appendix A, Equation 10 of [190]. The sum of quotients at the tail of Equation 7.2, of the form $(\eta_\iota/\sigma_\iota)^2$, are pull terms that constrain the nuisance parameters to the scale of the systematic uncertainty [191, 192].

The systematic uncertainties used in this analysis are described in Section 7.2.2 and Table 8.2. Systematics are categorized as correlated or uncorrelated among reactors, detectors or energy bins. Correlated or uncorrelated categories refer to whether the systematic uncertainty affects all elements of a class (such as reactors) either simultaneously or individually. Correlated systematic uncertainties are canceled by the near-far detector pair comparison; uncorrelated systematics can be reduced thusly, but not canceled.

7.2.2 Systematic Uncertainties

The uncertainties in the model, as seen in Equation 7.4 are explained below. As mentioned in Section 7.2.1, the uncertainties break down into three categories: those pertaining to the reactors, detectors, or both (overall). In this model, the reactor and detector uncertainties are uncorrelated, while the overall uncertainties are reactor-detector-correlated, and either energy correlated or uncorrelated. Table 8.2 lists the values of the systematic uncertainties assumed in the model.

The uncertainty in the predicted antineutrino rate owes to thermal power instrumentation, fission rate calculations and the time-dependent burn up process [185, 193]. Using past reactor experiments [47, 32] as a guide, since Daya Bay had yet to begin operation, the reactors uncertainties on the antineutrino flux, both correlated and uncorrelated, and on the fuel composition uncertainty were assigned values of 2%.

1. Reactor-related uncertainties

   (a) σ^c_{core}: the uncorrelated reactor power (antineutrino flux) normalization uncertainty for each core.

   (b) $\sigma^c_{^{241}\text{Pu}}$, $\sigma^c_{^{238}\text{U}}$, and $\sigma^c_{^{239}\text{Pu}}$: the uncertainties on the isotopic fractions in the fuel. Although there are four isotopes, the total reactor power provides one constraint, so three independent uncertainties exist.

2. Detector-related uncertainties

   (a) σ^d_{det}: the uncorrelated detector normalization uncertainty.

   (b) σ^d_{scale}: the antineutrino energy scale uncertainty.

   (c) σ_{b2b}: the bin-to-bin uncertainty, an additional term in the denominator of the χ^2 accounting for the energy uncertainty at the bin demarcations not modeled by other parameters [8].

   (d) σ^s_{acc}: the accidentals background normalization uncertainty

(e) σ^s_{fast}: the fast neutron background normalization uncertainty

(f) σ^s_{iso}: the ^{8}He and ^{9}Li normalization uncertainty

3. Overall reactor and detector uncertainties

(a) $\sigma_{\mathcal{H}}$: the quadrature sum of correlated reactor and detector normalization uncertainties (energy-independent).

(b) σ^b_{shape}: the energy-uncorrelated antineutrino spectrum uncertainty due to reactor fuel spectra and detector response. This uncertainty is uncorrelated among bins but correlated reactors and detectors.

	Uncertainty		Value (%)
Reactor	flux normalization	σ^c_{core}	2.0
	fuel composition	σ^c_{fuel}	2.0
Detector	detector normalization	σ^d_{det}	0.38
	energy scale	σ^d_{scale}	2.0
	energy resolution		12.0
	bin-to-bin	σ_{b2b}	0.3
	accidentals background	σ^s_{acc}	0.3
	fast neutron background	σ^s_{fast}	0.3
	^{9}Li/^{8}He background	σ^s_{iso}	0.3
Overall	overall normalization	$\sigma_{\mathcal{H}}$	2.8
	bin normalization	σ^b_{shape}	2.0

Table 7.3 Systematic uncertainty values in the sensitivity model. 0.38% is the nominal value of the detector systematic uncertainty given in the Daya Bay proposal, but 0.18% was seen as attainable.

7.3 Daya Bay Sensitivity to $\sin^2 2\theta_{13}$

The sensitivity is computed by assuming a reference flux without oscillation $o_b^d(\sin^2 2\theta_{13} = 0)$, then using the χ^2 to calculate the test flux f_b^d at the largest compatible value of $\sin^2 2\theta'_{13}$, for a given confidence level. The discovery limit is computed assuming a flux at $\theta_{13} > 0$ then using the χ^2 to calculate an upper and lower bound in $\sin^2 2\theta_{13}$ at the given confidence limit, where the lower bound is nonzero. Oscillation parameter Δm^2_{31} is fixed for both the basis and test fluxes for a given calculation.

The χ^2 function defined in Equation 7.2 is a function of both the basis and test values of θ_{13} as well as Δm^2_{31} and the nuisance parameters:

$$\chi^2 = \chi^2(\theta_{13}, \theta'_{13}, \Delta m^2_{31}, \vec{\eta})\,. \tag{7.5}$$

The sensitivity $\Delta\theta'_{13}$ at confidence limit equal to α is obtained from

$$\chi^2(\theta_{13}, \theta'_{13} = 0 + \Delta\theta'_{13}, \Delta m^2_{31}, \vec{\eta}_{\Delta\theta'_{13}}) - \chi^2_{min}(\theta_{13}, \theta'_{13} = 0, \Delta m^2_{31}, \vec{\eta}_0) = c_\alpha\,, \tag{7.6}$$

where c_α is determined from a χ^2 distribution with one degree of freedom. For $\alpha = 90\%$, the sensitivity limit, $c_\alpha = 2.71$. For every value of θ'_{13}, including $\theta'_{13} = 0$ and $\theta'_{13} = \Delta\theta'_{13}$, the χ^2 is minimized with a distinct set of $\vec{\eta}$. At the discovery precision, the value of $\theta'_{13} \pm \Delta\theta'_{13}$ is calculated in a similar fashion:

$$\chi^2(\theta_{13}, \theta'_{13} \pm \Delta\theta'_{13}, \Delta m^2_{31}, \vec{\eta}_{\Delta\theta'_{13}}) - \chi^2_{min}(\theta_{13}, 0, \Delta m^2_{31}, \vec{\eta}_0) = c_\alpha\,, \tag{7.7}$$

where for the discovery limit of $\alpha = 3\sigma$ or 5σ, $c_\alpha = 9$ or $c_\alpha = 25$ respectively.

Note that o_b^d and f_b^d are defined with the expectation values for the number of antineutrinos in each energy bin for the relevant value of θ_{13}, rather than discrete values, and without any statistical fluctuations. Therefore, the resulting limits are an average case, as though the experiment were repeated a large number of times. For a detailed discussion of this subject in GLoBES, see [194].

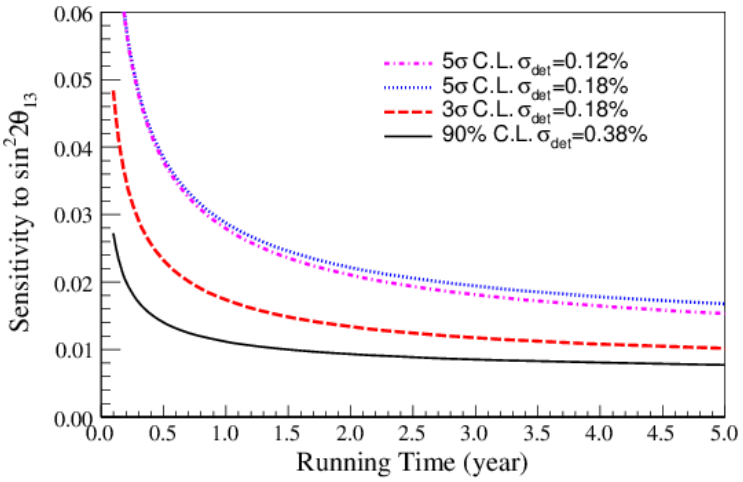


Figure 7.3 Solid line: Sensitivity of Daya Bay as a function of running time for the systematic uncertainties of Table 8.2 and $\Delta m^2_{31} = 2.40 \cdot 10^{-3}$ eV^2 [72]. Dashed lines: 3σ and 5σ confidence limits with improved detector systematic uncertainties.

7.3.1 Sensitivity and Discovery Reach

Figure 7.3 shows the sensitivity of Daya Bay as a function of running time for the model explained in Section 7.1, with $\Delta m^2_{31} = 2.40{\cdot}10^{-3}\,\mathrm{eV}^2$. After three years of data taking, Daya Bay is expected to reach a sensitivity of $\sin^2 2\theta_{13} = 0.0085$ at 90% confidence limit assuming an uncorrelated detector rate uncertainty of $\sigma_{\mathrm{det}} = 0.38\%$. With a detector uncertainty of 0.18%, the discovery limit becomes a more appealing metric; for $\sigma_{\mathrm{det}} = 0.18\%$, Daya Bay is projected to reach a 3σ discovery limit of $\sin^2 2\theta_{13}$=0.012 and a 5σ discovery limit of $\sin^2 2\theta_{13}$=0.02. Table 7.4 shows the 3σ and 5σ discovery limit of Daya Bay for running times of one, three and five years, and detector uncertainty values of 0.12%, 0.18% and 0.38% (0.12% is a prediction associated with detector swapping to improve systematics; this was never attempted, however). For instance, with $\sigma_{\mathrm{det}} = 0.18\%$ and three years of data the experiment can discover $\theta_{13} \neq 0$ at 5σ confidence limit for $\sin^2 2\theta_{13} = 0.02$. For simplicity, the running time is accrued from the moment all detectors become operational and the systematic uncertainties are treated as constant. The improvement in sensitivity as a function of time in Figure 7.3 is purely statistical.

Figure 7.4 provides Daya Bay's sensitivity and discovery limit with respect to both $\sin^2 2\theta_{13}$ and Δm^2_{31} for three years of data taking and assuming $\sigma_{\text{det}} = 0.38\%$. The left panel shows 90% and 3σ contours from the model of Section 7.1. The Daya Bay experiment is optimized for a measurement of $\sin^2 2\theta_{13}$ in the region around Δm^2_{31}=2.5·10^{-3} eV^2, which is reflected in Figure 7.4. The right panel of Figure 7.4 compares the model to the projection calculated in the Daya Bay TDR. The two are consistent within $1.5{\cdot}10^{-3}\,\text{eV}^2 < \Delta m^2_{31} < 3.0{\cdot}10^{-3}\,\text{eV}^2$, which is a much wider range of possible Δm^2_{31} measurements than expected when the model was formed [72]. Outside this region, the two calculations are less consistent, and differences are attributed to the three detector-three reactor simplification assumed in the TDR, and the energy-dependence in the respective χ^2s. Figure 7.5 illustrates the discovery limit in $\sin^2 2\theta_{13}$ and Δm^2_{31} for additional cases of running time and detector uncertainty.

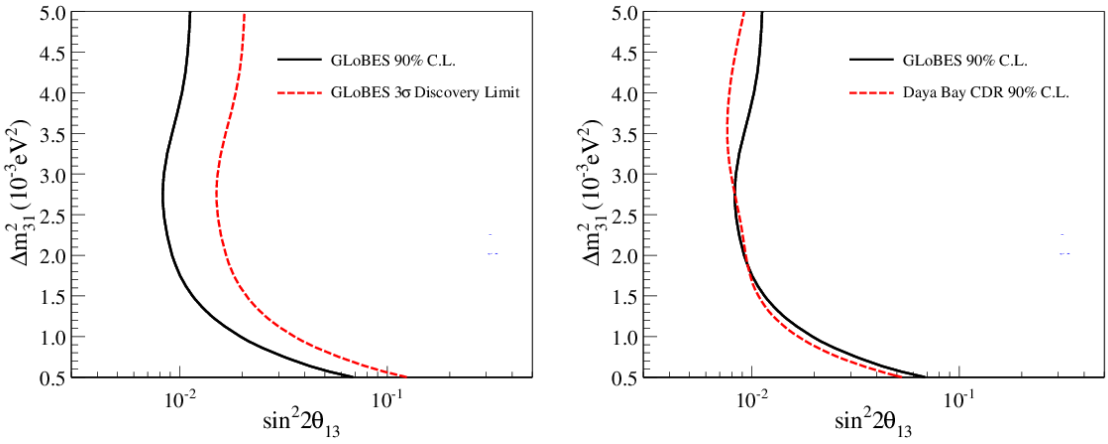


Figure 7.4 Left: The sensitivity and the 3σ discovery limit of Daya Bay based on the model of Section 7.1. Right: Comparison between the sensitivity predicted by the model and the Daya Bay proposal [8]. Agreement in the then-allowed region of Δm^2_{31} (Δm^2_{31}=$2.40^{+0.20}_{-0.15}{\cdot}10^{-3}$ eV^2 [72]) is nearly exact; the difference outside this region is due to the differences in the modeling of the number of detectors and reactors, and the χ^2 parameterization.

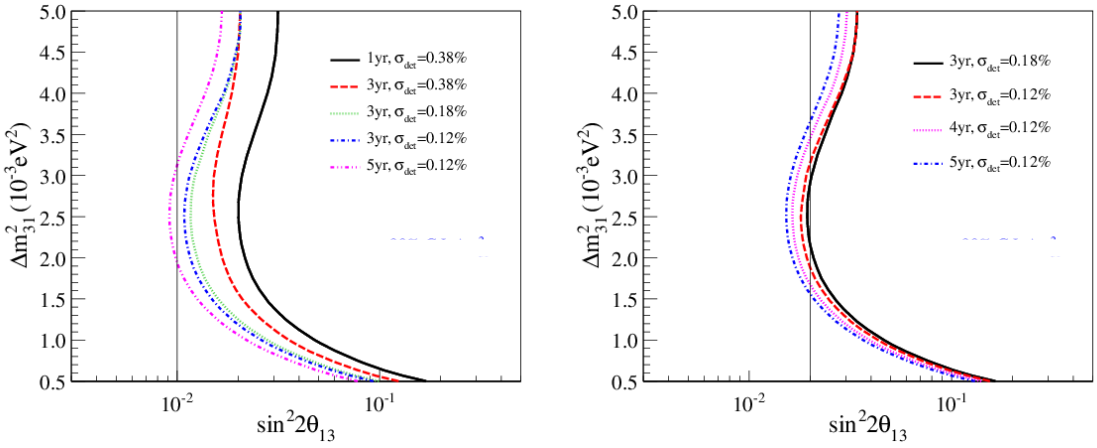


Figure 7.5 The 3σ (left) and 5σ (right) discovery reach for sample cases of running time and uncorrelated detector normalization uncertainty value.

7.3.2 Systematic Uncertainty Studies

The ultimate sensitivity of Daya Bay at the end of its run is limited by systematic uncertainties. As seen in Figure 7.3, the precision of Daya Bay improves dramatically with statistics only for about a year of running time. After that point, the sensitivity becomes flat in time at an asymptote determined by the given systematics. Therefore, it is informative to investigate that ultimate limit as a function of systematic uncertainty values.

Figure 7.6 shows the sensitivity of Daya Bay after three years of data taking as systematic uncertainties are varied from 0 to 2%. The curves are calculated by varying one uncertainty at a time while keeping the others constant at their nominal values. The dominant error is clearly the uncorrelated detector rate uncertainty σ_{det}; the sensitivity is most responsive to changes to σ_{det}, and it is thus set aside in its own plot. To achieve Daya Bay's sensitivity goal of $\sin^2 2\theta_{13} < 0.01$ at 90% confidence, the detector uncertainty must be held below 0.5%. Besides the detector uncertainty, the effects of most systematic uncertainties are mitigated by the near-far comparison. For example, the uncorrelated reactor normalization uncertainty is larger than the detector analog, but each reactor's flux is detected at each detector, so in the near-far comparison, the impact is reduced. Note that the scale of 0–2% is chosen to unify the comparison— it is not the most appropriate scale for the uncertainties σ_{b2b} and

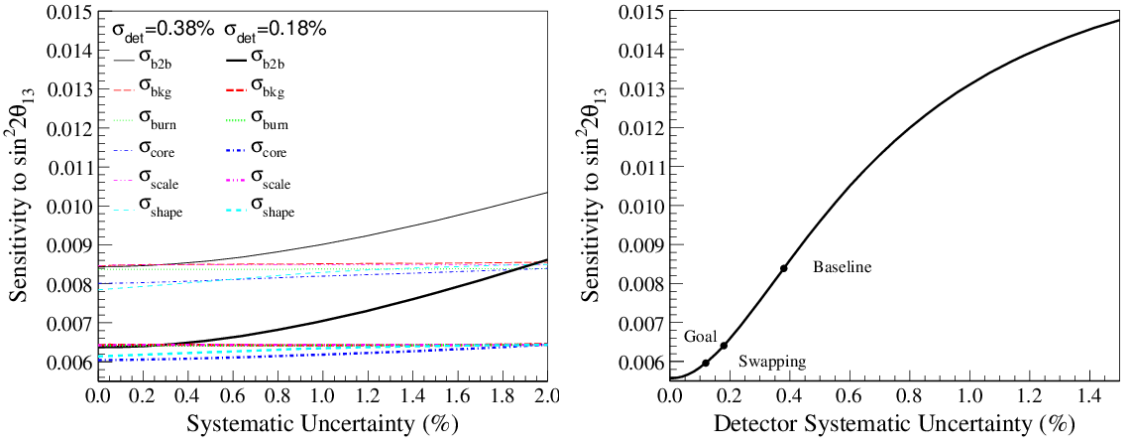


Figure 7.6 Left: Sensitivity after three years running as a function of each systematic uncertainty value. The thin lines correspond to a detector systematic uncertainty value of 0.38%, while the thick lines below correspond to a detector systematic uncertainty value of 0.18% (and occur lower in sensitivity value in the plot). Right: Change in the sensitivity with respect to the detector systematic uncertainty, the dominant systematic uncertainty in the error budget. The three points indicate the baseline, goal, and swapping values defined in the Technical Design Report [8].

σ_{det}. This inflates the significance of the bin-to-bin uncertainty, which appears to be the second most influential uncertainty, when in reality it is among the least important. σ_{b2b} is on the scale of 0.3%–0.5% in the sensitivity model, but rendered obsolete in the data analysis of Chapter 9.

The reactor systematic uncertainties are of special importance as well, because the reactors are beyond the control of the collaboration. Thus, even though flux uncertainties are partially canceled in the near-far detector comparison, there is more potential to fail to understand the flux.

The reactor flux uncertainty is mitigated partially in two ways. First, the flux contribution of any reactor to any detector is only one of six reactors. Second, the oscillation measurement comes from differences at detectors; in the comparison of near-far detectors, only the differences in flux contributions is significant because the common component will cancel.

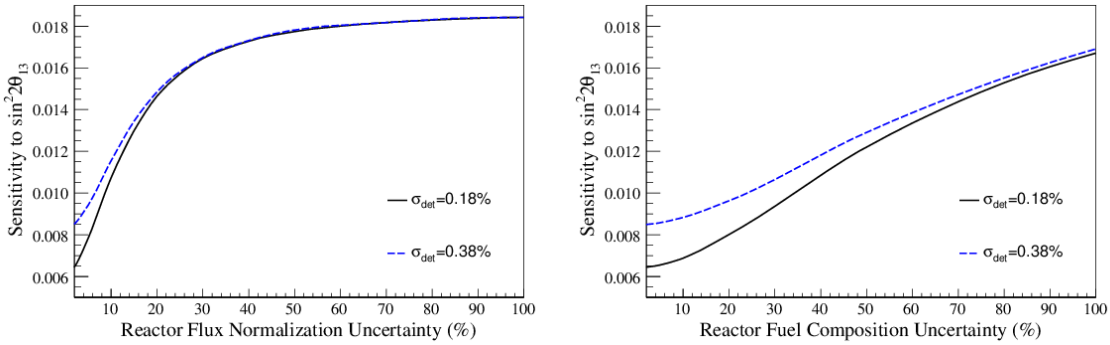


Figure 7.7 Left: Sensitivity to $\sin^2 2\theta_{13}$ as a function of the uncorrelated reactor flux normalization uncertainty, σ_{core}, assuming either 0.18% or 0.38% for the detector systematic uncertainty, and σ_{fuel}=2%. Right: Sensitivity to $\sin^2 2\theta_{13}$ as a function of the reactor fuel composition uncertainty, σ_{fuel}, assuming either 0.18% or 0.38% for the detector systematic uncertainty, and σ_{core}=2%.

The left plot in Figure 7.7 shows the sensitivity of Daya Bay as a function of the uncorrelated reactor flux normalization uncertainty, σ_{core}. All six cores have the same given uncertainty value, but their corresponding nuisance parameters are independent. Meanwhile, the reactor fuel composition uncertainty is held constant at 2%. For flux normalization uncertainties varying from 2% to 100%, the sensitivity degrades from $\sin^2 2\theta_{13} = 0.0085$ to $\sin^2 2\theta_{13} = 0.018$, plateauing above an uncertainty of about 40%. For Daya Bay to reach its goal sensitivity of $\sin^2 2\theta_{13} < 0.01$, the uncertainties on the reactor antineutrino rates must be below 6% assuming $\sigma_{\text{det}} = 0.38\%$, or 8% assuming $\sigma_{\text{det}} = 0.18\%$, if the fuel uncertainty is known to ∼2%.

The same exercise is conducted with the isotopic reactor fuel composition uncertainty. While the flux normalization uncertainty is kept constant, fuel uncertainty σ_{fuel} is varied from 2% to 100%, allowing the proportions of ^{235}U, ^{239}Pu, ^{238}U, and ^{241}Pu to change. The results are shown in the right panel of Figure 7.7. Daya Bay is less sensitive to the fuel composition uncertainty, as indicated by the more gradual rise in the σ_{fuel} curve compared to σ_{core}. In reaching 100%, the sensitivity to $\sin^2 2\theta_{13}$ rises to 0.017 from 0.0085, assuming $\sigma_{\text{det}} = 0.38\%$. For Daya Bay to reach its goal sensitivity of $\sin^2 2\theta_{13} < 0.01$, the uncertainties on the reactor

fuel fractions must be below 21% assuming $\sigma_{\text{det}} = 0.38\%$, or 35% assuming $\sigma_{\text{det}} = 0.18\%$, when the reactor antineutrino flux normalization is known to about 2%. Table 7.5 expands upon the variation of σ_{core} and σ_{fuel}, together, in the more critical space of $1\% < \sigma_{\text{core}} < 10\%$ and $2\% < \sigma_{\text{fuel}} < 20\%$.

Detector Uncertainty $\sigma_{\rm det}$	Running Time	$\sin^2 2\theta_{13}$ Sensitivity 90% confidence limit	Discovery Reach 3σ	5σ
0.38%	1 yr	0.011	0.020	0.034
0.38%	3 yr	0.0085	0.015	0.026
0.38%	5 yr	0.0077	0.014	0.023
0.18%	1 yr	0.0095	0.017	0.029
0.18%	3 yr	0.0064	0.012	0.019
0.18%	5 yr	0.0056	0.010	0.017
0.12%	1 yr	0.0092	0.017	0.028
0.12%	3 yr	0.0060	0.011	0.018
0.12%	5 yr	0.0051	0.0092	0.015

Table 7.4 Sensitivity (90% confidence limit) and 3σ and 5σ discovery reach for various detector uncertainty values and running times. Scenarios with $\sigma_{\rm det}$=0.12% were considered during the design of the experiment, to be pursued by swapping detectors among sites. But this plan was eliminated due to operational constraints of the experiment and lack of need.

$\sin^2 2\theta_{13}$ sensitivity, 90% confidence limit, $\sigma_{\text{det}} = 0.38\%$					
fuel composition	core flux uncertainty (%)				
uncertainty (%)	1	2	3	5	10
2	0.00829	0.00849	0.00874	0.00941	0.0115
5	0.00840	0.00857	0.00881	0.00947	0.0116
10	0.00867	0.00882	0.00904	0.00967	0.0118
20	0.00950	0.00962	0.00981	0.0104	0.0123

$\sin^2 2\theta_{13}$ sensitivity, 90% confidence limit, $\sigma_{\text{det}} = 0.18\%$					
fuel composition	core flux uncertainty (%)				
uncertainty (%)	1	2	3	5	10
2	0.00618	0.00644	0.00686	0.00782	0.0107
5	0.00629	0.00654	0.00690	0.00790	0.0108
10	0.00665	0.00687	0.00722	0.00816	0.0110
20	0.00782	0.00800	0.00828	0.00906	0.0116

Table 7.5 Sensitivity to $\sin^2 2\theta_{13}$ at various combinations of reactor flux normalization and reactor fuel composition uncertainties, assuming either σ_{det} equal to either 0.18% or 0.38%.

7.3.3 Limited Detector Sensitivity

The sensitivity curves versus time from this analysis inspired the collaboration to pursue an early measurement of $\sin^2 2\theta_{13}$. Natural questions arose such as how well Daya Bay could perform in the short term, and the optimum configuration of detectors for both short term and long term results.

7.3.3.1 Early Measurement of $\sin^2 2\theta_{13}$

Based in part on the sensitivity studies, the collaboration realized an opportunity to measure $\sin^2 2\theta_{13}$ early with a subset of the detectors. The detectors available were determined by the pace of construction, and their deployment was informed by the sensitivity studies. The first two detectors were operated for three months at the Daya Bay near site, as the collaboration validated their performance [67]. Meanwhile, construction of the remaining detectors continued. After the first two detectors' performance was validated, and given the pace of detector assembly and civil construction, it became evident that the collaboration could operate six detectors at three sites [195].

With two detectors ensconced at the near site, and the far site being the most crucial location for gathering data, three options emerged for the deployment of detectors at the three sites: 2–0–4, 2–1–3 and 2–2–2. The X–Y–Z notation refers to the number of detectors at the Daya Bay Near, Ling Ao Near, and Far sites respectively.

The 2–0–4 configuration maximizes statistics at the far site, and is logistically less complicated because detectors are only installed at one additional site. As seen from Figure 7.8, which compares 2–0–4 to 2–2–2 and 2–0–2, the 2–0–4 configuration leads 2–2–2 for short running times. However, after 1.5 months the 2–2–2 configuration is superior because 2–2–2 handles reactor systematics better. The 2–0–4 configuration leaves much more uncertainty about the Ling Ao reactor flux. Hence, 2–0–4 was eliminated from consideration.

Either the 2–1–3 or 2–2–2 configurations provide constraints to the Ling Ao reactor flux. 2–1–3 maximizes far site statistics, while 2–2–2 provides two detectors to monitor Ling Ao, which better disentangles reactor and detector systematics. Even with the added monitoring,

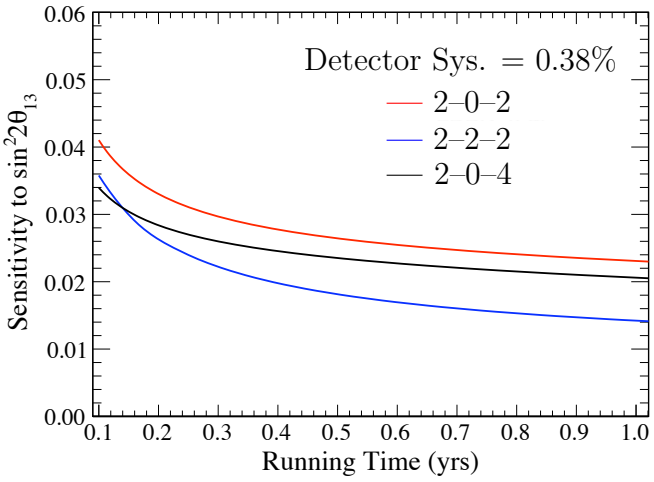


Figure 7.8 Sensitivity for configurations 2–0–2, 2–2–2 and 2–0–4 for short running times [73]. The X–Y–Z notation refers to the number of detectors at the Daya Bay Near, Ling Ao Near, and Far sites respectively

2–2–2 under performs 2–1–3 by about 10% over the short term, as shown in Table 7.6. Hence, the collaboration chose to pursue 2–1–3.

Figure 7.9 illustrates the discovery potential versus time for the 2–1–3 configuration over the short term. At the 3σ level, much of the then-available space for θ_{13} is quickly cut away, even if systematics are assumed to be large. The large systematics cases were studied due to the concern that the systematics might not be fully understood during the short running item. The sample values of $\sigma_{det} = 0.6\%$ and 0.8% are arbitrary. At half a year of data taking, and assuming a detector systematic of 0.38%, Daya Bay is projected to measure $\sin^2 2\theta_{13}$ at a precision better than 0.03. At 5σ, Daya Bay could muster a precision of 0.05. The early run even matches up well with RENO [74], as Figure 7.10 demonstrates. RENO's target sensitivity to $\sin^2 2\theta_{13}$ of 0.02 at 90% confidence is matched by the 2–1–3 configuration in about four months.

3σ $\sin^2 2\theta_{13}$ Discovery Limit				
	2 months	3 months	4 months	6 months
2–1–3	0.0462	0.0393	0.0353	0.0304
2–2–2	0.0518	0.0437	0.0390	0.0332

Table 7.6 Comparison of candidate six detector deployment schemes. Values are the 3σ discovery limit assuming a detector systematic uncertainty of 0.38% [13].

Figure 7.11 projects the discovery reach of Daya Bay through both the six and eight detector deployments. The six detector configuration is expected to run for half a year followed by an offline period, during which the discovery limit is constant. After the eight detector deployment is initiated and commissioned, it rapidly improves upon the six detector limit. This rapid improvement is vital, for it demonstrates that any delay in deploying eight detectors caused by running the six detectors poses a small disadvantage compared to the gain from the early result.

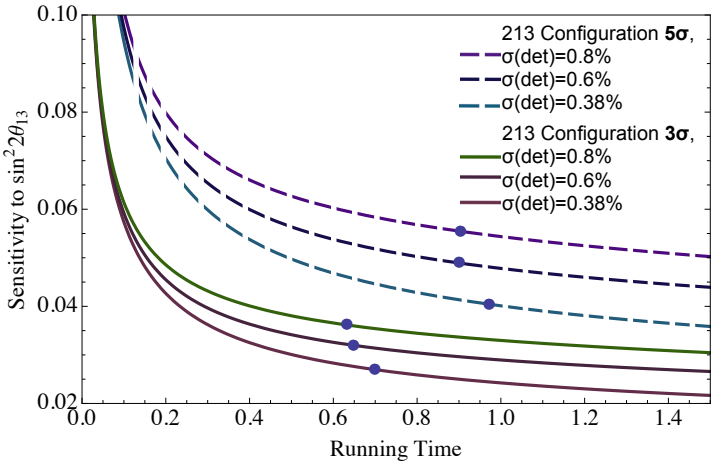


Figure 7.9 The discovery limit of the 2–1–3 configuration at 3σ and 5σ versus running time. Three uncorrelated detector systematic uncertainties are considered because at the time the six detector analysis was being considered, the actual uncertainty was yet unknown. For comparison, the dots indicate the moment that the rate of change of the curve is –0.001/month.

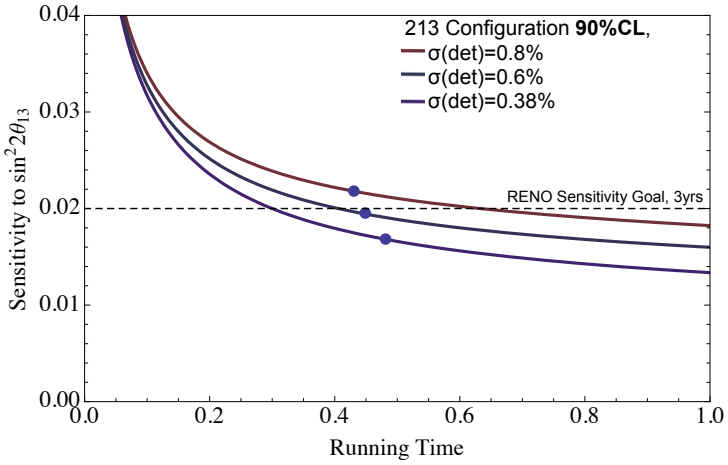


Figure 7.10 The sensitivity (90% confidence) of the 2–1–3 configuration versus running time compared to RENO's goal at full running time [74]. Daya Bay's short term six detector analysis is competitive.

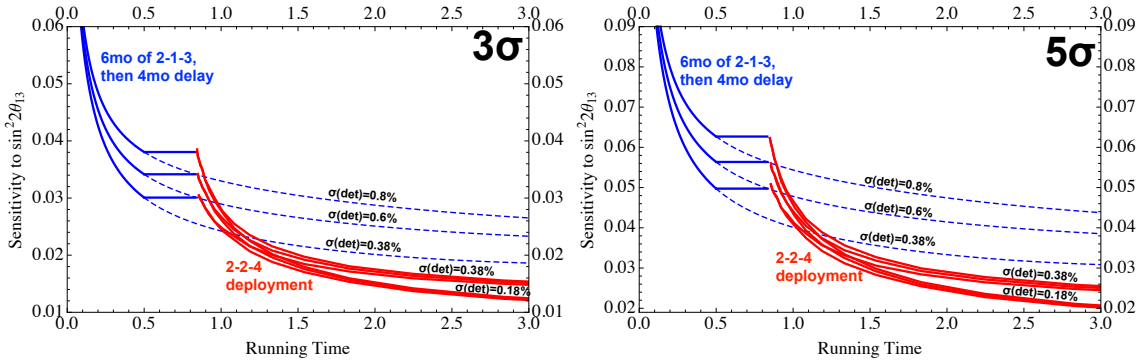


Figure 7.11 The 3σ and 5σ discovery reach for Daya Bay for the transition from the six detector analysis to eight detectors. The solid blue line shows the limit for six detectors, assuming detector uncertainties of $\sigma_{det} = 0.38\%$, 0.6% or 0.8%. After six months of data taking, the experiment is taken offline for a projected four months to install the last two detectors, during which the limit stays flat. After the installation of all detectors, the red line indicates the discovery limit for the anticipated range of σ_{det}, between 0.18% and 0.38%.

7.3.3.2 Lost Detectors

The collaboration was concerned about the possibility of losing a detector or pair, and inquired about the impact of this on the experiment's sensitivity. While unlikely, the possibility existed if a detector malfunctioned, or a detector or pair exhibited much higher systematics than the rest. Figure 7.12 describes the sensitivity if a detector or pair were removed from analysis. The left panel shows that the loss of sensitivity of the experiment is small, about 10% after three years. Losing a detector at the Daya Bay near site is the least consequential, which reflects the high statistics gathered at that site. Losing a detector at the Ling Ao near site is worse, since those two detectors constrain the flux of four nearby reactors, as opposed to two reactors at the Daya Bay near site. Losing either a far site detector or Ling Ao near are interestingly equivalent, even though gathering statistics at the far site is most crucial. For running times beyond a year, losing a Ling Ao near detector causes a worse degradation in the sensitivity than losing a far detector. Only one detector observing four reactors causes the experiment to be more prone to systematic uncertainties. For early running times, when the experiment is still statistics-dominated, losing a far site detector is more consequential, hence the cross-over at one year.

The loss of a pair of detectors follows the same pattern of site importance and lost sensitivity. Losing a Daya Bay near site-far site pair is less consequential than losing a Ling Ao near site-far site pair. Only two representative cases are shown in the right panel of Figure 7.12 because the collaboration assumed detector will be deployed in pairs, near to far.

Due the small change in sensitivity with the loss of one or two detectors, the correct course of action in the case they do go down is to tolerate the loss. The alternative of swapping detectors is a massive undertaking that has the potential to damage functioning detectors, or alter their systematic uncertainties. Upon review of these scenarios, the collaboration decided swapping was an unfavorable choice.

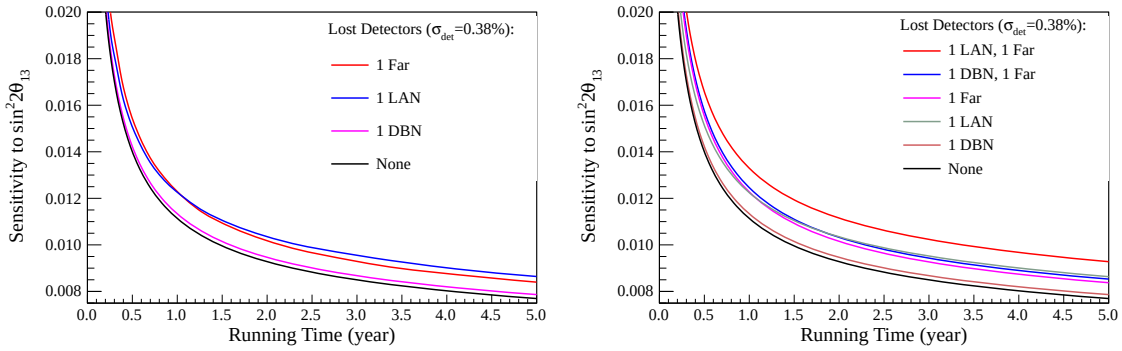


Figure 7.12 Sensitivity to $\sin^2 2\theta_{13}$ versus running time for incomplete configurations of Daya Bay. Left: The loss of one detector. Right: The loss of one detector or a near-far pair.

7.4 Summary

A model of the Daya Bay experiment was produced given the expected experimental attributes laid out in the proposal, such as the anticipated baselines and systematic uncertainties. This model was then used to predict the sensitivity of the experiment to $\sin^2 2\theta_{13}$ over a period of running time, under nominal circumstances as well as for different schemes of detector deployment and systematics.

The sensitivity investigations were vital to the collaboration in that it proved the feasibility of performing the initial six detector measurement of $\sin^2 2\theta_{13}$. It was further helpful in defining targets for systematic uncertainties and understanding their relative significance.

Chapter 8

Oscillation Analysis Modeling and Validation

The oscillation analysis method described in this chapter mathematically models systematic uncertainties and neutrino oscillations, which it then combines with reactor flux predictions, antineutrino data and backgrounds to calculate $\sin^2 2\theta_{13}$, Δm^2_{32}, Δm^2_{31} and $\mathcal{H}$ (the normalization difference between data and the reactor flux predictions).

Validations on the analysis model consist of tests on Monte Carlo samples generated with the model and generated externally by other groups within the collaboration. In each case the goal is for the analysis model to return the expected values of oscillation parameters. Some tests involved internal Monte Carlo samples with expectation values in each bin, while some used multiple samples with different statistical fluctuations. The analysis model was in agreement with expectation and demonstrated proper relationships among systematic uncertainties and oscillation parameters. The results of applying this model to data, and thus my contribution to the collaboration's published measurements, are presented in Chapter 9.

8.1 Daya Bay Experiment Model

The measurement of oscillation parameters at Daya Bay is accomplished using a χ^2 model that combines inverse beta decay (IBD) data and backgrounds (Chapter 6), flux predictions (Chapter 3), and systematics (Section 8.1.1). By varying the χ^2, the model calculates the best fit values and confidence limits for $\sin^2 2\theta_{13}$, Δm^2_{32} and $\mathcal{H}$, which is the overall normalization between data and prediction, and describes the relationships among the oscillation parameters and systematic uncertainties.

The oscillation measurements are extracted from the minimization of the χ^2 of Equation 8.17 with respect to systematic uncertainties and oscillation physics. The χ^2 compares the antineutrino rate and spectrum at six detectors, over a chosen number of energy bins, to the expected flux from six reactors accounting for neutrino oscillations and systematics. The χ^2 model will be explained in detail in Section 8.1.2, but it follows the functional form:

$$\chi^2 = \sum_{\text{all bins}} \left(T(1+\eta) - O + O \log \frac{O}{T(1+\eta)} \right) + \sum_{\iota} \left(\frac{\eta_\iota}{\sigma_\iota} \right)^2 , \tag{8.1}$$

or its familiar approximation

$$\chi^2 = \sum_{\text{all bins}} \frac{(T(1+\eta) - O)^2}{T} + \sum_{\iota} \left(\frac{\eta_\iota}{\sigma_\iota} \right)^2 , \tag{8.2}$$

where T is the prediction and O is the data.

The minimization is performed numerically over the set of nuisance parameters $\vec{\eta}$ that represent the systematics and oscillations, explained in detail in Section 8.1.1. The minimum of the χ^2 represents the best overall agreement between the data and a hypothesis antineutrino flux that includes oscillations and systematics, because the basis of the χ^2 is the difference between the data and predicted flux for each bin. The hypothesis flux is the original reactor prediction multiplied by terms typically of the form $(1+\eta_\iota)$ on each bin, where the nuisance parameters η_ι or functions of η_ι are small adjustments that depend on detector, reactor or energy, and are varied during the minimization. In other words, for all possible values of oscillation parameters, the systematics are adjusted during the minimization to evaluate the agreement; the best agreement is the reported measurement.

The heart of the χ^2 is the squared difference between data and prediction, and is followed by the sum of pull terms. Pull terms are the prior constraints on the nuisance parameters equal to the uncertainty in the case of systematics, or in the case of Δm^2_{32}, prior measurements. Pull terms take the form $(\eta_\iota/\sigma_\iota)^2$ and the χ^2 is constructed so that the expected values of η_ι are all 0. There is no pull term for $\sin^2 2\theta_{13}$ as there is no prior measurement; it is a free (unconstrained) parameter.

Measurements are derived from parameter values at the χ^2 minimum, while error bars are taken from the span of the region $\Delta\chi^2$ from the minimum. The value of $\Delta\chi^2$ depends on

the confidence interval desired and the number of degrees of freedom. For instance, the error bar quoted for a single measured parameter has one degree of freedom, and a confidence interval of 1σ, for $\Delta\chi^2$=1. For one degree of freedom, an $N\sigma$ confidence limit corresponds to $\Delta\chi^2=N^2$, which for more degrees of freedom (such as a two dimensional contour plot between $\sin^2 2\theta_{13}$ and Δm^2_{32}), the $\Delta\chi^2$ required is larger.

8.1.1 Physical Processes and Systematics

To arrive at the antineutrino flux expectation, the predicted reactor fluxes are corrected for a sequence of reactor and detector physical processes and systematic uncertainties, which are explained in the following subsections. Tables 8.1 summarizes the systematics in order of application alongside their number of nuisance parameters and correlations. Table 8.2 lists the values of the systematic uncertainties.

Corrections and uncertainties are applied in the proper sequence, following the production, propagation, then detection of the antineutrinos. First, physical processes inside the reactor are applied. This includes adjustments to the normalizations of the fission fraction, spent nuclear fuel and nonequilibrium reactor-uncorrelated uncertainty contributions. These uncertainties emanate from fuel consumption, fuel that is expended but still radioactive, and lowest order reactor isotopic fluxes, respectively. Following that, the reactor-correlated $\beta \rightarrow \bar{\nu}$ conversion normalization is adjusted, which is the theoretical uncertainty on the antineutrino flux originating from the fact that all reactor decay spectral measurements were performed on beta particles, then extrapolated to antineutrinos.

The antineutrinos then propagate outward isotropically, during which the oscillation occurs; the detectors sample these antineutrinos from all reactors at once. Reactor flux summation occurs at known proportions and with uncertainties on reactor power, correlated and uncorrelated. Inside the detectors, the effects likewise follow a logical order. The IAV correction occurs first because this represents an immediate loss of photons for some antineutrinos that would interact in the succeeding processes. Processes involving the photons are

		Correlations		
Correction or Systematic Uncertainty	Parameters in fit	Det.	Core	Energy
Flux predictions at reactor	—			
Fission fraction	N_{core}	—	U	C
Spent nuclear fuel	N_{core}	—	U	C
Nonequilibrium reactor contributions	N_{core}	—	U	C
Reactor and energy-correlated $\beta \rightarrow \bar{\nu}$ conversion	1	C	C	C
Oscillation	2	—	—	—
Sum the core contributions	N_{core}	—	U	C
IAV correction	—			
IAV correction energy-correlated uncertainty	N_{det}	U	—	C
Detector nonlinearity	4	C	—	C
Linear energy scale (relative)	N_{det}	U	—	—
Energy resolution	—			
Rebin data to user-chosen binning	—			
Detector normalization	N_{det}	U	—	—
Overall correlated normalization	1	C	C	C
Bin normalization	N_{bin}	C	C	U
Accidental backgrounds	N_{det}	U	—	U
Cosmogenic backgrounds	N_{det}	U	—	U
fast neutron backgrounds	N_{det}	U	—	U
AmC backgrounds	2	C	—	C
C(α, n)O backgrounds	0			
Compute χ^2 with nuisance parameters totaling	$6N_{det}+4N_{core}+N_{bin}+10$			

Table 8.1 The sequence of corrections and uncertainties applied in the antineutrino prediction model, starting from the initial antineutrino flux predicted at the reactors to the final antineutrino expectation at the detector based on oscillations, and reactor and detector effects. The number of fitting parameters, and their correlations are shown: "U" indicates uncorrelated, "C" indicates correlated, "—" indicates no relevance.

Category	Uncertainty	Value
Reactor Uncorrelated	Reactor normalization	0.5%
	Fission fraction	100%
	Spent nuclear fuel	100%
	Nonequilibrium flux	100%
	$\beta \to \bar{\nu}$ conversion	100%
Detector Uncorrelated	Detector normalization	0.20% or 0.16% + $0.24\eta_{scale}$
	IAV correction	100%
	Energy scale	0.35%
	Detector response	100%
Reactor and Detector Correlated	Overall correlated normalization	3.55%
	Uncorrelated bin normalization	See Figure 8.15
Backgrounds	Accidentals (EH1, EH2, EH3)	0.28%, 0.3%, 0.47%
	Fast neutrons (EH1, EH2, EH3)	17%, 18%, 71%
	Cosmogenics (EH1, EH2, EH3)	52%, 55%, 55%
	AmC (normalization, shape)	45%, 15%
	C(α, n)O	0

Table 8.2 The values of systematic uncertainties in the model; see Table 8.1 for descriptions. Where uncertainties are listed at 100%, the uncertainty is relative to the size of the correction not the detector data. Of these, all corrections but detector response take the form of fixed spectra added with a normalization nuisance parameter. The detector normalization uncertainty is reduced from 0.20% to 0.16% when the effect of the energy scale on the 6 MeV cut is accounted for explicitly by the $0.24\eta_{scale}$ term, which is the default choice. The IAV and $\beta \to \bar{\nu}$ conversion uncertainties each have two components, energy-correlated/detector-uncorrelated and energy-uncorrelated/detector-correlated. The energy-uncorrelated/detector-correlated components are absorbed into the bin normalization. Background uncertainties and are quoted as a percentage of the background rate.

applied next, including the nonlinearity correction and the linear energy scale shift. After that, the energy resolution, which is a consequence of the final number of detected photons, is applied. Since at this stage all energy-based corrections have been applied, the number of energy bins is reduced from the initial 240 to a smaller quantity chosen for the χ^2 analysis. The smaller number, which can be varied, increases the statistics per bin, decreases analysis

times and offers better visualization of the spectra. Last, the remaining normalizations are applied— on each detector rate, each energy bin, and background species— and the χ^2 is computed. Note that detector corrections are not applied to backgrounds that are measured from the data, while calculated backgrounds already account for detector effects.

8.1.1.1 Predicted Reactor Spectra

The predicted spectra are shown in Figure 8.1 as emitted from the reactors, before any oscillations or detector effects occur. The flux predictions are calculated in antineutrino energy then shifted to visible energy, the space in which the comparison with data is made. The conversion occurs at next to leading order in nucleon mass $(1/M)$ according to [144].

For simplicity, the first order conversion follows Equation 8.5:

$$E_{\bar{\nu}} = E_{e^+} + \Delta_{np} + K_{recoil} \qquad \text{antineutrino energy} \tag{8.3}$$

$$E_{vis} = E_{e^+} + m_e \qquad \text{definition of visible energy} \tag{8.4}$$

$$E_{vis} \simeq E_{\bar{\nu}} - \Delta_{np} + m_e \qquad \text{approximate expression of visible energy} \tag{8.5}$$

The kinetic energy K_{recoil} of the neutron is typically about 10 keV, which can be ignored at this level.

When calculating E_{vis} to the next order, the scattering angle between the antineutrino and positron, and the neutron energy must be accounted for:

$$\begin{aligned} E_{vis} &= E_{e^+} + m_e \\ &= (E_{\bar{\nu}} - \Delta KE)\left(1 - (E_{\bar{\nu}}/m_p)\left(1 - v_e^{(0)}\langle\cos\theta\rangle\right)\right) + m_e \end{aligned} \tag{8.6}$$

where

$$\Delta KE = \frac{1}{2}\left(\Delta_{np}(m_n + m_p) - m_e^2\right)/m_p \tag{8.7}$$

$$\langle\cos\theta\rangle = -0.034 v_e^{(0)} + 2.4 E_{\bar{\nu}}/m_p \tag{8.8}$$

$$v_e^{(0)} = \sqrt{1 - (m_e/E_{e^+})^2}\,. \tag{8.9}$$

The numerical difference between the E_{vis} of Equations 8.5 and 8.6 ranges from zero to 0.16 MeV from low to high $E_{\bar{\nu}}$.

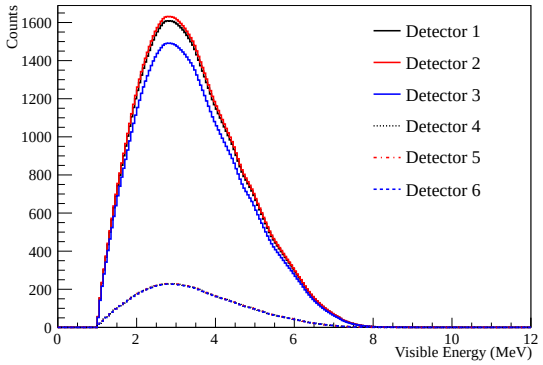


Figure 8.1 Predicted reactor spectra at each detector, without oscillations, over 240 energy bins [51]. Statistics correspond to the latest data set.

8.1.1.2 Fission Fraction

The fuel composition is known at any point in time to at least 95% accuracy by power plant simulations, as discussed in Section 3.2; the other 5% is distributed among the main four isotopes: ^{235}U, ^{238}U, ^{239}Pu, ^{241}Pu [8]. The fission fraction uncertainty spectrum is derived from the 5% shift in fuel composition that produces that largest effect, which is a shift from ^{235}U to ^{239}Pu and vice versa. Performing this shift yields the spectrum shown in Figure 8.3 that can be added as a contribution to each reactor spectra with reactor-uncorrelated nuisance parameters as normalizations. By construction the uncertainty is 100% of the Figure 8.3 spectrum [51].

8.1.1.3 Spent Nuclear Fuel

Antineutrinos from spent nuclear fuel have the spectrum indicated in Figure 8.4 [196]. The uncertainty on the flux is a reactor-uncorrelated normalization of 100%, which is due to the lack of proprietary information provided to the collaboration regarding the spent fuel mass and age. The spent fuel is stored in six water pools located 30 m away from their source reactor [6].

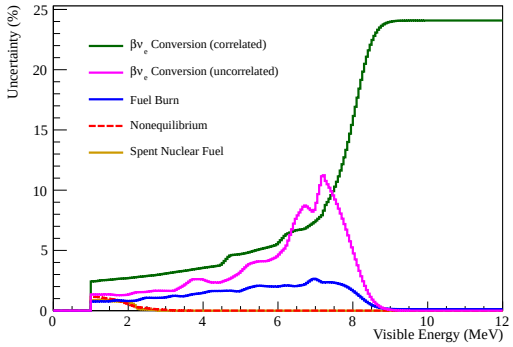


Figure 8.2 Reactor flux uncertainties: spent nuclear fuel and nonequilibrium fluxes at low energy, as well as fission fraction and the $\beta \to \bar{\nu}$ conversion spectra. The $\beta \to \bar{\nu}$ conversion is correlated among reactors, but one component is energy-correlated while the other is energy-uncorrelated [51].

8.1.1.4 Nonequilibrium Flux

The nonequilibrium flux is the contribution to the antineutrino flux from isotopes other than the top four. The ILL experiments [135, 136, 137] that measured most of the reactor antineutrino flux from ^{235}U, ^{239}Pu and ^{241}Pu were performed by the irradiation of reactor fuel for 36 h, after which the beta spectra was measured. The nonequilibrium isotopes were unable to come into equilibrium over such a short irradiation time, so their small contribution has a proportionally large uncertainty. This uncertainty has the spectrum indicated in Figure 8.4, a subpercent addition for low energy bins. The contribution is normalized at each reactor with a reactor-uncorrelated uncertainty of 100% [51].

8.1.1.5 $\beta \to \bar{\nu}$ Conversion

The reactor antineutrino flux is derived from measurements of beta particles from the beta decay of reactor isotopes, which is then extrapolated to antineutrinos [140, 51]. Uncertainties introduced in this conversion can be decomposed into two components— energy-uncorrelated/reactor-correlated and energy-correlated/reactor-correlated— both shown in Figure 8.5.

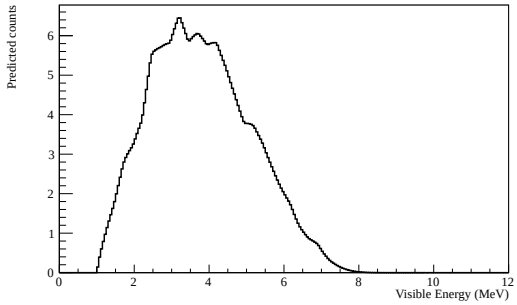


Figure 8.3 The fission fraction uncertainty spectrum, in this example from Daya Bay Nuclear Power Plant 1 (DBNPP1) to Detector 1 at the Daya Bay near site, at the statistics and efficiencies of the latest data set. The uncertainty spectra are normalized with nuisance parameters then added or subtracted to each reactor-detector flux prediction.

The energy-uncorrelated/reactor-correlated uncertainty is combined with other energy-uncorrelated systematics, such as the IAV correction, into the bin normalization uncertainty discussed in Section 8.1.1.12. It is applied as a normalization nuisance parameter on each bin independent of the other bins, identically across all detectors or reactors, with the uncertainty shown in Figure 8.5.

The energy-correlated/reactor-correlated $\beta \rightarrow \bar{\nu}$ component is a contribution added equally to each reactor flux, with the given spectrum, and a single normalization nuisance parameter. The uncertainty is 100% relative to the size of the added contribution.

8.1.1.6 Oscillation and Reactor Flux Summation

The reactor flux predictions are generated without oscillations due to either θ_{12}, θ_{23} or θ_{13}. After all reactor systematics are applied, the antineutrino flux is reduced by the oscillation probability based on antineutrino energy (calculated at the midpoints of 240 bins) and the baseline between each reactor and detector. Then, the antineutrino flux incident at each detector is determined by summing over reactor contributions, while applying the reactor-uncorrelated normalization uncertainty of 0.5%.

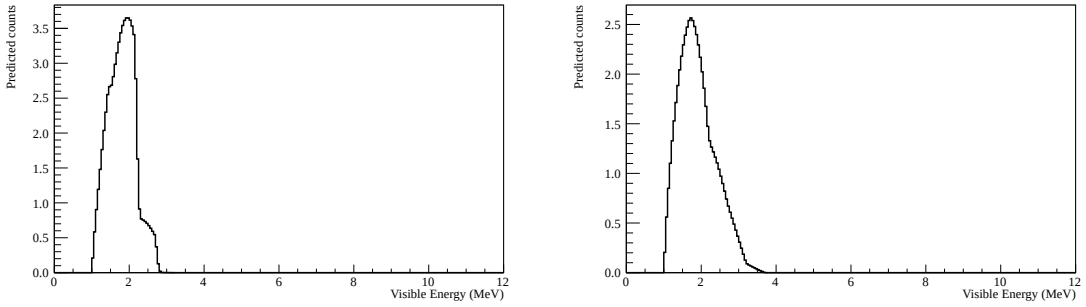


Figure 8.4 Left: The spent nuclear fuel uncertainty spectrum. Right: nonequilibrium uncertainty spectrum. Plotted are contributions from Daya Bay Nuclear Power Plant 1 (DBNPP1) to Detector 1 at the Daya Bay near site, at the statistics and efficiencies of the latest data set. The uncertainty spectra are normalized with nuisance parameters then added or subtracted to each reactor-detector flux prediction.

The survival probability— that is, the fraction of the antineutrinos that remain in the $\overline{\nu}_e$ state— includes all oscillation channels as applied to the reactor flux:

$$\begin{aligned} P_{surv} = 1 \;\; &- \;\; \cos^4\theta_{13}\sin^2 2\theta_{12}\sin^2(\tfrac{1.27\,\mathrm{MeV}}{\mathrm{km{\cdot}eV^2}}\,\Delta m^2_{21}\,L/E) \\ &- \;\; \cos^2\theta_{12}\sin^2 2\theta_{13}\;\;\sin^2(\tfrac{1.27\,\mathrm{MeV}}{\mathrm{km{\cdot}eV^2}}\,\Delta m^2_{31}\,L/E) \\ &- \;\; \sin^2\theta_{12}\sin^2 2\theta_{13}\;\;\sin^2(\tfrac{1.27\,\mathrm{MeV}}{\mathrm{km{\cdot}eV^2}}\,\Delta m^2_{32}\,L/E) \end{aligned} \tag{8.10}$$

The oscillation parameters θ_{12}, θ_{23} and Δm^2_{21} are fixed to their Particle Data Group 2012 values [1], listed in Table 8.3. The uncertainties on θ_{12} and θ_{23} are neglected because the oscillation contribution is minuscule. The χ^2 fit to data is performed with Δm^2_{32} as the fit parameter with Δm^2_{31} constrained to be:

$$\Delta m^2_{31} = \Delta m^2_{21} \pm \Delta m^2_{32}\,, \tag{8.11}$$

where $+\Delta m^2_{32}(-\Delta m^2_{32})$ is for normal(inverted) hierarchy, specified before the fit. Thus, the masses are fit as a pair, and the small uncertainty in Δm^2_{21} is propagated to the Δm^2_{32} uncertainty. The parameter $\eta_{\Delta m^2_{32}}$ is typically unconstrained, but may be constrained by a pull term $(\eta_{\Delta m^2_{32}}/\sigma_{\Delta m^2_{32}})$ to the prior measurement value and uncertainty. Quantities $\Delta m^2_{32prior}$ and $\sigma_{\Delta m^2_{32}}$ are supplied from previous experiments or the PDG.

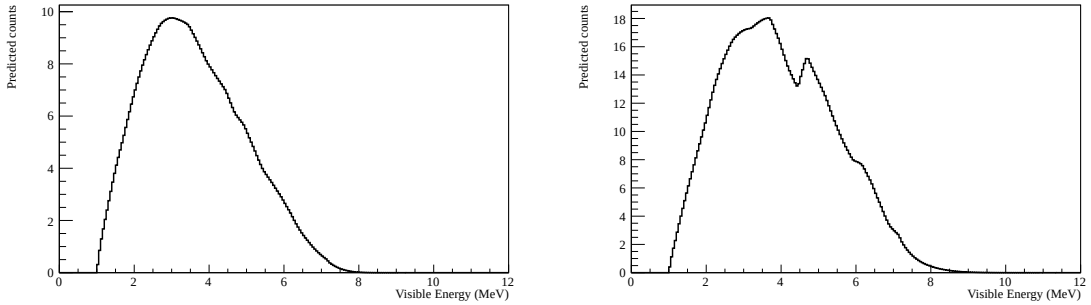


Figure 8.5 The $\beta \to \bar{\nu}$ conversion uncertainty spectra, in this example from Daya Bay Nuclear Power Plant 1 to Detector 1 at the statistics and efficiencies of the latest data set. Left: energy-correlated/reactor-correlated spectrum; right: energy-uncorrelated/ reactor-correlated spectrum. The spectra are normalized with nuisance parameters then added or subtracted to each reactor-detector flux prediction.

8.1.1.7 IAV Correction

The inner acrylic vessel (IAV), the thin wall that separates a detector's target volume from the gamma catcher, causes a slight distortion in the detected visible energy because some positrons will deposit energy into the vessel wall, but the acrylic does not scintillate. When this occurs the detector loses these photons, which results in some IBD events registering as having lower energy. To account for this, the reactor flux is adjusted by one static correction, and two uncertainty spectra [75].

The matrix that effects the static correction is shown in Figure 8.6. The matrix is nearly unit diagonal, but sparse off-diagonal elements reduce the energy of a small proportion of events. The uncertainties are divided into correlated and uncorrelated components, and are provided in Figure 8.7. The detector-uncorrelated/energy-correlated uncertainty has a fixed spectrum that is added independently to each detector with a detector-uncorrelated normalization nuisance parameter and associated uncertainty of 100%. The detector-correlated/ energy-uncorrelated component affects all detectors equally, and is combined into the bin normalization uncertainty discussed in Section 8.1.1.12.

Parameter	Value	Parameter	Value
Δm^2_{21}	$7.50 \pm 0.02{\cdot}10^{-5}\,\mathrm{eV}^2$	$\sin^2 2\theta_{12}$	0.857
Δm^2_{31}	$\pm\Delta m^2_{32} + \Delta m^2_{21}$	$\sin^2 2\theta_{13}$	—
Δm^2_{32}	$2.32 \pm 0.12{\cdot}10^{-3}\,\mathrm{eV}^2$	$\sin^2 2\theta_{23}$	—

Table 8.3 Oscillation parameter values assumed in the model. By choice, Δm^2_{32} is the fit parameter and Δm^2_{31} is constrained to $\Delta m^2_{31} = \pm\Delta m^2_{32} + \Delta m^2_{21}$, where +1(–1) is for normal(inverted) hierarchy.

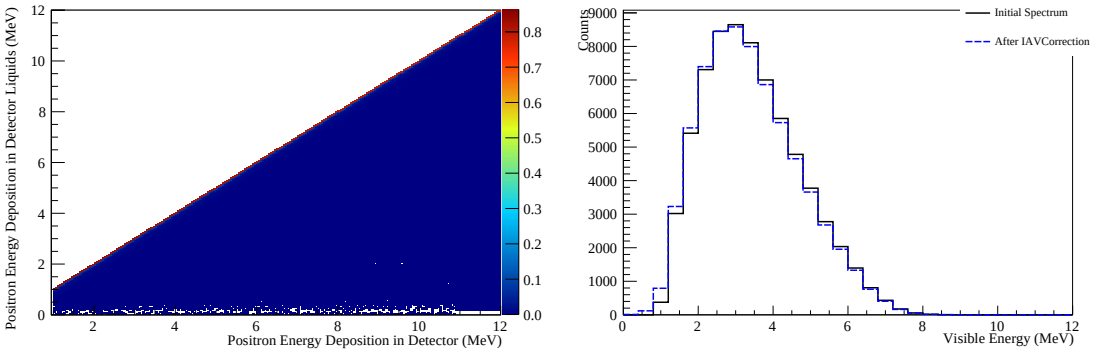


Figure 8.6 Left: IAV correction matrix [75]. It is highly diagonal, with some off-diagonal elements representing events that lose energy in the acrylic. Right: application of the IAV correction matrix to a typical IBD spectrum.

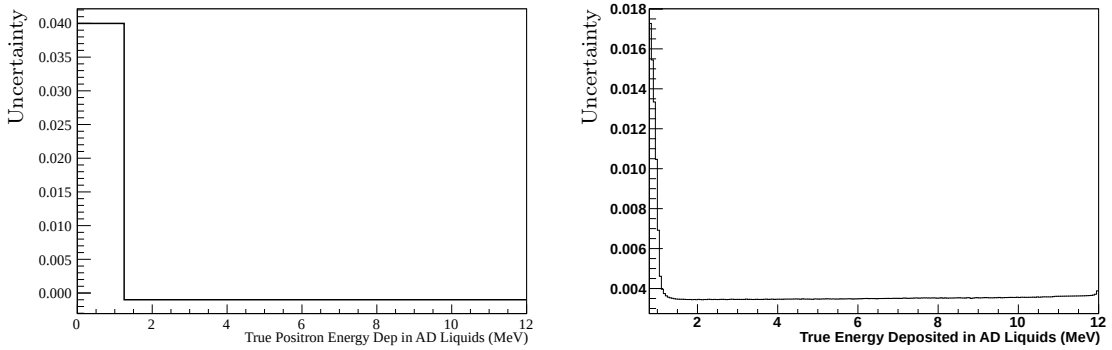


Figure 8.7 IAV correction uncertainty spectra. Left: detector-uncorrelated/ energy-correlated. Right: detector-correlated/energy-uncorrelated. The spectra are normalized with nuisance parameters then added or subtracted to each reactor-detector flux prediction.

8.1.1.8 Detector Nonlinearity and Energy Scale

Besides the conversion from antineutrino energy to visible detected energy absent detector effects, a distortion must be applied to the predicted antineutrino flux to account for how accurately the detector reports a given energy. The energy deposited in the detector differs from that read out by 0–7%, which depends on energy [3]. This bias can be decomposed into two components: a detector response function that is nonlinear and affects all detectors likewise, and an energy scale, which is smaller, linear and detector-uncorrelated. Both corrections are applied together in the analysis as:

$$E_{\text{detected}} = E_{\text{deposited}} \left(1 + f_{nl}(E, \eta_1 ... \eta_4)\right) \left(1 + \eta_d\right) \tag{8.12}$$

for detector d, where η_d and $f_{nl}(E)$ are small corrections representing the energy scale and detector response function respectively.

The detector response function is based on the impact of the scintillator and the electronics. The scintillator component is dependent on the particle energy and identity (specifically, the charge and mass), and is nonlinear due to the emission of Cherenkov radiation and scintillator quenching [3]. The emission of Cherenkov light depends on energy of the particle and the square of its charge [197]. Quenching refers to the lack of emission of light by the scintillator: the energy released by de-excitation is absorbed in other degrees of freedom such as heat.

The scintillator component is described by the empirical relation

$$f_{scint} = \frac{p_0 + p_3 E_{dep}}{1 + p_1 e^{-p_2 E_{dep}}} \,. \tag{8.13}$$

The electronics component is a double exponential [198]:

$$f_{elec} = \alpha_1 e^{E_{dep}/\tau_1} \cdot \alpha_2 e^{E_{dep}/\tau_2} \,. \tag{8.14}$$

The first exponential reduces the bias introduced by the front end electronics (FEE) by aligning the length of the readout window with the effective FEE charge integration time. The second exponential is Monte Carlo-based.

The parameters in the nonlinearity are determined from energy deposited by gamma rays and electrons in the data, and related to positrons by Monte Carlo. Several mono-energetic gamma rays from calibration sources and detector radiation, and the continuous spectrum of ^{12}B, were used in particular.

Uncertainty propagation is handled by constructing the nonlinearity as the primary model described above, plus four alternatives. The alternatives are based on similar principles to the primary model, but differ about 1.5% for positron energies. In Equation 8.12, the function f_{nl} has the form

$$f_{nl} = f_0 + \sum_{\iota=1}^{4} \eta_\iota (f_\iota - f_0)\,, \tag{8.15}$$

where the nuisance parameters η_ι are constrained to pull terms with uncertainties of 100%. By construction, if any of the three η are zero and the remaining $\eta = 1$, this represents a substitution of that f_ι for f_0.

The function f_{nl} is plotted in Figure 8.8. The solid black line represents the baseline correction (all η_ι=0), and the colored curves correspond to 1σ variations: one $\eta_\iota = \pm\sigma_\iota$ while other $\eta_\iota = 0$.

Since the detectors are identical at the sub-percent level, the differences among detector responses are small and linear. This is the energy scale, the η_d term in Equation 8.12. The nuisance parameters η_d are detector-uncorrelated, but along with the detector response parameters, are among the few that are not normalizations. The η_d are tied to pull terms with uncertainty 0.35%.

8.1.1.9 Energy Resolution

The energy resolution is the precision at which an energy can be measured in a detector with finite photons. For a true energy E, the measured E' is actually distributed according

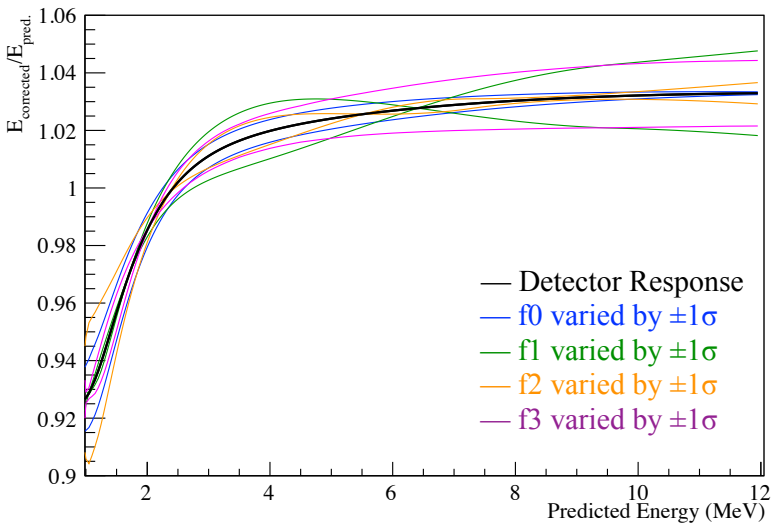


Figure 8.8 The $E_{\text{meas.}}/E_{\text{dep.}}$ ratio (f_{nl} of Equation) from the nonlinearity function of Equation 8.8. The solid black line is the baseline correction, and the colored lines represent the variation of the four fit parameters by 1σ.

to a Gaussian of width σ_E centered at E. The form of the energy resolution for Daya Bay detectors is [199]:

$$\sigma_E = \sqrt{0.022^2 + 0.079^2/E + 0.016^2/E^2}\,. \tag{8.16}$$

The three terms in Equation 8.16 correspond to detector spatial nonuniformity (~ 1), photostatistics ($\sim 1/\sqrt{E}$) and PMT effects ($\sim 1/E$) respectively. The photostatistics term, which dominates, is the most common contributor to an experimental energy resolution. Figure 8.10 shows an IBD spectrum before and after the application of the energy resolution. Note that the energy resolution has no uncertainty associated with it; rather the energy resolution is the uncertainty itself.

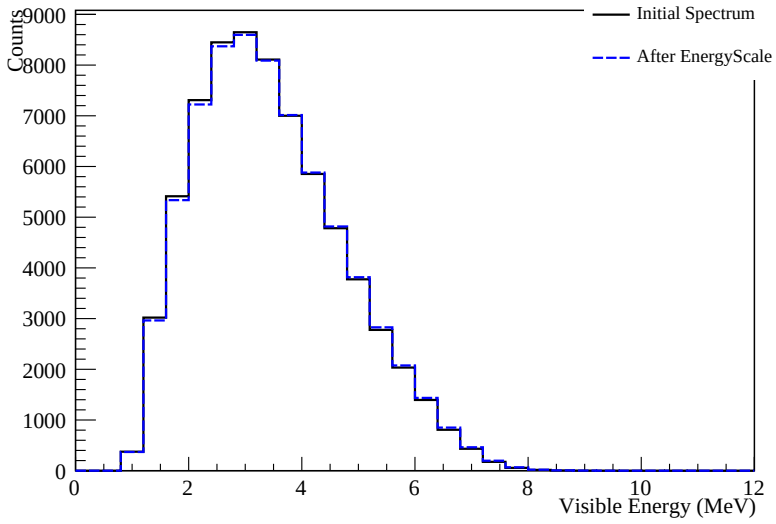


Figure 8.9 A 1% energy scale applied to a typical detector flux prediction.

8.1.1.10 Rebinning

After every energy-dependent effect is applied to the predicted antineutrino spectra, the spectra are rebinned from the original 240 down to N_{bins}, the number of bins over which the χ^2 is calculated.

8.1.1.11 Backgrounds

Five backgrounds are included in the model, and are discussed in more detail in Section 6.5:

- Accidentals— Coincidental emissions of radiation that combine to match IBD timing and deposited energy. [200]
- Cosmogenic ^{9}Li/^{8}He— muon-produced isotopes that survive long enough to escape muon veto cuts, but decay in such a way to mimic the IBD signal [76].
- Fast neutrons— Spallation neutrons created by energetic muons that do not pass through the muon veto. The neutrons deposit energy as they thermalize in the detector, then capture on a gadolinium nucleus.

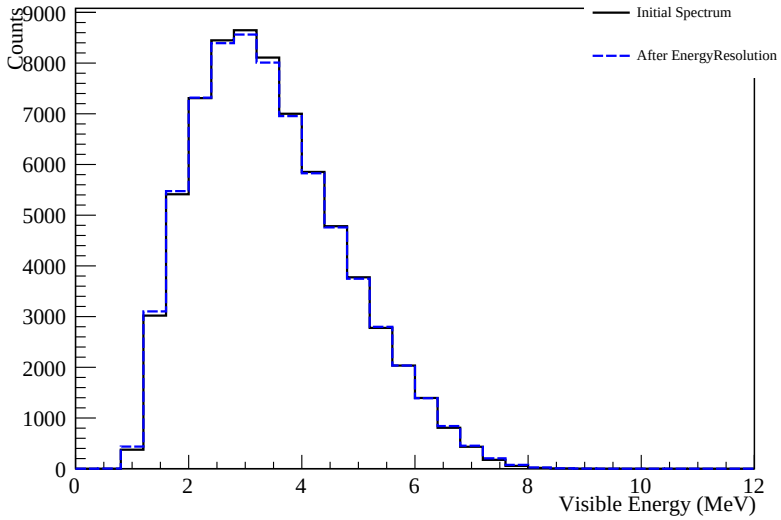


Figure 8.10 Application of energy resolution based on Equation 8.16 to a typical detector flux prediction.

- AmC— Neutrons emitted from calibration sources atop the detector can mimic an IBD signal in the same manner as the fast neutron background [77, 201].
- C(α, n)O— Similar to the AmC background, but the neutron emanates from detector materials [78].

The normalizations of the accidental, fast neutron and cosmogenic backgrounds are nuisance parameters of the fit, detector-uncorrelated, and tied to pull terms with uncertainties indicated in Table 8.2. The fit parameters of the AmC background are both detector-correlated; one is a normalization and the other adjusts the shape. Finally, the C(α, n)O contribution is merely added into the prediction— its rate is too small to require a nuisance parameter. All of the backgrounds are plotted in Figures 8.11 through 8.14 except the fast neutrons, which are flat in energy.

Background spectral uncertainties are negligible because the background contributions are already small compared to the IBD spectra, and the shape uncertainties would be smaller yet and detector-correlated, since the background physics is the same across detectors and

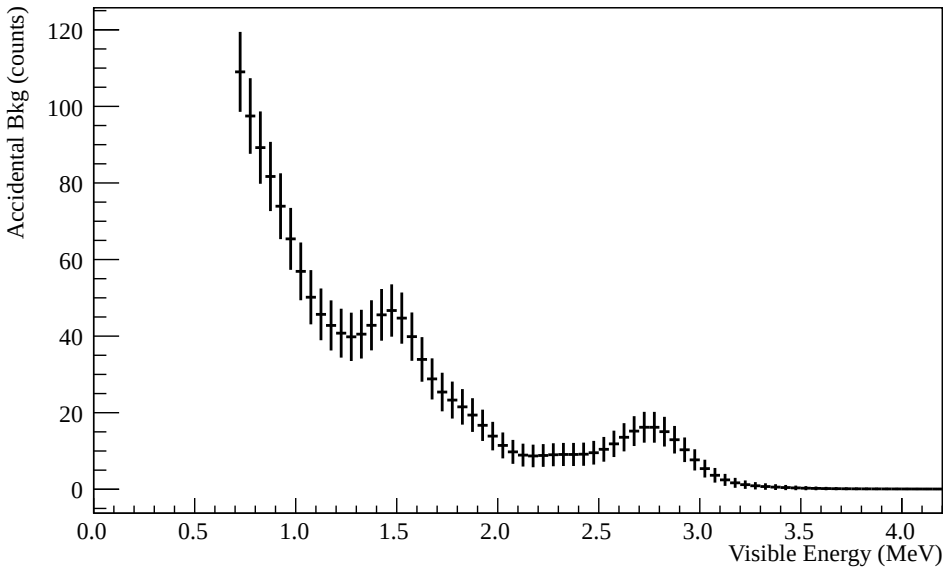


Figure 8.11 The accidentals spectrum for Detector 1.

the detectors are identical. If the background shape uncertainty were applied, it would be a small contribution to the bin normalization uncertainty.

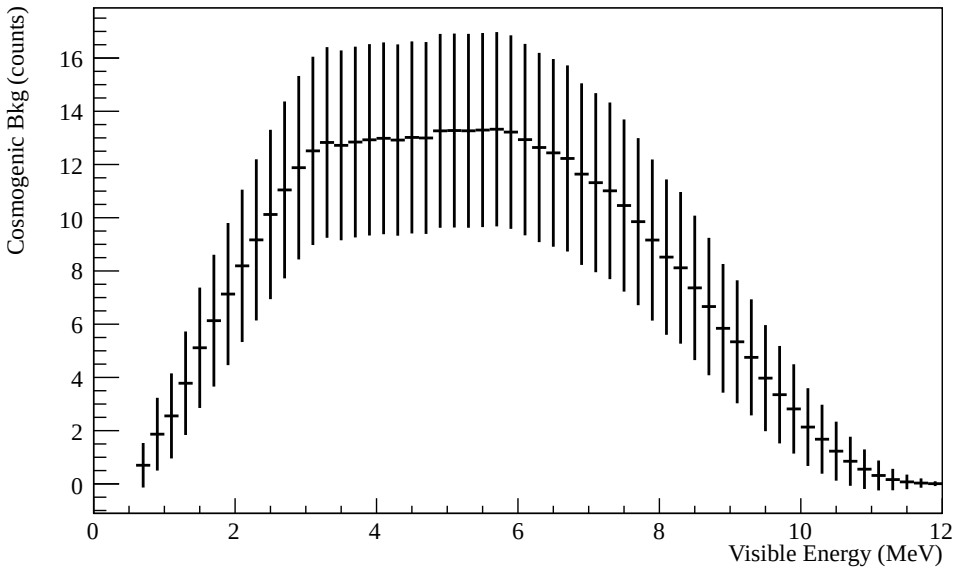


Figure 8.12 The ^{9}Li/^{8}He spectrum for Detector 1, from [76].

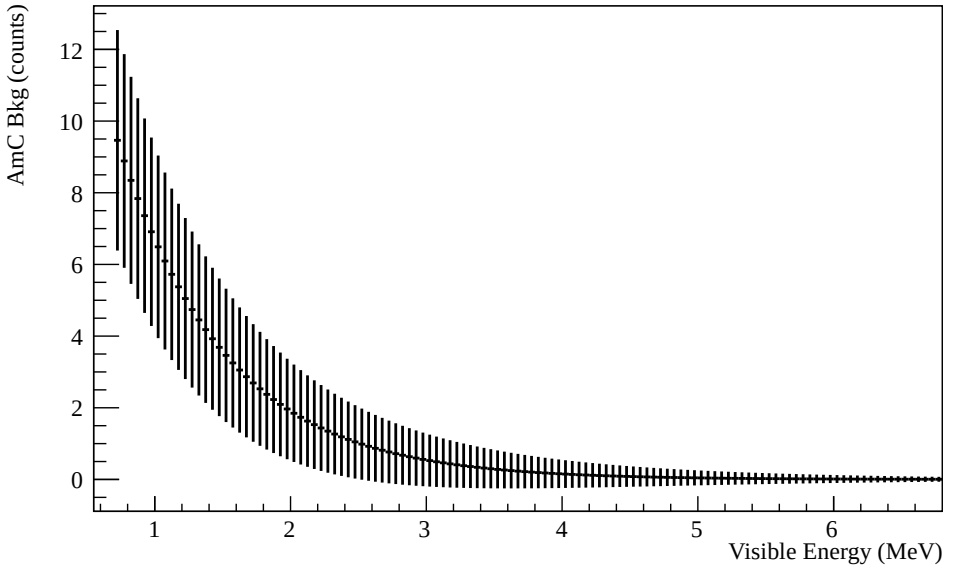


Figure 8.13 The AmC spectrum for Detector 1, from [77].

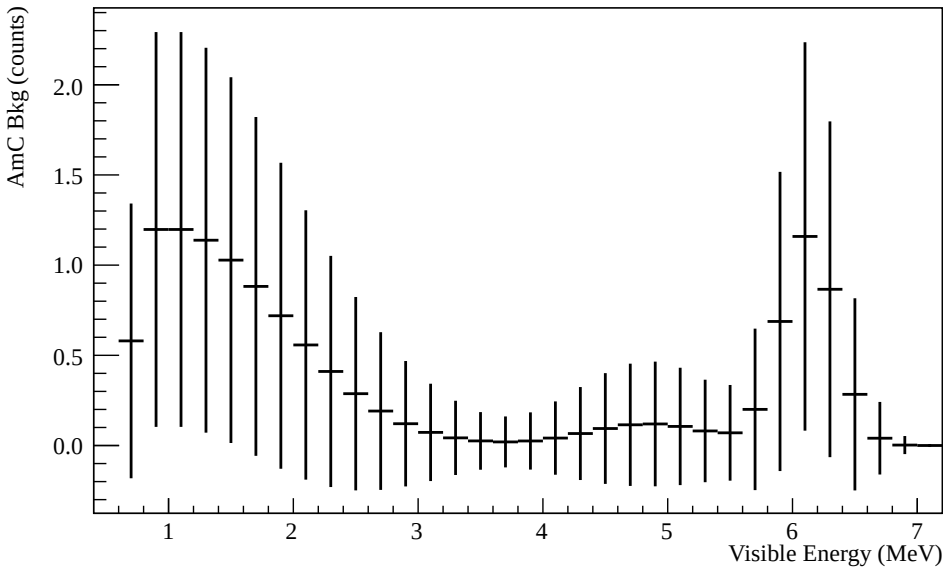


Figure 8.14 The C(α, n)O spectrum for Detector 1, from [78].

8.1.1.12 Detector and Energy Bin Normalizations

Last, there are three normalizations applied to the predicted antineutrino fluxes: detector-uncorrelated, overall-correlated, and energy bin. The detector-uncorrelated normalization uncertainty concerns the differences in overall efficiency across detectors; it is dominated by the relative uncertainty in the delayed energy cut efficiency. The detector-uncorrelated normalization is broken down into a general detector efficiency, and an energy-scale-dependent component. The energy scale contribution to the detector normalization is related to reconstructing the energy at the delayed energy cut.

The overall (reactor, detector and energy) correlated uncertainty is calculated from the uncertainty in absolute detection efficiency, which is more difficult to understand than detector-to-detector differences, combined with power uncertainties across all reactors.

The bin normalization parameters are uncorrelated among energy bins but correlated among detectors and reactors. The nuisance parameters are regulated by pull terms for each bin determined by the size of the combined reactor and detector systematic uncertainties. The reactor contribution comes from the $\beta \rightarrow \bar{\nu}$ conversion process, including the ^{238}U contribution, which is itself divided into two components. The reactor-correlated/energy-correlated $\beta \rightarrow \bar{\nu}$ effect was discussed in Section 8.1.1.5. The reactor-correlated/energy-uncorrelated $\beta \rightarrow \bar{\nu}$ component contributes to the bin normalization, and can be seen in Figure 8.5. The detector contributions comes from the energy-uncorrelated/detector-correlated component of the IAV uncertainty, seen in Figure 8.7. Figure 8.15 shows the bin normalization uncertainties with all three contributions combined.

8.1.2 χ^2 Model

The Pearson [202] χ^2 model for Daya Bay is too complicated a function to comprehensibly record in one equation. Starting with the initial predicted reactor spectra F_{bcd}, the steps

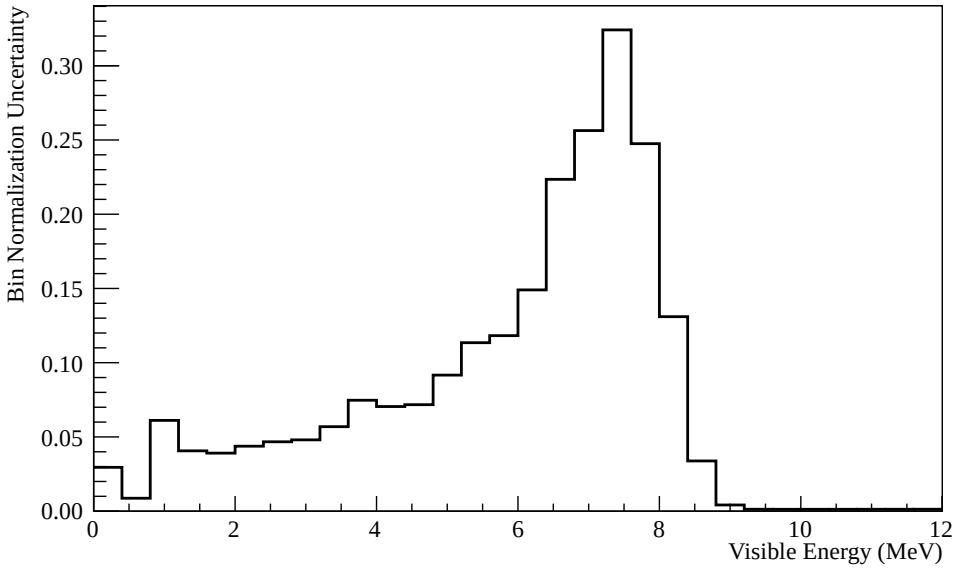


Figure 8.15 The magnitude of the energy-uncorrelated/detector-reactor-correlated bin normalization uncertainty. Due to the $\beta \rightarrow \bar{\nu}$ and IAV uncertainties, each bin can fluctuate in the fit according to the uncertainty above.

below describe the corrections performed to arrive at the final as-detected antineutrino prediction, which is compared to data to calculate the oscillation parameters. This culminates in the χ^2 functions of Equations 8.17 and 8.18.

1. Start with the initial predicted spectra at each reactor, integrating reactor power over the fuel composition, detector live-time and the data period:

   F_{bcd}, for detector d, reactor c, energy bin b.

2. Include fission fraction uncertainty spectra T_b with nuisance parameter η_c^{FF}. The expected baseline fission fraction contribution is already included in the predictions—the fit is for any excess or deficit.

   $F_{bcd} + \eta_c^{FF} T_b$

3. Include the spent nuclear fuel (SNF) uncertainty spectra W_b with nuisance parameter η_c^{SNF}. The expected spent nuclear fuel contribution is already included in F_{bcd}:

   $F_{bcd} + \eta_c^{FF} T_b + \eta_c^{SNF} W_b$

4. Include the nonequilibrium contribution (NEQ) uncertainty spectra V_b with nuisance parameter η_c^{NEQ}. The expected nonequilibrium flux is already included in F_{bcd}:

   $F_{bcd} + \eta_c^{FF} T_b + \eta_c^{SNF} W_b + \eta_c^{NEQ} V_b$

5. Add the reactor-correlated $\beta \to \bar{\nu}$ conversion (CNV) uncertainty spectrum U_b with nuisance parameter η^{CNV}. The baseline contribution is already included in F_{bcd}:

   $F_{bcd} + \eta_c^{FF} T_b + \eta_c^{SNF} W_b + \eta_c^{NEQ} V_b + \eta^{CNV} U_b$

6. Define this as F^*_{bcd}

7. Multiply in the survival probability, $P^{SUR}_{bcd}(L_{cd}, E_b|\theta_{13}, \Delta m^2_{32}, \text{MH})$, where MH is the mass hierarchy, to the flux at each reactor-detector baseline:

   $F^*_{bcd} P^{SUR}_{bcd}(L_{cd}, E_b|\theta_{13}, \Delta m^2_{32}, \text{MH})$

8. Sum the reactor contributions with a normalization nuisance parameter accounting for the uncorrelated reactor power uncertainty:

   $R_{bd} = \sum_c (1 + \eta_c^r) F^*_{bcd} P^{SUR}_{bcd}$

9. Apply the IAV correction matrix M^{IAV}:

   $(R_{bd})^{IAV} = M^{IAV}_{ee'} (R_{bd})_e$

10. Include the IAV uncertainty spectrum (I_b) with nuisance parameter η_d^{IAV}:

    $(R_{bd})^{IAV} + \eta_d^{IAV} I_b$

11. Apply detector response function with four nuisance parameters η_ι^{nl}:

    above, with $E \to \left(1 + f_{nl}(E|\eta_1^{nl} ... \eta_4^{nl})\right) E$

12. Apply relative linear energy scale: $E \to E(1 + \eta_d^{SCL})$:

    above, with $E \to E(1 + \eta_d^{SCL})$

13. Apply detector resolution:

    above, with $E \to f_{res}(E) E$

14. Define the above as R^*_{bd}.

15. Rebin from 240 bins to B bins.

16. Scale R^*_{bd} by the remaining normalization uncertainties for detector efficiency, bin normalization, and overall normalization:

    $R^*_{bd}\left(1+\eta_d+0.24\eta_d^{SCL}\right)(1+\eta_b)(1+\mathcal{H})$

17. Add in background spectra k:

    $R^*_{bd}+\sum_k(1+\eta_d^k)B^k_{bd}$

18. Define this modified prediction as $\widetilde{R}_{bd}$.

19. Compute the χ^2 with modified prediction R^*_{bd} and IBD candidates O_d.

    Exact Logarithmic Formulation:

$$\chi^2(\theta_{13},\Delta m^2_{32}) \;=\; \min(\vec{\eta})\sum_{db}\widetilde{R}_{bd}-O_{bd}+O_{bd}\log\frac{O_{bd}}{\widetilde{R}_{bd}}+\sum_{\iota}\left(\frac{\eta_\iota}{\sigma_\iota}\right)^2+\left(\frac{\eta_{\Delta m^2_{32}}}{\sigma_{\Delta m^2_{32}}}\right)^2 \quad (8.17)$$

    Approximate Quadratic Formulation:

$$\chi^2(\theta_{13},\Delta m^2_{32}) \;=\; \min(\vec{\eta})\sum_{db}\frac{\left(\widetilde{R}_{bd}-O_{bd}\right)^2}{\widetilde{R}_{bd}}+\sum_{\iota}\left(\frac{\eta_\iota}{\sigma_\iota}\right)^2+\left(\frac{\eta_{\Delta m^2_{32}}}{\sigma_{\Delta m^2_{32}}}\right)^2 \quad (8.18)$$

8.1.3 Numerical χ^2 Minimization

The numerical minimizer used in this analysis is a ROOT [203] implementation of Minuit2 [204]. The Migrad algorithm was chosen to perform the minimization, based on reputation and comparison with other algorithms such as Simplex and Fumili. Baseline settings are: Strategy 1 where 0 is cursory and 2 is more thorough; Precision 10^{-8}, which refers to the precision of the minimized χ^2 function; and Tolerance 10^{-5}, which refers to the tolerance of the estimated distance to minimum predicted from the function derivatives $\mathrm{d}\chi^2/\mathrm{d}\eta_\iota$. These settings were found empirically to produce the most accurate results and a reliable minimization. The minimizer is run in multithreading mode, which enables it to calculate on up to 16 parallel processors [205, 206].

8.2 Validation with Internal Monte Carlo

The χ^2 model is validated by fitting the nominal predicted antineutrino flux against a toy Monte Carlo generated from the same flux with imposed characteristics, such as oscillation parameters or systematic distortions. The first test of the fitter is to generate a single Monte Carlo with known, feasible oscillation parameters, no systematics effects, and expectation values in each bin (that is, no statistical fluctuations). This exact Monte Carlo is then fit to recover those oscillation parameter values and all systematic nuisance parameters equal to zero. This important test can determine flaws, especially coding errors, but is limited due to its circularity. Other Monte Carlo validations performed include examining in detail fits to toy Monte Carlo with statistical fluctuations, searching for biases in fits to many Monte Carlo samples with random fluctuations, and fits to independently generated Monte Carlo.

8.2.1 Monte Carlo Generation

Toy Monte Carlo samples are generated from the Huber-French flux predictions corresponding to the full data period, over 240 bins, at each detector. Unless otherwise stated, samples are programmed to exhibit the oscillation parameter values listed in Table 8.3, including $\sin^2 2\theta_{13} = 0.10$ and $\Delta m^2_{32} = 2.32{\cdot}10^{-3}\,\mathrm{eV}^2$, and normal hierarchy. The Monte Carlos are constructed with all systematics as modeled in Section 8.1.1, but unless indicated otherwise, systematic nuisance parameters are set to zero, signifying no systematic distortions. All static corrections like the energy smearing are included, as well as the nominal background contamination.

Fluctuations of statistics and systematic nuisance parameters are induced in some samples for dedicated tests. Accordingly, Poisson statistical fluctuations are applied to each of the 240 bins before rebinning down to N_{bins}. Systematic nuisance parameters are varied according to a Gaussian at zero with a width equal to the given systematic uncertainty.

8.2.2 Validation on Monte Carlo Without Statistical Fluctuations

The initial test of the fitter is to construct Monte Carlo samples with known oscillation probabilities, without statistical fluctuations or systematic effects, then measure the correct oscillation values in a fit comparing this Monte Carlo to the nominal flux prediction. In this case, the fitter recovers the correct oscillation parameters ($\sin^2 2\theta_{13} = 0.10$ and $\Delta m^2_{32} = 2.32{\cdot}10^{-3}\,\mathrm{eV}^2$) to one part in 10^5 to 10^6, and systematic nuisance parameters (all $\eta_\iota = 0$) to at most one part in 10^4. These precisions are at level of the numerical minimizer tolerance. The fit takes place with unconstrained oscillation parameters over 24 energy bins, assuming normal hierarchy. Figures 8.16 through 8.20 provide the best fit $\Delta\chi^2$ ($\Delta\chi^2 \equiv \chi^2 - \chi^2_{min}$) versus $\sin^2 2\theta_{13}$, Δm^2_{32} and the overall normalization parameter $\mathcal{H}$, while Figures 8.21 through 8.23 show diagnostics.

8.2.2.1 Best Fits

The measured values of oscillation and systematic nuisance parameters on the exact Monte Carlo sample are:

- $\sin^2 2\theta_{13} = 0.0999982^{+0.008850}_{-0.008793}$
- $\Delta m^2_{32} = 2.32003^{+0.179}_{-0.190}{\cdot}10^{-3}\,\mathrm{eV}^2$
- $\mathcal{H} = (-3.31842 \cdot 10^{-6})^{+0.029796}_{-0.028551}$
- all other $\eta_\iota < 10^{-4}$
- $\chi^2_{min} = 1.84677$.

The resulting χ^2 is approximately symmetric in the region of $0.6 < \sin^2 2\theta_{13} < 0.14$, or $\pm 4\sigma$, while plateauing for larger values of $\sin^2 2\theta_{13} > \sim 0.20$. Figure 8.17, $\Delta\chi^2(\sin^2 2\theta_{13},\ \Delta m^2_{32})$, demonstrates that this is due to the interplay of $\sin^2 2\theta_{13}$ and Δm^2_{32}, for which a detailed explanation is presented in Section 9.1.1. Figures 8.18 and 8.19 show the $\Delta\chi^2$ as a function of Δm^2_{32} and $\mathcal{H}$ respectively.

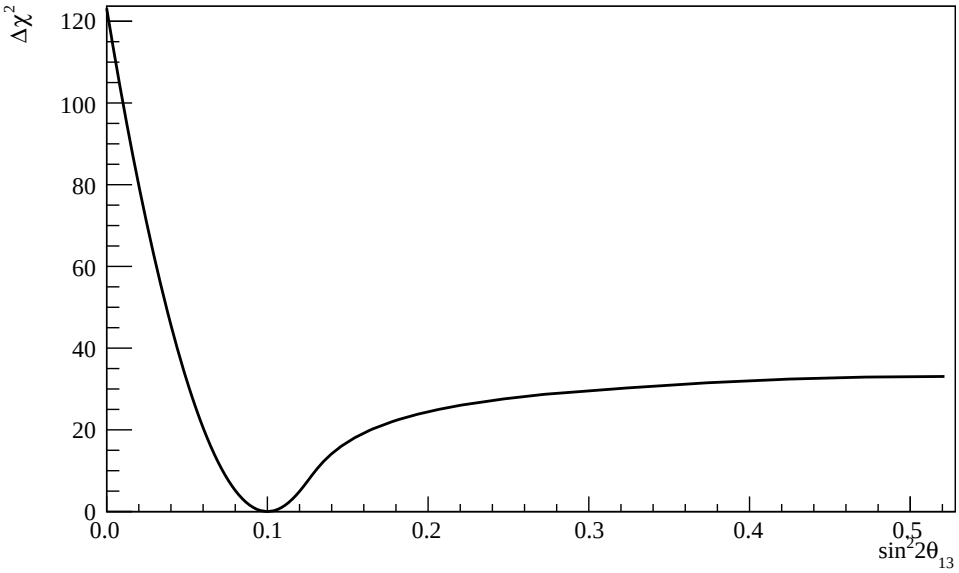


Figure 8.16 $\Delta\chi^2(\sin^2 2\theta_{13})$ for a fit to Monte Carlo with no statistical fluctuations, generated with $\sin^2 2\theta_{13} = 0.10$ and $\Delta m^2_{32} = 2.32{\cdot}10^{-3}\,\mathrm{eV}^2$.

8.2.2.2 Best Fit Diagnostics

Figures 8.21 and 8.22 provide the covariance and correlation matrices. The covariance matrix is approximately diagonal with the largest on-diagonal elements among small scale uncertainties like high energy bin normalizations, and IAV and reactor systematic normalizations. The off-diagonal elements are small, with the greatest entries among the detector response nonlinearity and reactor systematics.

The correlation matrix exhibits its largest correlations among the normalization parameters on adjacent energy bins, and among energy bins and detector response parameters. This is to be expected because adjacent bins are similar in energy and should fluctuate together. Meanwhile, the detector response parameters and the overall normalization should be highly correlated with the energy bin normalizations because the latter are the most general spectral adjustment made.

Figure 8.23 shows the correlations of the oscillation parameters specifically with each other and all the systematic nuisance parameters. The correlations typically range within ± 0.2. $\sin^2 2\theta_{13}$ is much more correlated with detector normalization parameters than is Δm^2_{32}, while Δm^2_{32} its most correlated with the normalization of the small AmC flux at low energies.

The diagnostic plots compare well to those calculated during the fit to data, seen in Figures 9.6 through 9.8. The covariance and correlation matrices are nearly identical between Monte Carlo and data; the correlations among oscillation parameters and systematics vary only on the order of 0.01. This demonstrates that the Monte Carlo and data spectra are similar enough that the matrices are determined almost entirely by the construction of the model.

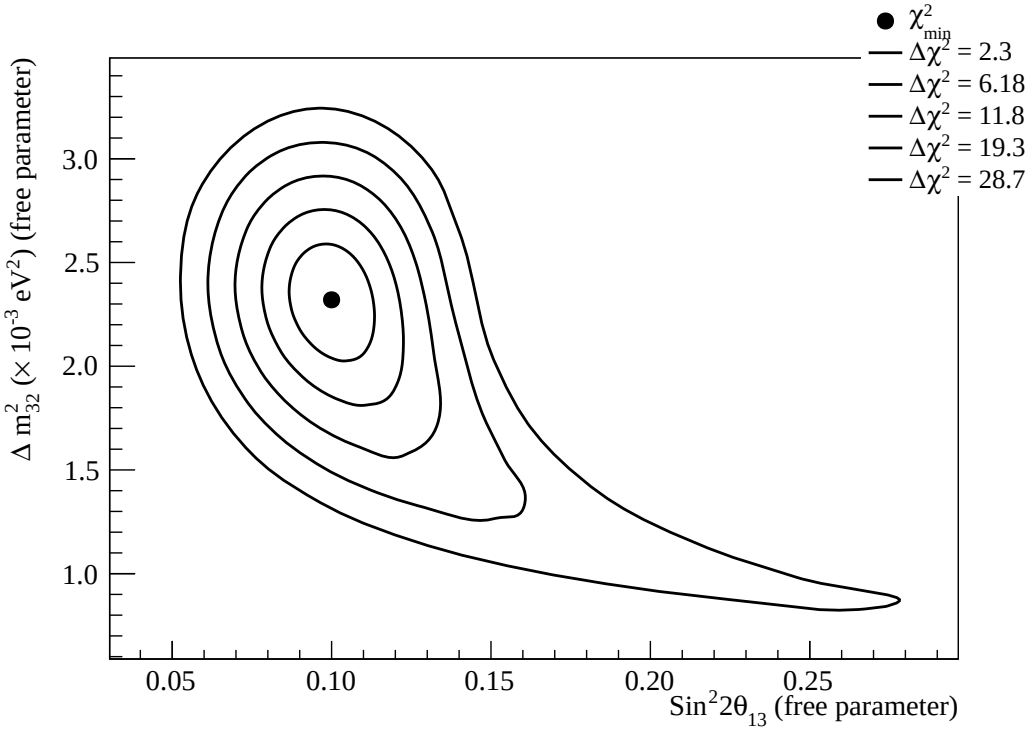


Figure 8.17 $\Delta\chi^2(\sin^2 2\theta_{13},\, \Delta m^2_{32})$ for a fit to Monte Carlo with no statistical fluctuations, generated with $\sin^2 2\theta_{13} = 0.10$ and $\Delta m^2_{32} = 2.32{\cdot}10^{-3}\,\mathrm{eV}^2$.

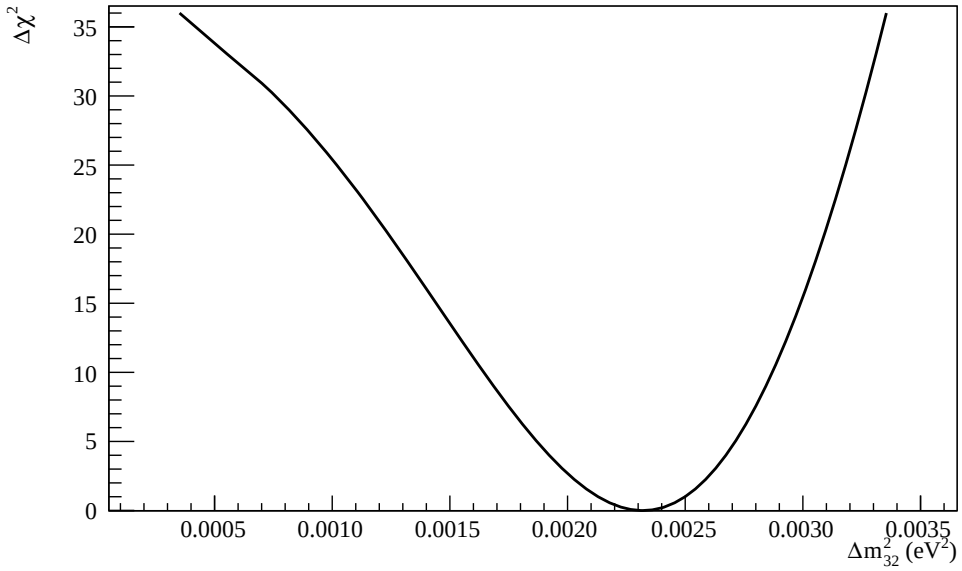


Figure 8.18 $\Delta\chi^2(\Delta m^2_{32})$ for a fit to Monte Carlo with no statistical fluctuations, generated with $\sin^2 2\theta_{13} = 0.10$ and $\Delta m^2_{32} = 2.32{\cdot}10^{-3}\,\mathrm{eV}^2$.

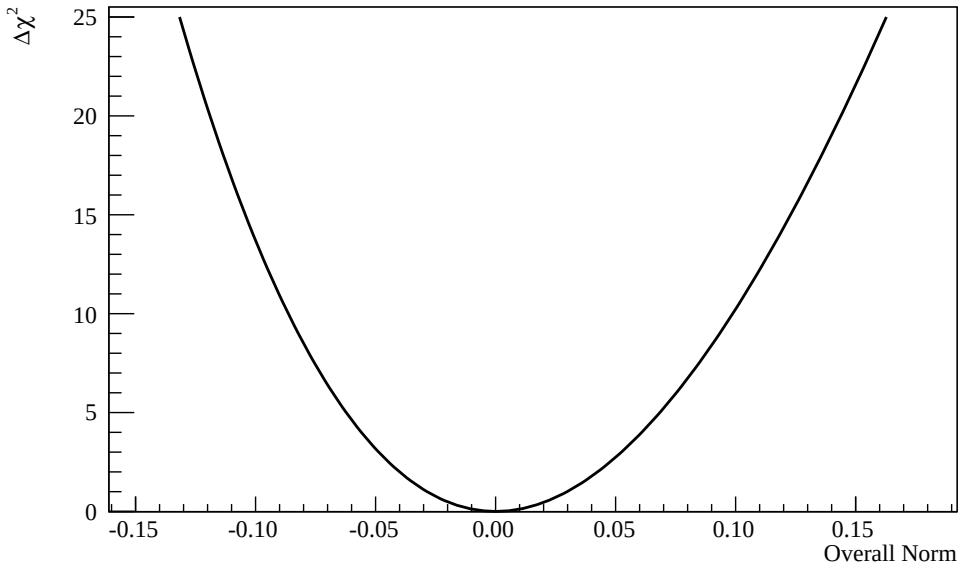


Figure 8.19 $\Delta\chi^2(\mathcal{H})$ for a fit to Monte Carlo with no statistical fluctuations, generated with $\sin^2 2\theta_{13} = 0.10$ and $\Delta m^2_{32} = 2.32{\cdot}10^{-3}\,\mathrm{eV}^2$.

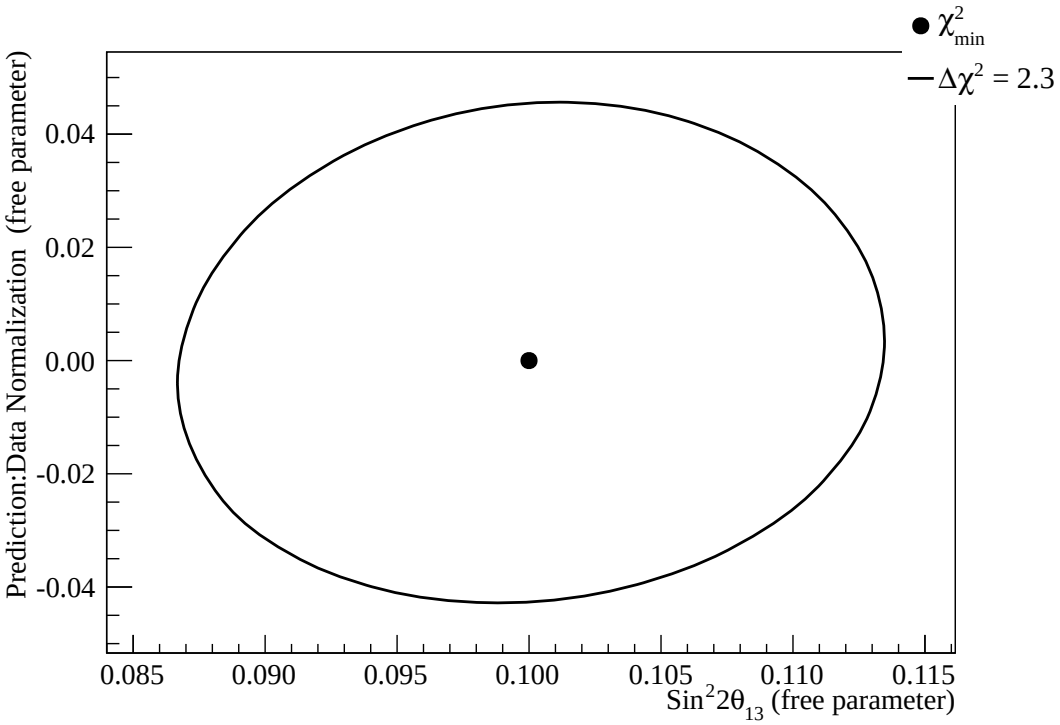


Figure 8.20 $\Delta\chi^2(\sin^2 2\theta_{13}, \mathcal{H})$ for a fit to Monte Carlo with no statistical fluctuations, generated with $\sin^2 2\theta_{13} = 0.10$ and $\Delta m^2_{32} = 2.32{\cdot}10^{-3}\,\mathrm{eV}^2$.

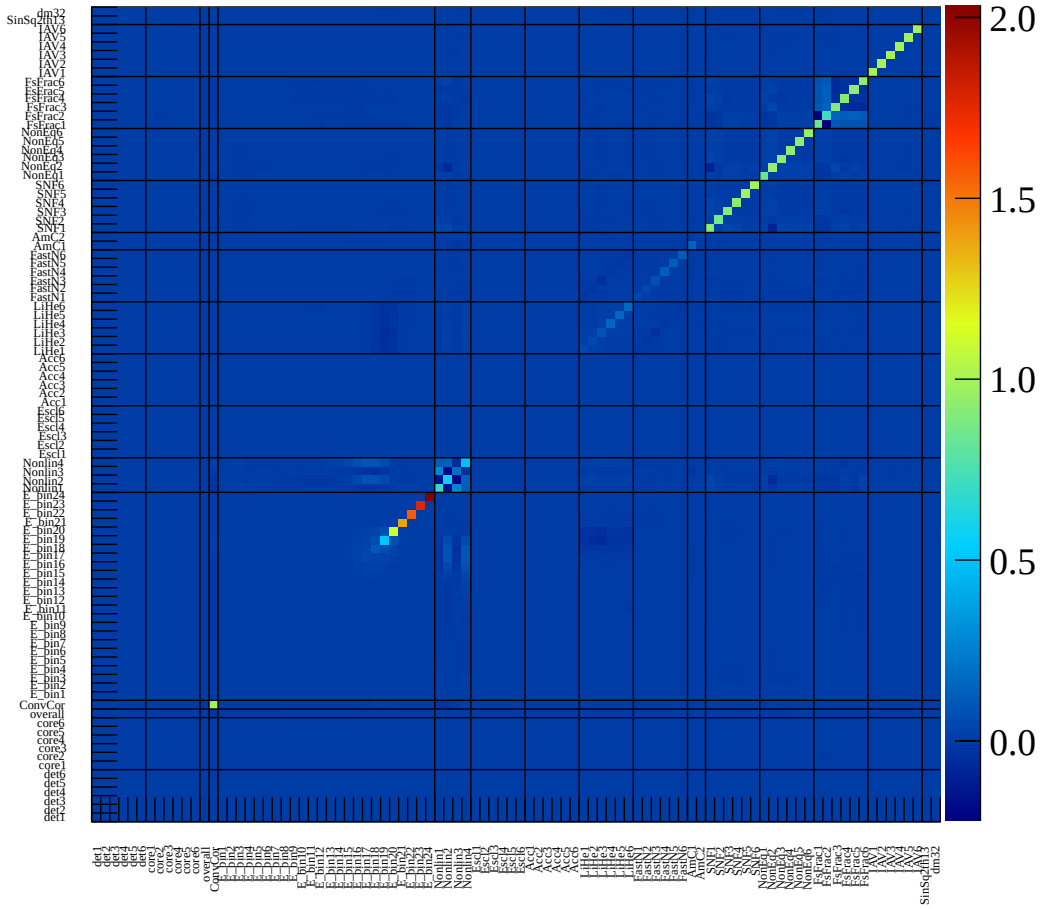


Figure 8.21 For a validation Monte Carlo sample without statistical fluctuations, the covariance matrix is shown. Variable names are listed on the axes.

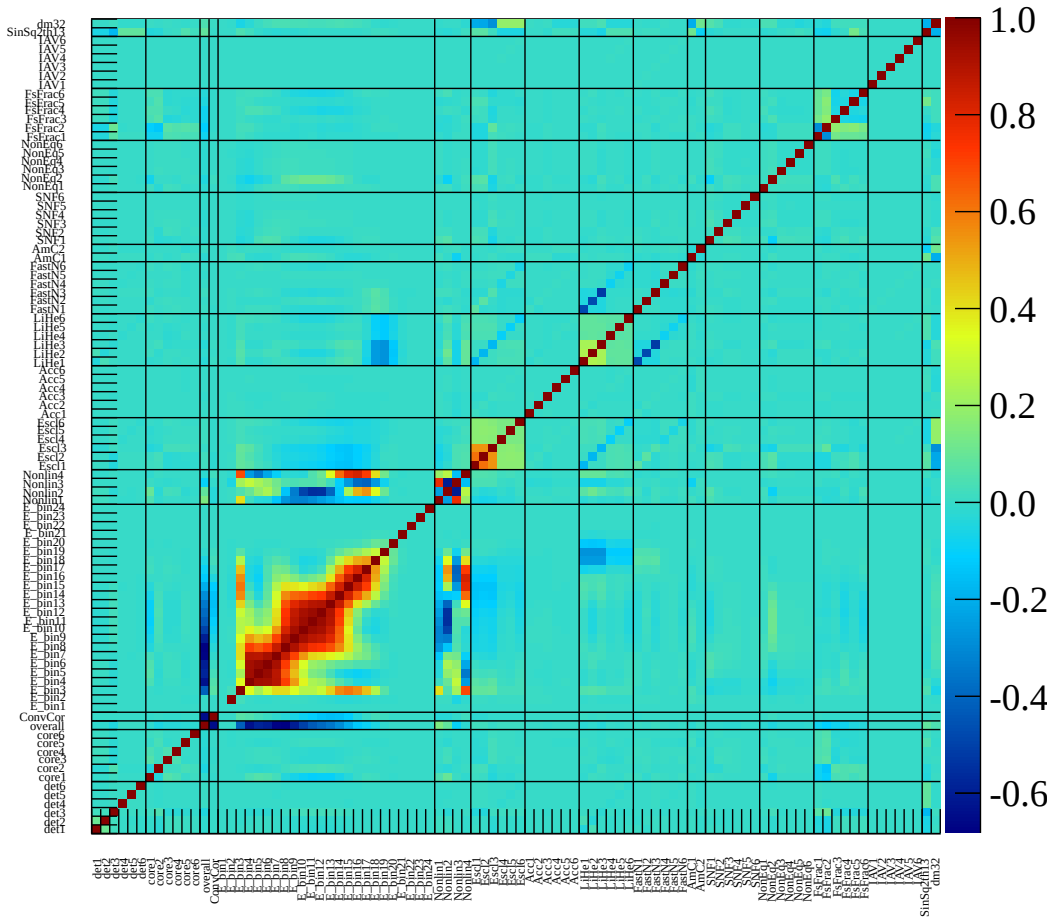


Figure 8.22 For a validation Monte Carlo sample with no statistical fluctuations, a matrix of fit parameter correlations is shown. Variable names are listed on the axes.

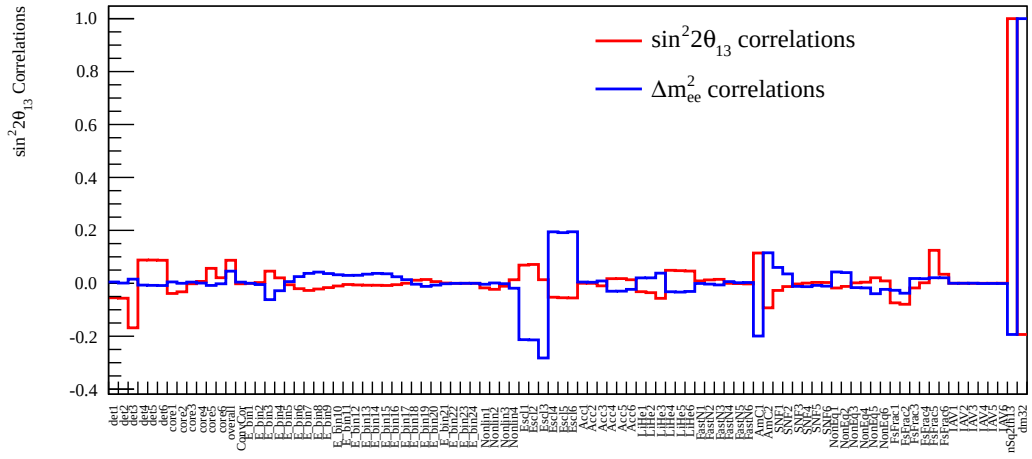


Figure 8.23 For a validation Monte Carlo sample with no statistical fluctuations, the correlations of oscillation parameters with systematic nuisance parameters are shown. Variable names are listed on the axes.

8.2.2.3 Accuracy over Wider $\sin^2 2\theta_{13}$ and Δm^2_{32} Ranges

It is crucial for the fitter to be reliable over a wide range of potential oscillation values, and that any limitations are noted. The range of accuracy of the model is verified by testing on Monte Carlo samples generated with all systematic nuisance parameters fixed to zero, no statistical fluctuations, and oscillation parameters varied over the following ranges:

$$0 < \sin^2 2\theta_{13} < 0.2$$

$$0 < \Delta m^2_{32} < 4.64 \cdot 10^{-3}\,\mathrm{eV}^2\,.$$

The upper limits are twice the test values of 0.10 and $2.32{\cdot}10^{-3}\,\mathrm{eV}^2$.

A series of standard fits were performed with oscillation parameters varied over the full range in a 21×21 grid, in which the starting oscillation values match the inputs. For each point, Figure 8.24 provides the fitted accuracy of $\sin^2 2\theta_{13}$ and Δm^2_{32}, the χ^2_{min} value, and numerical minimizer success [79]. The model converges over a wider range of $\sin^2 2\theta_{13}$ and Δm^2_{32} than is expected to be observed at Daya Bay [1, 68]. Over this anticipated span, the inaccuracy is much smaller than the uncertainty of the individual measurements, about one part in 10^5. The measurements do exhibit difficulty in the low oscillation limit, the approximate ranges of $\Delta m^2_{32} < 1{\cdot}10^{-3}\,\mathrm{eV}^2$, $\sin^2 2\theta_{13} < 0.01$ and the combination of $\Delta m^2_{32} > 4{\cdot}10^{-3}\,\mathrm{eV}^2$ and $\sin^2 2\theta_{13} < 0.05$. This is not surprising or alarming because these conditions represent small and indiscernible oscillation signals, for which Daya Bay would be an awful experiment. In that case, an alternate may be needed, such as directly comparing data to Monte Carlo samples in the fitting process and employing covariance matrices to reduce the number of nuisance parameters [207].

Table 8.4 focuses on five points in particular, representing potential 3σ variation in $\sin^2 2\theta_{13}$ and Δm^2_{32}, and a central value [1, 68]. For ($\sin^2 2\theta_{13}$, Δm^2_{32}) points of (0.07, 2.05), (0.07, 2.65), (0.10, 2.35), (0.13, 2.05), and (0.13, 2.65), where the units of Δm^2_{32} as listed are $10^{-3}\mathrm{eV}^2$, the fitter reproduces the expected parameter values within 30 ppm or less. Notably,

the error bars on $\sin^2 2\theta_{13}$ and Δm^2_{32} correlate to the size of the oscillation signal: the larger the oscillation, the smaller the error bar as expected. The size of the error bar on $\mathcal{H}$ does not track the oscillation signal strength since it is unrelated to the signal.

Expected	$\sin^2 2\theta_{13}$: 0.07, 0.10 or 0.13	Relative Difference: ~0	Δm^2_{32}: 2.05, 2.35 or 2.65 $\cdot 10^{-3}\,\mathrm{eV}^2$	Relative Difference: ~0	Overall Normalization: ~0	χ^2_{min}: ~0
Rate+Shape	$0.0999981^{+0.008313}_{-0.008322}$	$-1.9\cdot10^{-5}$	$2.35002^{+0.169}_{-0.179}$	$8.5\cdot10^{-6}$	$-0.000006^{+0.032922}_{-0.031684}$	$-5.7\cdot10^{-6}$
Rate+Shape	$0.0699965^{+0.011297}_{-0.009596}$	$-3.5\cdot10^{-5}$	$2.05007^{+0.280}_{-0.235}$	$3.4\cdot10^{-5}$	$-0.000003^{+0.032962}_{-0.031476}$	$-2.8\cdot10^{-6}$
Rate+Shape	$0.129998^{+0.010146}_{-0.009436}$	$-2.0\cdot10^{-5}$	$2.05003^{+0.113}_{-0.161}$	$1.5\cdot10^{-5}$	$-0.000013^{+0.032981}_{-0.031691}$	$-1.3\cdot10^{-5}$
Rate+Shape	$0.0699979^{+0.008425}_{-0.008463}$	$-2.1\cdot10^{-5}$	$2.65002^{+0.224}_{-0.239}$	$7.5\cdot10^{-6}$	$0.000009^{+0.032986}_{-0.031436}$	$8.5\cdot10^{-6}$
Rate+Shape	$0.129999^{+0.008010}_{-0.008069}$	$-1.0\cdot10^{-5}$	$2.65002^{+0.119}_{-0.091}$	$7.5\cdot10^{-6}$	$-0.000016^{+0.032656}_{-0.031740}$	$-1.6\cdot10^{-5}$

Table 8.4 Fits to a five-point grid of $\sin^2 2\theta_{13}$ and Δm^2_{32}: (0.01, $2.35\cdot10^{-3}\,\mathrm{eV}^2$), (0.07, $2.05\cdot10^{-3}\,\mathrm{eV}^2$), (0.13, $2.05\cdot10^{-3}\,\mathrm{eV}^2$), (0.07, $2.65\cdot10^{-3}\,\mathrm{eV}^2$), (0.13, $2.65\cdot10^{-3}\,\mathrm{eV}^2$), with rate+shape and rate-only χ^2s. The fitter replicates the expected results to at least 30 parts per million.

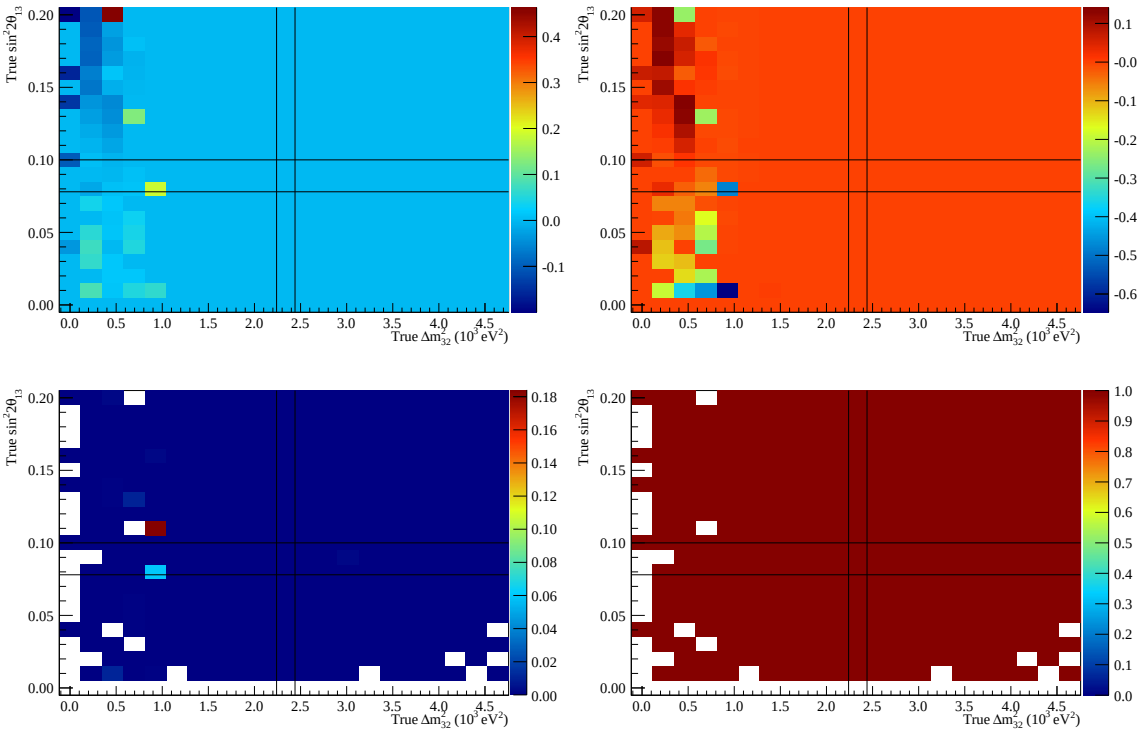


Figure 8.24 The accuracy of the fitter is verified using Monte Carlo samples generated with oscillation parameters sampled over the ranges $0 \geq \sin^2 2\theta_{13} \geq 0.2$ and $0 \geq \Delta m^2_{32} \geq 4.64 \cdot 10^{-3}\,\mathrm{eV}^2$. Clockwise from the top left the plots show: $(\sin^2 2\theta_{13}\big|_{fitted} - \sin^2 2\theta_{13}\big|_{true})$, $(\Delta m^2_{32}\big|_{fitted} - \Delta m^2_{32}\big|_{true})$, χ^2_{min} and fit success or failure. The axes indicate the oscillation parameter values used to generate the Monte Carlo sample at that point. The thin horizontal and vertical lines indicate the previous measurement error bars on $\sin^2 2\theta_{13}$ and Δm^2_{32} respectively [68, 1]. Note that failures of the fit appear as zero in all the plots.

8.2.2.4 Error Budget

The error budget is a measure of the contribution of each systematic to the total uncertainty margin of the measured $\sin^2 2\theta_{13}$ and Δm^2_{32}. The contribution of a systematic is determined from both its physical significance within the model, and the magnitude of the uncertainty. For instance, the detector normalization uncertainty is highly important because it directly competes with the interpretation of rate deficits as oscillation signals, however its magnitude is much smaller than the other uncertainties. Hence, it lies in the middle of the error budget. The overall normalization in contrast is less physically important as a systematic because its effect does not resemble an oscillation signal, but it is unconstrained in the fit, pushing it toward the top of the list.

The error budget is established by first finding the error bar for the chosen oscillation parameter from a fit to a statistics-only χ^2. Then, for each systematic uncertainty, another fit is performed with that systematic alone enabled in the χ^2. All other systematic fit parameters are fixed to zero. The contribution of that systematic uncertainty is defined as the resulting uncertainty minus the statistics-only uncertainty, in quadrature:

$$\sigma_{sys} \equiv \sqrt{\sigma^2_{stat\,only} - \sigma^2_{stat+sys}}\,. \tag{8.19}$$

Table 8.5 shows the uncertainty contributions normalized to 100%.

Systematic	$\sin^2 2\theta_{13}$ (%)	Δm^2_{32} (%)
None (statistics only)	19.2	20.1
Bin normalization	14.4	12.4
Overall normalization	11.7	11.9
$\beta \to \bar{\nu}$ conversion	9.5	11.1
Energy scale	6.8	12.5
Fission fraction	7.9	9.8
Reactor normalization	6.9	7.2
Backgrounds	6.5	5.4
Detector normalization	2.9	4.4
Detector response	5.1	3.6
Nonequilibrium	5.2	1.8
Spent nuclear fuel	4.0	0.0
IAV	0.0	0.0

Table 8.5 The error budget for a Monte Carlo without statistical fluctuations. The size of each contribution is a determined by a trade off between the physical importance of the uncertainty and its magnitude. Important systematics like the detector uncorrelated normalization are understated because the uncertainty value is small.

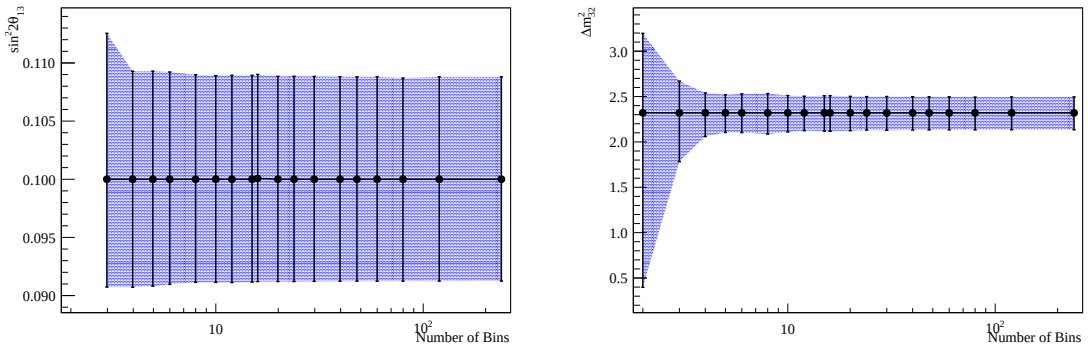


Figure 8.25 Measurements of $\sin^2 2\theta_{13}$ and Δm^2_{32} on a toy Monte Carlo samples without fluctuations, as a function of N_{bins}. Left: $\sin^2 2\theta_{13}$, right: Δm^2_{32}. As the number of bins increases, the spectral distortion information becomes better resolved, which results in a stronger Δm^2_{32} measurement. The measurement of $\sin^2 2\theta_{13}$ is less dependent on shape information.

8.2.2.5 Best Fits Versus N_{bins}

The plots in Figure 8.25 show the best fit $\sin^2 2\theta_{13}$ and Δm^2_{32} to the same Monte Carlo sample with no statistical fluctuations, rebinned down to various N_{bins}. The measurement central values of both parameters are independent of the number of bins, but the error bars vary. The precision of the fit to Δm^2_{32} depends greatly on the number of bins as more bins better resolve the spectral information necessary to measure Δm^2_{32}. Since $\sin^2 2\theta_{13}$ is primarily a rate-based measurement, the precision of $\sin^2 2\theta_{13}$ versus N_{bins} is largely flat.

8.2.3 Validation on Monte Carlo with Statistical Fluctuations

In addition to testing on expectation value Monte Carlo, which was discussed in Section 8.2.2, fits to a Monte Carlo sample with statistical fluctuations are described below. As before, the Monte Carlo are constructed with $\sin^2 2\theta_{13} = 0.10$, $\Delta m^2_{32} = 2.32{\cdot}10^{-3}\,\mathrm{eV}^2$, normal hierarchy and rebinned to 24 energy bins. Figures 8.26 though 8.30 show the χ^2 as a function of $\sin^2 2\theta_{13}$, Δm^2_{32} and the overall normalization $\mathcal{H}$. Figures 8.31 through 8.35 show a slate of diagnostics including the covariance matrix, correlations and nuisance parameter distributions.

Unsurprisingly, there are few differences among the best fits to both Monte Carlo. The parameters measured based on the fluctuated are as follows:

- $\sin^2 2\theta_{13} = 0.101832^{+0.008542}_{-0.008567}$
- $\Delta m^2_{32} = 2.45398^{+0.165}_{-0.174}{\cdot}10^{-3}\,\mathrm{eV}^2$
- $\mathcal{H} = 0.00444054^{+0.030077}_{-0.028530}$
- $\chi^2_{min} = 91.2207$. $\mathrm{N_{DOF}} = 6{*}24{-}3$. $\chi^2/\mathrm{N_{DOF}} = 0.646956$.

The oscillation parameter values are consistent with the exact Monte Carlo case well within 1σ, and the $\chi^2_{min} < 1$. However, the error bars on $\sin^2 2\theta_{13}$ and Δm^2_{32} have decreased by about 5%. Aside from the slight shifts in $\sin^2 2\theta_{13}$ and Δm^2_{32}, the χ^2 contours look similar between the two cases. The $\Delta\chi^2(\sin^2 2\theta_{13})$ and $\Delta\chi^2(\Delta m^2_{32})$ for the fluctuated Monte Carlo (Figures 8.26 and 8.27) are deeper and more narrow. The plateau for high $\sin^2 2\theta_{13}$ occurs at the same $\sin^2 2\theta_{13}$ value, but at a higher χ^2 value. This is also seen in the $\Delta\chi^2(\sin^2 2\theta_{13}, \Delta m^2_{32})$ contour in Figure 8.29: the protrusion at high $\sin^2 2\theta_{13}$-low Δm^2_{32} is mitigated. The deeper χ^2 curve and ensuing smaller error bars suggest that the statistical fluctuations reduce the set of solutions in $\sin^2 2\theta_{13}$ and Δm^2_{32} at a given confidence limit. The χ^2 contours involving $\mathcal{H}$ are unchanged.

The measurement diagnostics have also changed little between the two cases. The covariance matrices are nearly identical, while the correlations among systematics are slightly

greater in the fluctuated Monte Carlo. (Compare Figures 8.31–8.33 to corresponding plots in Section 8.2.2.2). Larger correlations, for instance, are seen among more energy bins in the fluctuated Monte Carlo rather than just among local bins in the exact Monte Carlo. Also, the detector shape and bin effects are more interrelated in the fluctuated case, including the bin, overall and $\beta \to \bar{\nu}$ normalizations, and the detector response parameters. The correlations between oscillation parameters and systematics are approximately preserved as well. The largest change in these correlations is among the Δm^2_{32} parameter and the backgrounds normalizations. However, as with the no fluctuations case, the correlations are still small, mostly below 0.2 in magnitude.

Finally, Figures 8.34 and 8.35 provide the distribution of nuisance parameters divided by uncertainties. Most quotients are less than one in magnitude, and their histogram exhibits a narrow peak about zero. Of these nuisance parameter divided by uncertainty values, the largest concern the energy scale of detectors three and six. However, there is no pattern among the energy scales at all detectors, so the cause is likely random. For instance, there are no patterns among detectors at the same site or near versus far. These values compare trivially to the case of exact Monte Carlo, in which all nuisance parameters are at or near zero.

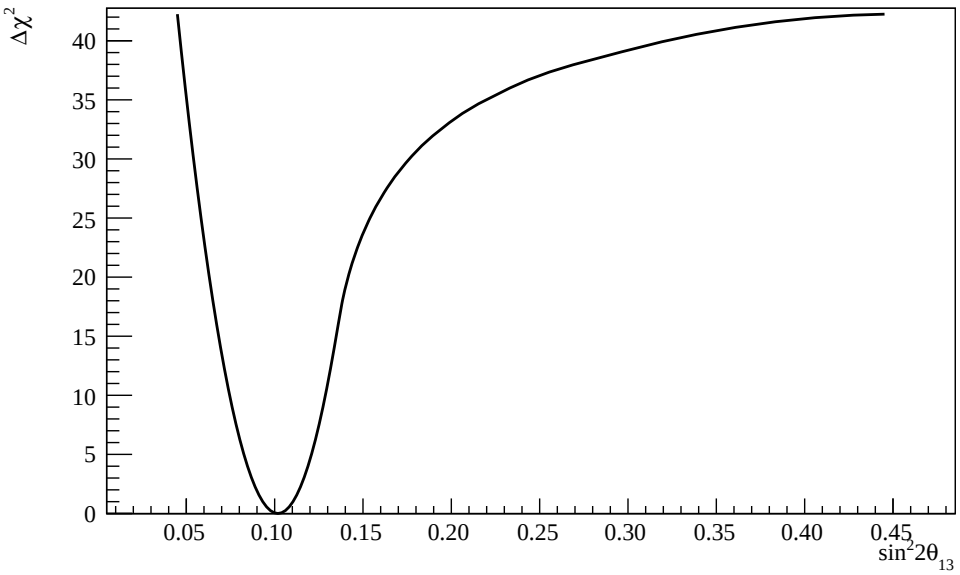


Figure 8.26 $\Delta\chi^2(\sin^2 2\theta_{13})$ for a Monte Carlo programmed with $\sin^2 2\theta_{13} = 0.10$ and Δm^2_{32} $= 2.32{\cdot}10^{-3}\,\mathrm{eV}^2$, with statistical fluctuations, and fit over 24 energy bins.

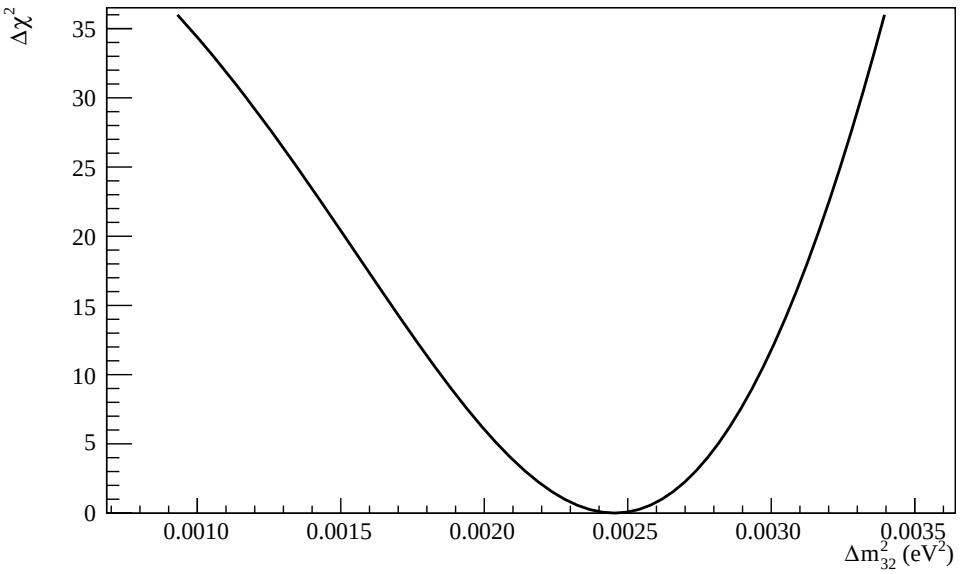


Figure 8.27 $\Delta\chi^2(\Delta m^2_{32})$ for a Monte Carlo programmed with $\sin^2 2\theta_{13} = 0.10$ and $\Delta m^2_{32} = 2.32{\cdot}10^{-3}\,\mathrm{eV}^2$, with statistical fluctuations, and fit over 24 energy bins.

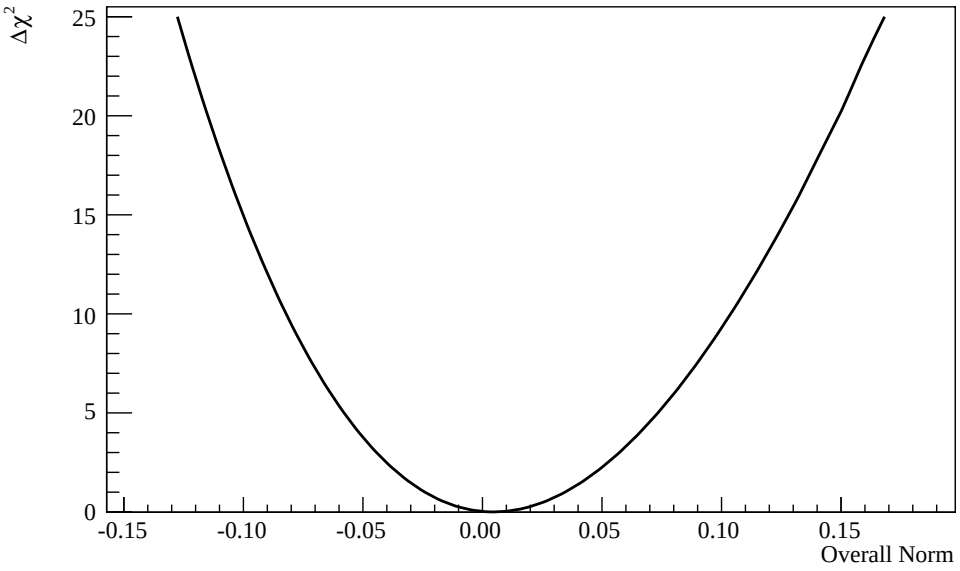


Figure 8.28 $\Delta\chi^2(\mathcal{H})$ for a Monte Carlo programmed with $\sin^2 2\theta_{13} = 0.10$ and $\Delta m^2_{32} = 2.32{\cdot}10^{-3}\,\mathrm{eV}^2$, with statistical fluctuations, and fit over 24 energy bins.

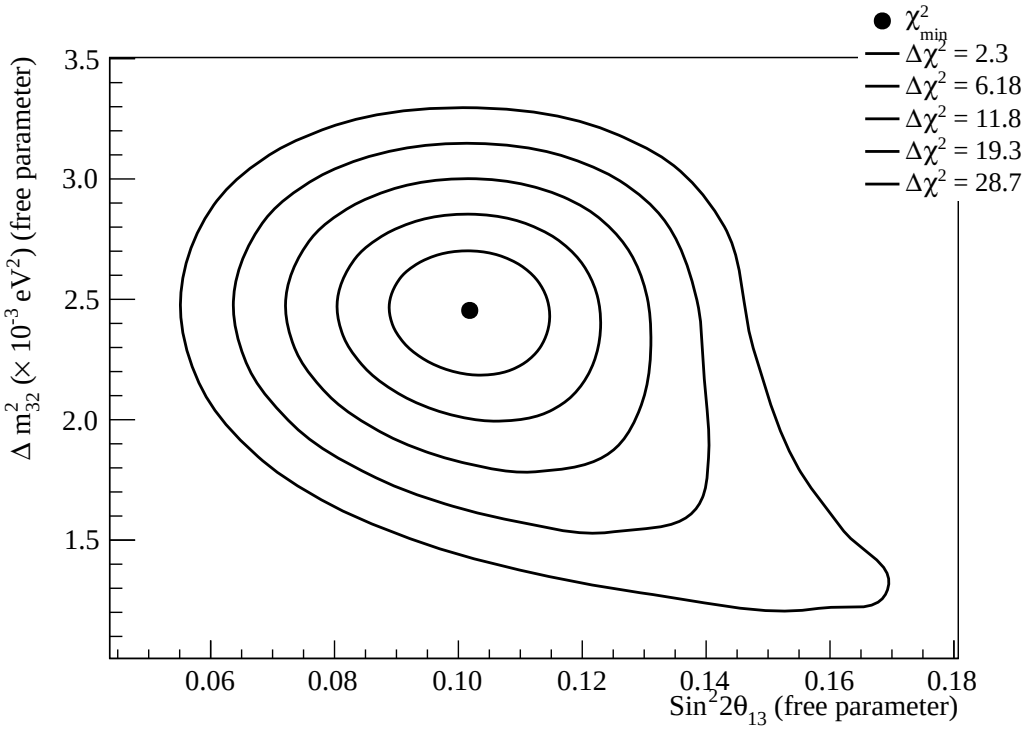


Figure 8.29 $\Delta\chi^2(\sin^2 2\theta_{13},\, \Delta m^2_{32})$ for a validation Monte Carlo run. The Monte Carlo is programmed with $\sin^2 2\theta_{13} = 0.10$ and $\Delta m^2_{32} = 2.32{\cdot}10^{-3}\,\mathrm{eV}^2$, with statistical fluctuations, and fit over 24 energy bins. Compared with Figure 8.17, the tail at high $\sin^2 2\theta_{13}$ and low Δm^2_{32} has abated.

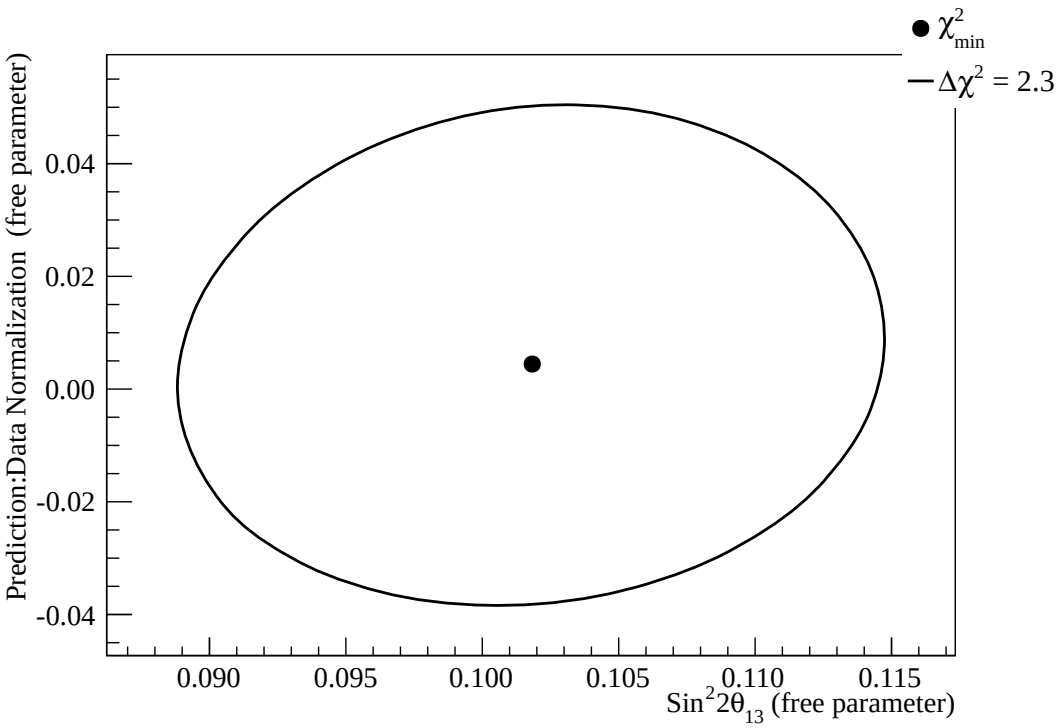


Figure 8.30 $\Delta\chi^2(\sin^2 2\theta_{13}, \mathcal{H})$ for a validation Monte Carlo run. The Monte Carlo is programmed with $\sin^2 2\theta_{13} = 0.10$ and $\Delta m^2_{32} = 2.32{\cdot}10^{-3}\,\mathrm{eV}^2$, with statistical fluctuations, and fit over 24 energy bins.

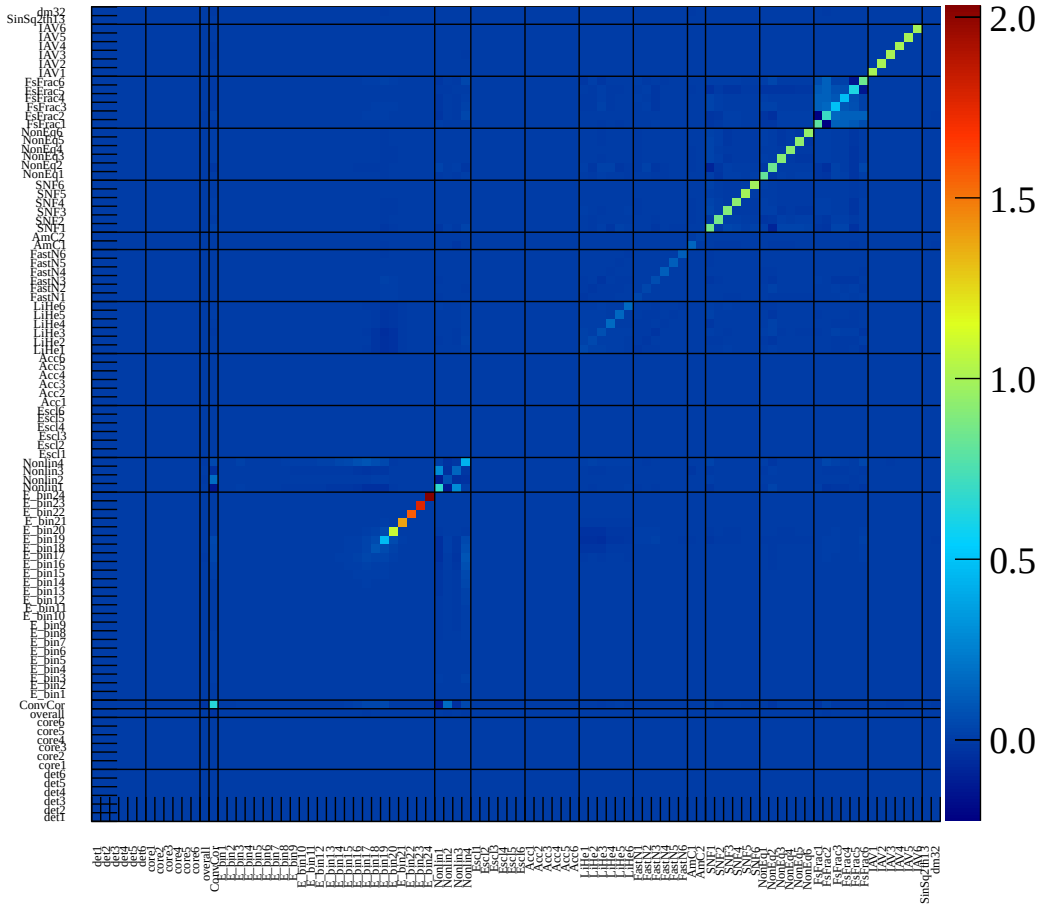


Figure 8.31 Covariance matrix for a Monte Carlo programmed with $\sin^2 2\theta_{13} = 0.10$ and $\Delta m^2_{32} = 2.32{\cdot}10^{-3}\,\mathrm{eV}^2$, with statistical fluctuations, and fit over 24 energy bins. Variable names are listed on the axes.

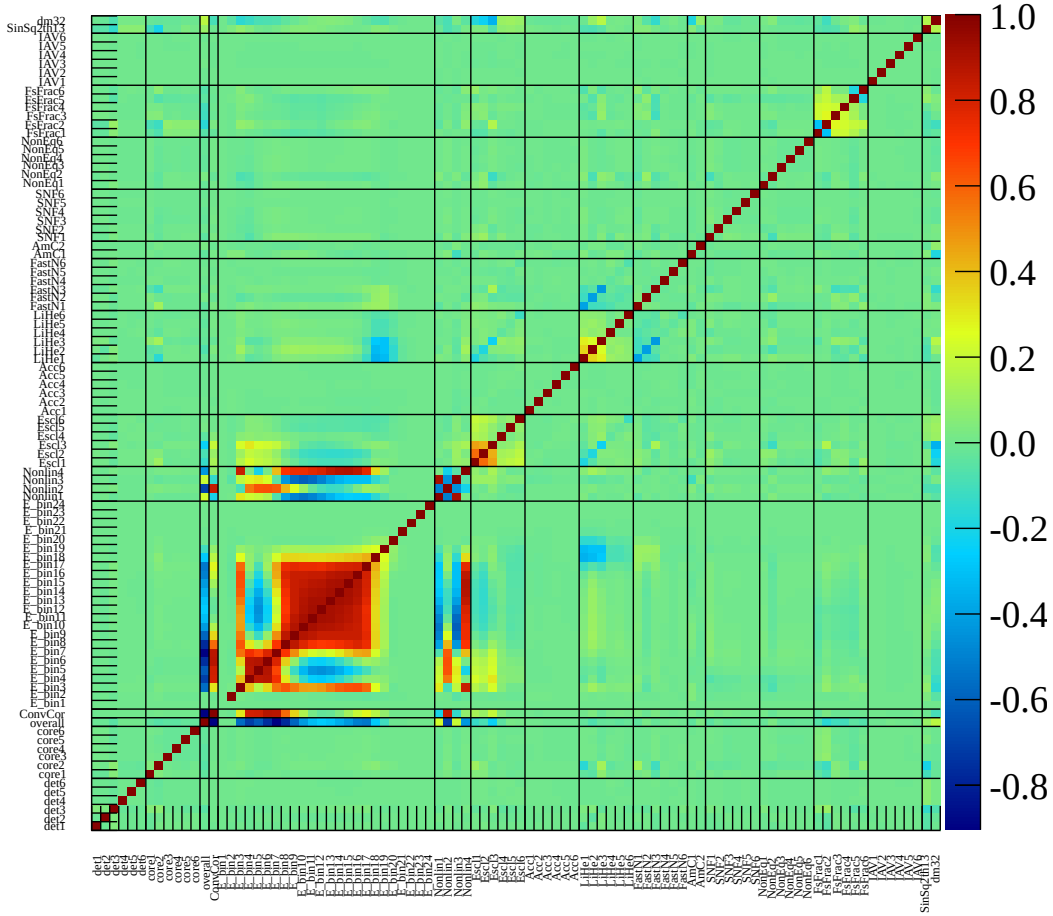


Figure 8.32 Correlation matrix for a Monte Carlo programmed with $\sin^2 2\theta_{13} = 0.10$ and $\Delta m^2_{32} = 2.32{\cdot}10^{-3}\,\mathrm{eV}^2$, with statistical fluctuations, and fit over 24 energy bins. Variable names are listed on the axes.

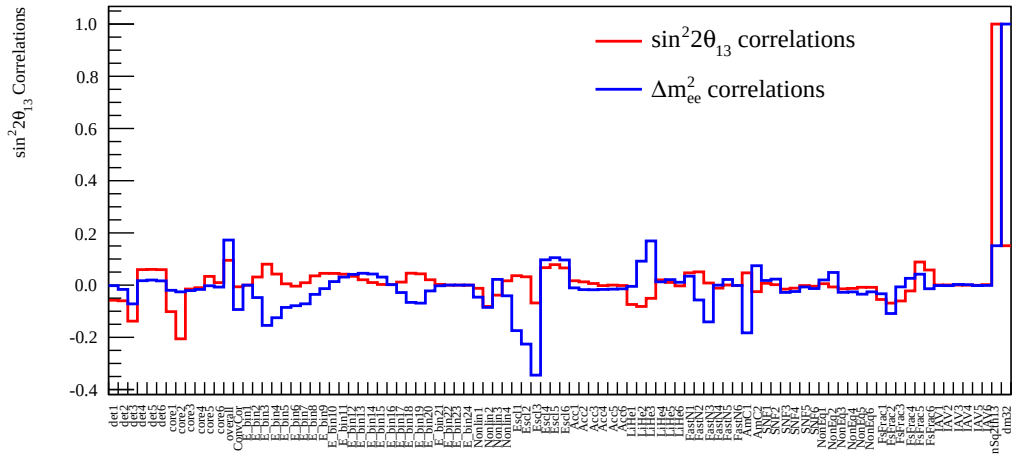


Figure 8.33 Correlations of $\sin^2 2\theta_{13}$ and Δm^2_{32} with systematic fit parameters for a Monte Carlo programmed with $\sin^2 2\theta_{13} = 0.10$ and $\Delta m^2_{32} = 2.32{\cdot}10^{-3}\,\mathrm{eV}^2$, with statistical fluctuations, and fit over 24 energy bins. Variable names are listed on the axes.

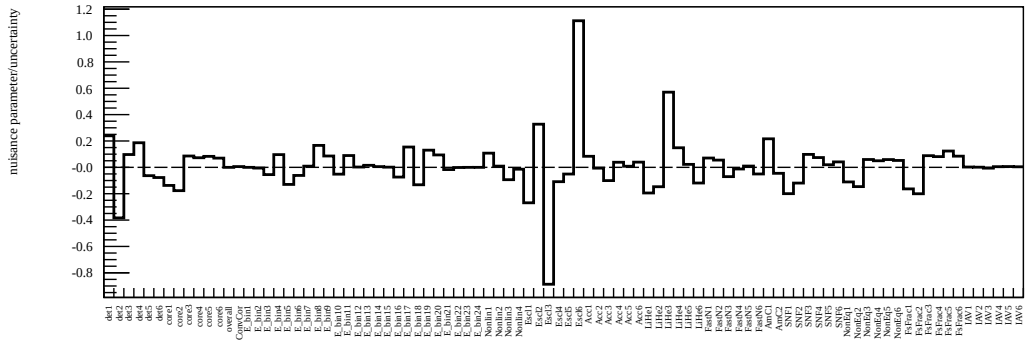


Figure 8.34 Values of nuisance parameter divided by uncertainty (η_i/σ_i) for a Monte Carlo programmed with $\sin^2 2\theta_{13} = 0.10$ and $\Delta m^2_{32} = 2.32{\cdot}10^{-3}\,\mathrm{eV}^2$, with statistical fluctuations, and fit over 24 energy bins.

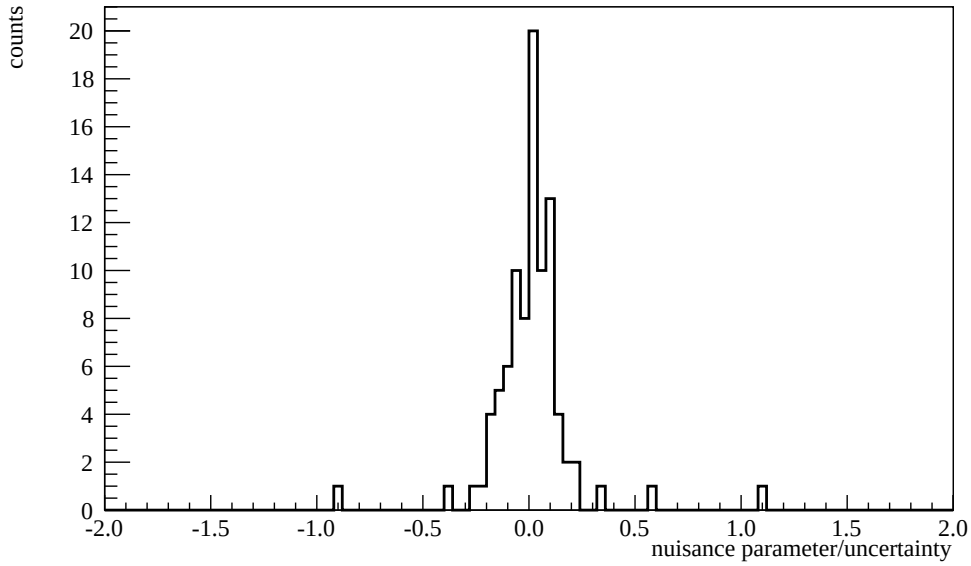


Figure 8.35 Distribution of nuisance parameter divided by uncertainty (η_i/σ_i) for a validation Monte Carlo run. Variable names are listed on the axes. The Monte Carlo is programmed with $\sin^2 2\theta_{13} = 0.10$ and $\Delta m^2_{32} = 2.32{\cdot}10^{-3}\,\mathrm{eV}^2$, with statistical fluctuations, and fit over 24 energy bins.

8.2.4 Many Monte Carlo with Statistical Fluctuations

It is useful to understand how the fitting code performs over a large set of Monte Carlo samples that are equivalent except for random statistical fluctuations. After running on a sufficiently large set, the mean of the distribution of measured oscillation parameters should coincide with the actual programmed values, while the spread of the distribution should be the same magnitude as the uncertainty of the measurement. If the mean diverges significantly from the true value, this may indicate a bias in the model. If the coverage of the distribution is abnormally wide or narrow, then the model is too sensitive to the fluctuations.

Statistical fluctuations are applied to the Monte Carlo spectra according to Poisson statistics after all detector and reactor model components have been implemented. Each sample uses a distinct random seed.

For comparison sake, another type of fluctuation is studied— fluctuations of systematic parameters. The Monte Carlo are nominally generated with nuisance parameters governing the systematics set to zero, denoting no systematic influence. But, the Monte Carlo samples in the systematic fluctuation case are generated with those parameters valued randomly according to a Gaussian of width equal to the uncertainty, centered at zero. For instance, if the detector normalization nuisance parameter for detector three is -1% in a given Monte Carlo, then the rate of detector three is scaled down 1% as though there were a systematic loss of efficiency. While the systematic fluctuations pose a rougher investigation the fitter, it is still useful to determine whether the fitter is obviously biased by, or unable to handle, small shifts in systematics.

8.2.4.1 Oscillation Parameter Spread

Figures 8.36 through 8.41 show the distributions of $\sin^2 2\theta_{13}$, Δm^2_{32} and measurements for 1000 Monte Carlo samples with statistical fluctuations (left) or systematic fluctuations (right). The Monte Carlo samples are generated with $\sin^2 2\theta_{13} = 0.10$, $\Delta m^2_{32} = 2.32{\cdot}10^{-3}\,\mathrm{eV}^2$ and normal hierarchy, and fit with 24 bins.

The mean of the fits to $\sin^2 2\theta_{13}$ and Δm^2_{32} agree with the expected mean well within the measurement uncertainties, and with good coverage. The mean $\sin^2 2\theta_{13}$ and Δm^2_{32} values are 0.1009 and $2.311{\cdot}10^{-3}\,\mathrm{eV}^2$ respectively, which are off the true values by less than a percent. The mean measurements from the systematics fluctuated Monte Carlo are even closer at 0.1001 and $2.317{\cdot}10^{-3}\,\mathrm{eV}^2$. The differences are an order of magnitude smaller than the precision of the measurements, which are 10% and 7% for $\sin^2 2\theta_{13}$ and Δm^2_{32} respectively. Hence, even if the differences were completely considered a bias and combined into the uncertainty of the measurement, the measurement uncertainties would change negligibly. The values of χ^2_{min} are peaked about 69 and 27 for the statistical and systematic fluctuated samples respectively. Evidently, the impact of statistical fluctuations on the fit is greater than the fluctuated systematics.

The technique of generating the Monte Carlo with systematic fluctuations is volatile because the random, Gaussian distribution of systematic parameters may lead to a small number of extreme values. In 17 out of the 1000 Monte Carlo samples, the sample was deemed nonphysical, as reflected in fits with χ^2_{min} values of up to 6000. These are cut out, reducing the set to 983 samples.

The joint plots of $\sin^2 2\theta_{13}$, Δm^2_{32} and the χ^2_{min} show no correlations for the statistical-fluctuation sample. The only correlation present is that between the measured $\sin^2 2\theta_{13}$ and Δm^2_{32} values among the Monte Carlo samples with systematics fluctuations. This correlation is small and negative, and corresponds to conserved oscillation probability— small $\sin^2 2\theta_{13}$ and large Δm^2_{32}, and vice versa, compensate for each other.

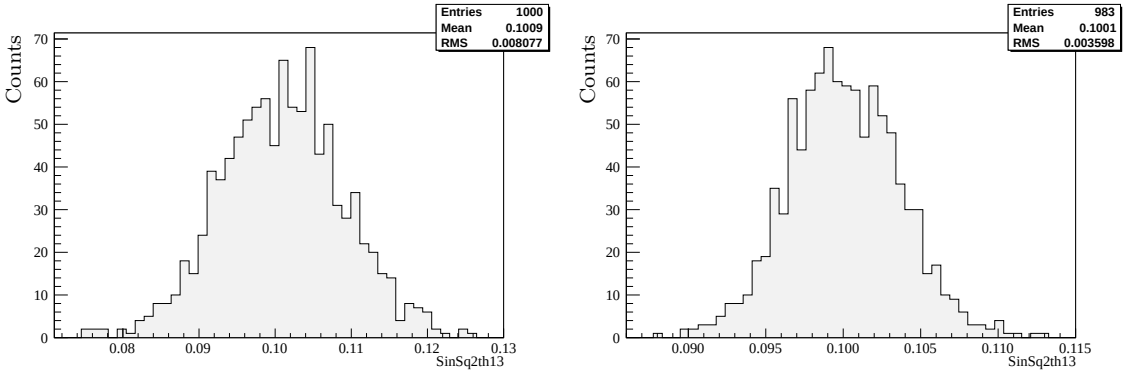


Figure 8.36 Distribution of measured $\sin^2 2\theta_{13}$ values over 1000 Monte Carlo samples generated with either statistical fluctuations (left) or fluctuations of systematics (right). The programmed oscillation parameter values are $\sin^2 2\theta_{13} = 0.10$ and $\Delta m^2_{32} = 2.32{\cdot}10^{-3}\,\mathrm{eV}^2$.

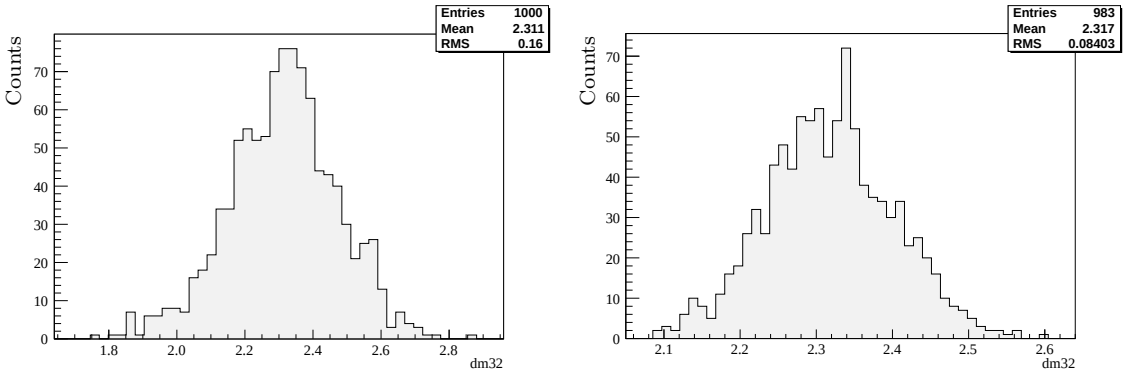


Figure 8.37 Distribution of measured Δm^2_{32} values over 1000 Monte Carlo samples generated with either statistical fluctuations (left) or fluctuations of systematics (right). The programmed oscillation parameter values are $\sin^2 2\theta_{13} = 0.10$ and $\Delta m^2_{32} = 2.32{\cdot}10^{-3}\,\mathrm{eV}^2$.

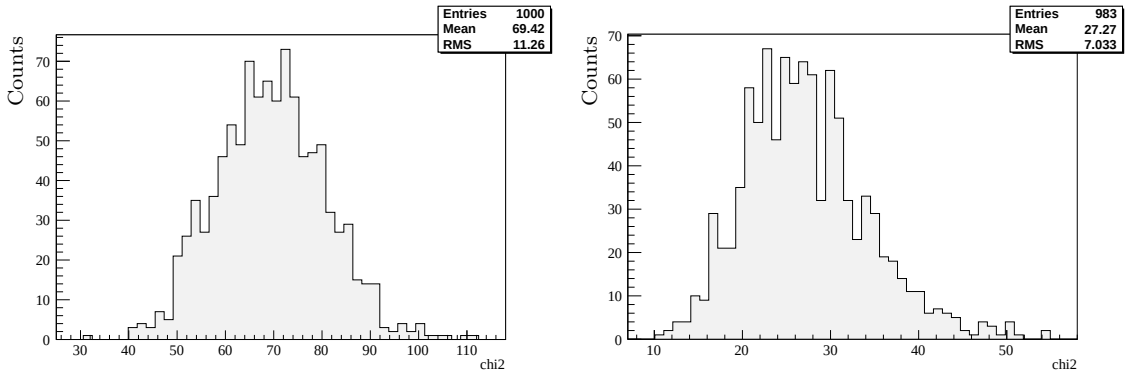


Figure 8.38 Distribution of measured χ^2_{min} values over 1000 Monte Carlo samples generated with either statistical fluctuations (left) or fluctuations of systematics (right). The programmed oscillation parameter values are $\sin^2 2\theta_{13} = 0.10$ and $\Delta m^2_{32} = 2.32{\cdot}10^{-3}\,\mathrm{eV}^2$.

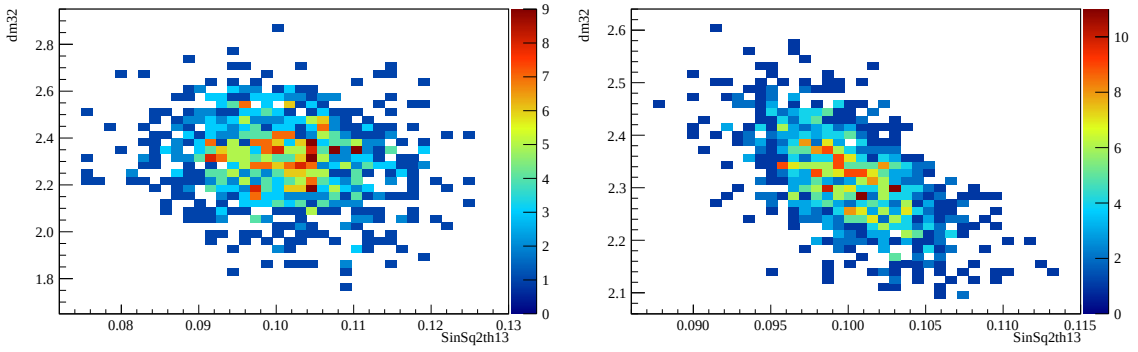


Figure 8.39 Measured $\sin^2 2\theta_{13}$ and Δm^2_{32} values over 1000 Monte Carlo samples generated with either statistical fluctuations (left) or fluctuations of systematics (right). The programmed oscillation parameter values are $\sin^2 2\theta_{13} = 0.10$ and $\Delta m^2_{32} = 2.32{\cdot}10^{-3}\,\mathrm{eV}^2$.

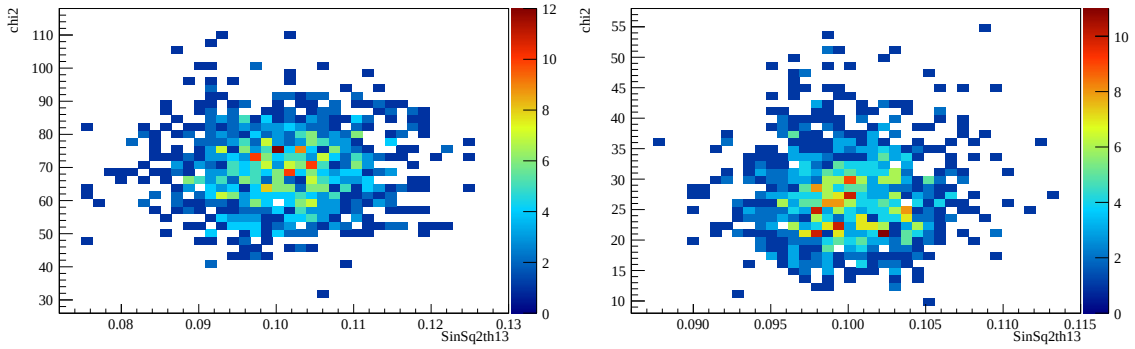


Figure 8.40 Measured $\sin^2 2\theta_{13}$ and χ^2_{min} values over 1000 Monte Carlo samples generated with either statistical fluctuations (left) or fluctuations of systematics (right). The programmed oscillation parameter values are $\sin^2 2\theta_{13} = 0.10$ and $\Delta m^2_{32} = 2.32{\cdot}10^{-3}\,\mathrm{eV}^2$.

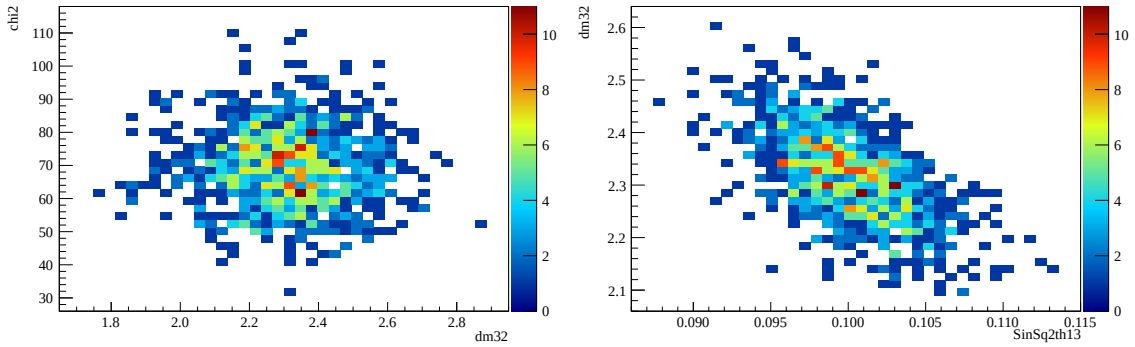


Figure 8.41 Measured Δm^2_{32} and χ^2_{min} values over 1000 Monte Carlo samples generated with either statistical fluctuations (left) or fluctuations of systematics (right). The programmed oscillation parameter values are $\sin^2 2\theta_{13} = 0.10$ and $\Delta m^2_{32} = 2.32{\cdot}10^{-3}\,\mathrm{eV}^2$.

8.2.4.2 Fitting with Only Oscillation Parameters

As a cross-check, a simpler fit is conducted with only $\sin^2 2\theta_{13}$, Δm^2_{32} and $\mathcal{H}$ enabled, on the same 1000 Monte Carlo samples with statistical fluctuations. Systematic nuisance parameters are removed from the fit and set to zero. The results can be seen in Figures 8.42 through 8.43, which show the distributions of $\sin^2 2\theta_{13}$, Δm^2_{32} and χ^2_{min}. The measured $\sin^2 2\theta_{13}$ and Δm^2_{32} agree well with expectation and the measurements of Section 8.2.4.1. The mean measured $\sin^2 2\theta_{13}$ improves from 0.1009 to 0.1007 with the simpler fit, suggesting a role for the systematics in the deviation, but the difference is minuscule.

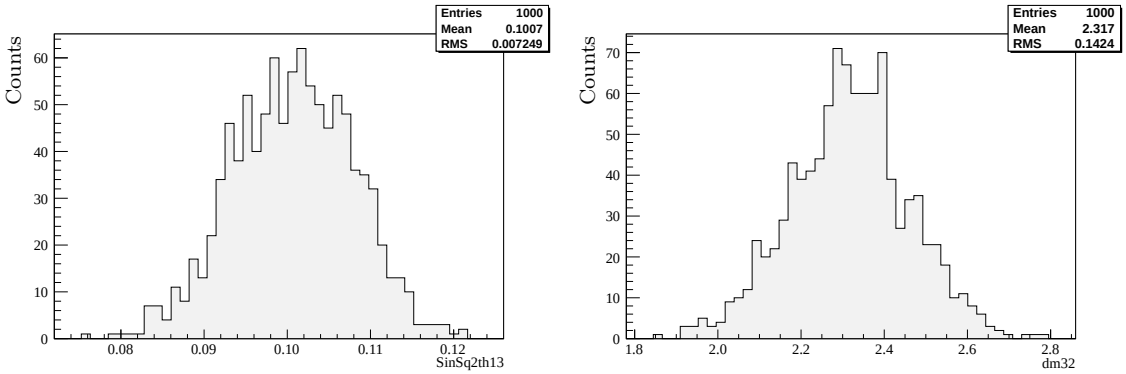


Figure 8.42 Measured $\sin^2 2\theta_{13}$ (left) and Δm^2_{32} (right) values over 1000 Monte Carlo samples with statistical fluctuations. Only $\sin^2 2\theta_{13}$, Δm^2_{32} and $\mathcal{H}$ were enabled during the fit. The programmed oscillation parameter values are $\sin^2 2\theta_{13} = 0.10$ and $\Delta m^2_{32} = 2.32{\cdot}10^{-3}\,\mathrm{eV}^2$.

8.2.5 Commutation of Model Components

The experiment model is built up true to the proper order of systematics and corrections, following the antineutrinos as they propagate from reactors to detectors. However, it is

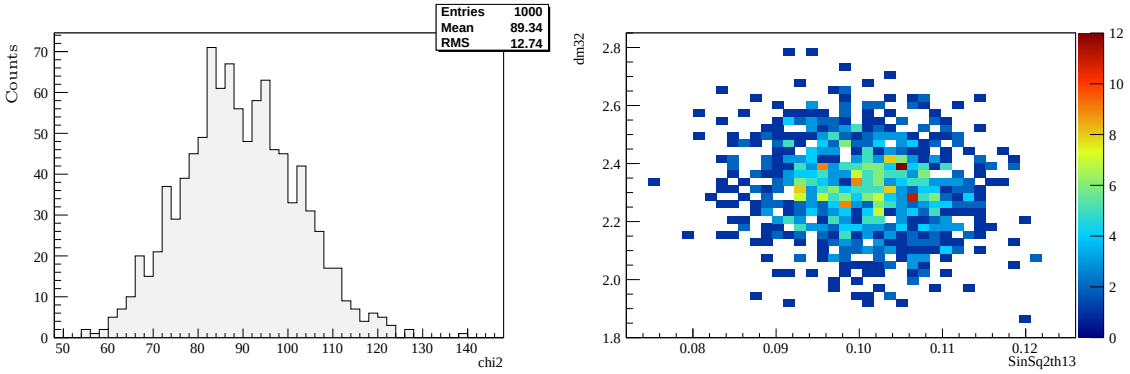


Figure 8.43 Measured χ^2_{min} values (left) and both $\sin^2 2\theta_{13}$ and Δm^2_{32} (right) over 1000 Monte Carlo samples with statistical fluctuations. Only $\sin^2 2\theta_{13}$, Δm^2_{32} and $\mathcal{H}$ were enabled during the fit. The programmed oscillation parameter values are $\sin^2 2\theta_{13} = 0.10$ and $\Delta m^2_{32} = 2.32{\cdot}10^{-3}\,\mathrm{eV}^2$.

possible for the ordering of effects to be incorrect or ambiguous, which can potentially alter the measurements if corrections and fit parameters do not commute. It is therefore of note to examine the significance of reordering of components.

An important example is the energy bin normalization, whose parameters are uncorrelated among bins but correlated otherwise. The bin normalization has contributions from both reactor and detector physics: the reactor $\beta \to \bar{\nu}$ conversion process and the detector IAV correction. There is therefore an argument to apply the bin normalization at the beginning of the model progression with the reactor systematics, or at the end with the detector systematics Applying two sets of bin normalization parameters would be redundant and risk the convergence of the fit. 0 These are not necessarily equivalent, since the spectrum changes in between due to other components of the model such as energy scale and resolution.

The nominal position of the bin normalization within the model and the alternative early position have been tested on Monte Carlo samples as a strong example of commutation. Two runs of 25 fits were performed with the bin normalization parameter applied either early to the raw predicted reactor spectra, or at the very end after all detector effects, which is standard. This represents the widest possible, physically meaningful variation. The 25 fits were performed on Monte Carlo with a programmed value of $\sin^2 2\theta_{13} = 0.10$,

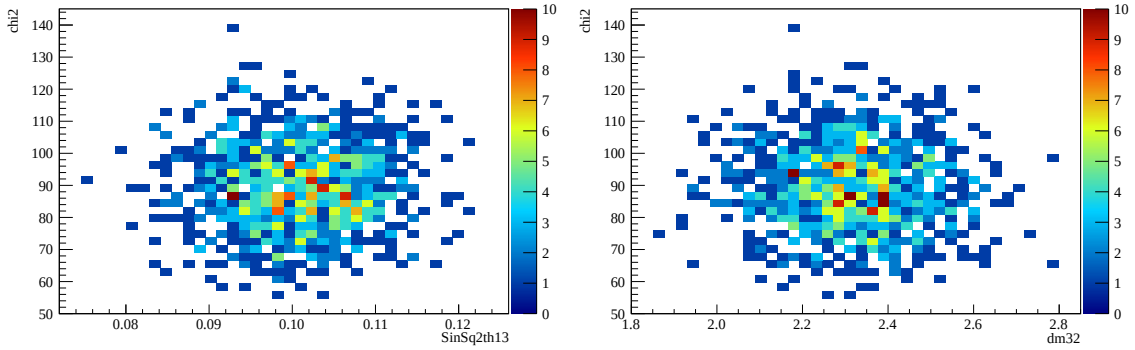


Figure 8.44 Measured $\sin^2 2\theta_{13}$ and χ^2_{min} values (left) and Δm^2_{32} and χ^2_{min} (right) over 1000 Monte Carlo samples with statistical fluctuations. Only $\sin^2 2\theta_{13}$, Δm^2_{32} and $\mathcal{H}$ were enabled during the fit. The programmed oscillation parameter values are $\sin^2 2\theta_{13} = 0.10$ and $\Delta m^2_{32} = 2.32{\cdot}10^{-3}\,\mathrm{eV}^2$.

$\Delta m^2_{32} = 2.32{\cdot}10^{-3}\,\mathrm{eV}^2$ and statistical fluctuations, which were seeded the same for both bin normalization placements. On average there was a difference in best fits of 0.5%, for instance a best fit $\sin^2 2\theta_{13}$ equal to 0.10 versus 0.1005. The study was repeated with exaggerated bin normalization uncertainties, (an additional 8% uncertainty in every bin), but the trend held.

In the current model, the bin normalization is fitted toward the end of the chain, a choice made because the spectra have taken a more final form, and because the relevant detector effects will have been included. At the reactor level, energy bins below the IBD threshold of 1.8 MeV have not been filled yet, but the IAV contribution is predominantly at low energies.

8.3 Validation with External Monte Carlo

Testing the fitting code on internal Monte Carlo— that is, Monte Carlo generated using the same fitting code infrastructure— is effective at detecting coding errors and minimizer pathologies. But, testing on independent Monte Carlo samples can detect accuracy issues that internal Monte Carlo cannot.

In addition to the work presented in this dissertation, three other Daya Bay analysis groups produced four additional oscillation measurement models and Monte Carlo sets.

These are independent of each other, but heavily related since ideas are shared and data analysis techniques are developed jointly. The five analyses are labeled and described below:

- JJL and XIN— Related analyses based on a minimized χ^2 with covariance matrices to reduce nuisance parameters [208].
- IHP— Minimized χ^2 with variable bin widths [209].
- LBL— χ^2 minimized only over oscillation parameters. Systematics are handled exclusively by covariance matrices [207].
- WIS— The subject of this dissertation.

Each group produced five Monte Carlos, at ($\sin^2 2\theta_{13}$, Δm^2_{32}) values of (0.07, 2.05), (0.07, 2.65), (0.10, 2.35), (0.13, 2.05), and (0.13, 2.65), where the units on Δm^2_{32} are 10^{-3}eV^2.

Measurements of $\sin^2 2\theta_{13}$ and Δm^2_{32} from each model, performed on every Monte Carlo sample, produce consistent results across all models. This includes fits performed by WIS and by other groups on WIS Monte Carlo. Figures 8.45 and 8.46 show a collage of $\sin^2 2\theta_{13}$ and Δm^2_{32} measurements produced by each fitter on each Monte Carlo where results have been provided by the various groups. This work typically agrees with the other groups within 2%, both in fitting their Monte Carlo samples, and the other groups' fits to WIS samples. The largest discrepancy involving the WIS model is 4–5%, which occurs when WIS fits the two low $\sin^2 2\theta_{13}$ Monte Carlos of LBL and XIN, and when JJL, XIN, and LBL fit the WIS low $\sin^2 2\theta_{13}$–low Δm^2_{32} Monte Carlo. The overall distribution of discrepancies among all groups is typically about ±3%. The largest consistent discrepancy involving the WIS model is that other groups typically measure Δm^2_{32} to be lower by 0–2% when fitting to WIS Monte Carlo. This is in good agreement given that the measurement precision in $\sin^2 2\theta_{13}$ and Δm^2_{32} are 10% and 7% respectively, and the five models are independent. The models contain several physically justifiable differences, such as how each treats background spectra, detector response and energy scale.

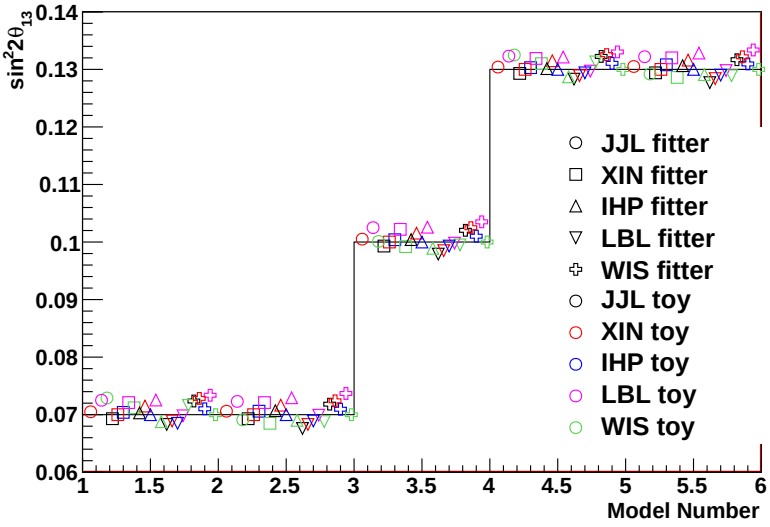


Figure 8.45 Measurements of $\sin^2 2\theta_{13}$ with five models performed on five Monte Carlo samples [79]. The samples are generated at five ($\sin^2 2\theta_{13}$, Δm^2_{32}) points: (0.07, 2.05), (0.07, 2.65), (0.10, 2.35), (0.13, 2.05), and (0.13, 2.65), where the units on Δm^2_{32} are 10^{-3}eV^2.

8.4 Summary

The oscillation analysis model reports measurements of oscillation parameters based on a χ^2 function. The χ^2 model contains representations of oscillation physics and systematic uncertainties that are used to modify a reactor flux prediction, which is then compared to data. The combination of oscillation parameters and systematics that best describe the data are interpreted as the measured oscillation parameters. Additionally, the systematics are varied within the χ^2 to define the precision at which the parameters are measured.

The model has been validated by a variety of tests. The analysis reproduces desired parameter values when operated on Monte Carlo samples, which provides an effective consistency check. The model also reproduces expected oscillation parameters using Monte Carlo samples generated independently by other analysts within the collaboration.

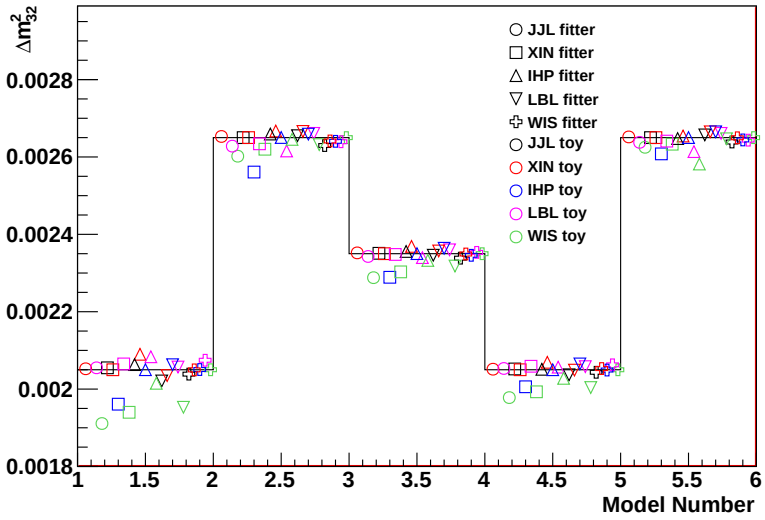


Figure 8.46 Measurements of Δm^2_{32} with five models performed on five Monte Carlo samples [79]. The samples are generated at five ($\sin^2 2\theta_{13}$, Δm^2_{32}) points: (0.07, 2.05), (0.07, 2.65), (0.10, 2.35), (0.13, 2.05), and (0.13, 2.65), where the units on Δm^2_{32} are 10^{-3}eV^2.

Chapter 9

Measurements of Oscillation Parameters $\sin^2 2\theta_{13}$ and Δm^2_{32}

The discussion that follows presents the oscillation measurements I performed, along with diagnostic information, and various in-depth studies. This effort represents my main contribution to the analysis of Daya Bay data, and the oscillation measurements Daya Bay contributed to the physics community. My analysis was conducted as part of a group in which I focused on the statistical analysis and model building while others focused on detector and reactor analysis. But, of course, there was mutual involvement of each contributor to each topic. Our analysis was one of four unique efforts that cross-checked one another and collaborated toward the final goal of publishing measurements of $\sin^2 2\theta_{13}$ and Δm^2_{32}. My analysis was distinct in that it was the only uniform-binned χ^2, and could offer diagnostics that others did not, such as measurements versus the number of bins and the rate of change in nuisance parameters over changes in oscillation parameters and bins.

9.1 Primary Measurement of $\sin^2 2\theta_{13}$ and Δm^2_{32}

The primary measurement of oscillation parameters $\sin^2 2\theta_{13}$ and Δm^2_{32} is calculated from the Data Set 3, utilizing both event rate deficits and spectral distortions, with several analysis choices imposed. Unless otherwise stated, the measurements presented in this chapter are based on the model explained in Section 8.1 with the energy scale fit disabled. Deliverables $\sin^2 2\theta_{13}$, Δm^2_{32} and the overall normalization $\mathcal{H}$ are fit as free parameters, while previously measured oscillation parameters take their values from the 2012 PDG [1]. The data are

binned into 24 energy bins, normal hierarchy ($m_3 > m_2 > m_1$) is assumed, and the Huber-French antineutrino flux model provides the predicted antineutrino rates and spectra. The choice of 24 bins is a middle ground between the 1 and 240 that are permitted by internal collaboration conventions. Normal hierarchy is an arbitrary choice, while the Huber-French flux model is used since it is more internal to the collaboration. In every case, analysis choices are confirmed by direct investigation not to bias the results.

9.1.1 Best Fit Results

With $\sin^2 2\theta_{13}$, Δm^2_{32} and $\mathcal{H}$ unconstrained, and 24 energy bins, the measured oscillation parameters are:

- $\sin^2 2\theta_{13} \ = 0.0880922^{+0.008816}_{-0.008843}$
- $\Delta m^2_{32} = 2.54407^{+0.166}_{-0.176} \cdot 10^{-3}\,\mathrm{eV}^2$
- $\Delta m^2_{31} = 2.61907 \cdot 10^{-3}\,\mathrm{eV}^2$
- $\mathcal{H} = -0.0301548^{+0.029158}_{-0.027540}$
- $\chi^2_{min} = 114.426$. $\mathrm{N_{DOF}} = 6$*24–3. $\chi^2/\mathrm{N_{DOF}} = 0.81153$

The best fit oscillation parameters are in excellent agreement with past Daya Bay measurements [68], the world average [5], and the cross-checks discussed in succeeding sections. The precisions of $\sin^2 2\theta_{13}$ and Δm^2_{32} are established at about 10% and 7% respectively. The overall normalization between data and prediction is -3%, with an uncertainty of 100%, thus demonstrating consistency between the two, and no evidence of reactor neutrino anomalies [210]. The expected uncertainty on $\mathcal{H}$, which would have be used to constrain $\mathcal{H}$ were it not free, would be 3.6%. This stems from a detector normalization uncertainty of 1.9%, and a 3% reactor normalization uncertainty [7]. The χ^2_{min} at best fit is 114.4 for 141 degrees of freedom (144 energy bins across all six detectors, less three unconstrained fit parameters). The value of $\chi^2_{min}/\mathrm{N_{DOF}} = 0.81153$ is lower than the expected value of about one, which

indicates that perhaps statistical fluctuations were calmer than an average expectation, or that the systematic uncertainties were overestimated.

The plots in Figures 9.1 through 9.5 provide the best fit $\Delta\chi^2$ as a function of one or two of $\sin^2 2\theta_{13}$, Δm^2_{32} and $\mathcal{H}$, where

$$\Delta\chi^2 \equiv \chi^2 - \chi^2_{min}\,. \tag{9.1}$$

In each case the model is the same and $\sin^2 2\theta_{13}$, Δm^2_{32} and $\mathcal{H}$ are unconstrained parameters of the fit, but the variables plotted are different.

For lower confidence limits, the $\sin^2 2\theta_{13}$-Δm^2_{32} contours of Figure 9.1 resemble regular ellipses. The major and minor axes of the ellipses are aligned with the variable axes, which indicates that the parameters are reasonably uncorrelated. But, as the confidence limit increases to 5σ, distortion grows in the large $\sin^2 2\theta_{13}$-small Δm^2_{32} region. This is because a low value of Δm^2_{32} can subtly mimic the effect of $\sin^2 2\theta_{13}$. By construction of Daya Bay, the valley of the survival probability aligns with the statistical peak of the far site spectrum. But, very small values of Δm^2_{32} push the tail of the oscillation curve onto the spectral peak instead. This happens at the near sites as well, but the impact is subdued because at the near sites, the valley of the survival probability curve is already off-peak. Thus, low values of Δm^2_{32} reduce the oscillation probability at all detectors but more so at the far site. A high $\sin^2 2\theta_{13}$ compensates for the small oscillation magnitude to allow this solution to match the data at large confidence limits. This ambiguity was not seen in the rate-only analysis because the Δm^2_{32} parameter is constrained. In fact, the rate-only fit is impossible with a free Δm^2_{32} for the reasons above.

Similarly, Figure 9.2 provides the $\sin^2 2\theta_{13}$-$\mathcal{H}$ 1σ contour. That the ellipse is aligned with the $\sin^2 2\theta_{13}$ and $\mathcal{H}$ axes also indicates an appropriate level of independence among them. Since the Δm^2_{32} measurement is determined primarily from the spectral shape measurement, and not the rate information, the Δm^2_{32}-$\mathcal{H}$ contour is uninteresting.

Figures 9.2 through 9.5 show the $\Delta\chi^2$ as a function of $\sin^2 2\theta_{13}$, Δm^2_{32} and $\mathcal{H}$ respectively. The measurement precision of each parameter can be read off the plot at the relevant confidence limit ($N\sigma$ corresponds to $\Delta\chi^2{=}N^2$). Note that the normalization of the confidence limit differs between the two-dimensional plot and the one-dimensional. The confidence level of 1σ for instance is defined as 68% of the central area of a normal distribution, but the normal distribution of one and two variables have different scales. Hence, the 1σ ellipse cannot be projected onto one axis to determine the 1σ confidence interval of a single variable.

9.1.2 Best Fit Diagnostics

Table 9.1, and Figures 9.6 through 9.12 illustrate the diagnostics of the fit, including: parameter correlations, the covariance matrix, nuisance parameter values, and the fit-parameter-adjusted prediction compared to data.

The correlation matrix of Figure 9.6 shows normal relationships. Most non-diagonal values are close to zero (limited correlations), while the diagonal elements are one, by definition. Most correlated fit parameters are those that operate on the spectrum in similar ways. Nearby energy bins are highly correlated, reflecting the smooth adjustment of the spectrum during the fit. The energy bin normalizations are more correlated with other shape effects than other parameters because the adjustment of the bin normalization is the most general shape operation in the model. For instance, the energy bin normalizations are anticorrelated with the overall normalization, suggesting that the overall normalization compensates for the rate changes ensuing from the shape adjustment. Other off-diagonal (anti)correlations can be seen among the backgrounds and reactor spectrum blocks.

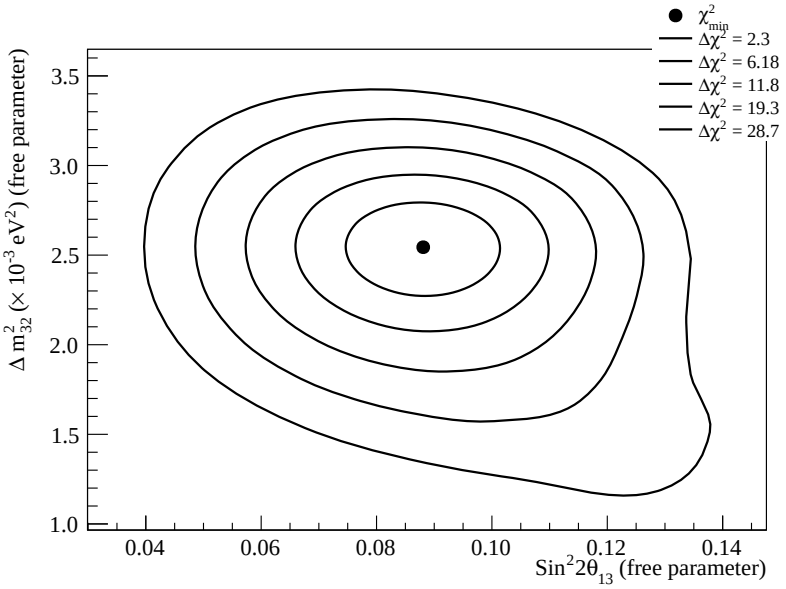


Figure 9.1 Best fit $\sin^2 2\theta_{13}$-Δm^2_{32} contours for rate and shape data, where the overall normalization $\mathcal{H}$, $\sin^2 2\theta_{13}$ and Δm^2_{32} are free parameters, and normal hierarchy is assumed. The central dot denotes the best fit, and the five contours correspond to two-dimensional 1–5σ confidence limits.

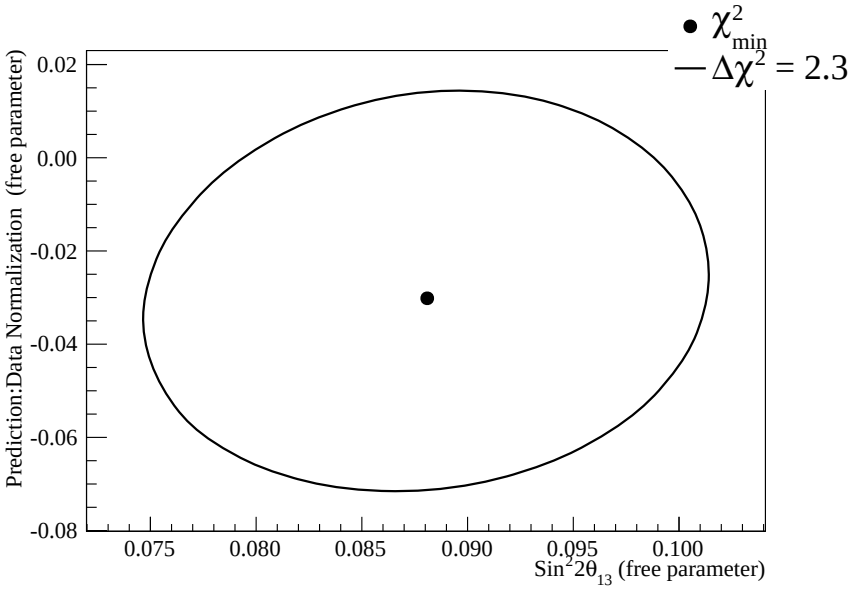


Figure 9.2 Best fit $\sin^2 2\theta_{13}$-$\mathcal{H}$ 1σ contour for rate and shape data, where $\mathcal{H}$, $\sin^2 2\theta_{13}$ and Δm^2_{32} are free parameters and normal hierarchy is assumed. The central dot denotes the best fit.

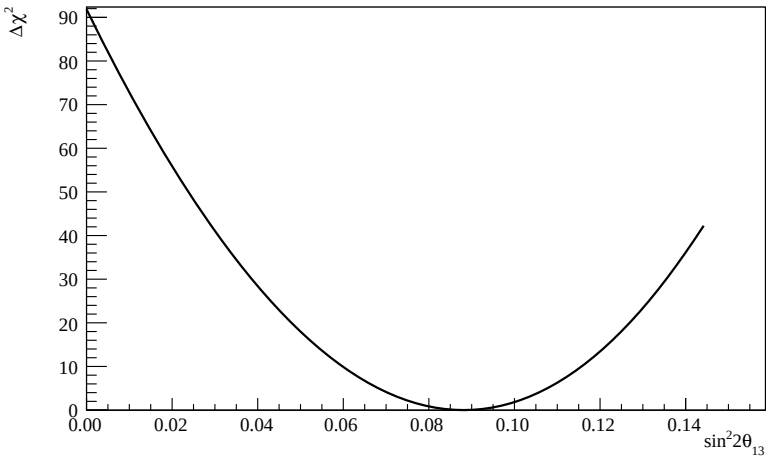


Figure 9.3 The best fit $\Delta\chi^2(\sin^2 2\theta_{13})$ from the rate and shape analysis with $\sin^2 2\theta_{13}$, Δm^2_{32} and $\mathcal{H}$ as free parameters and normal hierarchy assumed.

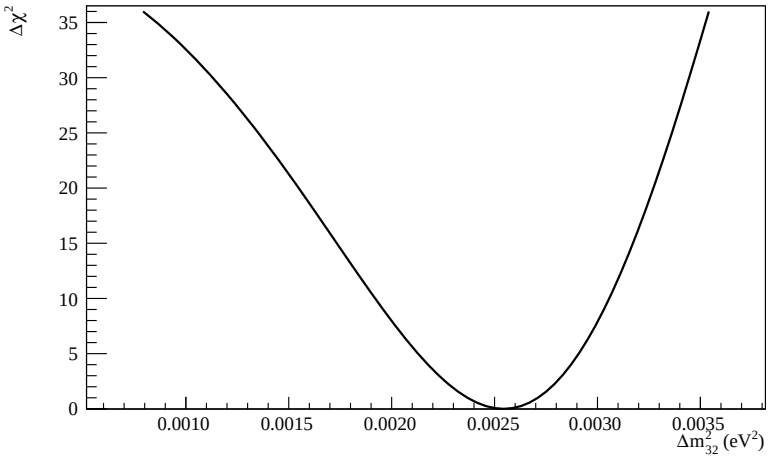


Figure 9.4 The best fit $\Delta\chi^2(\Delta m^2_{32})$ from the rate and shape analysis, with $\sin^2 2\theta_{13}$, Δm^2_{32} and $\mathcal{H}$ as free parameters and normal hierarchy assumed.

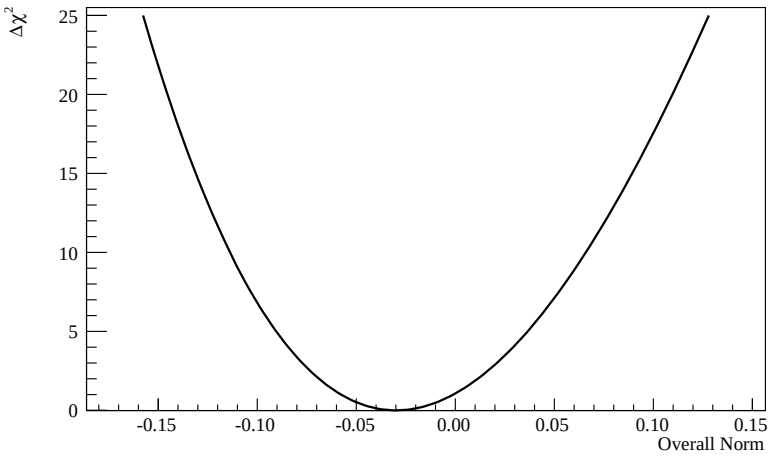


Figure 9.5 The best fit $\Delta\chi^2(\mathcal{H})$ to rate and shape data, with $\sin^2 2\theta_{13}$, Δm^2_{32} and $\mathcal{H}$ as free parameters and normal hierarchy assumed.

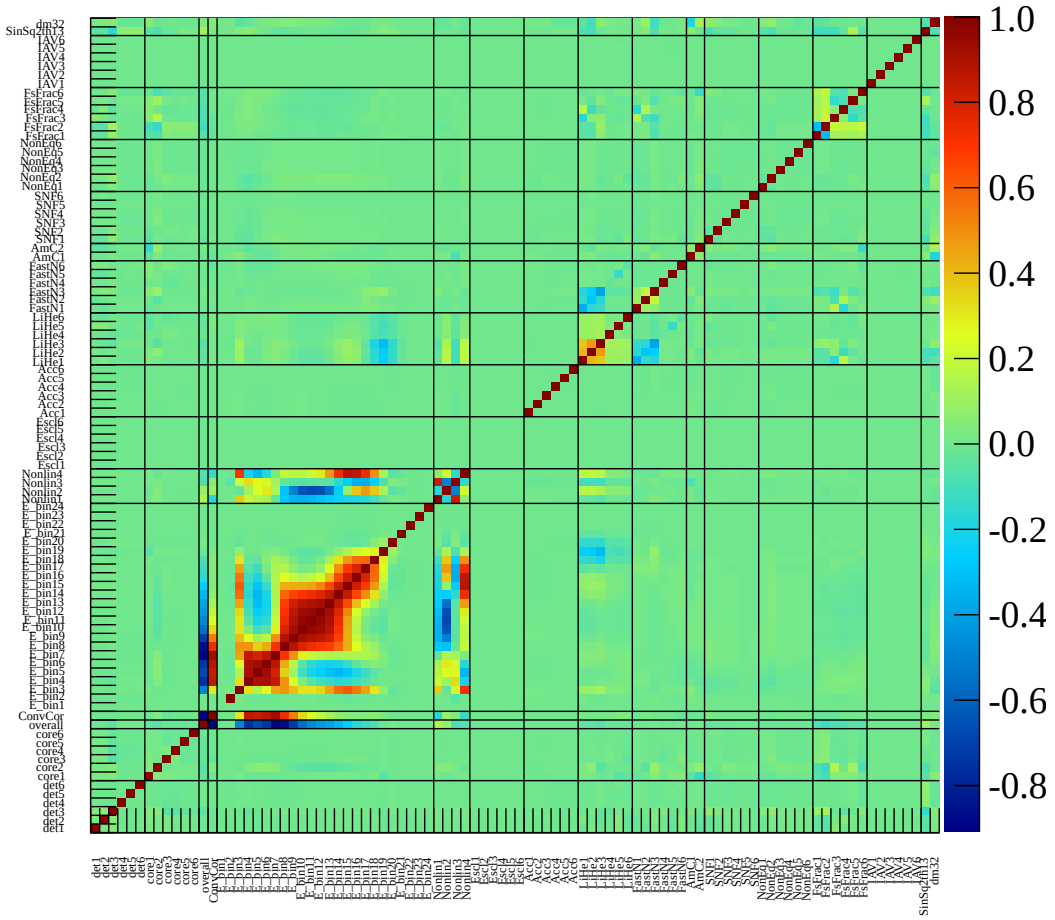


Figure 9.6 Correlation matrix from the rate and shape and shape analysis. Variable names are listed on the axes.

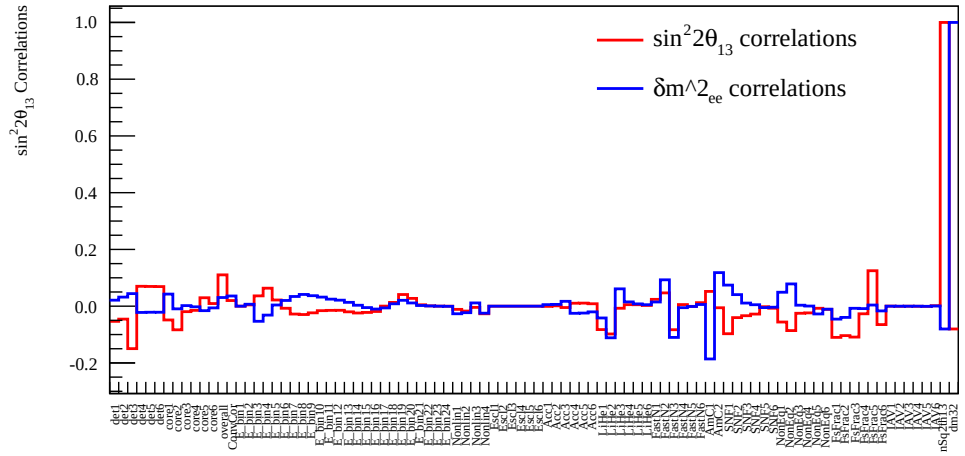


Figure 9.7 Correlations between $\sin^2 2\theta_{13}$ and Δm^2_{32} and the systematic fit parameters from the rate and shape analysis. Fit parameters are listed on the axes.

Specific correlations of $\sin^2 2\theta_{13}$ and Δm^2_{32} with systematics are shown in Figure 9.7. For both $\sin^2 2\theta_{13}$ and Δm^2_{32}, the correlations with systematics are small, mostly within ± 0.1, ranging as far as -0.2. Often times, a mirrored relationship is seen between the correlations of $\sin^2 2\theta_{13}$ and Δm^2_{32} with systematics, where the signs of the correlation are opposite. The correlation between $\sin^2 2\theta_{13}$ and Δm^2_{32} is < 0.1.

The covariance matrix in Figure 9.8 is diagonal, which validates the use of the standard χ^2 of the form

$$\chi^2 = \frac{(A-B)^2}{\sigma_A^2} \ ,$$

or its logarithmic expression, with factors of $1/\sigma^2$ rather than explicit reference to the covariance matrix. Large off-diagonal entries in the covariance matrix would indicate such strong correlations among fit parameters that the covariance matrix would need to be calculated ahead of time and input into the χ^2.

The largest off-diagonal values are seen among the detector response nonlinearity parameters, and the fission fraction, the largest reactor-uncorrelated shape uncertainty. Even in these cases, the off-diagonal entries are small. Not all diagonal elements are equal, however.

Most are nearly zero. Several of the diagonal entries are near unity: those that correspond to the spent nuclear fuel, nonequilibrium correction, fission fraction and IAV correction. These have in common that they are relatively minor systematics, and except for the IAV correction, they are reactor-based. The diagonal elements for normalizations to energy bins 21–24 are greater than 1, up to as high as 2. These energy bins are are sparsely populated or empty. This is related to the ^{238}U treatment in the flux prediction, discussed in Section 9.1.9. When the ^{238}U is treated as energy bin-correlated, these entries are approximately one.

Table 9.1 decomposes the χ^2_{min} value into several parts: the pull term $(\eta_\iota/\sigma_\iota)^2$ for each systematic, and the statistical portion of χ^2, defined to be:

$$\chi^2_{stat} \equiv \chi^2 - \sum_\iota (\eta_\iota/\sigma_\iota)^2 \,. \tag{9.2}$$

The χ^2 function and the pull terms are discussed in Section 8.1. Nuisance parameters η_ι are ideally zero by construction, so departure from zero in the fit represents tension, yielding a larger pull term value. In terms of raw contribution, the statistical part of χ^2_{min} dominates by two orders of magnitude, contributing about 94% to χ^2_{min}. Evidently, the systematic nuisance parameters are small with respect to their uncertainties, which suggests that the model describing the data is satisfactory. Among the pull terms, the background normalization is largest by a factor of two at 4% contribution, followed by the bin normalizations. The other systematic pull terms are minuscule, except for those representing the detector nonlinearity.

This pull term information is explored further in Figures 9.9 and 9.10, which provide a lineup and histogram of $(\eta_\iota/\sigma_\iota)$ values, respectively. All of the $(\eta_\iota/\sigma_\iota)$ are well within 0 ± 1, as would be expected for a fit without undue tension. The distribution of the pull terms is approximately a normal distribution, which also bodes well for the model.

Particular attention is paid to the detector nonlinear response parameters, since this is the least well understood detector uncertainty. Figure 9.11 provides the baseline nonlinearity

curve ($E_{corrected}/E_{predicted}$) in black, the 1σ uncertainty on each of the four fit parameters in color, and the final best fit nonlinearity curve. The best fit curve is covered by the 1σ bands for all energies, which suggests the function and parameterization are good corrections for the data.

After all fitting is performed, Figure 9.12 shows the data divided by the best fit prediction calculated for the 24 energy bins, expressed in 240 bins for better detail. Data points varying about unity with no energy dependence would represent an ideal fit. Overall the data points are well distributed about unity with few significant trends visible as a function of energy. The only exception is a small excess at the three near sites at 1 MeV. At this energy, few antineutrino events can be found, but the accidental spectrum peaks. The excess is consistent with Table 9.1, in which the background normalization parameters show the most tension among the systematics.

9.1.3 Energy Scale Treatment

One important modification has been made to the model in Section 8.1. In the course of the fit, it was determined that there is insufficient information to fit both Δm^2_{32} and the energy scale parameters reliably. This naturally occurs because these fit parameters affect the oscillation in degenerate ways. Energy scale parameter η_e, and mass fit parameter η_m, enter the oscillation equation as:

$$P_{\overline{\nu}_e \to \overline{\nu}_e} \simeq 1 - \sin^2 2\theta_{13} \sin^2 \left(1.267 \frac{\Delta m^2_{32}(1+\eta_m)L}{E(1+\eta_e)} \right) . \tag{9.3}$$

Since η_e and η_m are small, $(1+\eta_m)$ is equivalent to $(1-\eta_e)$ by Taylor expansion because the factor of $(1+\eta_e)$ is in the denominator, and so there is effectively a degeneracy between

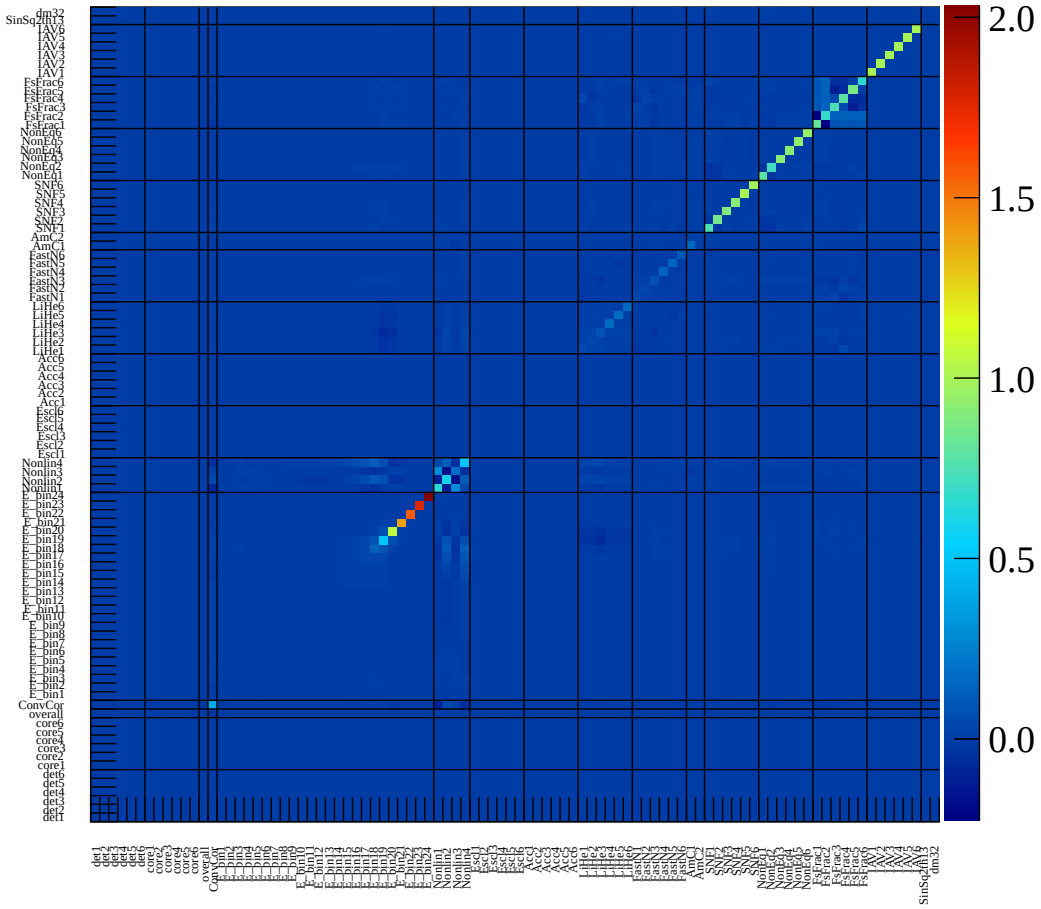


Figure 9.8 Covariance matrix from the rate and shape analysis. Variable names are listed on the axes.

Contributions to χ^2_{min}, rate and shape analysis:		
From statistical part	107.493 / 144 = 0.746	93.94%
From detector normalization	0.065 / 6 = 0.011	0.057 %
From reactor normalization	0.007 / 6 = 0.001	0.006 %
From bin normalization	2.146 / 24 = 0.089	1.876 %
From nonlinearity	0.628 / 4 = 0.157	0.549 %
From background normalization	3.835 / 19 = 0.202	3.352 %
From $\beta \to \bar{\nu}$ energy-correlated	$2.445{\cdot}10^{-4}$ / 1 = $2.445{\cdot}10^{-4}$	0.000 %
From IAV det-uncorr./energy-corr.	0.001 / 6 = 0.0002	0.001 %
From spent fuel	0.078 / 6 = 0.013	0.068 %
From nonequilibrium	0.075 / 6 = 0.013	0.066 %
From fission fraction	0.097 / 6 = 0.016	0.085 %
Total χ^2_{min}	114.43 / (6*24–3) = 0.811	

Table 9.1 The contribution of each systematic to the χ^2_{min} value of the rate and shape analysis. Except for the statistical part, the quantities above are the size of each set of pull terms $(\eta_\iota/\sigma_\iota)^2$, in total and where applicable averaged per detector, reactor or bin. The statistical part is the lead term in the χ^2: $\chi^2 - \sum(\eta_\iota/\sigma_\iota)^2$. The percentages are based on the total pull terms per systematic.

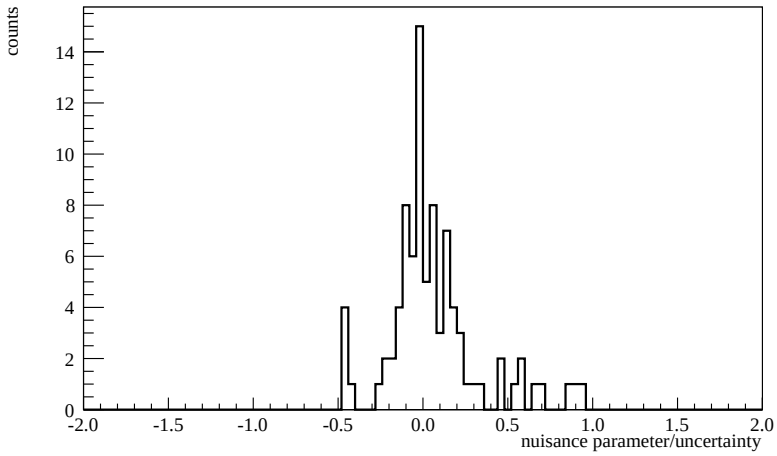


Figure 9.9 Histogram of systematic nuisance parameters divided by uncertainty values $(\eta_\iota/\sigma_\iota)$ at best fit to rate and shape data.

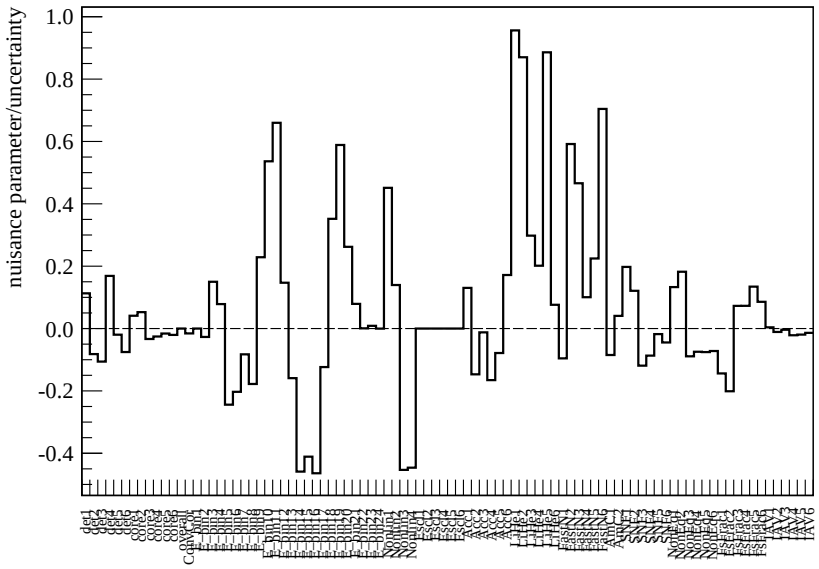


Figure 9.10 Systematic nuisance parameters divided by uncertainties (η_ι/σ_ι) at best fit from a rate and shape analysis, where Δm^2_{32} is unconstrained and normal hierarchy is assumed. Variable names are listed on the axes.

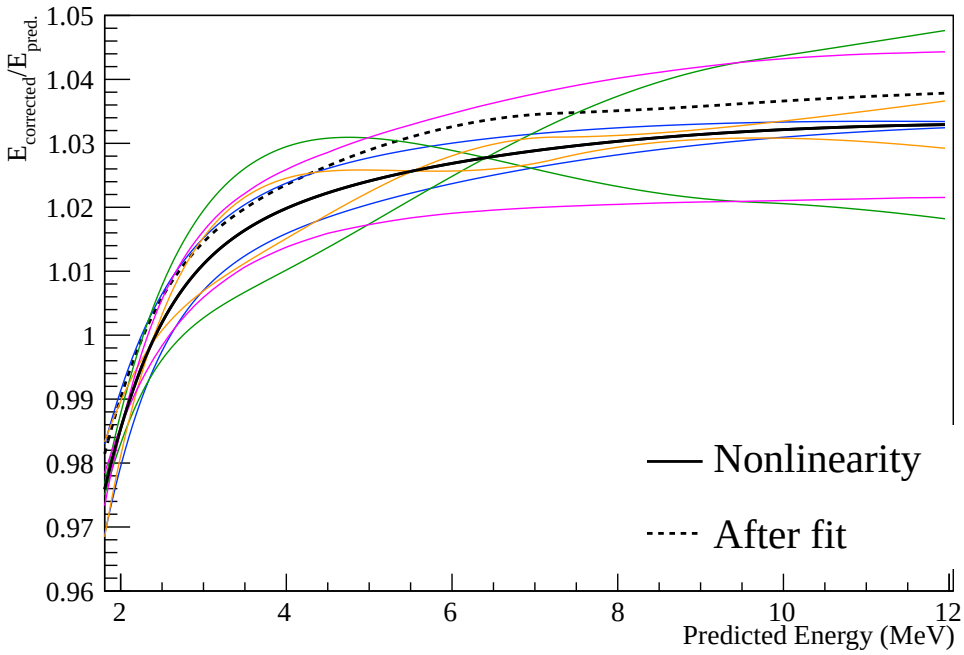


Figure 9.11 The detector response model is indicated by the solid black line. 1σ uncertainties on the four individual nonlinearity parameters are indicated by the colored lines. The dashed line shows the best fit detector response after fit parameters are applied.

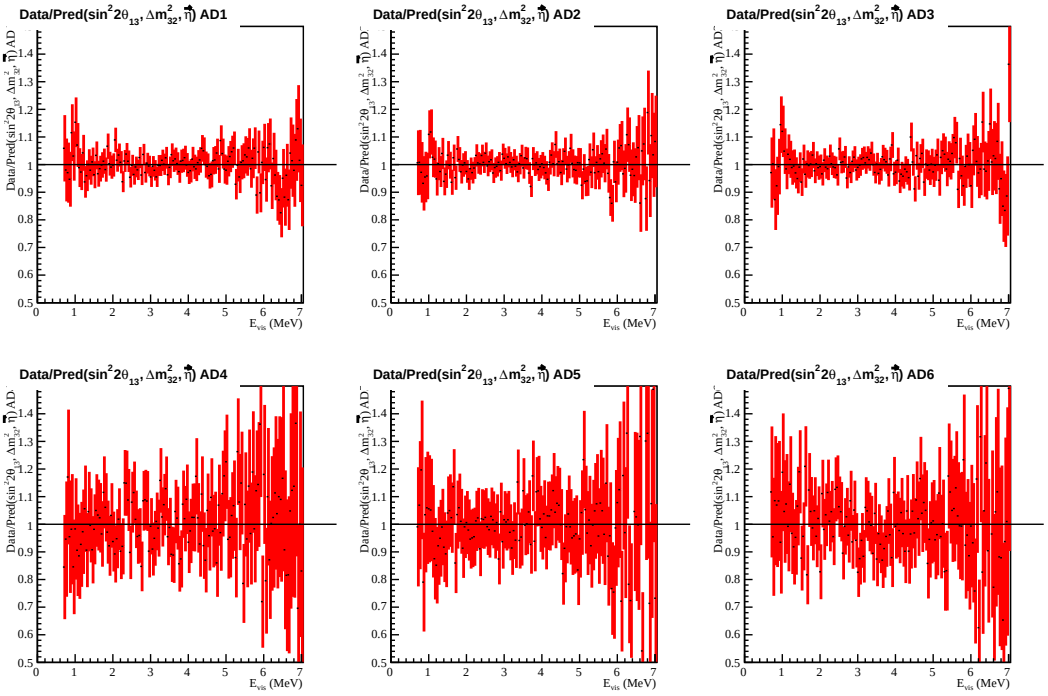


Figure 9.12 Ratio of data in 240 bins divided by the predicted flux, which includes the best fit systematics and oscillation from the 24 bin rate and shape analysis.

them. With the energy scale parameters enabled or disabled, the best fit value differs by 3.5%, while the best fit $\sin^2 2\theta_{13}$ differs negligibly. As a result, it was decided to delineate these two cases.

With the parameters enabled, in the denominator of the oscillation probability, the best fit Δm^2_{32} is $2.63{\cdot}10^{-3}\,\mathrm{eV}^2$. With the energy scale parameters disabled— $\eta_e{\to}0$ in Equation 9.3— the best fit Δm^2_{32} is $2.54{\cdot}10^{-3}\,\mathrm{eV}^2$. See Table 9.2. When enabled, the energy scale best fit values range from $2.3{\cdot}10^{-5}$ to $2.6{\cdot}10^{-3}$ in magnitude, indicating a small correction to the energy:

Detector 1 : −0.00190460	Detector 4 : 0.00171523
Detector 2 : −0.00088426	Detector 5 : 0.00262531
Detector 3 : −0.00002362	Detector 6 : −0.00098870

The baseline analysis of disabled energy scale parameters was chosen after considering the factors above and the Δm^2_{32} fits from other groups, some of which employed techniques that reduced the total number of fit parameters, in the process agreeing with $\Delta m^2_{32}{=}2.54{\cdot}10^{-3}\,\mathrm{eV}^2$.

The alternative of combining the energy scale and Δm^2_{32} nuisance parameters is approximately equivalent to removing the energy scale. To combine the parameters, the factor of $1/(1+\eta_e)$ in the denominator would be replaced with $(1-\eta_e)$ by Taylor expansion, assuming η_e is small. The numerator then contains a factor of $(1+\eta_m)(1-\eta_e) \simeq (1+\eta_m-\eta_e)$, where the right hand side again relies on the smallness of the parameters. The parameters can be replaced by a single parameter η', with combined uncertainty $\sigma'^2 = \sigma_e^2 + \sigma_m^2$. However, the uncertainty σ_e is much smaller than σ_m. In fact, when Δm^2_{32} is unconstrained, its uncertainty is effectively infinite.

Figure 9.13 shows $\sin^2 2\theta_{13}$-Δm^2_{32} contours with and without the energy scale parameters. The contours look similar; the largest differences are the overall shift by 3.5% in the Δm^2_{32} direction, and the distortion toward the low Δm^2_{32}-high $\sin^2 2\theta_{13}$ region. The reason for

the distortion is the same as described in Section 9.1.1, although exacerbated due to more freedom in the fit that comes with more systematic uncertainties.

Detector Model	$\sin^2 2\theta_{13}$ fit	Δm^2_{32} fit	Normalization fit	χ^2_{min}
No Energy Scale	$0.0880922^{+0.008816}_{-0.008843}$	$2.54407^{+0.166}_{-0.176}\cdot 10^{-3}\,\mathrm{eV}^2$	$-0.0301548^{+0.029158}_{-0.027540}$	114.426
With Energy Scale	$0.0878818^{+0.008782}_{-0.008792}$	$2.63444^{+0.194}_{-0.205}\cdot 10^{-3}\,\mathrm{eV}^2$	$-0.0302676^{+0.029147}_{-0.027528}$	111.532

Table 9.2 Rate and shape analysis results with either the energy scale fit parameters disabled (primary analysis) or enabled.

9.1.4 Best Fit Spectra

Figures 9.14 through 9.19 provide the IBD and background data as well as the predicted spectra at each stages of the fit, for each detector. The order of effects applied in the fit is the same as their order in the legend.

9.1.5 Error Budget

The contributions of the various systematics to the best fit oscillation parameters is useful to understand, but difficult to quantify. It can be approximated by the prescription below, with the results tabulated in Table 9.3. The size of the contribution is determined by both

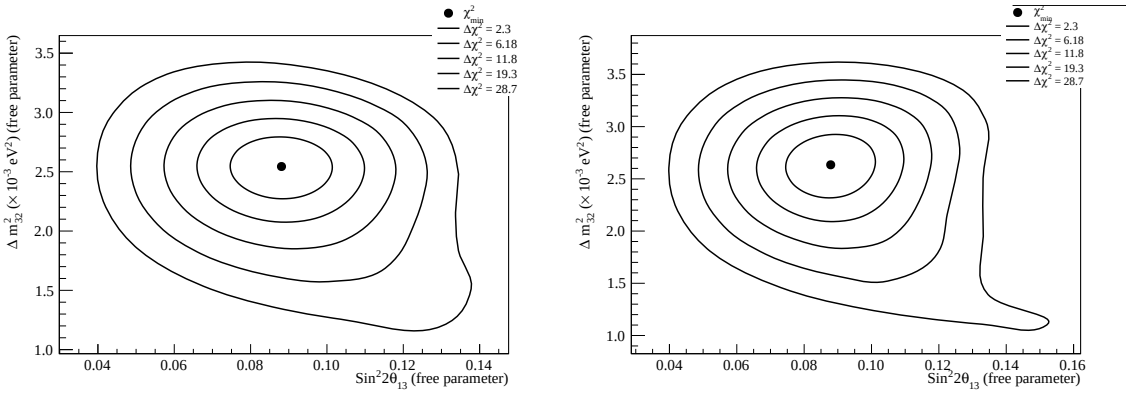


Figure 9.13 Best fit contours $\Delta\chi^2(\sin^2 2\theta_{13}, \Delta m^2_{13})$ for rate and shape data with the exclusion of the energy scale parameter (left) and its inclusion (right). The energy scale parameters and Δm^2_{32} form a possible degeneracy, which is difficult to resolve in a limited data set.

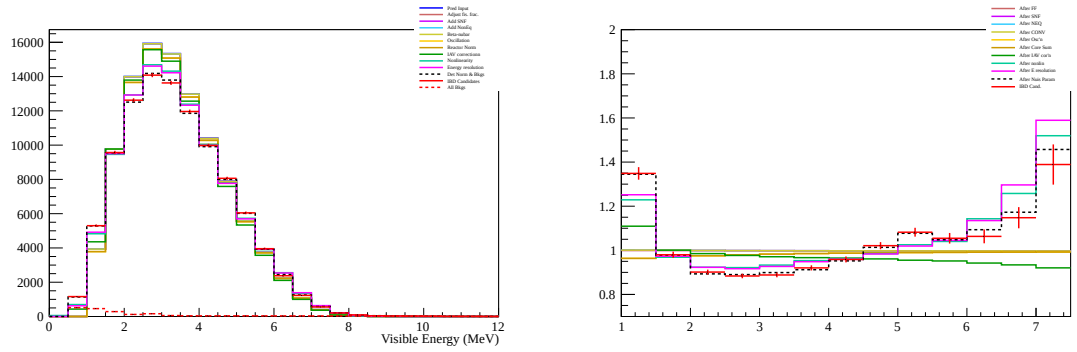


Figure 9.14 Detector 1 spectra after each stage of the rate and shape data fit: absolute (left) and ratio (right) in which the spectrum at each stage is divided by the initial unoscillated predicted spectrum (right). The model progression starts from the solid blue line, which is the initial reactor flux prediction, to the black dashed line, which includes best fit systematics and oscillations. In red are IBD candidates including backgrounds (solid line) and backgrounds (dashed).

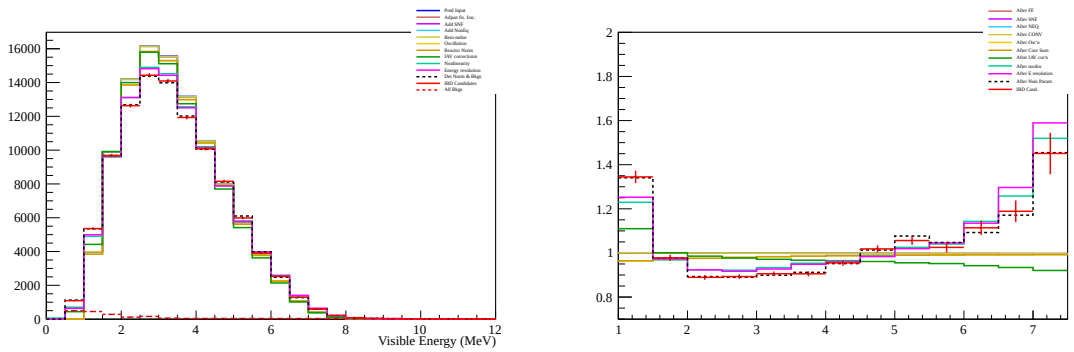


Figure 9.15 Detector 2 spectra after each stage of the rate and shape data fit: absolute (left) and ratio (right) in which the spectrum at each stage is divided by the initial unoscillated predicted spectrum (right). The model progression starts from the solid blue line, which is the initial reactor flux prediction, to the black dashed line, which includes best fit systematics and oscillations. In red are IBD candidates (solid line) and backgrounds (dashed).

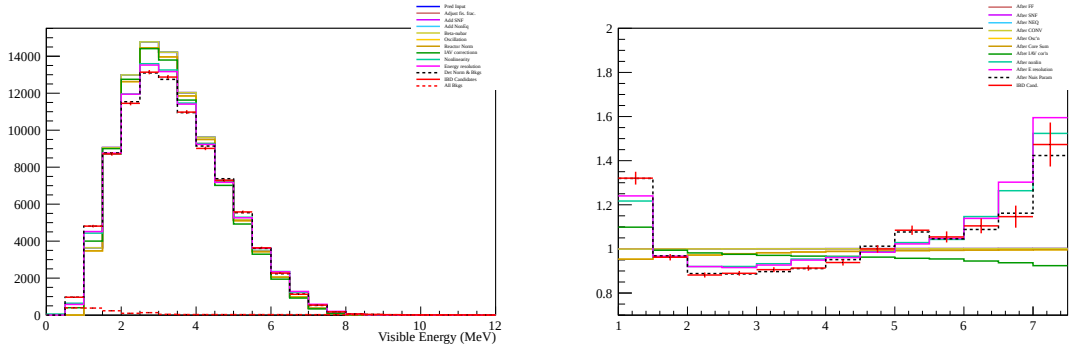


Figure 9.16 Detector 3 spectra after each stage of the rate and shape data fit: absolute (left) and ratio (right) in which the spectrum at each stage is divided by the initial unoscillated predicted spectrum (right). The model progression starts from the solid blue line, which is the initial reactor flux prediction, to the black dashed line, which includes best fit systematics and oscillations. In red are IBD candidates (solid line) and backgrounds (dashed).

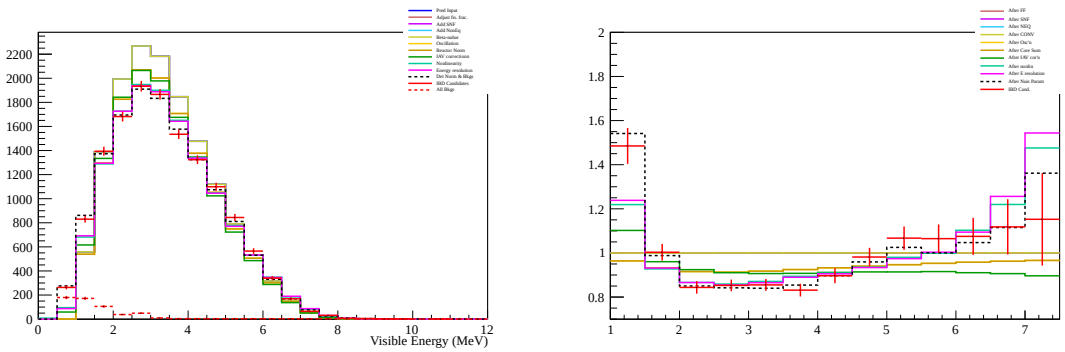


Figure 9.17 Detector 4 spectra after each stage of the rate and shape data fit: absolute (left) and ratio (right) in which the spectrum at each stage is divided by the initial unoscillated predicted spectrum (right). The model progression starts from the solid blue line, which is the initial reactor flux prediction, to the black dashed line, which includes best fit systematics and oscillations. In red are IBD candidates (solid line) and backgrounds (dashed).

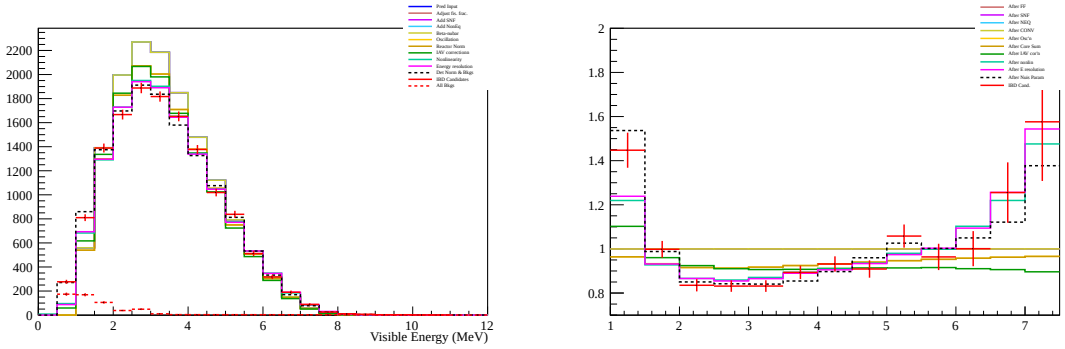


Figure 9.18 Detector 5 spectra after each stage of the rate and shape data fit: absolute (left) and ratio (right) in which the spectrum at each stage is divided by the initial unoscillated predicted spectrum (right). The model progression starts from the solid blue line, which is the initial reactor flux prediction, to the black dashed line, which includes best fit systematics and oscillations. In red are IBD candidates (solid line) and backgrounds (dashed).

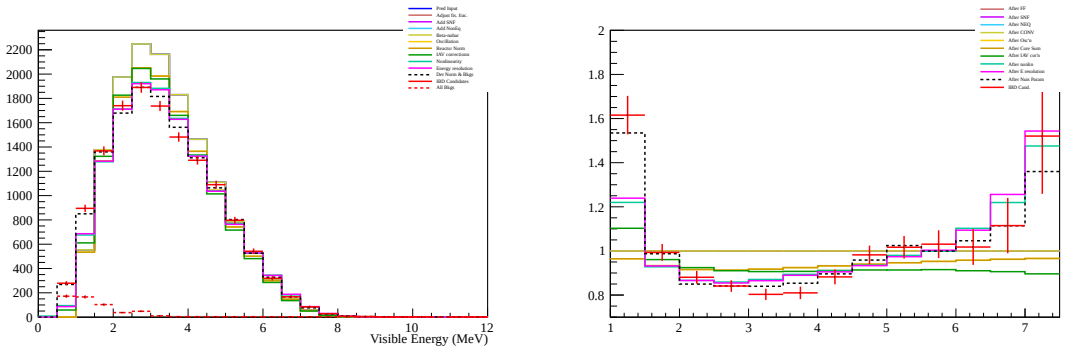


Figure 9.19 Detector 6 spectra after each stage of the rate and shape data fit: absolute (left) and ratio (right) in which the spectrum at each stage is divided by the initial unoscillated predicted spectrum (right). The model progression starts from the solid blue line, which is the initial reactor flux prediction, to the black dashed line, which includes best fit systematics and oscillations. In red are IBD candidates (solid line) and backgrounds (dashed).

the importance of the systematic within the model, and the magnitude of its uncertainty value.

To approximate the size of each contribution, a series of simplified models are used in which only one or zero systematics are included. For the case of no systematics, the model is a straight fit of oscillation parameters determined entirely by the statistics. The precision of such a fit is defined as σ_{stat} below. For $\sin^2 2\theta_{13}$ and Δm^2_{32}, σ_{stat} is:

$$\sigma_{stat}(\sin^2 2\theta_{13}) = 0.0071 \qquad \sigma_{stat}(\Delta m^2_{32}) = 0.13 \cdot 10^{-3}\,\mathrm{eV}^2 \tag{9.4}$$

To study the impact of a given systematic, it is enabled individually within the model, then a fit yields the quantity $\sigma_{stat+sys}$. Finally, the quantity σ_{sys} is determined from subtraction in quadrature:

$$\sigma^2_{sys} \equiv \sigma^2_{stat+sys} - \sigma^2_{stat} \tag{9.5}$$

The method is only an approximation and is susceptible to two drawbacks. First, it is insensitive to correlations among systematics. Secondly, a fit with limited uncertainties is sometimes a fit with a bad model. Such a limited model is not at all designed to explain the data observed, so the results of such a fit must be considered cautiously. For example, the best fits to Δm^2_{32} with only either the detector or reactor normalization uncertainties enabled yields $\sigma_{sys+stat} < \sigma_{stat}$. In this case, a sign reversal was imposed upon Equation 9.5, and the results were consistent with the expectation that detector and reactor rate uncertainty contributions to Δm^2_{32} are small, as Δm^2_{32} is primarily a shape-based measurement.

9.1.6 Best Fit Versus Number of Bins

To further ensure the veracity of the oscillation measurement, it is important to examine the fit result as a function of the number of energy bins chosen. If the fit did depend strongly on $\mathrm{N_{bins}}$, then that choice would have to be carefully justified, and the differences accounted for in the measurement uncertainties. The data provided by the collaboration is binned into 240 bins from 0–12 MeV, regardless of whether there are possibly antineutrino events in a given bin. For the χ^2 analysis, the 240 bins are combined beforehand into any divisor, $\mathrm{N_{bins}}$.

Error Budget			
$\sin^2 2\theta_{13}$:		Δm^2_{32}:	
statistics	27%	statistics	24%
reactor	6%	reactor	3%*
detector rate	7%	detector rate	4%*
nonlinearity	13%	nonlinearity	17%
background	5%	background	5%
bin norm	13%	bin norm	19%
fission fraction	12%	fission fraction	9%
spent nuclear fuel	4%	spent nuclear fuel	2%
nonequilibrium	4%	nonequilibrium	3%
IAV	0%	IAV	0%
$\beta \to \bar{\nu}$ conversion	9%	$\beta \to \bar{\nu}$ conversion	12%

Table 9.3 Error budget computed for $\sin^2 2\theta_{13}$ and Δm^2_{32} via one- or zero-systematic fits. Asterisks denote sign reversal in Equation 9.5.

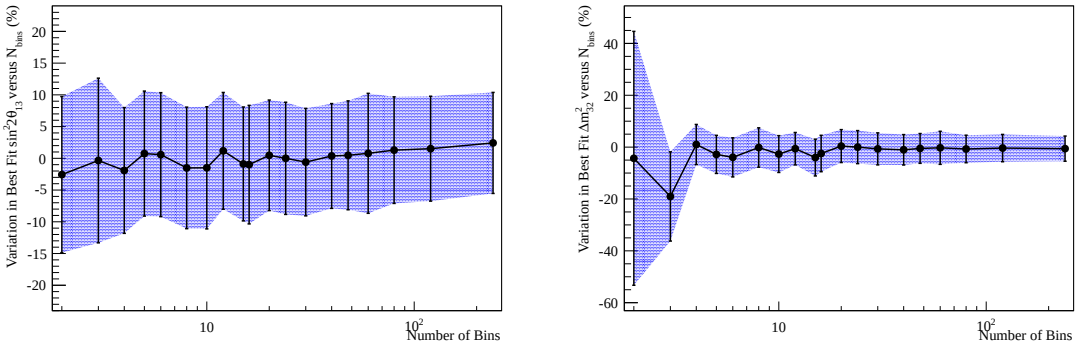


Figure 9.20 Best fit $\sin^2 2\theta_{13}$ (left) and Δm^2_{32} (right) versus number of energy bins. The y-axis is the deviation (%) from the primary measurement at 24 bins.

For the most part the choice is arbitrary, except for the special case of $N_{bins} = 1$, which leads to a rate-only measurement.

Figure 9.20 demonstrates the consistency of the fit over all choices from 2-240. The $\sin^2 2\theta_{13}$ measurement gradually becomes more precise as the number of bins increases. This is expected as more spectral information is being provided to the fit. The central values vary little, with a slight increasing linear trend. This is natural since the rate-only and the rate and shape analyses differ slightly; the trend represents a gradual transition from one to the other.

The Δm^2_{32} figure shows a much greater dependence of the fit precision on the number of bins. This is proper since the Δm^2_{32} fit is predicated on spectral shape information. The more bins available, the better resolved the spectral information. After $N_{bins} \simeq 4$, the fit is flat with no slope.

9.1.7 Alternate Flux Models

There are three popular and similar models to predict the antineutrino flux from reactor isotopes. One of the most recent models, "Huber-French," is the basis of this analysis because it is new and more internal to the collaboration. It was selected before fits were performed.

The flux prediction "ILL Vogel-Engel" is the original standard, based off the beta spectra of isotopes irradiated at ILL, with the conversion to antineutrino spectra calculated from known decay branches. "ILL-Muller," like the Huber-French model, is a reanalysis of the ILL data with modern decay knowledge. ILL-Mueller is the choice of the Double Chooz collaboration.

The fits performed with data using all three flux models are listed in Table 9.4. The measurement of $\sin^2 2\theta_{13}$ demonstrates slight dependence on the flux model chosen, varying from 0.0881 to 0.0895, or 1.6%. The measurement of Δm^2_{32} varies by no more than 0.2%. The primary difference between the models is the overall rate predicted, hence the larger effect on $\sin^2 2\theta_{13}$. Table 9.4 also provides the normalization of the data to prediction, showing values of about 0–3%. This matches known differences.

Flux Model	$\sin^2 2\theta_{13}$ fit	Δm^2_{32} fit	Normalization fit	χ^2_{min}
Huber-French	$0.0880922^{+0.008816}_{-0.008843}$	$2.54407^{+0.166}_{-0.176}\cdot 10^{-3}\,\mathrm{eV}^2$	$-0.0301548^{+0.029158}_{-0.027540}$	114.426
ILL Vogel-Engel	$0.0887427^{+0.008823}_{-0.008867}$	$2.54721^{+0.165}_{-0.175}\cdot 10^{-3}\,\mathrm{eV}^2$	$-0.016588^{+0.044743}_{-0.040986}$	104.636
ILL Mueller	$0.0894608^{+0.008783}_{-0.008786}$	$2.54932^{+0.163}_{-0.169}\cdot 10^{-3}\,\mathrm{eV}^2$	$-9.977138\cdot 10^{-4}{}^{+0.029488}_{-0.026805}$	119.166

Table 9.4 Rate and shape analysis with three antineutrino flux models. Huber-French is the primary flux model of this analysis. The oscillation parameter measurements vary little, but the overall normalization $\mathcal{H}$ varies to match the predicted rates.

9.1.8 Search for Alternate Minima

Numerical minimizers are designed to find the global minimum of a function, but can suffer from two failure modes. The minimizer could return a local minimum instead, or may find a set of solutions corresponding to the same minimum, then report one of them. To examine the possibility of this happening with the given χ^2 and minimizer, the minimizer is initialized at randomized starting values rather than at the best guess, a vector of zeroes.

By construction, the best fit nuisance parameters should be normally distributed close to zero. During the process of the minimization, the fit parameters are adjusted from their initial guesses to their final values. By setting the initial guesses not to zero but randomly

according to a uniform distribution:

$$0.2 * (\mathcal{X} - 0.5), \quad 0 \geq \mathcal{X} \geq 1, \tag{9.6}$$

the odds are increased that the minimizer will return an alternative minima, or fail to return a result. If any of these χ^2_{min} values are lower than the nominal minimization, then the nominal analysis will have been incorrect. If the minimizer reports the same χ^2_{min} with different oscillation parameter values, then those new values must be considered equally as best fits, resulting in larger uncertainties. Failure to return a minimum, which did not occur in this study, would not be cause for concern. The minimizer is working over 86 dimensions in the case of 24 energy bins, so with such a large space to cover, unrealistic initial guesses can place all minima out of reach.

A search is conducted with 1000 trials with randomized initial guesses. The resulting values of χ^2_{min} are histogrammed in Figure 9.21. Figure 9.21 is divided into four regimes, in which the domain is restricted to show more detail. A small fraction, 0.5%, of the runs produced extremely high χ^2_{min}. In the region around 130%–200% of the best fit χ^2_{min} there are a couple of peaks, presumably representing local minima. These comprise 6.7% of runs. The remaining 92.8% are clustered below χ^2_{min}=123. Of these, 90.1% are at the exact best fit χ^2_{min} of 114.426, while an additional 2% lie between χ^2_{min} and $\chi^2_{min} + 1$.

Figure 9.22 shows the best fit $\sin^2 2\theta_{13}$ and Δm^2_{32} for $\chi^2_{min} < 125$ and χ^2_{min}=114.426. From the former, the larger χ^2_{min} values correspond to high $\sin^2 2\theta_{13}$-low Δm^2_{32} or low $\sin^2 2\theta_{13}$-high Δm^2_{32} pairs, which are close to the true minimum and conserve the total oscillation rate. The latter panel shows the spread in $\sin^2 2\theta_{13}$ and Δm^2_{32} for the exact best fit. The variance at the exact best fit is small, as exhibited further by Figures 9.23 and 9.24. At the exact best fit, $\sin^2 2\theta_{13}$=0.0881$\pm$9.89$\cdot 10^{-6}$ while Δm^2_{32}=(2.544$\pm$0.000117)$\cdot 10^{-3}$ eV^2, which are in agreement with the reported results. Here, the uncertainty comes from the RMS of the distributions. Studying the $\sin^2 2\theta_{13}$ and Δm^2_{32} distributions for $\chi^2 \leq \chi^2_{min} + 1$ is similar to the standard treatment for the 1σ error bars. In so doing, the central values remain the same, but the uncertainties increase to $\sin^2 2\theta_{13}$=0.0881$\pm$2.55$\cdot 10^{-5}$ and Δm^2_{32}=(2.544$\pm$0.000905)$\cdot 10^{-3}$ eV^2.

In either case, the additional uncertainty on the best fit oscillation parameters due to the numerical minimizer itself is negligible.

9.1.9 Treatment of ^{238}U Systematic

The antineutrino flux of isotope ^{238}U is more difficult to predict because ^{238}U has a longer half-life, therefore past experiments to study its decays were insensitive [135, 136, 137]. As a result the ^{238}U prediction is theoretical [138], and comes with spectral uncertainties, primarily at energies above 9 MeV, that are more difficult to characterize. This uncertainty is reactor-correlated, but the extent to which it is energy-correlated or energy-uncorrelated is not yet fully understood. As a baseline it is taken as energy-uncorrelated during the fit, included as a contribution to the energy bin normalization. This is more conservative and recommended by the collaboration.

For comparison, the analysis performed with the ^{238}U uncertainty treated as energy-correlated, and hence included as a contribution to the $\beta \rightarrow \bar{\nu}$ uncertainty during the fit, is shown in Table 9.5. Since the uncertainty acts in a more restricted manner, the best fit values change negligibly, but uncertainty margins decrease slightly while the χ^2_{min} value increases. Any scheme in which the uncertainty was partially correlated and uncorrelated in energy would lie in between these two end cases.

While the oscillation parameter measurements remain the same despite the ^{238}U treatment changes, the relationship between the systematic uncertainties deviates somewhat. Figure 9.25 compares the covariance matrices in both cases. The only appreciable difference is that the diagonal elements for the normalizations of bins 21–24 are larger (>1) in the

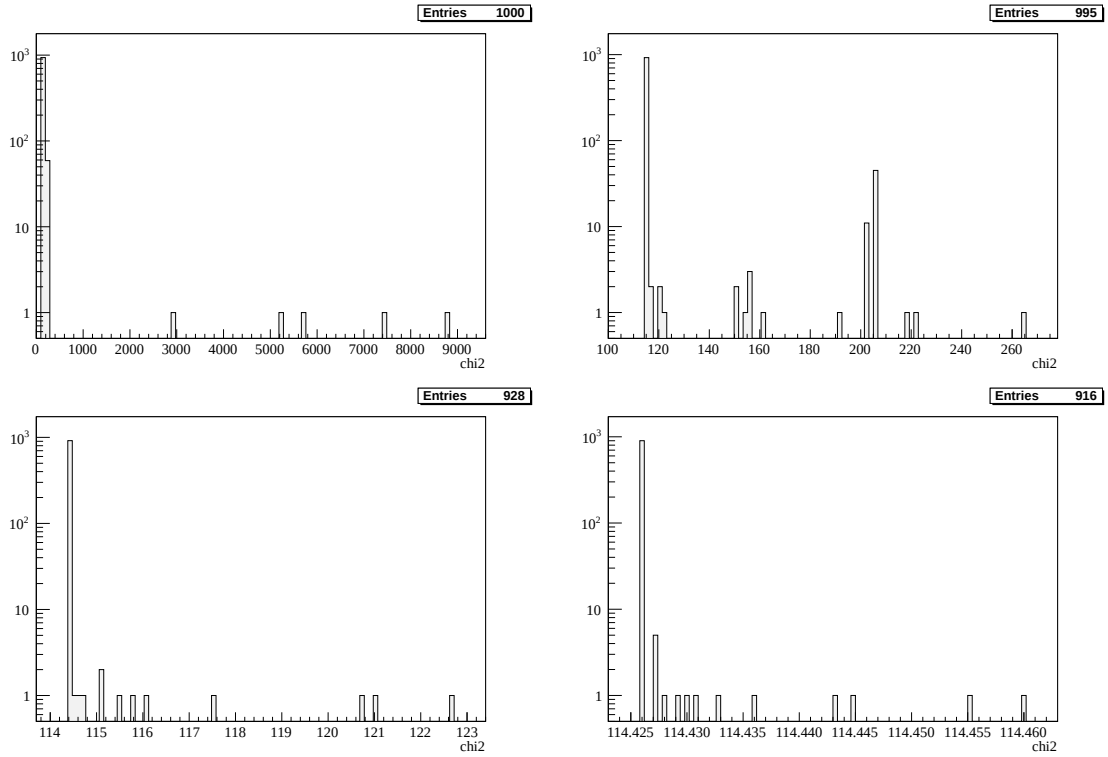


Figure 9.21 Histogram of χ^2_{min} values for 1000 fits to data with random starting values for nuisance parameters. The histograms successively zoom into the low χ^2_{min} region. Top left: all results. Top right: $\chi^2_{min}< 270$. Bottom left: $\chi^2_{min}< 125$. Bottom right: $\chi^2_{min}< 114.48$. The true $\chi^2_{min} = 114.26$.

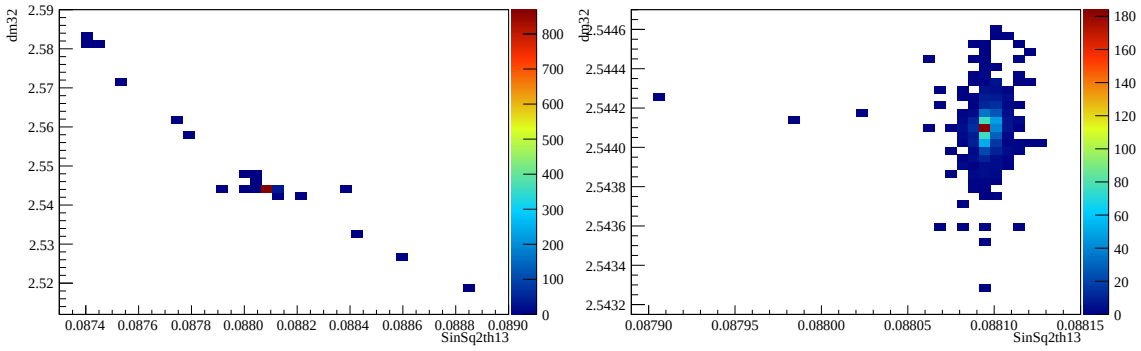


Figure 9.22 Best fit $\sin^2 2\theta_{13}$ and Δm^2_{32} for fits with randomized starting values of nuisance parameters. Left: $\chi^2_{min} < 125$. Right: $\chi^2_{min} = 114.426$, the true minimum.

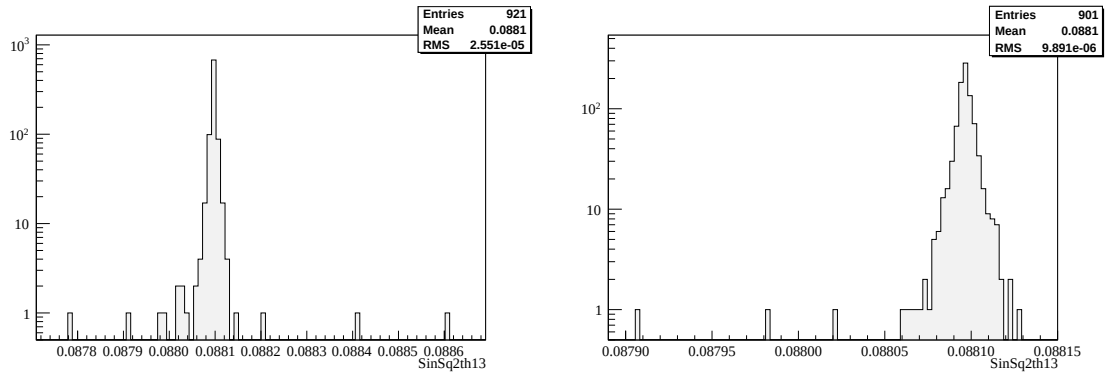


Figure 9.23 Best fit values of $\sin^2 2\theta_{13}$ for randomized nuisance parameter starting values. Left: χ^2_{min}<115.426. Right: χ^2_{min}=114.426. The small RMS of the spread of fit values indicates the χ^2 minimization process does not add significantly to the uncertainty of the fit result.

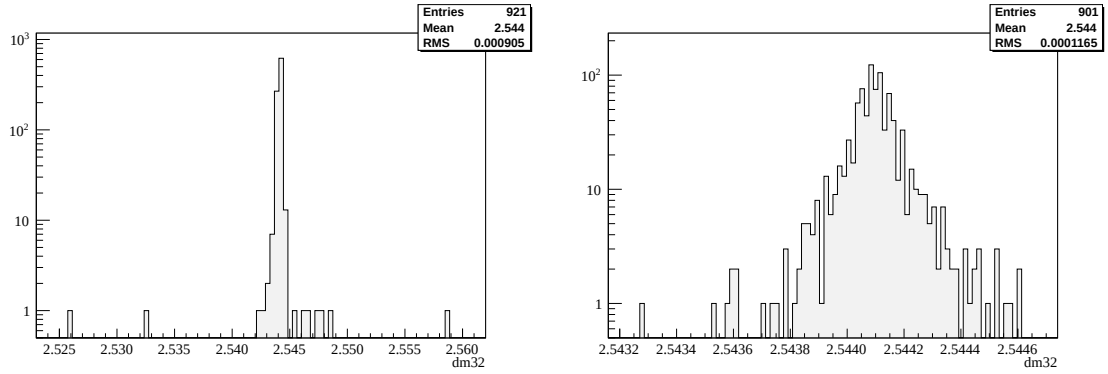


Figure 9.24 Best fit values of Δm^2_{32} for randomized nuisance parameter starting values. Left: χ^2_{min}<115.426. Right: χ^2_{min}=114.426. The small RMS of the spread of fit values indicates the χ^2 minimization process does not add significantly to the uncertainty of the fit result.

energy-uncorrelated case. These bins are sparsely populated with the largest uncertainties. Likewise, Figure 9.26 compares the correlation matrices, demonstrating greater systematic to systematic correlations in the energy-uncorrelated case.

Flux Model	$\sin^2 2\theta_{13}$ fit	Δm^2_{32} fit	Normalization fit	χ^2_{min}
Correlated	$0.0876239^{+0.008805}_{-0.008835}$	$2.54137^{+0.166}_{-0.176}\cdot 10^{-3}\,\mathrm{eV}^2$	$-0.0350230^{+0.030158}_{-0.029191}$	121.247
Uncorrelated	$0.0880922^{+0.008816}_{-0.008843}$	$2.54407^{+0.166}_{-0.176}\cdot 10^{-3}\,\mathrm{eV}^2$	$-0.0301548^{+0.029158}_{-0.027540}$	114.426

Table 9.5 Rate and shape analysis with the spectral uncertainty of the ^{238}U either energy-correlated or energy-uncorrelated. The nominal case is energy-uncorrelated.

9.2 Measurement with Constrained Δm^2_{32}, and Neutrino Mass Hierarchy

Previous experiments have performed measurements on Δm^2_{32}, so it is informative to input this prior information into the fit. The oscillation parameter measurement with Δm^2_{32} constrained is performed in the same manner as the primary fit, but with Δm^2_{32} tied to a pull term with finite uncertainty. The central value and uncertainty on Δm^2_{32} in the model is $\Delta m^2_{32} = 2.32 \pm 0.12 \cdot 10^{-3}\,\mathrm{eV}^2$, the world average at the time the model was created [1]. Even though the true uncertainty on Δm^2_{32} is $^{+0.12}_{-0.08}$, an asymmetric error bar is numerically a poor choice for the minimizer because the minimization would require separate cases, i.e. $\eta > 0$ and $\eta \leq 0$, which would cause a discontinuity in $\mathrm{d}\chi^2/\mathrm{d}\eta$ at $\eta = 0$, and hence an unreliable minimization. To be conservative, the error bar is symmetrized to the larger uncertainty value. The case of $\Delta m^2_{32} = 2.41 \pm 0.10$ is of interest as well, because after the model was written, the MINOS experiment released a measurement of $\Delta m^2_{\mu\mu} = 2.41^{+0.09}_{-0.10}$, where $|\Delta m^2_{\mu\mu}| \simeq |\Delta m^2_{32}|$ [4].

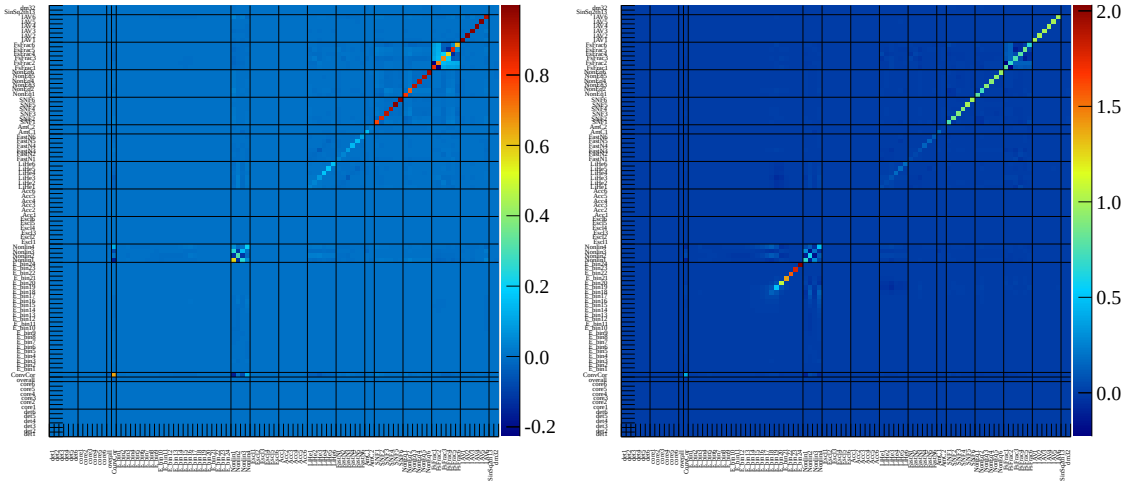


Figure 9.25 Covariance matrix for analyses with the ^{238}U flux uncertainties energy-correlated (left) or uncorrelated (right). The latter is the primary analysis.

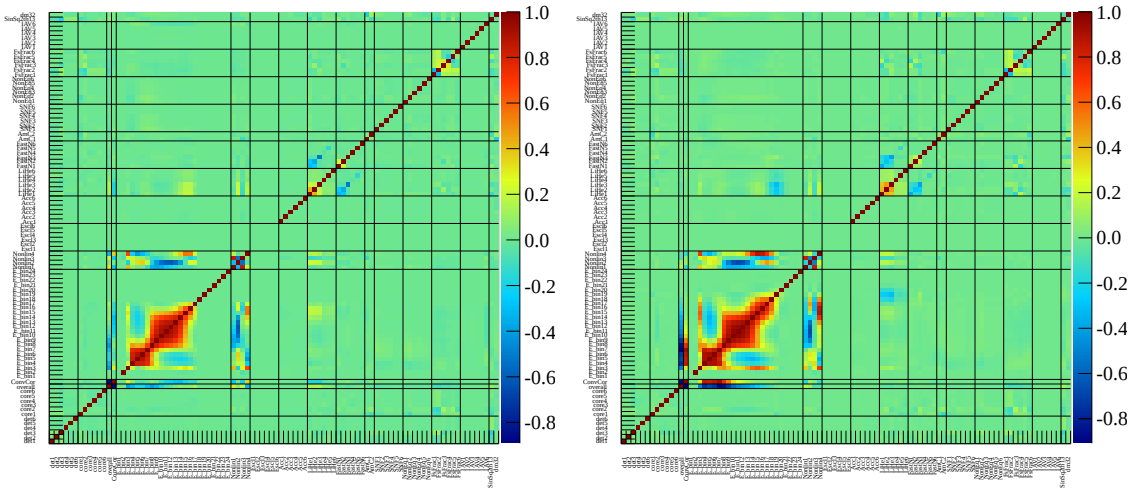


Figure 9.26 Correlation matrix for analyses with the ^{238}U flux uncertainties energy-correlated (left) or uncorrelated (right). The latter is the primary analysis.

Furthermore, because Δm^2_{32} is constrained, the neutrino mass hierarchy becomes more important. While Δm^2_{32} is the fit parameter, Δm^2_{32} and Δm^2_{31} are effectively fit as a pair because Δm^2_{31} is constrained to Δm^2_{32} by the relation

$$\begin{aligned} \Delta m^2_{31} &= |\Delta m^2_{32}| + \Delta m^2_{21} \quad \text{(Normal Hierarchy)} \\ \Delta m^2_{31} &= -|\Delta m^2_{32}| + \Delta m^2_{21} \quad \text{(Inverted Hierarchy)}, \end{aligned} \tag{9.7}$$

where Δm^2_{21}=7.50$\pm$0.02$\cdot 10^{-5}\,\text{eV}^2$.

The measured oscillation parameters for the fits with free or constrained Δm^2_{32}, assuming normal or inverted hierarchy, are presented in Table 9.6. For the constrained Δm^2_{32} cases, the best fits are close to the constraint value, but shifted toward the free Δm^2_{32} best fit value by less than 1σ. The difference is least for the $\Delta m^2_{32} = 2.41\cdot 10^{-3}\,\text{eV}^2$ case, since that value is closer to the free fit value. Overall the Δm^2_{32} fits are consistent among the free and constrained cases to about 1σ.

Between the normal and inverted hierarchy assumptions, Δm^2_{32} and Δm^2_{31} approximately swap values with a sign change on Δm^2_{31}. This occurs because reactor oscillations are insensitive to the sign of Δm^2_{32} and Δm^2_{31}. Δm^2_{32} and Δm^2_{31} are thus fit as a pair where either one (depending on the hierarchy assumption) is larger in magnitude than the other by an amount Δm^2_{21}.

The best fit values of $\sin^2 2\theta_{13}$ and the normalization change only slightly between the fits with constrained and free Δm^2_{32}, and do so in a manner that counterbalances the tension in the Δm^2_{32} fit. The best fit Δm^2_{32} value when unconstrained is higher than the constrained Δm^2_{32} fit values, so $\sin^2 2\theta_{13}$ and $\mathcal{H}$ absorb the difference. The error bars correspond to the Δm^2_{32} fit: where Δm^2_{32} is constrained, Δm^2_{32} error bars are smaller, while $\sin^2 2\theta_{13}$ error bars are slightly larger, reflecting the tension between the constraint and the free best fit. The χ^2_{min} value changes little between normal and inverted hierarchy, thus showing no preference to either.

Δm^2_{32} status	$\sin^2 2\theta_{13}$	Δm^2_{32}	Δm^2_{31}	Normalization	$\chi^2_{min}/\mathrm{N_{DOF}}$
Free Δm^2_{32}, NH	$0.0880922^{+0.008816}_{-0.008843}$	$2.54407^{+0.166}_{-0.176}$	2.61907	$-0.0301548^{+0.029158}_{-0.027540}$	0.811530
Free Δm^2_{32}, IH	$0.0880961^{+0.008812}_{-0.008846}$	$2.64750^{+0.166}_{-0.176}$	−2.57250	$-0.0301329^{+0.029137}_{-0.027562}$	0.811530
Δm^2_{32}=2.32±0.12, NH	$0.0882200^{+0.008881}_{-0.008916}$	$2.39009^{+0.100}_{-0.102}$	2.46509	$-0.0314527^{+0.029069}_{-0.027502}$	0.813683
Δm^2_{32}=2.32±0.12, IH	$0.0883126^{+0.008955}_{-0.008976}$	$2.41880^{+0.102}_{-0.104}$	−2.34380	$-0.0321766^{+0.029044}_{-0.027479}$	0.822251
Δm^2_{32}=2.41±0.10, NH	$0.0881714^{+0.008850}_{-0.008879}$	$2.44306^{+0.087}_{-0.088}$	2.51806	$-0.0309632^{+0.029075}_{-0.027520}$	0.808990
Δm^2_{32}=2.41±0.10, IH	$0.0882526^{+0.008900}_{-0.008940}$	$2.46624^{+0.088}_{-0.089}$	−2.39124	$-0.0317001^{+0.029044}_{-0.027501}$	0.815524

Table 9.6 Rate and shape analysis with different cases of Δm^2_{32} constraint or hierarchy. Units of Δm^2_{32} and Δm^2_{31} are $10^{-3}\mathrm{eV}^2$ and NH(IH) stands for normal(inverted) hierarchy. Δm^2_{31} is not fit, but equated to either $\Delta m^2_{31} = \Delta m^2_{21} + \Delta m^2_{32}$ (NH) or $\Delta m^2_{31} = \Delta m^2_{21} - \Delta m^2_{32}$ (IH).

9.2.1 Best Fits

Figures 9.27 and 9.28 provide the best fit $\sin^2 2\theta_{13}$-Δm^2_{32} 1σ contours for the cases of free Δm^2_{32}, both mass hierarchies, and constrained Δm^2_{32}, both hierarchies. The contours are similar in shape, with approximately the same coverage in $\sin^2 2\theta_{13}$, but the contours shift slightly in Δm^2_{32}. The constrained-Δm^2_{32} contours are expectedly much thinner in the Δm^2_{32} dimension than the free Δm^2_{32} case, and lie much closer to the constraint value than the free Δm^2_{32} value.

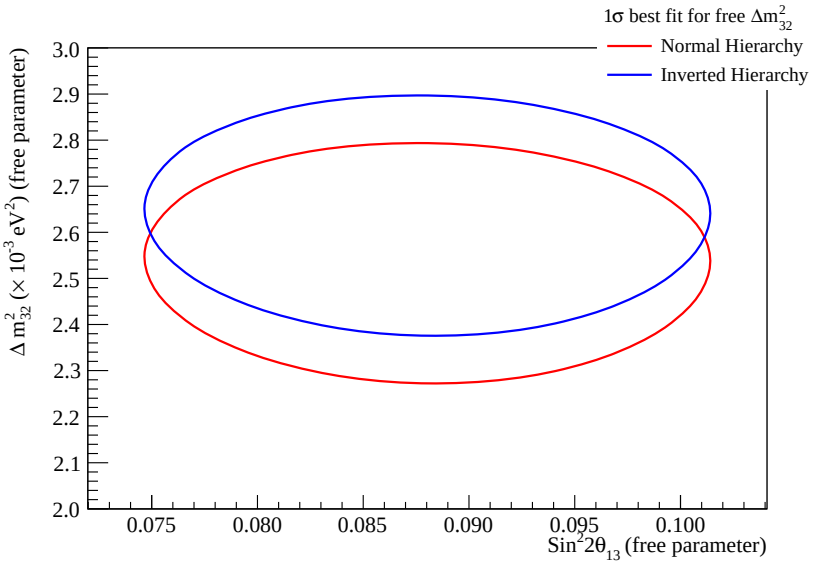


Figure 9.27 1σ $\sin^2 2\theta_{13}$-Δm^2_{32} contours for rate and shape analyses with unconstrained Δm^2_{32}, and both normal and inverted hierarchy.

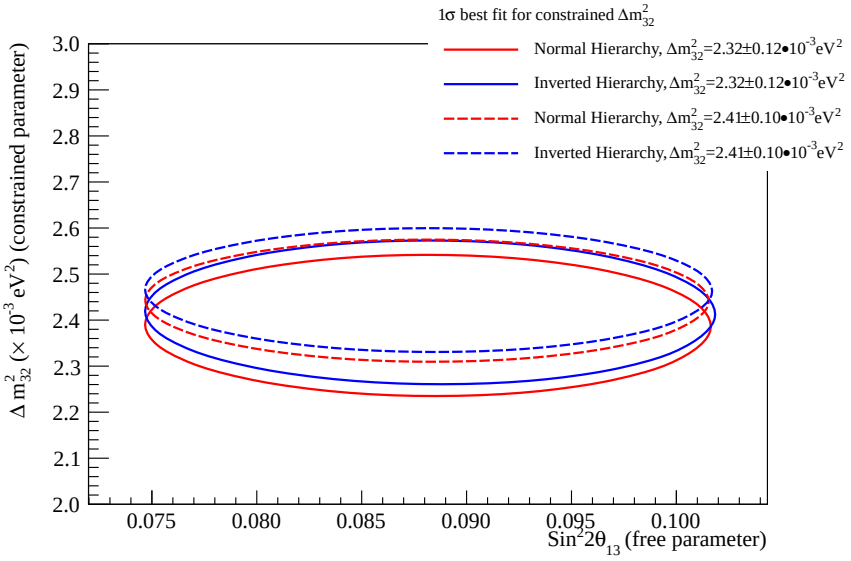


Figure 9.28 1σ $\sin^2 2\theta_{13}$-Δm^2_{32} contours for rate and shape analyses with two cases of constrained Δm^2_{32}, and both normal and inverted hierarchy.

9.2.2 Best Fit Diagnostics

Table 9.7 and Figures 9.29 through 9.33 provide various diagnostics for the case of $\Delta m^2_{32} = 2.32 \pm 0.12$ and normal hierarchy. In Table 9.7, the contributions of systematics and statistics to the overall best fit χ^2_{min} are listed. As in the case of the free Δm^2_{32} fit (Table 9.1), the dominant contribution by far is the statistical part, followed distantly by the largest set of systematic pull terms, those pertaining to the background normalizations.

Figures 9.29 and 9.30 describe the correlations among the systematics and oscillation parameters, and Figure 9.31 shows the covariance matrix. The correlations with Δm^2_{32} constrained are nearly identical to that of the free Δm^2_{32} (Figures 9.6 and 9.7), even those correlations with Δm^2_{32} itself. All correlations of systematics with oscillation parameters are smaller than 0.2 in magnitude, while the only significant correlations among distinct systematics are those that are closely related, such as normalizations of neighboring bins. The covariance matrix likewise changes little from the free Δm^2_{32} fit (Figure 9.8), even those elements related to Δm^2_{32}.

Pull terms information is provided in Figures 9.32 and 9.33. One sees that little tension is present, demonstrated by the lack of pull terms larger than unity. The pull terms of systematics change little from the free Δm^2_{32} case (Figures 9.9 and 9.10).

Contributions to χ^2_{min}, constrained Δm^2_{32}:		
From statistical part	108.336 / 144 = 0.752331	93.8%
From detector normalization	0.066 / 6 = 0.0110748	0.06%
From reactor normalization	0.006 / 6 = 0.00103994	0.005%
From bin normalization	2.129 / 24 = 0.0887223	1.8%
From nonlinearity	0.658 / 4 = 0.164446	0.6%
From background normalization	3.838 / 19 = 0.201993	3.3%
From $\beta \to \bar{\nu}$ energy-correlated	0.000 / 1 = 0.000259345	0.0002%
From IAV det-uncorr./energy-corr.	0.001 / 6 = 0.00018437	0.0008%
From spent fuel	0.053 / 6 = 0.00888131	0.05%
From nonequilibrium	0.048 / 6 = 0.00793229	0.04%
From fission fraction	0.066 / 6 = 0.011067	0.06%
From Δm^2_{32} pull term	0.341 / 1 = 0.340992	0.3%
Total χ^2_{min}	115.54 / (6*24–2) = 0.814	

Table 9.7 The contribution of each systematic to the value of χ^2_{min} for a rate and shape analysis with Δm^2_{32}=2.32±0.12 and normal hierarchy. Except for the statistical part, the quantities listed are the size of each set of pull terms $(\eta_\iota/\sigma_\iota)^2$, in total and where applicable averaged per detector, reactor or bin. The percentages are based on the total pull terms per systematic. The statistical part is the lead term in the χ^2: $\chi^2 - \sum(\eta_\iota/\sigma_\iota)^2$.

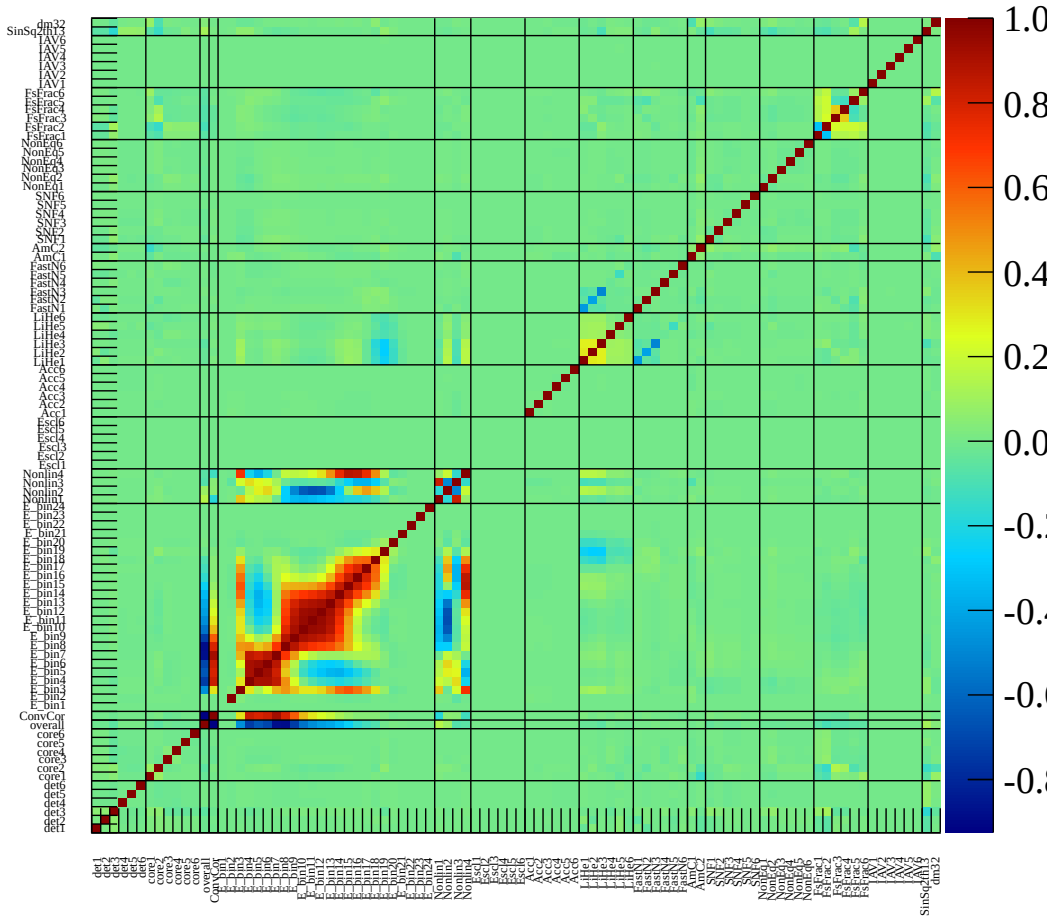


Figure 9.29 Correlation matrix from a rate and shape analysis where Δm^2_{32} is constrained to Δm^2_{32}=2.32±0.12, assuming normal hierarchy. Variable names are listed on the axes.

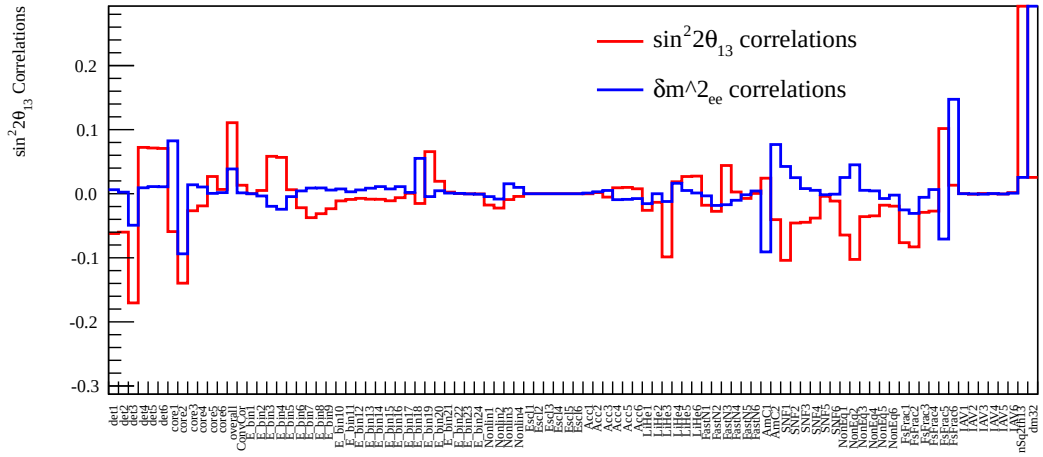


Figure 9.30 Correlations among oscillation parameters and systematics from a rate and shape analysis where Δm^2_{32} is constrained to Δm^2_{32}=2.32±0.12, assuming normal hierarchy. Variable names are listed on the axes.

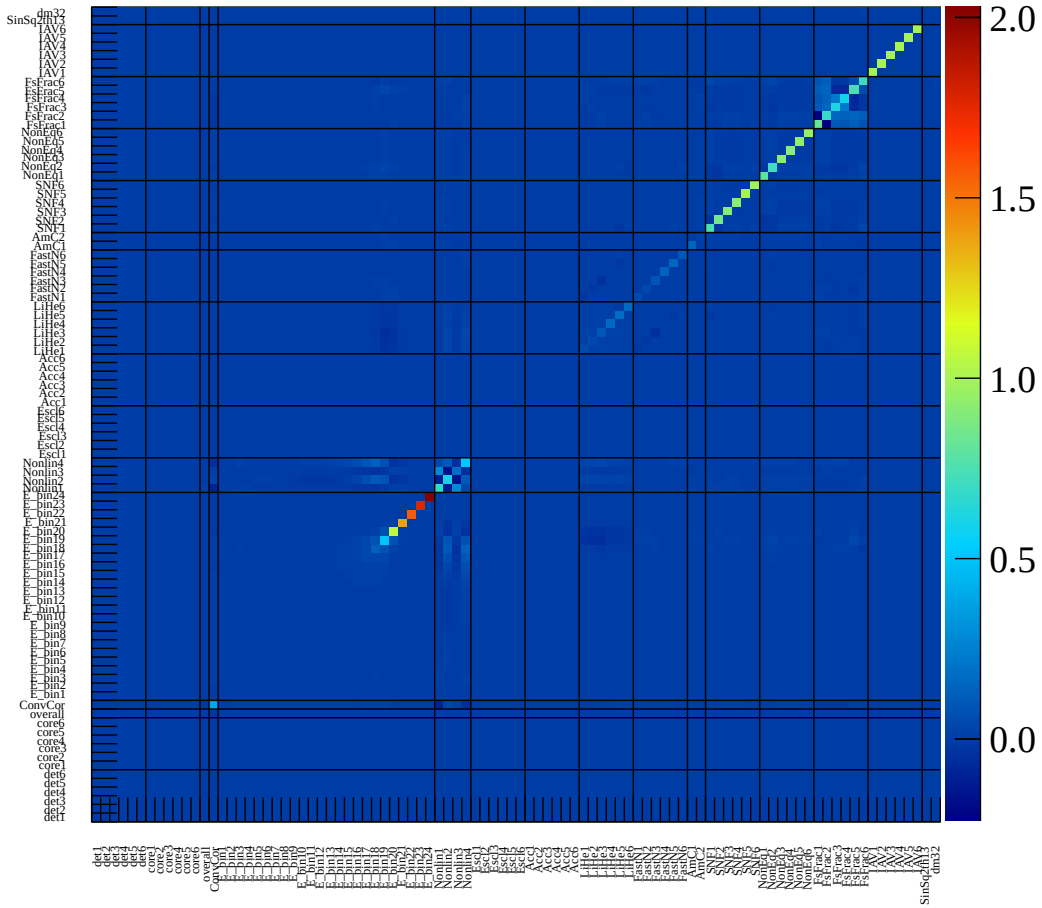


Figure 9.31 Covariance matrix from a rate and shape analysis where Δm^2_{32} is constrained to Δm^2_{32}=2.32±0.12, assuming normal hierarchy. Variable names are listed on the axes.

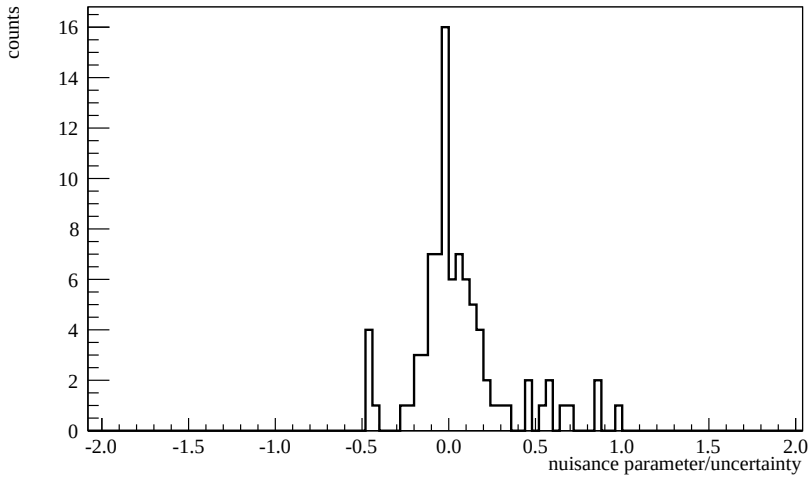


Figure 9.32 Histogram of systematic nuisance parameters divided by uncertainties (η_ι/σ_ι) at best fit from a rate and shape analysis where Δm^2_{32} is constrained to $\Delta m^2_{32} = 2.32 \pm 0.12$, assuming normal hierarchy.

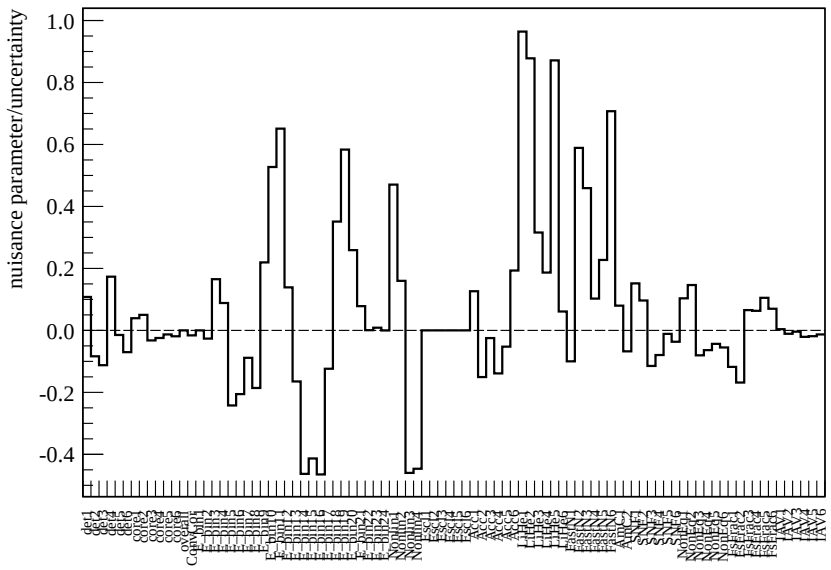


Figure 9.33 Systematic nuisance parameters divided by uncertainties (η_ι/σ_ι) at best fit from a rate and shape analysis where Δm^2_{32} is constrained to $\Delta m^2_{32} = 2.32 \pm 0.12$, assuming normal hierarchy. Variable names are listed on the axes.

9.3 Measurement with Detector Rates Only

A rate-only analysis is noteworthy to provide a consistency check on the rate plus shape and shape-only analyses, and to understand the role of various sources of information and systematics.

The rate-only analysis is performed by combining all statistics into one energy bin per detector. Spectral systematic uncertainties are converted into an overall rate uncertainty by combining their effects over each bin, accounting for their energy correlations. Similar uncertainties are combined into a reduced set based on their reactor and detector correlations until the only remaining uncertainties are detector-uncorrelated, reactor-uncorrelated and overall-correlated normalizations. The combinations are listed specifically in Table 9.8. Backgrounds in particular are not fit separately, but combined into detector rates and uncertainties.

Oscillation parameter Δm^2_{32} is constrained to $\Delta m^2_{32} = 2.32 \pm 0.12{\cdot}10^{-3}\,\mathrm{eV}^2$. If not for the constraint, $\sin^2 2\theta_{13}$ and Δm^2_{32} would be impossible to fit together because both control the rates at the detector.

9.3.1 Best Fit Results

For the rate-only analysis, with Δm^2_{32} constrained and assuming normal hierarchy, the measured oscillation parameters are:

- $\sin^2 2\theta_{13} \ = 0.0859752^{+0.009127}_{-0.009190}$
- $\Delta m^2_{32} = 2.32029 \pm 0.120 \cdot 10^{-3}\,\mathrm{eV}^2$
- $\Delta m^2_{31} = 2.39529 \cdot 10^{-3}\,\mathrm{eV}^2$
- $\mathcal{H} = -0.0296895^{+0.005142}_{-0.005072}$
- $\chi^2_{min} = 0.435143$. $\mathrm{N_{DOF}} = 6\text{–}2$. $\chi^2_{min}/\mathrm{N_{DOF}} = 0.108786$

	Correlations		
Uncertainty grouping	Detector	Core	Energy
Uncorrelated detector normalization	U	—	—
Backgrounds	U	—	U
IAV	U	—	C
Uncorrelated reactor normalization	—	U	C
Fission fraction	—	U	C
Spent nuclear fuel	—	U	C
Nonequilibrium flux	—	U	C
Overall correlated normalization	C	C	C
$\beta \to \bar{\nu}$ conversion	—	C	C
Detector nonlinearity	C	—	C
Bin normalization	C	C	U

Table 9.8 The reduction of uncertainties in the rate-only analysis. Uncertainties listed on the indented lines are combined into a single uncertainty above. Correlations are also listed: "U" indicates uncorrelated, "C" indicates correlated, "—" indicates no relevance.

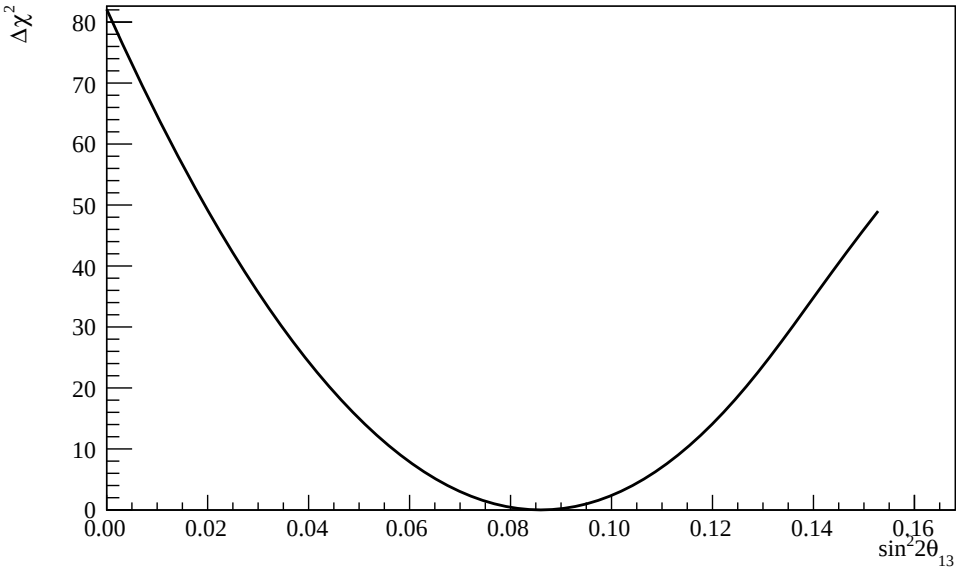


Figure 9.34 The best fit $\Delta\chi^2(\sin^2 2\theta_{13})$ for the rate-only analysis.

The measurement of $\sin^2 2\theta_{13}$ is consistent with the rate and shape measurement of $\sin^2 2\theta_{13} = 0.0881 \pm 0.0088$. The error bar of $^{+0.0091}_{-0.0092}$ is slightly larger than the overall rate and shape error bar of ± 0.0088, demonstrating that most of the measurement comes from the rate information (the shape-only error bar is much larger). The Δm^2_{32} measurement is dominated by its constraint. The overall normalization is also consistent between the two analysis, although the error bar shrinks to ± 0.0051 from $^{+0.029}_{-0.028}$. This occurs because many shape-based fit parameters that also affect the rates have been combined, thus removing competition among parameters that must be mutually varied during the minimization.

Figures 9.34 through 9.36 show the $\Delta\chi^2$ versus $\sin^2 2\theta_{13}$, Δm^2_{32} and $\mathcal{H}$ individually. These curves are slightly more symmetric than those of the rate and shape analysis. Figures 9.37 and 9.38 provide the two dimensional 1σ contours. The $\sin^2 2\theta_{13}$-Δm^2_{32} contour is symmetric in both axes, while the $\sin^2 2\theta_{13}$-$\mathcal{H}$ contour shows significant positive correlation because varying $\sin^2 2\theta_{13}$ and $\mathcal{H}$ (as $1 - \mathcal{H}$ in the fitter) both decrease the flux for positive values.

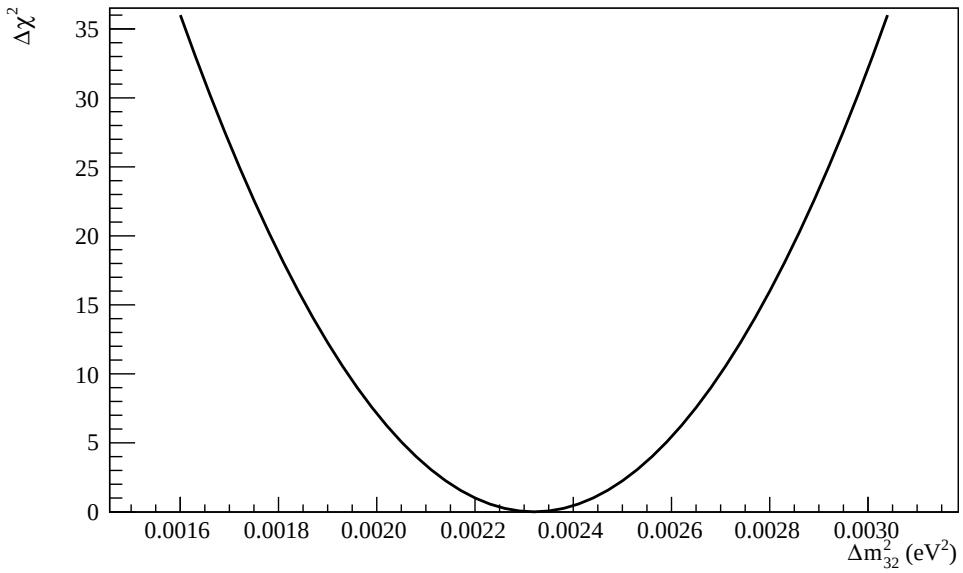


Figure 9.35 The best fit $\Delta\chi^2(\Delta m^2_{32})$ for the rate-only analysis. Δm^2_{32} is constrained to $\Delta m^2_{32} = 2.32 \pm 0.12 \cdot 10^{-3}\,\mathrm{eV}^2$ for the fit.

9.3.2 Best Fit Diagnostics

The diagnostics of the rate-only oscillation measurement are provided in Table 9.9 and Figures 9.39 through 9.43. The correlations in Figure 9.39 and 9.40 show expected behavior: correlations among systematics are small, but elevated for reactors or detectors in that share a site. Self-correlations are unity. Oscillation parameter correlations with systematics are are small, especially for constrained Δm^2_{32}. The $\sin^2 2\theta_{13}$ correlations are similar to those of the rate and shape analysis, although as seen in Figure 9.38 there is a larger correlation among $\sin^2 2\theta_{13}$ and $\mathcal{H}$. The covariance matrix of Figure 9.41 shows tiny values, especially

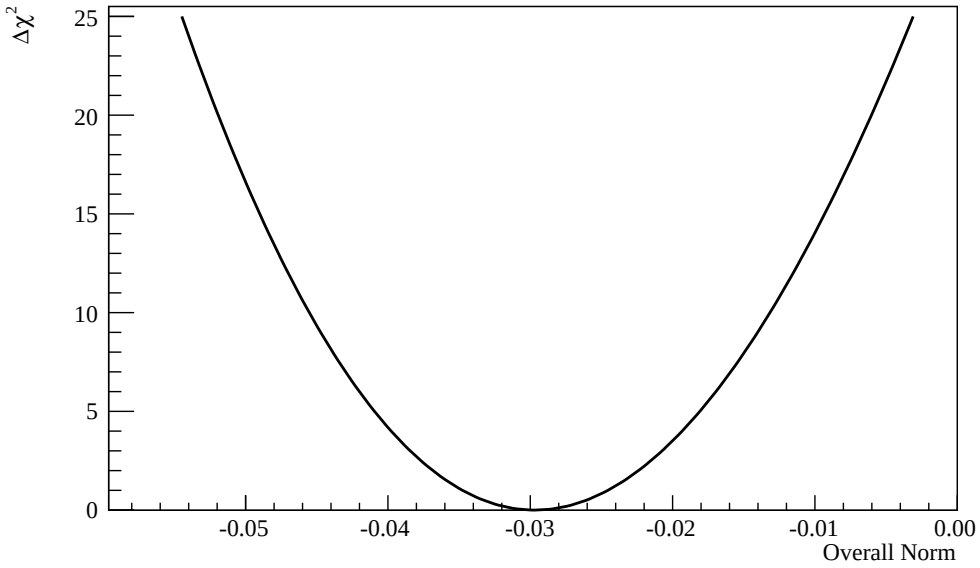


Figure 9.36 The best fit $\Delta\chi^2(\mathcal{H})$ for the rate-only analysis.

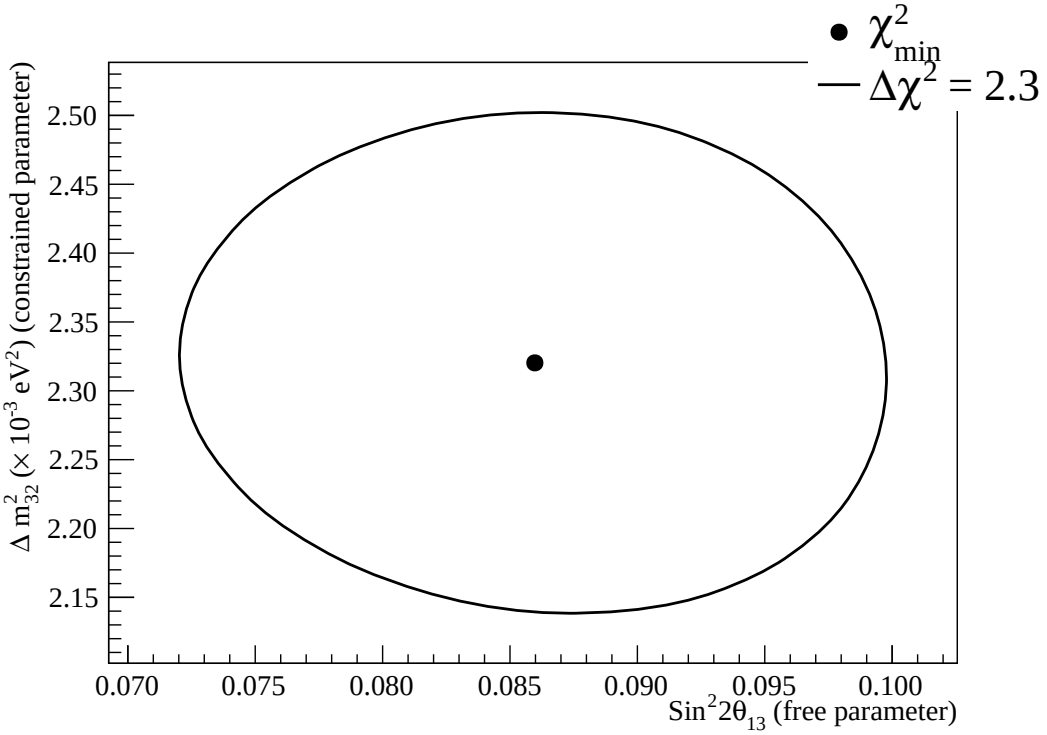


Figure 9.37 The best fit $\sin^2 2\theta_{13}$-Δm^2_{32} point from a rate-only analysis surrounded by the 1σ contour.

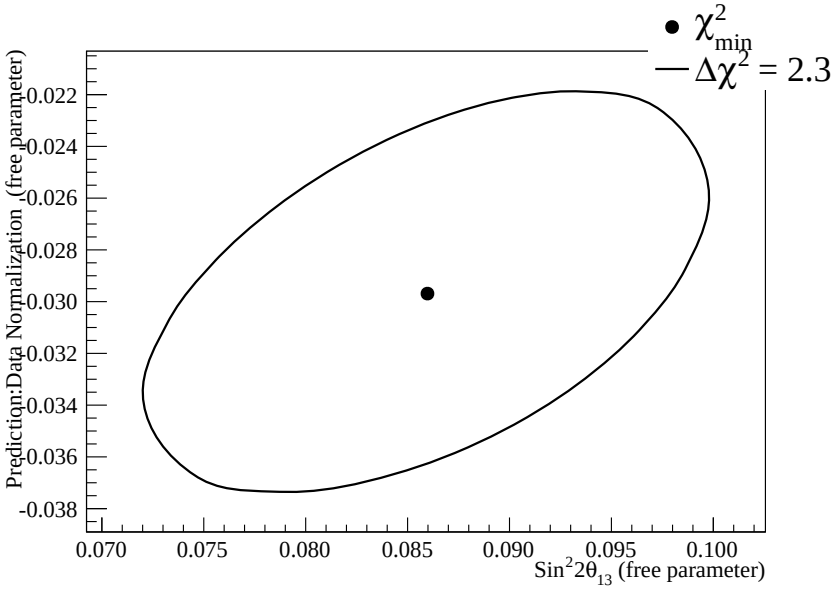


Figure 9.38 The best fit $\sin^2 2\theta_{13}$-$\mathcal{H}$ point from a rate-only analysis surrounded by the 1σ contour.

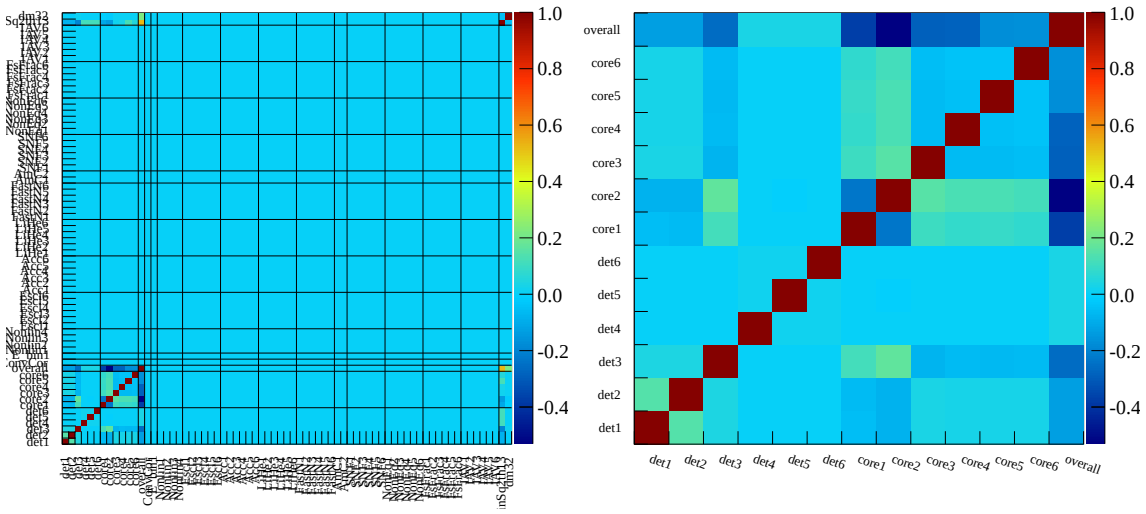


Figure 9.39 Correlation matrix from a rate-only analysis. The right matrix is the zoomed-in portion of the left plot showing systematics, but omitting the oscillation parameters which are in the upper right of the left plot. Variable names are listed on the axes.

for detector uncertainty entries. Again, similarities are seen among the reactors or detectors that share a site.

Like the rate and shape fits, the rate-only fit shows that the statistical part of the χ^2 dominates the χ^2_{min} value as seen in Table 9.9. The statistical part is an order of magnitude larger than the detector uncertainty, which is three times that of the reactor uncertainty. The Δm^2_{32} pull term is negligible. Clearly, the detector nuisance parameters are displaced from zero more than the reactor nuisance parameters, as also seen in Figures 9.42 and 9.43. No pull term is larger in magnitude than 0.10.

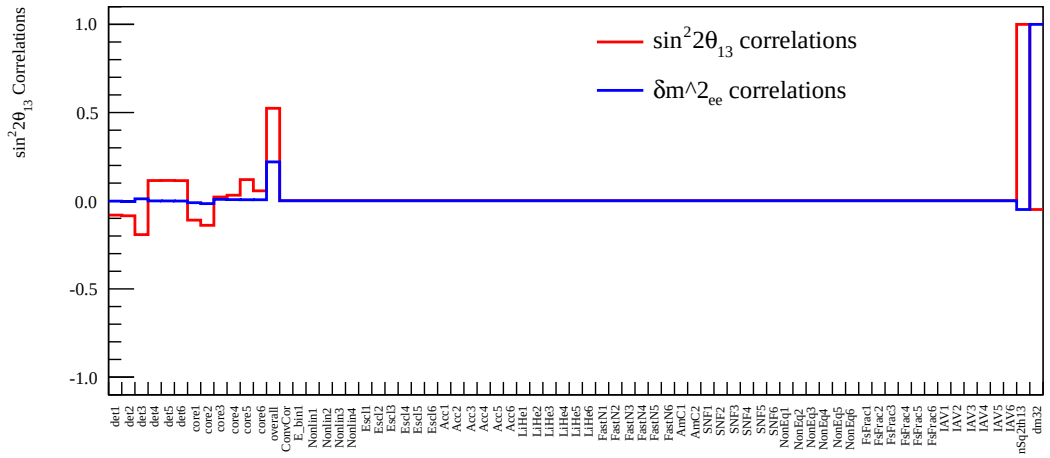


Figure 9.40 Oscillation parameter correlations with systematics from a rate-only analysis. Variable names are listed on the axes.

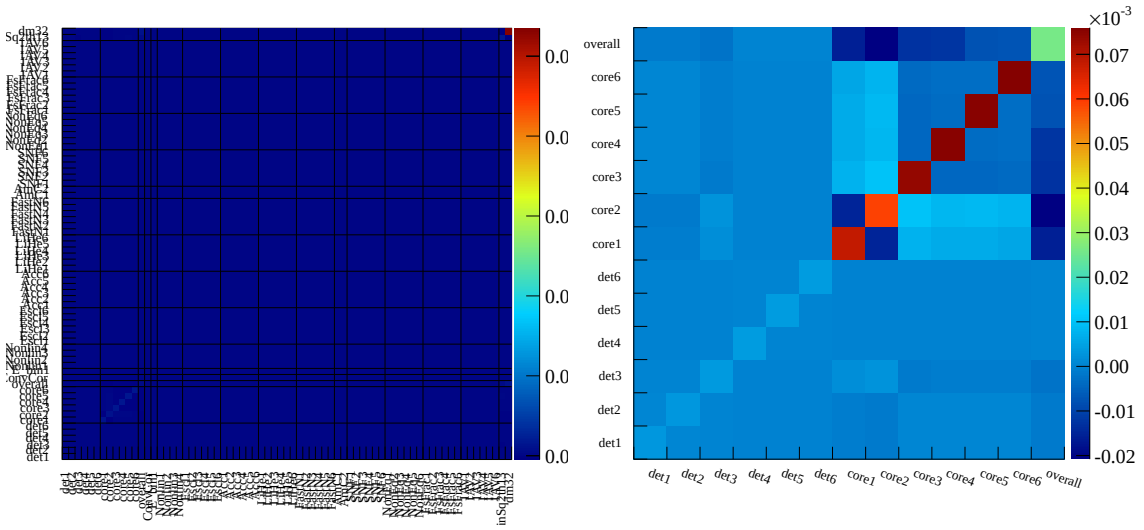


Figure 9.41 Covariance matrix from a rate-only analysis. The right matrix is the zoomed-in portion of the left plot showing systematics, but omitting the oscillation parameters which are in the upper right of the left plot. Variable names are listed on the axes.

Contributions to χ^2_{min}, rate-only analysis:		
From statistical part	0.378 / 6 = 0.0631	86.9%
From detector normalization	0.044 / 6 = 0.0073	10.1%
From reactor normalization	0.013 / 6 = 0.0022	3.0%
From Δm^2_{32} pull term	$6.002{\cdot}10^{-6}$ / 1 = $6.002{\cdot}10^{-6}$	0.0014%
Total χ^2_{min}	0.435143 / (6–2) = 0.108786	

Table 9.9 The contribution of each systematic to χ^2_{min} for the rate-only analysis. Except for the statistical part, the quantities above are the size of each set of pull terms $(\eta_\iota/\sigma_\iota)^2$, in total and where applicable averaged per detector, reactor or bin. The statistical part is the lead term in the χ^2: $\chi^2 - \sum(\eta_\iota/\sigma_\iota)^2$. The percentages are based on the total pull terms per systematic.

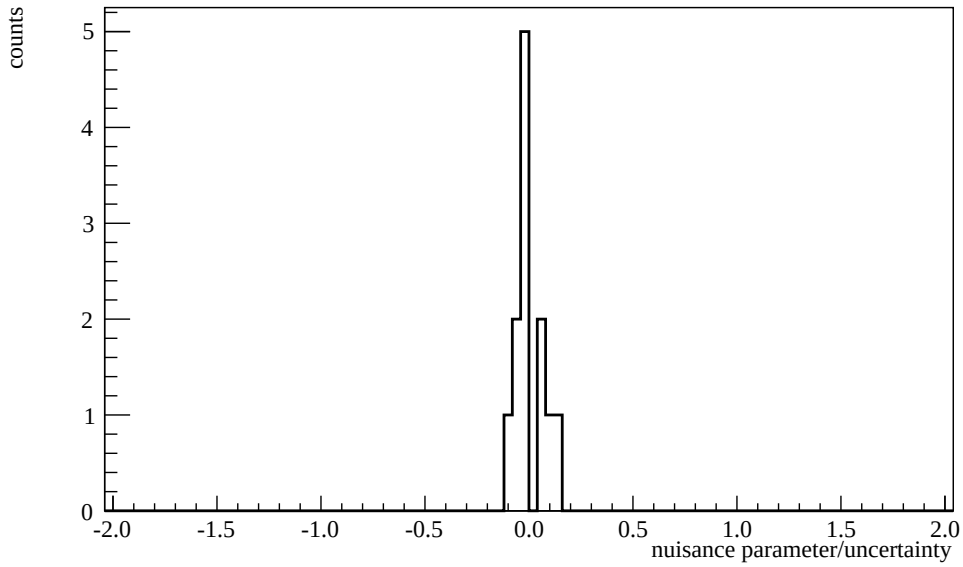


Figure 9.42 Histogram of systematic nuisance parameters divided by uncertainties $(\eta_\iota/\sigma_\iota)$ at best fit from a rate-only analysis.

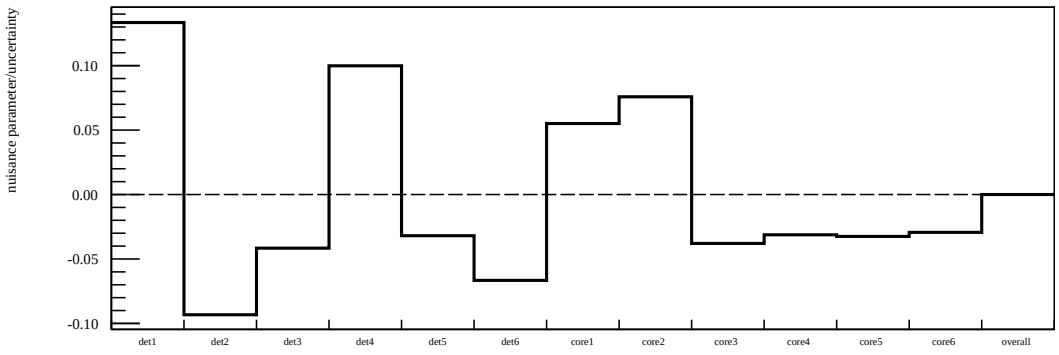


Figure 9.43 Nuisance parameters divided by uncertainties (η_ι/σ_ι) at best fit from a rate-only analysis. Variable names are listed on the axes.

9.4 Measurement with Spectral Distortions Only

A shape-only analysis is of interest to determine what can be understood from oscillation-induced spectral distortions alone. Such an analysis corroborates the rate-based analysis and strengthens Daya Bay's observation of neutrino oscillations. Spectral distortion is a weaker channel because the shape information is more subtle and subject to harder to understand systematics.

The spectral distortion analysis is performed by removing the rate information from the fit, which is accomplished by setting the detector normalization nuisance parameters unconstrained ($\sigma_{det} \rightarrow \infty$). This way, any oscillation parameters set during the fitting process satisfy the detector rates. The overall normalization is hence removed because it becomes redundant and degenerate when the uncorrelated detector normalizations can vary freely in the fit. The reactor rate uncertainties are left untouched because reactor fluxes may differ in antineutrino spectra, due, for instance, to different reactor fuel burn up stages. All other uncertainties are treated as they were in the rate and shape analysis, and their rate effects are simply washed out by the free detector normalizations.

9.4.1 Best Fits

With Δm^2_{32} unconstrained, normal hierarchy, no energy scale fit parameters and 24 energy bins, the shape-only analysis yields the following oscillation parameter measurements:

- $\sin^2 2\theta_{13} \ = 0.114513^{+0.031989}_{-0.033189}$
- $\Delta m^2_{32} = 2.48879^{+0.162}_{-0.138} \cdot 10^{-3}\,\mathrm{eV}^2$
- $\Delta m^2_{31} = 2.56379 \cdot 10^{-3}\,\mathrm{eV}^2$
- $\chi^2_{min} = 112.903$. $\mathrm{N_{DOF}} = 6$*24–8. $\chi^2_{min}/\mathrm{N_{DOF}} = 0.83017$

Note that the overall normalization cannot be measured because all detector normalizations are unconstrained; all values of $\mathcal{H}$ are fit equally well. The fit value for $\sin^2 2\theta_{13}$ of

$0.114513^{+0.031989}_{-0.033189}$ is higher than the rate and shape fit of $0.0880922^{+0.008816}_{-0.008843}$, or the rate-only measurement of $0.0859752^{+0.009127}_{-0.009190}$. However, the error bars are more than three times larger, so all measurements agree at the 1σ level.

The shape-only measurement of Δm^2_{32} is consistent with the rate and shape measurement: $2.48879^{+0.162}_{-0.138}{\cdot}10^{-3}\,\mathrm{eV}^2$ versus $2.54407^{+0.166}_{-0.176}{\cdot}10^{-3}\,\mathrm{eV}^2$. However, the error bar is much smaller, especially the negative bound. The reason behind this is that the vast freedom of the unconstrained detector normalization nuisance parameters distorts the χ^2. The detector fit parameters settle on values much larger than their values in the rate and shape case, by a factor of five to ten. This allows the minimizer to find a minimum that would be unrealistic in the rate and shape analysis, and this new minimum is narrower in Δm^2_{32}.

Figures 9.44, 9.45 and 9.46 provide the χ^2 dependence on $\sin^2 2\theta_{13}$ and Δm^2_{32}. As can be seen in each figure, the precision of the measurement is much worse without the rate information. A 3σ measurement of $\sin^2 2\theta_{13}$ exclusive of $\sin^2 2\theta_{13}{=}0$ is no longer possible without the rate information. In addition, the contours depart from the more regular ellipses of the rate and shape measurement, while the $\Delta\chi^2(\Delta m^2_{32})$ is no longer well approximated by a parabolic form.

9.4.2 Best Fit Diagnostics

The correlations of parameters, seen in Figures 9.47 and 9.48, follow the correlations of the rate and shape fit except for the detector normalization parameters. Since they are free, the detector parameters vary together and farther away from their starting values during the course of the minimization than they do in the rate and shape fit, since they serve the purpose of washing out rate information rather than model the detectors. The covariance matrix, Figure 9.49, also changes little from the rate and shape fit.

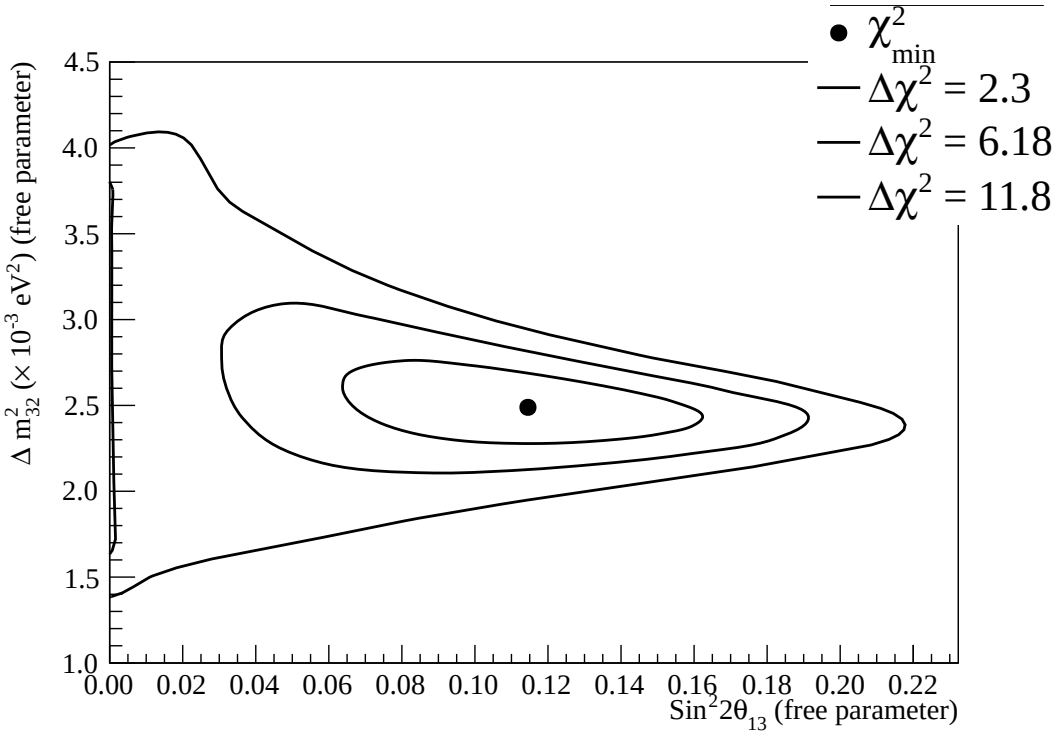


Figure 9.44 The best fit $\sin^2 2\theta_{13}$-Δm^2_{32} point surrounded by 1–3σ contours from a shape-only analysis.

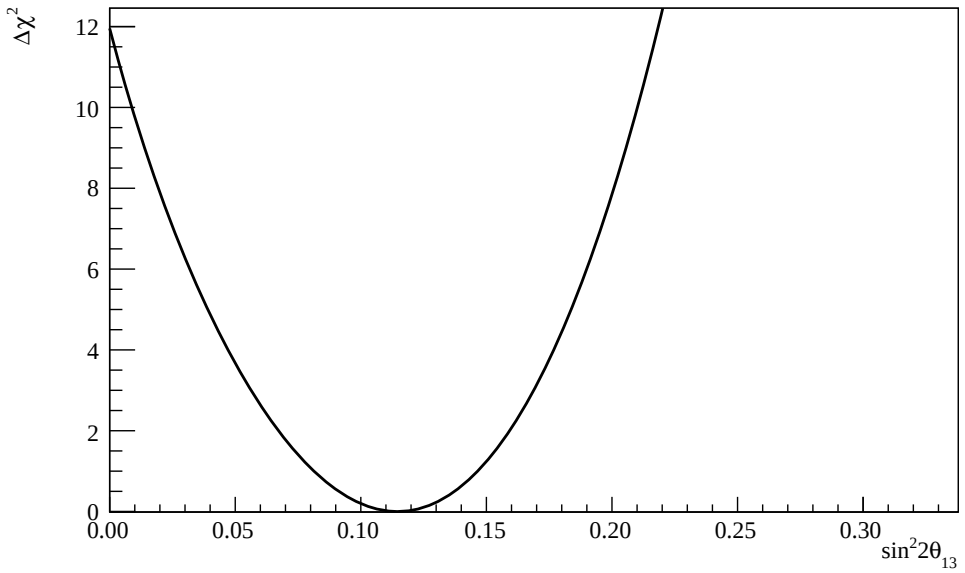


Figure 9.45 The best fit $\Delta\chi^2(\sin^2 2\theta_{13})$ from a shape-only analysis.

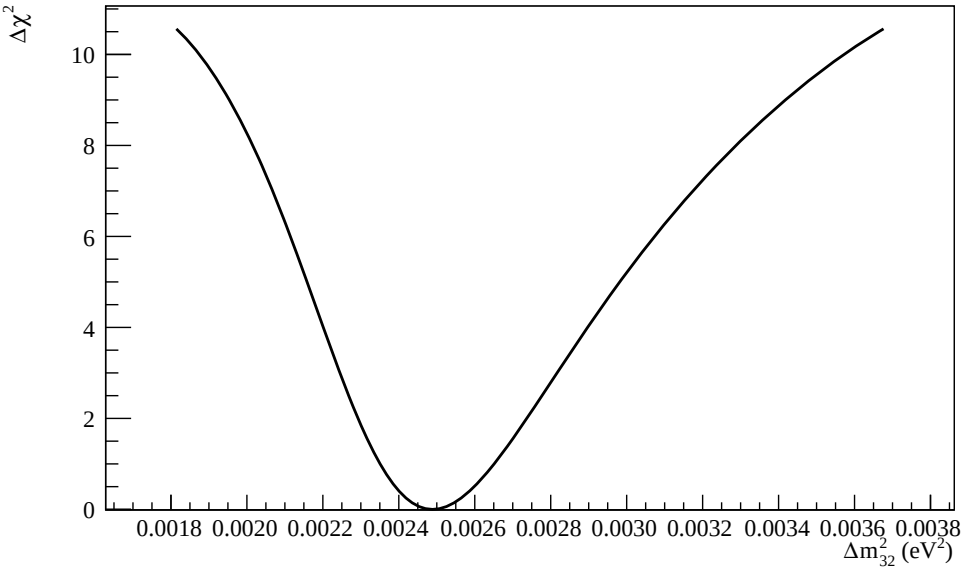


Figure 9.46 The best fit $\chi^2(\Delta m^2_{32})$ from a shape-only analysis.

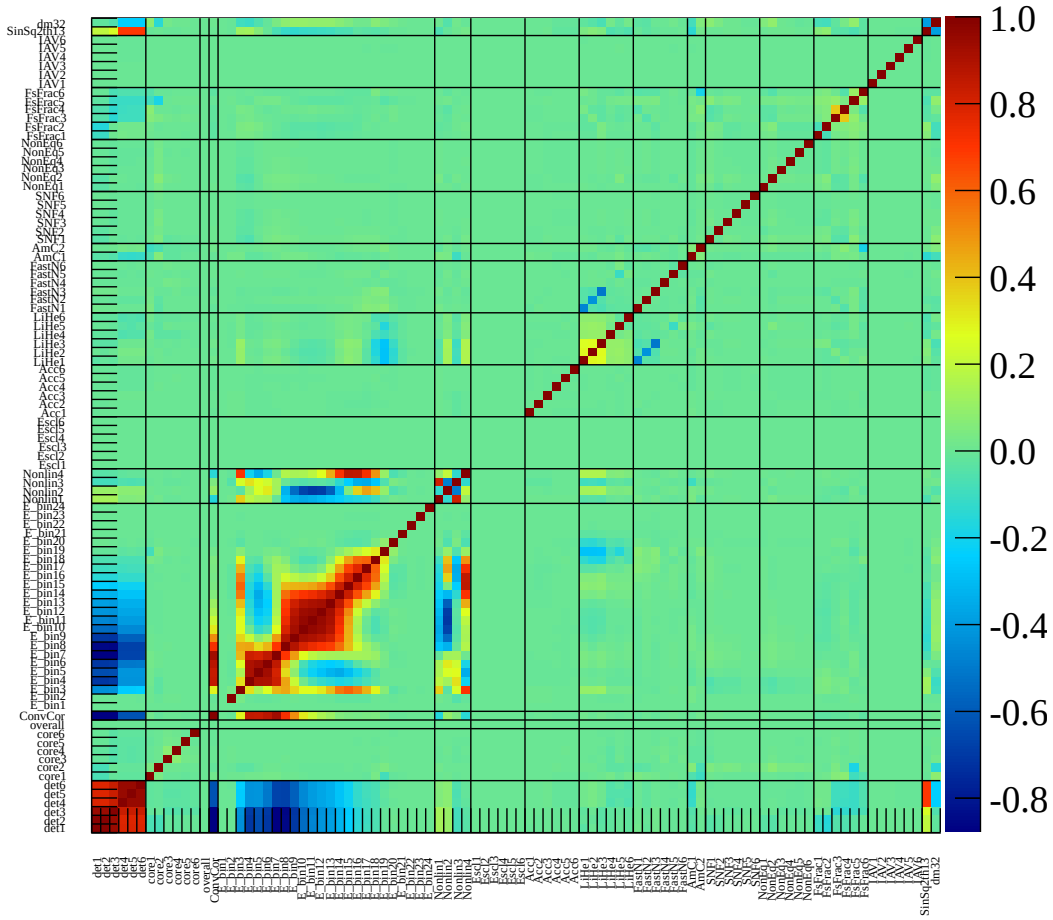


Figure 9.47 Correlation matrix from a shape-only analysis. Variable names are listed on the axes.

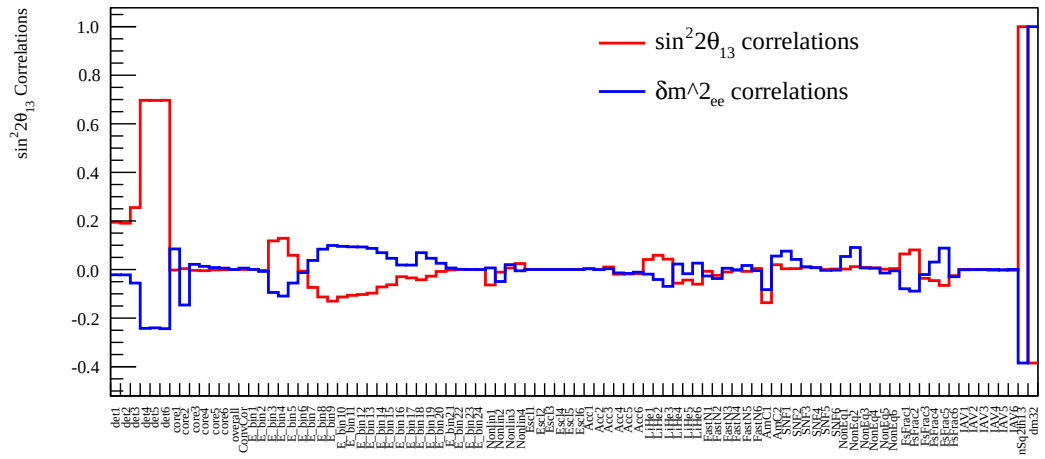


Figure 9.48 Correlations among oscillation parameters and systematics from a shape-only analysis. Variable names are listed on the axes.

The behavior of the constrained fit parameters follows the same pattern as in the rate and shape fit. The statistical part of the χ^2 contributes most to the overall χ^2_{min} value, followed by the background and bin normalizations. See Table 9.10. The best fit values of individual nuisance parameters divided by their uncertainties are provided by Figures 9.50 and 9.51, and demonstrate no untoward tension (no nuisance parameter values are greater than their associated uncertainties.) A look at the detector response nonlinearity in particular indicates a reasonable fit. The detector response curve as fit is close to the nominal detector response function, and enveloped by the uncertainty bands.

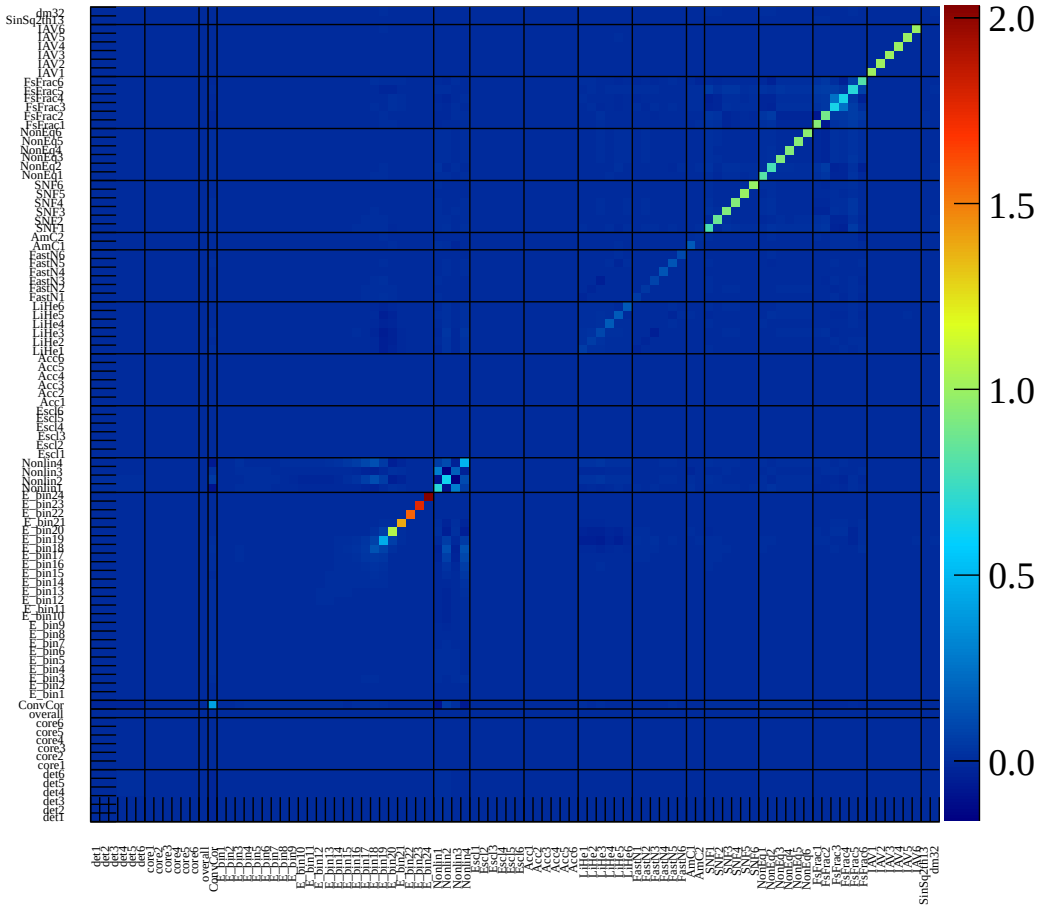


Figure 9.49 Covariance matrix from a shape-only analysis. Variable names are listed on the axes.

Contributions to χ^2_{min}, shape-only analysis:		
From statistical part	106.101 / 144 = 0.736814	94.0%
From reactor normalization	0.000 / 6 = 4.31648e-06	$2.3{\cdot}10^{-5}$%
From bin normalization	2.092 / 24 = 0.0871575	1.9%
From nonlinearity	0.587 / 4 = 0.146816	0.5%
From background normalization	3.876 / 19 = 0.203984	3.4%
From $\beta \to \bar{\nu}$ energy-correlated	0.001 / 1 = 0.000577926	$5.1{\cdot}10^{-4}$%
From IAV det-uncorr./energy-corr.	0.001 / 6 = 0.00023684	$1.3{\cdot}10^{-3}$%
From spent fuel normalization	0.058 / 6 = 0.00970062	0.05%
From nonequilibrium normalization	0.051 / 6 = 0.00850063	0.05%
From fission fraction	0.136 / 6 = 0.0226499	0.12%
Total χ^2_{min}	112.903 / (6*24–8) = 0.83017	

Table 9.10 The contribution of each systematic to χ^2_{min} from a shape-only analysis. Except for the statistical part, the quantities above are the size of each set of pull terms $(\eta_\iota/\sigma_\iota)^2$, in total and where applicable averaged per detector, reactor or bin. The statistical part is the lead term in the χ^2: $\chi^2 - \sum(\eta_\iota/\sigma_\iota)^2$. Since the detector normalizations are unconstrained but the overall normalization is disabled, the number of degrees of freedom is lower than the rate and shape analysis by five.

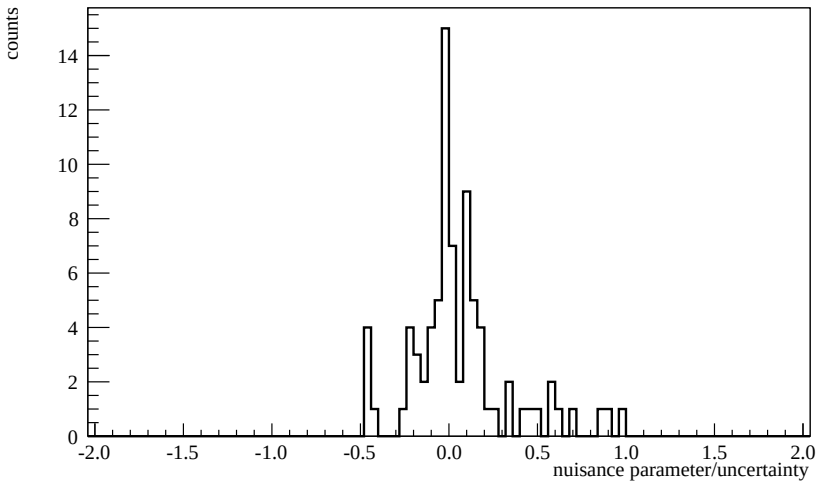


Figure 9.50 Histogram of systematic nuisance parameters divided by uncertainties $(\eta_\iota/\sigma_\iota)$ at best fit, from a shape-only analysis.

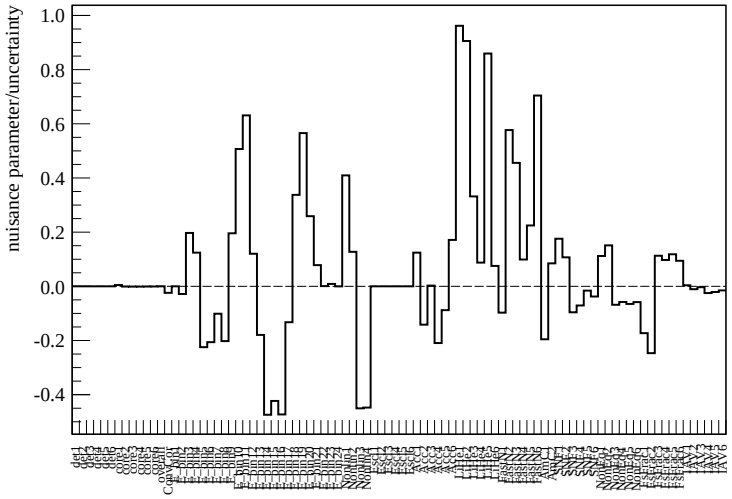


Figure 9.51 Systematic nuisance parameters divided by uncertainties (η_ι/σ_ι) at best fit from a shape-only analysis. Variable names are listed on the axes.

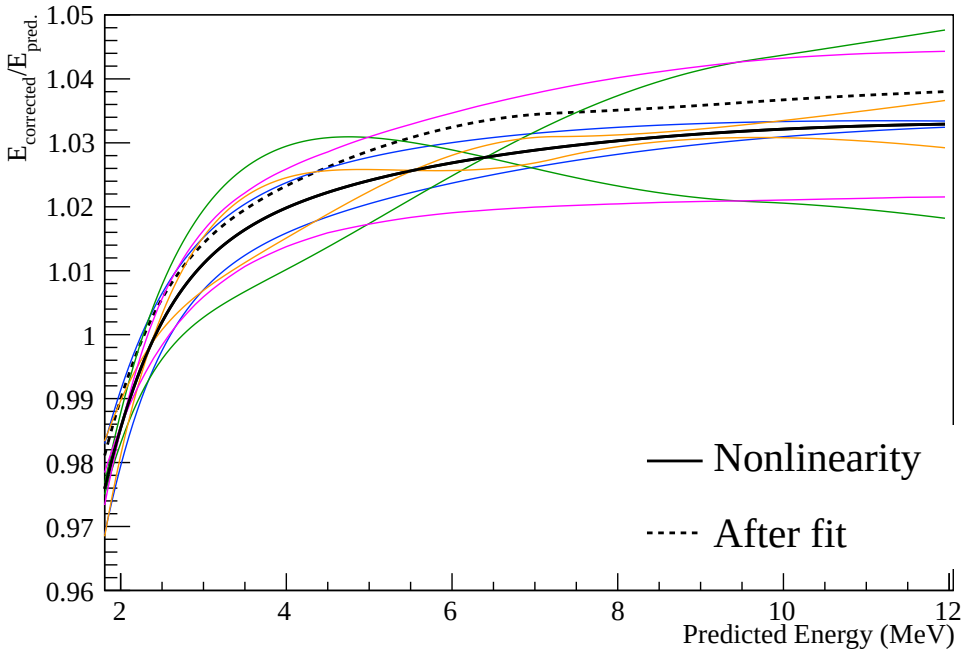


Figure 9.52 The detector response model is indicated by the solid black line, with 1σ uncertainties on each of the four nonlinearity parameters indicated by the colored lines. The dashed line shows the shape-only best fit detector response after fit parameters are applied.

9.4.3 Energy Scale Treatment

Table 9.11 compares the best fits performed when the energy scale parameters are disabled or enabled. Between these cases, the $\sin^2 2\theta_{13}$ measurement varies about 10% while the Δm^2_{32} measurement varies only 3%. The most significant difference is the precision of the Δm^2_{32} measurement. Recall the relationship between the Δm^2_{32} and energy scale fit parameters discussed in Section 9.1.3. These fit parameters interfere with each other, so the additional freedom in the contributes to the Δm^2_{32} uncertainty.

Figure 9.53 compares the $\sin^2 2\theta_{13}$-Δm^2_{32} contours. The addition of the energy scale widens the contours and renders the 3σ contour too difficult to calculate for the minimizer. The bounds on Δm^2_{32} between the two cases vary by about 50%.

Flux Model	$\sin^2 2\theta_{13}$ fit	Δm^2_{32} fit	χ^2_{min}
No Energy Scale	$0.114513^{+0.031989}_{-0.033189}$	$2.48879^{+0.162}_{-0.138}\cdot 10^{-3}\,\mathrm{eV}^2$	112.903
With Energy Scale	$0.101935^{+0.036145}_{-0.034451}$	$2.57364^{+0.265}_{-0.197}\cdot 10^{-3}\,\mathrm{eV}^2$	110.618

Table 9.11 Shape-only analysis results with either the energy scale fit parameters disabled (baseline choice) or enabled.

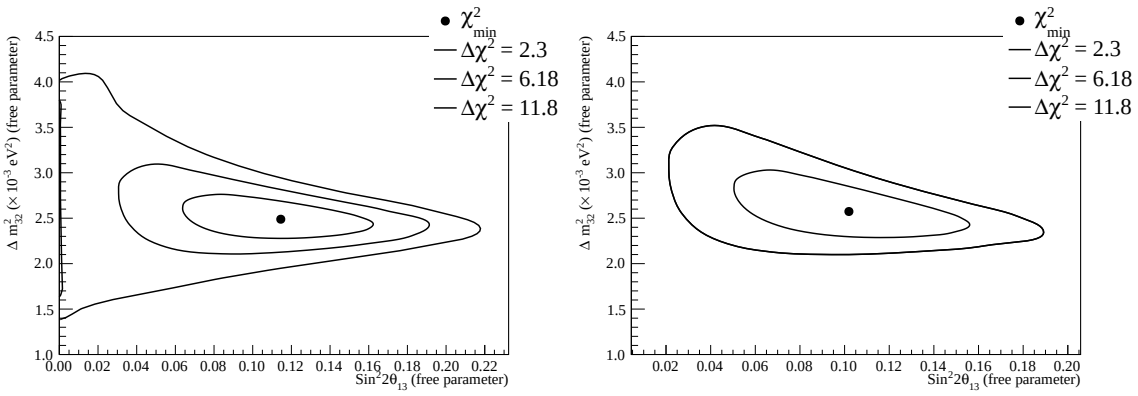


Figure 9.53 Best fit contours $\Delta\chi^2(\sin^2 2\theta_{13}, \Delta m^2_{32})$ for the shape-only fit with the exclusion of the energy scale parameter (left) and its inclusion (right).

9.5 Summary of Oscillation Measurements

A graphical summary of the $\sin^2 2\theta_{13}$ and Δm^2_{32} measurements performed under various scenarios presented throughout Chapter 9 are shown in Figures 9.54 and 9.55. The $\sin^2 2\theta_{13}$ measurements are generally consistent with each other, despite the fact that no prior information is available to constrain $\sin^2 2\theta_{13}$ in advance. The Δm^2_{32} measurements vary more but are all mutually consistent at the 1σ confidence level. The Δm^2_{32} measurement is more sensitive to imposed conditions, and is overall a more difficult measurement.

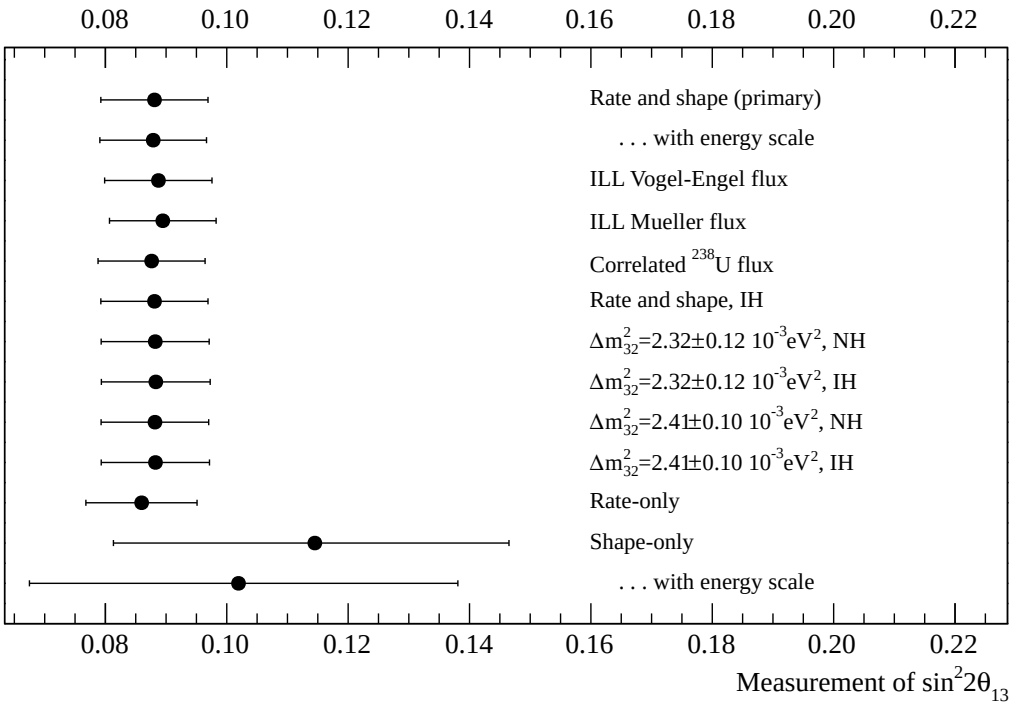


Figure 9.54 Summary of all the measurements of $\sin^2 2\theta_{13}$ presented in Chapter 9 under various conditions. Best fits and 1σ error bands are shown. The primary reported result is at the top; rate-only and shape-only represent analyses with limited information; the rest reflect analyses with alternate choices.

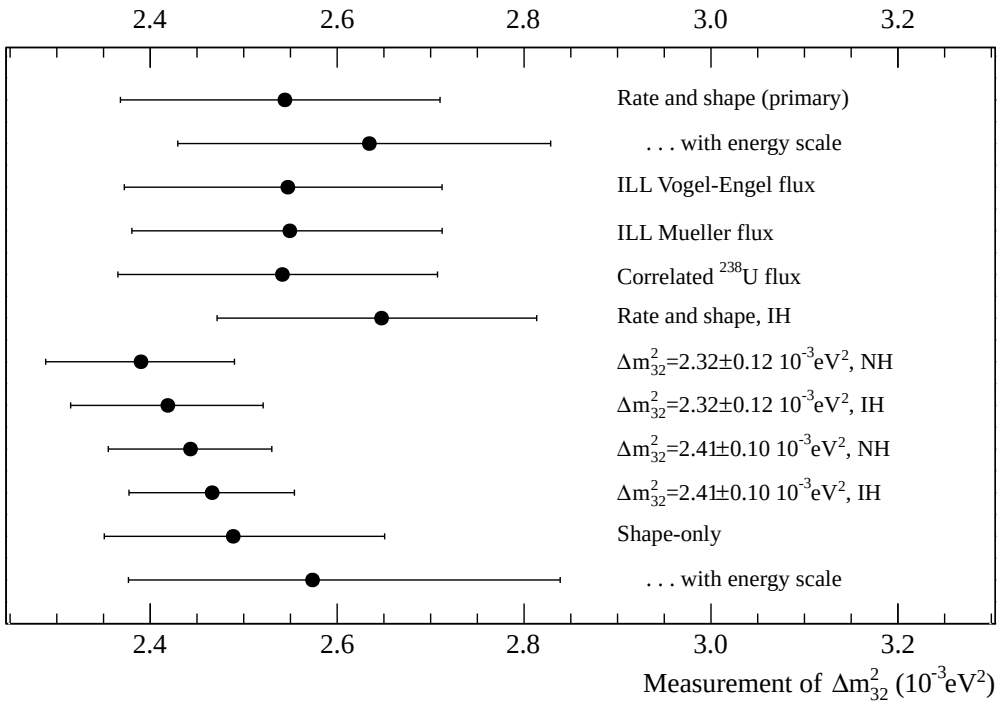


Figure 9.55 Summary of all the measurements of Δm^2_{32} presented in Chapter 9 under various conditions. Best fits and 1σ error bands are shown. The primary reported result is at the top; rate-only and shape-only represent analyses with limited information; the rest reflect analyses with alternate choices.

Chapter 10

Conclusion

While the phenomenon of oscillations among three neutrinos had been confirmed by previous experiments, the final mixing angle governing the process, θ_{13}, had yet to be measured before Daya Bay. The Daya Bay Reactor Neutrino Experiment consists of eight functionally identical detectors measuring the antineutrino rates and spectra from six nuclear reactors. Half of Daya Bay's detectors are deployed near the reactors, at flux-weighted distances of 500 m and 550 m, while the other half are deployed at a far site 1.6 km away. By taking advantage of the energy and distance dependence of neutrino oscillations, the far site is situated at a point that is maximally sensitive to θ_{13}, but minimally sensitive to the other oscillation parameters. Meanwhile, the near sites are only slightly sensitive to oscillations, providing two points for comparison.

Daya Bay's detectors observe electron antineutrinos via the inverse beta decay reaction ($\overline{\nu}_e + p \rightarrow n + e^+$), in which the electron antineutrino reacts with a proton to generate a positron and neutron. Both daughters are then detected to confirm an antineutrino event. The positron immediately annihilates with an electron, depositing energy in the detector indicative of the incoming antineutrino energy. A second deposition of energy from the capture of the neutron on a nucleus distinguishes the event from a background process.

The detectors take advantage of this unique antineutrino signal with a three-volume construction. The center of the detector consists of gadolinium-doped liquid scintillator that provides target protons while converting emitted gamma rays to detectable ultraviolet light, with the addition of gadolinium to enhance the neutron capture. A surrounding volume

contributes more scintillator (without gadolinium) to ensure sufficient gamma ray conversion, and around that a mineral oil buffer attenuates backgrounds from the photomultiplier tubes and support structures. Eight detectors were constructed such that after calibration, they measure the antineutrino rates identically within 0.20%, and energies within 0.35%.

The Daya Bay experiment originally sought to measure θ_{13} with a sensitivity of $\sin^2 2\theta_{13} = 0.01$ after three years of data taking. In reality, Daya Bay surpassed this goal by measuring $\sin^2 2\theta_{13}$ to a better precision, in a shorter running time, with fewer detectors. After 217 days of data taking with just three detectors deployed to the far site and three total at the near sites, the analysis presented in this work measures $\sin^2 2\theta_{13} = 0.088 \pm 0.0088$ and $\Delta m^2_{32} = 2.54^{+0.17}_{-0.18} \cdot 10^{-3}\,\mathrm{eV}^2$. This was accomplished with the joint analysis of neutrino rate and spectrum data.

This analysis combines detector data, reactor antineutrino flux predictions and systematic uncertainties to extract the values of the oscillation parameters and the precision at which they are measured. The deficit of antineutrinos at the far site relative to the near sites is a direct indication of the magnitude of neutrino oscillations, while the spectral shape information confirms the oscillation hypothesis and resolves the phase of oscillations. Although the root of the analysis lies in the relative comparison of detectors, the inclusion of reactor flux predictions is important to enable better modeling of uncertainties, and quantifies the overall compatibility of the data with the three neutrino oscillation hypothesis.

LIST OF REFERENCES

[1] **Particle Data Group** Collaboration, J. Beringer *et. al.*, *Review of Particle Physics (RPP)*, *Phys. Rev.* **D86** (2012) 010001.

[2] E. Giusarma, R. de Putter, S. Ho, and O. Mena, *Constraints on Neutrino Masses from Planck and Galaxy Clustering Data*, *Phys. Rev. D* **88** (Sep, 2013) 063515.

[3] **Daya Bay** Collaboration, F. P. An *et. al.*, *Spectral Measurement of Electron Antineutrino Oscillation Amplitude and Frequency at Daya Bay*, *Phys. Rev. Lett.* **112** (Feb, 2014) 061801.

[4] **MINOS** Collaboration, P. Adamson *et. al.*, *Measurement of Neutrino and Antineutrino Oscillations Using Beam and Atmospheric Data in MINOS*, *Phys.Rev.Lett.* **110** (2013), no. 25 251801, [arXiv:1304.6335].

[5] R. Leitner, *The Experimental Status of θ_{13} from the Point of View of the Electron (Anti)Neutrino Disappearance Experiments*, arXiv:1302.2409.

[6] J. Cao, *Update on Baselines and Spent Fuel Pool Locations*, *Internal Note #8432* (2012).

[7] F. An, L. Zhan, and W. Zhong, *Reactor Related Uncertainties in Shape Analysis*, *Internal Note #8788* (2013).

[8] **Daya Bay** Collaboration, X. Guo *et. al.*, *A Precision Measurement of the Neutrino Mixing Angle θ_{13} Using Reactor Antineutrinos at Daya Bay*, hep-ex/0701029.

[9] V. Kopeikin, L. Mikaelyan, and V. Sinev, *Reactor as a Source of Antineutrinos: Thermal Fission Energy*, *Phys. Atom. Nucl.* **67** (2004) 1892–1899, [hep-ph/0410100].

[10] HPGe Radioassay Facility, California Institute of Technology. Private correspondence.

[11] W. Gu, M. He, B.-Z. Hu, G. Li, J. Liu, Y. Liu, and H.-K. Tanaka, *EH1/EH2 Good Files*, *Internal Note #7464* (2012).

[12] C. Lewis, *Summary of Inputs for Daya Bay Event Rate and Sensitivity Calculations*, *Internal Note #2546* (2009).

[13] M. McFarlane, *Discovery Limits for 6 ADs, and the Transition to 8 ADs*, *Internal Note #7262* (2011).

[14] European Organization for Nuclear Research (CERN). http://home.web.cern.ch/.

[15] V. D. Barger and R. J. N. Phillips, *Collider Physics (Frontiers in Physics)*. Addison Wesley Publishing Company.

[16] http://neutrinoscience.blogspot.com/2011/06/.

[17] http://cerncourier.com/cws/article/cern/49351.

[18] O. Mena and S. Parke, *Unified Graphical Summary of Neutrino Mixing Parameters*, *Physical Review D* **69** (2004) 117301.

[19] C. Cowan, F. Reines, F. Harrison, H. Kruse, and A. McGuire, *Detection of the Free Neutrino: A Confirmation*, *Science* **124** (1956) 103–104.

[20] F. Reines and C. L. Cowan, *The Neutrino*, *Nature* **178** (1956) 446–449.

[21] G. Danby, J. Gaillard, K. A. Goulianos, L. Lederman, N. B. Mistry, *et. al.*, *Observation of High-Energy Neutrino Reactions and the Existence of Two Kinds of Neutrinos*, *Phys. Rev. Lett.* **9** (1962) 36–44.

[22] B. T. Cleveland, T. Daily, J. Raymond Davis, J. R. Distel, K. Lande, C. K. Lee, P. S. Wildenhain, and J. Ullman, *Measurement of the Solar Electron Neutrino Flux with the Homestake Chlorine Detector*, *The Astrophysical Journal* **496** (1998), no. 1 505.

[23] **KAMIOKANDE-II** Collaboration, K. Hirata *et. al.*, *Observation of a Neutrino Burst from the Supernova SN 1987a*, *Phys. Rev. Lett.* **58** (1987) 1490–1493.

[24] E. Alekseev, L. Alekseeva, I. Krivosheina, and V. Volchenko, *Detection of the Neutrino Signal from SN1987A in the LMC Using the INR Baksan Underground Scintillation Telescope*, *Phys. Lett.* **B205** (1988) 209–214.

[25] **DONUT** Collaboration, K. Kodama *et. al.*, *Observation of Tau Neutrino Interactions*, *Phys. Lett.* **B504** (2001) 218–224, [hep-ex/0012035].

[26] **Super-Kamiokande** Collaboration, Y. Fukuda *et. al.*, *The Super-Kamiokande Detector*, *Nucl. Instrum. Meth.* **A501** (2003) 418–462.

[27] Fukuda, Y. et al., *Evidence for Oscillation of Atmospheric Neutrinos*, *Phys. Rev. Lett.* **81** (Aug, 1998) 1562–1567.

[28] **Super-Kamiokande** Collaboration, R. Wendell *et. al.*, *Atmospheric Neutrino Oscillation Analysis with Sub-leading Effects in Super-Kamiokande I, II, and III*, *Phys. Rev.* **D81** (2010) 092004, [arXiv:1002.3471].

[29] **SNO** Collaboration, J. Boger *et. al.*, *The Sudbury Neutrino Observatory*, *Nucl. Instrum. Meth.* **A449** (2000) 172–207, [nucl-ex/9910016].

[30] **SNO** Collaboration, B. Aharmim *et. al.*, *Combined Analysis of all Three Phases of Solar Neutrino Data from the Sudbury Neutrino Observatory*, *Phys. Rev.* **C88** (2013) 025501, [arXiv:1109.0763].

[31] Eguchi, K. et al., *First Results from KamLAND: Evidence for Reactor Antineutrino Disappearance*, *Phys. Rev. Lett.* **90** (Jan, 2003) 021802.

[32] **KamLAND** Collaboration, S. Abe *et. al.*, *Precision Measurement of Neutrino Oscillation Parameters with KamLAND*, *Phys. Rev. Lett.* **100** (2008) 221803, [arXiv:0801.4589].

[33] **K2K** Collaboration, A. Rodriguez *et. al.*, *Measurement of Single Charged Pion Production in the Charged-Current Interactions of Neutrinos in a 1.3-GeV wide band beam*, *Phys. Rev.* **D78** (2008) 032003, [arXiv:0805.0186].

[34] **K2K** Collaboration, M. Ahn *et. al.*, *Measurement of Neutrino Oscillation by the K2K Experiment*, *Phys. Rev.* **D74** (2006) 072003, [hep-ex/0606032].

[35] R. M. Zwaska, *Accelerator Systems and Instrumentation for the NuMI Neutrino Beam*, *UMI-32-16264, FERMILAB-THESIS-2005-73* (2005).

[36] **LSND** Collaboration, A. Aguilar-Arevalo *et. al.*, *Evidence for Neutrino Oscillations from the Observation of Electron Antineutrino Appearance in a Muon Antineutrino Beam*, *Phys. Rev.* **D64** (2001) 112007, [hep-ex/0104049].

[37] Booster Neutrino Experiment. http://www-boone.fnal.gov/about_boone/.

[38] Y. Declais *et. al.*, *Search for Neutrino Oscillations at 15 Meters, 40 Meters, and 95 Meters from a Nuclear Power Reactor at Bugey*, *Nucl. Phys.* **B434** (1995) 503–534.

[39] **CALTECH-SIN-TUM** Collaboration, G. Zacek *et. al.*, *Neutrino Oscillation Experiments at the Gösgen Nuclear Power Reactor*, *Phys. Rev.* **D34** (1986) 2621–2636.

[40] G. Vidyakin, V. Vyrodov, Y. Kozlov, A. Martemyanov, V. Martemyanov, *et. al.*, *Limitations on the Characteristics of Neutrino Oscillations*, *JETP Lett.* **59** (1994) 390–393.

[41] F. Boehm, J. Busenitz, B. Cook, G. Gratta, H. Henrikson, *et. al.*, *Final Results from the Palo Verde Neutrino Oscillation Experiment*, *Phys. Rev.* **D64** (2001) 112001, [hep-ex/0107009].

[42] **RENO** Collaboration, J. Ahn *et. al.*, *Observation of Reactor Electron Antineutrino Disappearance in the RENO Experiment*, *Phys. Rev. Lett.* **108** (2012) 191802, [arXiv:1204.0626].

[43] **Double Chooz** Collaboration, F. Ardellier *et. al.*, *Double Chooz: A Search for the neutrino mixing angle Theta-13*, hep-ex/0606025.

[44] S. Jetter, *Spectral Measurement of Electron Antineutrino Oscillation Amplitude and Frequency at Daya Bay*, *Internal Note #9204* (2013).

[45] © Nokia and Microsoft Corporation.

[46] © AutoNavi, Google.

[47] **CHOOZ** Collaboration, M. Apollonio *et. al.*, *Search for Neutrino Oscillations on a Long Baseline at the CHOOZ Nuclear Power Station*, *Eur. Phys. J.* **C27** (2003) 331–374, [hep-ex/0301017].

[48] B. Seilhan, *Early Physics of the Daya Bay Reactor Antineutrino Experiment*. Illinois Institute of Technology.

[49] http://www.nrc.gov/reactors/pwrs.html.

[50] F. An, *Reactor Neutrino Flux Prediction and Uncertainties*, *Internal Note #7580* (2012).

[51] C. Lewis, *Reactor Uncertainties for Shape Analysis*, *Internal Note #8609* (2013).

[52] C. Lewis, *Measuring the Antineutrino Spectrum at the Daya Bay Nuclear Reactors*. University of Wisconsin, Madison.

[53] Amy Pagac and Al Riley. Private correspondence.

[54] H. Band, R. Brown, J. Cherwinka, J. Cao, Y. Chang, *et. al.*, *Acrylic Target Vessels for a High-Precision Measurement of θ_{13} with the Daya Bay Antineutrino Detectors*, *JINST* **7** (2012) P06004, [arXiv:1202.2000].

[55] H. Band, J. Cherwinka, L. Greenler, K. Heeger, P. Hinrichs, *et. al.*, *Target Mass Monitoring and Instrumentation in the Daya Bay Antineutrino Detectors*, *JINST* **8** (2013) T04001, [arXiv:1206.7082].

[56] J. Liu, B. Cai, R. Carr, D. Dwyer, W. Gu, *et. al.*, *Automated Calibration System for a High-Precision Measurement of Neutrino Mixing Angle θ_{13} with the Daya Bay Antineutrino Detectors*, arXiv:1305.2248.

[57] H. Huang, X. Ruan, J. Ren, C. Fan, Y. Chen, *et. al.*, *Manual Calibration System for Daya Bay Reactor Neutrino Experiment*, arXiv:1305.2343.

[58] K. M. Heeger and A. Pagac, *Daya Bay Near Hall Figures*, *Internal Note #7613* (2012).

[59] R. W. Hackenburg, K. Lau, L. Lebanowski, L. Littenberg, C. Lu, H. Lu, K. Luk, K. McDonald, L. Whitehead, and J. Wilhelmi, *The Muon Veto System of the Daya Bay Reactor Antineutrino Experiment*, *In preparation* (2013).

[60] © University of California - Lawrence Berkeley National Laboratory.

[61] IDS Imaging Development Systems GmbH. Dimbacher Strasse 6-8 D-74182 Obersulm, Germany, http://www.ids-imaging.com/index.php.

[62] Aptina Imaging. http://www.aptina.com.

[63] Vishay Intertechnology Inc. One Greenwich Place Shelton, CT, USA 06484 United States, http://www.vishay.com.

[64] Hamamatsu Photonics, Electron Tube Division. 314-5 Shimokanzo Iwata City, Shizuoka Pref., Japan, http://www.hamamatsu.com/.

[65] D. Dwyer, T. Hu, and Z. Wang, *Mini Dry Run: Preliminary Report*, *Internal Note #4536* (2010).

[66] C.-J. Lin, Y. Nakajima, J. P. Ochoa, and K. Tsang, *The AdSimple Reconstruction (Technical Note)*, *Internal Note #7334* (2013).

[67] **Daya Bay** Collaboration, F. An *et. al.*, *A Side-by-Side Comparison of Daya Bay Antineutrino Detectors*, *Nucl. Instrum. Meth.* **A685** (2012) 78–97, [arXiv:1202.6181].

[68] **Daya Bay** Collaboration, F. An *et. al.*, *Improved Measurement of Electron Antineutrino Disappearance at Daya Bay*, *Chin. Phys.* **C37** (2013) 011001, [arXiv:1210.6327].

[69] J. Cao, Z. Wang, L. Wen, Z. Yu, and L. Zhan, *Flasher Identification*, *Internal Note #6875* (2011).

[70] J. P. Ochoa, *Predicting the 9Li/8He Background Spectra*, *Internal Note #8860* (2013).

[71] G. Mention, T. Lasserre, and D. Motta, *A Unified Analysis of the Reactor Neutrino Program Towards the Measurement of the Theta13 Mixing Angle*, .

[72] T. Schwetz, M. Tortola, and J. W. F. Valle, *Three-Flavour Neutrino Oscillation Update*, *New J. Phys* **113011** (2008).

[73] M. McFarlane, *Sensitivity Information for Intermediate Configurations of Daya Bay*, *Internal Note #6014* (2011).

[74] **RENO** Collaboration, J. Ahn *et. al.*, *RENO: An Experiment for Neutrino Oscillation Parameter θ_{13} Using Reactor Neutrinos at Yonggwang*, arXiv:1003.1391.

[75] B. Littlejohn, *IAV Shape Distortion Correction for a Shape Analysis*, *Internal Note #8104* (2012).

[76] J. P. Ochoa, *Predicting the ^{9}Li Background Shape*, *Internal Note #8772* (2013).

[77] G. Cao, X. Chen, W. Gu, X. Ji, G. Li, J. Liu, and Z. Wang, *Summary of Strong AmC Analyses*, *Internal Note #8617*.

[78] Z. Yu and J. Zhao, *Alpha-n Background Spectrum Update*, *Internal Note #8716* (2013).

[79] M. McFarlane and D. Webber, *Toy Monte Carlo Fitter Comparison*, *Internal Note #9064* (2013).

[80] H. Georgi and S. L. Glashow, *Unity of All Elementary Particle Forces*, *Phys. Rev. Lett.* **32** (1974) 438–441.

[81] O. Eberhardt, G. Herbert, H. Lacker, A. Lenz, A. Menzel, U. Nierste, and M. Wiebusch, *Impact of a Higgs Boson at a Mass of 126 GeV on the Standard Model with Three and Four Fermion Generations*, *Phys. Rev. Lett.* **109** (Dec, 2012) 241802.

[82] G. Aad et. al., *Observation of a New Particle in the Search for the Standard Model Higgs Boson with the ATLAS Detector at the LHC*, *Physics Letters B* **716** (2012), no. 1 1–29.

[83] S. Chatrchyan et. al., *Observation of a new boson at a mass of 125 GeV with the CMS experiment at the LHC*, *Physics Letters B* **716** (2012), no. 1 30 – 61.

[84] D. Griffiths, *Introduction to Elementary Particles*. John Wiley & Sons, New York, USA.

[85] R. Feynman, *Space - Time Approach to Quantum Electrodynamics*, *Phys. Rev.* **76** (1949) 769–789.

[86] M. E. Peskin and D. V. Schroeder, *An Introduction To Quantum Field Theory*. Westview Press.

[87] W. Pauli, *Dear Radioactive Ladies and Gentlemen*, *Phys. Today* **31N9** (1978) 27.

[88] J. Chadwick, *The Intensity Distribution in the Magnetic Spectrum of Beta Particles from Radium (B + C)*, *Verh. Phys. Gesell.* **16** (1914) 383–391.

[89] J. Davis, Raymond, D. S. Harmer, and K. C. Hoffman, *Search for Neutrinos from the Sun*, *Phys. Rev. Lett.* **20** (1968) 1205–1209.

[90] **SNO** Collaboration, Q. R. Ahmad *et. al.*, *Measurement of the Rate of $\nu_e + d \to p + p + e^-$ Interactions Produced by ^8B Solar Neutrinos at the Sudbury Neutrino Observatory*, *Phys. Rev. Lett.* **87** (2001) 071301, [nucl-ex/0106015].

[91] S. Bilenky, *Introduction to the Physics of Massive and Mixed Neutrinos*. Lecture Notes in Physics. Springer.

[92] J. Schechter and J. Valle, *Neutrino Masses in SU(2) × U(1) Theories*, *Phys. Rev.* **D22** (1980) 2227.

[93] D. Caldwell, *Current Aspects of Neutrino Physics*. Physics and Astronomy. Springer.

[94] **CHOOZ** Collaboration, M. Apollonio *et. al.*, *Limits on Neutrino Oscillations from the CHOOZ Experiment*, *Phys. Lett.* **B466** (1999) 415–430, [hep-ex/9907037].

[95] **MINOS** Collaboration, P. Adamson *et. al.*, *Measurement of the Neutrino Mass Splitting and Flavor Mixing by MINOS*, *Phys. Rev. Lett.* **106** (2011) 181801, [arXiv:1103.0340].

[96] W. Winter, *Neutrino Physics*. Cambridge University Press.

[97] F. Reines and C. Cowan, *A Proposed Experiment to Detect the Free Neutrino*, *Phys. Rev.* **90** (1953) 492–493.

[98] F. Reines and C. Cowan, *Detection of the Free Neutrino*, *Phys. Rev.* **92** (1953) 830–831.

[99] B. Pontecorvo, *Inverse Beta Process*, *Camb. Monogr. Part. Phys. Nucl. Phys. Cosmol.* **1** (1991) 25–31.

[100] L. W. Alvarez, *A Proposed Experimental Test of the Neutrino Theory*, .

[101] R. Davis Jr., *Attempt to Detect the Antineutrinos from a Nuclear Reactor by the ^{37}Cl ($\bar{\nu}$,e^-) ^{37}A Reaction*, *Phys. Rev.* **97** (1955) 766–769.

[102] C.-S. Wu, E. Ambler, R. Hayward, D. Hoppes, and R. Hudson, *Experimental Test of Parity Conservation in Beta Decay*, *Phys. Rev.* **105** (1957) 1413–1414.

[103] T.-D. Lee and C.-N. Yang, *Question of Parity Conservation in Weak Interactions*, *Phys. Rev.* **104** (1956) 254–258.

[104] M. Goldhaber, L. Grodzins, and A. Sunyar, *Helicity of Neutrinos*, *Phys. Rev.* **109** (1958) 1015–1017.

[105] J. Christenson, J. Cronin, V. Fitch, and R. Turlay, *Evidence for the 2 Pi Decay of the K(2)0 Meson*, *Phys. Rev. Lett.* **13** (1964) 138–140.

[106] R. Bionta, G. Blewitt, C. Bratton, D. Casper, A. Ciocio, *et. al.*, *Observation of a Neutrino Burst in Coincidence with Supernova SN1987a in the Large Magellanic Cloud*, *Phys. Rev. Lett.* **58** (1987) 1494.

[107] J. Thomas and P. Vahle, *Neutrino Oscillations: Present Status and Future Plans*. World Scientific Publishing Company Incorporated.

[108] http://hep.bu.edu/~superk/.

[109] **Super-Kamiokande** Collaboration, Y. Fukuda *et. al.*, *Measurement of a Small Atmospheric Muon-Neutrino / Electron-Neutrino Ratio*, *Phys. Lett.* **B433** (1998) 9–18, [hep-ex/9803006].

[110] **Super-Kamiokande** Collaboration, Y. Fukuda *et. al.*, *Study of the Atmospheric Neutrino Flux in the Multi-GeV Energy Range*, *Phys. Lett.* **B436** (1998) 33–41, [hep-ex/9805006].

[111] Ahmad, Q. R. et al, *Direct Evidence for Neutrino Flavor Transformation from Neutral-Current Interactions in the Sudbury Neutrino Observatory*, *Phys. Rev. Lett.* **89** (Jun, 2002) 011301.

[112] **SNO** Collaboration, S. Ahmed *et. al.*, *Measurement of the Total Active B-8 Solar Neutrino Flux at the Sudbury Neutrino Observatory with Enhanced Neutral Current Sensitivity*, *Phys. Rev. Lett.* **92** (2004) 181301, [nucl-ex/0309004].

[113] **SNO** Collaboration, B. Aharmim *et. al.*, *Electron Energy Spectra, Fluxes, and Day-Night Asymmetries of B-8 Solar Neutrinos from Measurements with NaCl Dissolved in the Heavy-Water Detector at the Sudbury Neutrino Observatory*, *Phys. Rev.* **C72** (2005) 055502, [nucl-ex/0502021].

[114] J. F. Amsbaugh, J. Anaya, B. J.b, T. Bowles, M. Browne, *et. al.*, *An Array of Low-Background He-3 Proportional Counters for the Sudbury Neutrino Observatory*, *Nucl. Instrum. Meth.* **A579** (2007) 1054–1080, [arXiv:0705.3665].

[115] **The KamLAND** Collaboration, A. Gando *et. al.*, *Constraints on θ_{13} from A Three-Flavor Oscillation Analysis of Reactor Antineutrinos at KamLAND*, *Phys. Rev.* **D83** (2011) 052002, [arXiv:1009.4771].

[116] **K2K** Collaboration, A. Suzuki *et. al.*, *Design, Construction, and Operation of SciFi Tracking Detector for K2K Experiment*, *Nucl. Instrum. Meth.* **A453** (2000) 165–176, [hep-ex/0004024].

[117] S. Kawabata, R. Sugahara, T. Tauchi, N. Ujiie, Y. Watanabe, *et. al.*, *Topaz Barrel Electromagnetic Calorimeter*, *Nucl. Instrum. Meth.* **A270** (1988) 11.

[118] K. Nitta, E. Aliu, S. Andringa, S. Aoki, S. Choi, *et. al.*, *The K2K SciBar detector*, *Nucl. Instrum. Meth.* **A535** (2004) 147–151, [hep-ex/0406023].

[119] **K2K MRD GROUP** Collaboration, T. Ishii *et. al.*, *Near Muon Range Detector for the K2K Experiment: Construction and Performance*, *Nucl. Instrum. Meth.* **A482** (2002) 244–253, [hep-ex/0107041].

[120] **MiniBooNE** Collaboration, A. Aguilar-Arevalo *et. al.*, *Improved Search for $\bar{\nu}_\mu \to \bar{\nu}_e$ Oscillations in the MiniBooNE Experiment*, *Phys. Rev. Lett.* **110** (2013), no. 16 161801, [arXiv:1207.4809].

[121] **T2K** Collaboration, K. Abe *et. al.*, *The T2K Experiment*, *Nucl. Instrum. Meth.* **A659** (2011) 106–135, [arXiv:1106.1238].

[122] **T2K** Collaboration, K. Abe *et. al.*, *Precise Measurement of the Neutrino Mixing Parameter θ_{23} from Muon Neutrino Disappearance in an Off-axis Beam*, arXiv:1403.1532.

[123] **T2K** Collaboration, K. Abe *et. al.*, *Indication of Electron Neutrino Appearance from an Accelerator-produced Off-axis Muon Neutrino Beam*, *Phys. Rev. Lett.* **107** (2011) 041801, [arXiv:1106.2822].

[124] **RENO** Collaboration, S.-H. Seo, *New Results from RENO*, arXiv:1312.4111.

[125] **Double Chooz** Collaboration, Y. Abe *et. al.*, *Background-Independent Measurement of θ_{13} in Double Chooz*, arXiv:1401.5981.

[126] P5 Committee, *US Particle Physics: Scientific Opportunities: A Strategic Plan for the Next Ten Years*, *Phys. Rev.* **D39** (May, 2008) 3378.

[127] China Guangdong Nuclear Holding Company. Jinyu Building, No.100 North Road, West 3rd Ring, Beijing, China, 100048, http://www.cgnpc.com.cn.

[128] L. Mikaelyan and V. Sinev, *Neutrino Oscillations at Reactors: What Next?*, *Phys. Atom. Nucl.* **63** (2000) 1002–1006, [hep-ex/9908047].

[129] Z. Yu, L. Zhan, and L. Wen, *Sensitivity Using Rate+Spectrum*, *Internal Note #7699* (2012).

[130] http://environmentalchemistry.com/yogi/periodic/crosssection.html.

[131] **Daya Bay** Collaboration, F. An *et. al.*, *Observation of Electron-Antineutrino Disappearance at Daya Bay*, arXiv:1203.1669.

[132] http://www.areva.com/EN/maps-59/areva-worldwide-presence.html.

[133] http://www.nrc.gov/reading-rm/basic-ref/glossary.html.

[134] China Techenergy Co., Ltd.
http://www.ctecdcs.com/en/solutions/solution_03.html,
http://www.ctecdcs.com/en/solutions/solution_02.html.

[135] K. Schreckenbach, G. Colvin, W. Gelletly, and F. Von Feilitzsch, *Determination of the Antineutrino Spectrum from U-235 Thermal Neutron Fission Products up to 9.5 MeV*, *Phys. Lett.* **B160** (1985) 325–330.

[136] F. Von Feilitzsch, A. Hahn, and K. Schreckenbach, *Experimental Beta Spectra from Pu-239 and U-235 Thermal Neutron Fission Products and Their Correlated Antineutrino Spectra*, *Phys. Lett.* **B118** (1982) 162–166.

[137] A. Hahn, K. Schreckenbach, G. Colvin, B. Krusche, W. Gelletly, *et. al.*, *Antineutrino Spectra from Pu-241 and Pu-239 Thermal Neutron Fission Products*, *Phys. Lett.* **B218** (1989) 365–368.

[138] P. Vogel, G. Schenter, F. Mann, and R. Schenter, *Reactor Antineutrino Spectra and Their Application to Antineutrino Induced Reactions. 2.*, *Phys. Rev.* **C24** (1981) 1543–1553.

[139] T. Mueller, D. Lhuillier, M. Fallot, A. Letourneau, S. Cormon, *et. al.*, *Improved Predictions of Reactor Antineutrino Spectra*, *Phys. Rev.* **C83** (2011) 054615, [arXiv:1101.2663].

[140] P. Huber, *On the Determination of Antineutrino Spectra from Nuclear Reactors*, *Phys. Rev.* **C84** (2011) 024617, [arXiv:1106.0687].

[141] http://www.nndc.bnl.gov/ensdf/.

[142] Z. Bin, R. Xi-Chao, N. Yang-Bo, Z. Zu-Ying, A. Feng-Peng, and C. Jun, *A Study of Antineutrino Spectra from Spent Nuclear Fuel at Daya Bay*, *Chinese Physics C* **36** (2012), no. 1 1.

[143] X. Qian and W. Wang, *The Uncertainty on Total IBD Events Caused by the Time Averaging of Reactor Flux and Target Mass*, *Internal Note #7208* (2012).

[144] P. Vogel and J. F. Beacom, *The Angular Distribution of the Neutron Inverse Beta Decay, $\bar{\nu}_e + p \to e^+ + n$*, *Phys. Rev.* **D60** (1999) 053003, [hep-ph/9903554].

[145] H. Band, R. Brown, R. Carr, X. Chen, X. Chen, *et. al.*, *Assembly and Installation of the Daya Bay Antineutrino Detectors*, *JINST* **8** (2013) T11006, [arXiv:1309.1557].

[146] P. Huang, P. Li, Z. Fu, C. He, Y. Ding, J. Li, and M. Qi, *Study of Attenuation Length of Linear Alkylbenzene as LS Solvent*, *Journal of Instrumentation* **5** (2010), no. 08 P08007.

[147] W. Beriguete, J. Cao, Y. Ding, S. Hans, K. M. Heeger, *et. al.*, *Production of Gadolinium-Loaded Liquid Scintillator for the Daya Bay Reactor Neutrino Experiment*, arXiv:1402.6694.

[148] X. Chen, X. Luo, Y. Heng, L. Wang, X. Tang, X. Ma, H. Zhuang, H. Band, J. Cherwinka, Q. Xiao, and K. Heeger, *Leakage Tests of the Stainless Steel Vessels of the Antineutrino Detectors in the Daya Bay Reactor Neutrino Experiment*, *Science China Technological Sciences* **56** (2013), no. 1 148–151.

[149] K. Luk, *Radioactivity of Materials Considered or Used in Daya Bay*, *Internal Note #2576* (2011).

[150] Z. Wang, C. Yang, M. Guan, W. Zhong, J. Liu, Z. Zhang, Y. Ding, R. Wang, J. Cao, Y. Wang, and H. Lu, *Study of a Prototype Detector for the Daya Bay Neutrino Experiment*, *Nuclear Instruments and Methods in Physics Research Section A: Accelerators, Spectrometers, Detectors and Associated Equipment* **602** (2009), no. 2 489 – 493.

[151] H. Band, J. Cherwinka, M. Chu, K. Heeger, M. Kwok, *et. al.*, *Daya Bay Antineutrino Detector Gas System*, *JINST* **7** (2012) P11029, [arXiv:1210.0643].

[152] H. Band, J. Cherwinka, E. Draeger, K. Heeger, P. Hinrichs, *et. al.*, *The Daya Bay Antineutrino Detector Filling System and Liquid Mass Measurement*, *JINST* **8** (2013) P09015, [arXiv:1307.1089].

[153] J. Cao, M. Guan, J. Xu, and C. Yang, *Muon Flux Note*, *Internal Note #7604* (2012).

[154] M. A. et al., *The MACRO Detector at Gran Sasso*, *Nuclear Instruments and Methods in Physics Research Section A: Accelerators, Spectrometers, Detectors and Associated Equipment* **486** (2002), no. 3 663 – 707.

[155] R. Santonico and R. Cardarelli, *Development of Resistive Plate Counters*, *Nucl. Instrum. Meth.* **187** (1981) 377–380.

[156] H. Band, J. Cherwinka, K. Heeger, P. Hinrichs, M. McFarlane, *et. al.*, *Low-Background Monitoring Cameras for the Daya Bay Antineutrino Detectors*, *JINST* **7** (2012) P08005, [arXiv:1204.3500].

[157] Aptina Imaging. Private correspondence.

[158] **Borexino** Collaboration, G. Alimonti *et. al.*, *Science and Technology of BOREXINO: A Real Time Detector for Low-Energy Solar Neutrinos*, *Astropart. Phys.* **16** (2002) 205–234, [hep-ex/0012030].

[159] H. O. Back, *Internal Radioactive Source Calibration of the Borexino Solar Neutrino Experiment*. PhD thesis, Virginia Tech, Blacksburg, Virginia, 2004. Ph.D. Thesis.

[160] SENKO Advanced Components, Inc. 225 Cedar Hill Street Marlboro, MA, USA 01752, http://www.senkoadl.com.

[161] SENKO Advanced Components, Inc. Private correspondence.

[162] Cree, Inc. 4600 Silicon Drive Durham, NC, USA 27703, http://www.cree.com.

[163] National Control Devices, LLC. PO Box 455 Osceola, MO, USA 64776, http://www.controlanything.com.

[164] AMETEK Programmable Power, Inc. 9250 Brown Deer Road San Diego, CA 92121, http://www.sorensen.com.

[165] National Instruments Corporation. 11500 N Mopac Expwy Austin, TX 78759-3504, http://www.ni.com.

[166] S. Zhang, Y. Wang, M. Ye, X. Li, Y. Zhang, J. Xu, J. Min, X. Du, and L. Zeng, *Detector control system for Daya Bay Reactor Neutrino Experiment*, *Science China Technological Sciences* **56** (2013), no. 8 1966–1973.

[167] Low Background Facility at Lawrence Berkeley National Laboratories. Private correspondence.

[168] Z. Wang, L. Wen, Z. Yu, and L. Zhan, *Energy Calibration and Reconstruction (AdScaled)*, *Internal Note #7314* (2012).

[169] C. Zhang, *Absolute IBD Efficiency — IBD MC Revisited*, *Internal Note #7548* (2012).

[170] S. Chen, B.-Z. Hu, G. Hussain, X. Ji, Z. Wang, H. Wei, J. Yu, and Y. Zhang, *Measurement of Theta13 with Hydrogen Neutron Capture*, *Internal Note #8556* (2014).

[171] B. Littlejohn, *Delayed Tail Shape and Energy Cut Uncertainties for P12E*, *Internal Note #8720* (2013).

[172] X. Qian, *Summary of Energy Scale Check*, *Internal Note #7518* (2012).

[173] X. Qian and C. Zhang, *Check of Energy Scale Uncertainty of AdSimple*, *Internal Note #7682* (2012).

[174] G. Cao and L. Zhan, *The Absolute IBD Selection Efficiency*, *Internal Note #7686* (2012).

[175] X. Qian, W. Wang, and L. Wen, *Summary of the Flasher Studies*, *Internal Note #7434* (2012).

[176] Y. Nakajima, J. P. Ochoa, H. Steiner, and P. K. Tsang, *Lab Study of Flasher PMTsSD-0150, SD-0191, SD-1639, SD-1640*, *Internal Note #8140* (2012).

[177] C. Lewis, B. Littlejohn, M. McFarlane, and D. Webber, *True Prompt Energy Spectrum TechNote*, *Internal Note #8608* (2013).

[178] X. Qian and F. Wu, *Accidental Background of EH1/EH3*, *Internal Note #7396* (2012).

[179] P. Hinrichs, C. Lewis, B. Littlejohn, M. McFarlane, and D. Webber, *Wisconsin Six Detector Rate-Shape Fitter Technote*, *Internal Note #8607* (2013).

[180] L.-J. Wen, J. Cao, K.-B. Luk, Y.-Q. Ma, Y.-F. Wang, *et. al.*, *Measuring Cosmogenic* ^{9}Li *Background in a Reactor Neutrino Experiment*, *Nucl. Instrum. Meth.* **A564** (2006) 471–474, [hep-ex/0604034].

[181] P. Huber, M. Lindner, and W. Winter, *Simulation of Long-Baseline Neutrino Oscillation Experiments with GLoBES*, *Comput. Phys. Commun.* **167** (2005) 195, [hep-ph/0407333].

[182] P. Huber, J. Kopp, M. Lindner, M. Rolinec, and W. Winter, *New features in the simulation of neutrino oscillation experiments with GLoBES 3.0*, *Comput. Phys. Commun.* **177** (2007) 432–438, [hep-ph/0701187].

[183] J. Cao, *Sensitivity with Shortened Tunnel*, *Internal Note #4968* (2010).

[184] C. Bemporad, G. Gratta, and P. Vogel, *Reactor Based Neutrino Oscillation Experiments*, *Rev. Mod. Phys.* **74** (2002) 297, [hep-ph/0107277].

[185] K. Nakajima, K. Inoue, K. Owada, F. Suekane, A. Suzuki, G. Hirano, S. Kosaka, T. Ohta, and H. Tanaka, *A Simple Model of Reactor Cores for Reactor Neutrino Flux Calculations for the KamLAND Experiment*, *Nucl. Instrum. Meth. A* **569** (2006) 837.

[186] P. Vogel and J. Engel, *Neutrino Electromagnetic Form-Factors*, *Phys. Rev.* **D39** (1989) 3378.

[187] **Particle Data Group** Collaboration, C. Amsler *et. al.*, *Review of Particle Physics*, *Phys. Lett.* **B667** (2008) 1.

[188] A. Balantekin and D. Yilmaz, *Contrasting Solar and Reactor Neutrinos with a Non-Zero Value of Theta13*, *J. Phys.* **G35** (2008) 075007, [arXiv:0804.3345].

[189] G. Fogli, E. Lisi, A. Marrone, A. Palazzo, and A. Rotunno, *Hints of $\theta_{13} > 0$ from Global Neutrino Data Analysis*, *Phys. Rev. Lett.* **101** (2008) 141801, [arXiv:0806.2649].

[190] P. Huber, M. Lindner, T. Schwetz, and W. Winter, *Reactor Neutrino Experiments Compared to Superbeams*, *Nucl. Phys.* **B665** (2003) 487–519, [hep-ph/0303232].

[191] P. Huber, M. Lindner, and W. Winter, *Superbeams versus neutrino factories*, *Nucl. Phys.* **B645** (2002) 3–48, [hep-ph/0204352].

[192] G. L. Fogli, E. Lisi, A. Marrone, D. Montanino, and A. Palazzo, *Getting the Most from the Statistical Analysis of Solar Neutrino Oscillations*, *Phys. Rev. D* **66** (Sep, 2002) 053010.

[193] Z. Djurcic *et. al.*, *Uncertainties in the Antineutrino Production at Nuclear Reactors*, *J. Phys.* **G36** (2009) 045002, [arXiv:0808.0747].

[194] T. Schwetz, *What is the Probability that Theta13 and CP Violation Will be Discovered in Future Neutrino Oscillation Experiments?*, *Phys. Lett.* **B648** (2007) 54–59, [hep-ph/0612223].

[195] H. Band, *Why Wait for Eight?*, *Internal Note #5987* (2011).

[196] C. Lewis, *Revisiting the SNF*, *Internal Note #9408* (2013).

[197] I. Frank and I. Tamm, *Coherent Visible Radiation of Fast Electrons Passing Through Matter*, *C. R. Acad. Sci. URSS* **14** (1937) 109–114.

[198] S. Jetter, Y. Nakajima, and Q. Xin, *A Unified Non-Linearity Model for the Shape Analysis*, *Internal Note #8983* (2013).

[199] B. Littlejohn, *Energy Resolution for a Shape Analysis*, *Internal Note #8211* (2012).

[200] X. Qian and F. Wu, *Note of How We Get Singles and Accidentals*, *Internal Note #7679* (2012).

[201] W. Gu, G. Li, and J. Liu, *AmC Background Note*, *Internal Note #8979* (2013).

[202] K. Pearson, *X. On the criterion that a given system of deviations from the probable in the case of a correlated system of variables is such that it can be reasonably supposed to have arisen from random sampling*, *The London, Edinburgh, and Dublin Philosophical Magazine and Journal of Science* **50** (1900), no. 302 157–175.

[203] R. Brun and F. Rademakers, *ROOT: An Object Oriented Data Analysis Framework*, *Nucl. Instrum. Meth.* **A389** (1997) 81–86.

[204] F. James and M. Winkler, *Minuit Users Guide*, *CERN, Geneva* (2004).

[205] P. Hinrichs, M. McFarlane, and D. Webber, *UW Fitting Code, and How to Speed Up Minimizers*, *Internal Note #8440* (2012).

[206] https://www.physics.wisc.edu/resources/computing.

[207] Y. Nakajima, J. P. Ochoa, and P. K. Tsang, *A Measurement of* $\sin^2(2\theta_{13})$ *and* Δm^2 *at Daya Bay Using Rate and Shape Information*, *Internal Note #8774* (2013).

[208] J. Ling, X. Qian, W. Wang, and C. Zhang, *BCW Rate+Shape Analysis Technote*, *Internal Note #8768* (2013).

[209] G. Cao, M. He, J. Soren, Z. Yu, L. Zhan, F. Zhang, and W. Zhong, *Oscillation Parameter Fit Using Rate Plus Shape*, *Internal Note #8925* (2013).

[210] C. Zhang, X. Qian, and P. Vogel, *Reactor Antineutrino Anomaly with Known* θ_{13}, *Phys. Rev.* **D87** (2013) 073018, [arXiv:1303.0900].